DUCTILITY OF REINFORCED CONCRETE

MASONRY SHEAR WALLS

By

MARWAN MOHAMED TAREK SHEDID

B. Sc.

A Thesis

Submitted to the School of Graduate Studies

in Partial Fulfillment of the Requirements

For the Degree

Master of Applied Science

McMaster University

MASTER OF APPLIED SCIENCE (2006)   McMaster University

(CIVIL ENGINEERING)   Hamilton Ontario

TITLE: Ductility of Reinforced Concrete Masonry Shear Walls

AUTHOR: Marwan Shedid, B.SC. (Ain Shams University)

SUPERVISOR: Professor R. G. Drysdale

NUMBER OF PAGES: xix, 244.

ABSTRACT

To assess the ductility of shear walls under earthquake loading, more experimental evidence is strongly needed. Ductile response can be achieved through the development of a flexural plastic hinge at the base characterized by yielding of the vertical reinforcement. The length of the plastic hinge and the ultimate curvatures within this region are the essential parameters affecting the ductility and ultimate displacements of reinforced masonry shear walls. The discrepancies in existing information regarding the length of plastic hinges and ultimate curvature may be attributed to the effects of many shear wall parameters such as distribution and amount of vertical and horizontal steel, level of axial load, and wall aspect ratio.

The focus of this study was to evaluate the effect of different parameters on plastic hinge length, energy dissipation, and on general ductility of masonry shear walls. To address the aforementioned goal, six fully grouted reinforced masonry walls were tested under fully reversed cyclic lateral loading. All walls were designed to experience ductile flexural failure. The test matrix was chosen to investigate the effects of the amount and distribution of vertical reinforcement and the level of applied axial load on the lateral loading response and ductility of reinforced masonry shear walls. To examine the effects of these parameters, measurements of the applied loads, vertical and horizontal displacements as well as strains in the reinforcing bars were used to analyze the behaviour of the walls. Also, from these measurements, other quantities used in analysis were

determined, including displacement ductilities, curvature profiles, energy dissipation and equivalent plastic hinge length.

The results show high ductile capability in the plastic hinge region and very little degradation of strength for cyclic loading. High levels of energy dissipation in the reinforced concrete masonry shear walls were achieved by flexural yielding of the vertical reinforcement. All walls showed increasing hysteretic damping ratios with increase in displacement. Results showed that displacement ductility and energy dissipation were highly sensitive to increases in amount of vertical reinforcement but were less dependent on the level of applied axial stress. The results of this study also showed that the measured plastic zone length decreases with increase of the amount of reinforcement while it is almost the same for the different levels of axial stress. Based on the test results, it was shown that reinforced concrete masonry shear walls may be utilized in high intensity seismic areas with performance meeting or exceeding current expectations.

DEDICATIONS

To my Mother & Father,

To my Brother,

& To my Wife.

ACKNOWLEDGMENTS

All praise and gratitude be to ALLAH with the blessings
of whom the good deeds are fulfilled.

I wish to express my deep gratitude to my advisor Prof. Robert Drysdale for his interest, encouragement and insight throughout this research. His constructive criticism had a major impact on developing my way of thinking and research. I would like to thank Prof. Ahmad Hamid for his support and supervision during the initial phase of setting up the test matrix for this research. Sincere thanks are due to Dr. Wael El Dakhakhni for his assistance and advice during the period of the research. I would like to thank Eng. Shawn Miller for his assistance during the experimental work. A word of thanks is due to the technicians Mr. David Perrett, Mr. Maurice Forget and Mr. Bernard Neuwenhuis for their help in the laboratory.

The financial supports of the Ontario Research and Development Challenge Fund (ORDCF) through the McMaster University Centre for Effective Design of Structures, and McMaster University are gratefully acknowledged. Provision of mason time by Ontario Masonry Contractors Association and Canada Masonry Design Centre is appreciated. The supply of concrete blocks and grout by Boehmer Block Ltd is gratefully acknowledged.

I would like thank my Professor Osama Hamdy for teaching me reinforced concrete structures design during my senior year. His continuous support, encouragement and guidance when I was a demonstrator in the Structural

Department in Ain Shams University are invaluable. I am also very grateful to Professor El Mostafa Hegazy who first introduced me to the challenging science of Earthquake Engineering and by his way of teaching made me fall in love with it.

At last but not the least, I would especially like to say that no words can express my gratitude to my parents, Maha and Tarek and to my brother, Mostafa, for everything they did, and are still doing for me. Without their continuous support, love, prayer and encouragement throughout my life I would have never been the one I am now. Special thanks are due to my wife, Yasmine, for her patience, understanding, and unwavering encouragement during the past year. Many thanks to my grandma, Nan, for her care and for everything she has done for me during my stay in Canada.

TABLE OF CONTENTS

CHAPTER ONE – INTRODUCTION

CHAPTER TWO - EXPERIMENTAL PROGRAM

LIST OF FIGURES

Page

LIST OF TABLES

Page

LIST OF SYMBOLS

A_{cr} Cracked cross section area of wall

A_e Effective area resisting shear

A_g Horizontal cross section area of wall (ie: length x thickness)

A_h Area of horizontal reinforcement in a typical cross section

A_r Aspect ratio of wall (ie: height/ length)

A_s Area of vertical reinforcement in the wall

c Distance from compression fibres to the neutral axis

C_m Compression force in cross section of a masonry wall

c_y Length of compression zone at first yield of reinforcement

c_u Length of compression zone corresponding to maximum load

d_b Reinforcing bar diameter

d_i Distance from the compression fibre to the location of reinforcement

d_1 Distance from extreme compression fibre to the first tension bar

E_i Energy dissipation at any displacement level

E_y Energy dissipation corresponding to yield displacement

E_m Modulus of elasticity ($850 \times f'_m$)

f'_g Compressive strength for grout

f'_m Average compressive strengths of masonry four course prisms

f_s Tensile stress in vertical reinforcement

f_y Yield strength of vertical reinforcement

G_m Shear modulus ($0.4 E_m$ for rectangular sections)

h_w Wall height

I_{cr} Cracked moment of inertia of wall

I_e Effective moment of inertia of wall

I_g Gross moment of inertia of wall

k Stiffness of walls (load/ displacement)

l_w Wall length

l_p Plastic hinge length

M_u Moment resistance at maximum strain in masonry

M_y Moment resistance at first yield of reinforcement

P Applied axial load

Q_u Flexural shear capacity at strain of 0.0025 in masonry

Q_y Lateral load resistance at first yield of reinforcement

R_d Ductility-related force modification factor

R_o Overstrength-related force modification factor

R_{size} Overstrength-related force modification factor that accounts for rounding of sizes and dimensions

R_φ Overstrength-related force modification factor that accounts for reduction factors

R_y Overstrength-related force modification factor that accounts for actual yield to minimum specified yield

R_{sh} — Overstrength-related force modification factor that accounts for strength enhancement due to strain hardening

R_{mech} — Overstrength-related force modification factor that accounts for the development of sequential plastic hinges in redundant structures

S_h — Vertical spacing between horizontal reinforcement

t — Thickness of wall

T — period of structure

T_s — Tension force in cross section of a masonry wall

V — Top load acting on the wall

V_m — Shear strength of masonry wall provided by the masonry

V_{max} — Maximum shear strength of the wall

V_s — Shear strength of masonry wall provided by horizontal steel

V_u — Lateral load resistance at maximum strain in masonry

V_u^s — Shear capacity of masonry wall

Δ_p — Plastic displacement of wall

Δ_{shear} — Shear displacement

Δ_u — Lateral wall displacement at maximum compressive strain

Δ_y — Lateral wall displacement at first yield of reinforcement

ε_{mu} — Maximum compressive strain in masonry

ε_y — Yield strain of steel reinforcement

ζ_{eq} — Equivalent viscous damping

φ_u — Curvature at the base of the wall at maximum strain in masonry

φ_y — Curvature at the base of the wall at first yield of reinforcement

μ_Δ — Displacement ductility

μ_φ — Curvature ductility

θ_y — Rotation of the wall at first yield of reinforcement;

θ_p — Plastic rotation of the wall

ρ_h — Ratio of steel reinforcement in horizontal direction

ρ_v — Ratio of steel reinforcement in vertical direction

CHAPTER 1

INTRODUCTION

1.1   Background

Masonry is one of the oldest forms of construction and has been characterized by its ease of construction and durability. Traditional masonry was able to resist large compressive forces and was quite durable. Although the tensile strength of traditional masonry was generally quite low, the weight of the massive walls and the floors was usually sufficient to offset the tensile stresses caused by minor lateral loads. However, a series of earthquakes during the 19th and the 20th century (Imperial Valley (1892), San Fernando (1906), Long Beach (1933), San Fernando (1971), and Northridge (1994)) illustrated the seismic vulnerability of these massive unreinforced masonry structures. Collapse and deterioration of many unreinforced masonry buildings during earthquakes slowed down the development of masonry while steel and reinforced concrete started to be used as modern structural materials.

Despite the delayed development as a modern material, masonry buildings remained a popular form for economically enclosing space in low seismic areas. For high seismic regions, the need for a more ductile and earthquake resistant form of masonry construction resulted in the development of reinforced masonry. Due to poor performance of unreinforced masonry during earthquakes, seismic design of all masonry structures commonly involves a high level of conservatism. However, the results of many studies, referenced by Sucuoglu and McNiven

(1991), have consistently revealed that reinforced masonry, when properly proportioned, detailed and constructed with satisfactory workmanship, provides adequate safety against seismic forces as will be discussed later.

Shear walls, which represent the vertical components of the lateral load resisting system of any masonry structure, transfer lateral loads from a horizontal diaphragm above to a diaphragm or wall below, or to the foundation; they also act as loadbearing walls to carry gravity loads to the foundation. Reinforced masonry shear walls have been widely used as the main lateral load resistance systems in medium-rise buildings because of their inherently large lateral stiffness and large lateral load resistance. These characteristics contribute to provide adequate drift control for well designed structural walls.

The advent of masonry shear wall systems was accompanied by a large number of experimental investigations. A large portion of the shear wall masonry research conducted to date has been dedicated to studying the in-plane behaviour of masonry under different combinations of axial load and lateral shear force. Studies investigating the in-plane behaviour of reinforced masonry shear walls identified flexural and shear types of failure mechanisms.

Flexural failure is characterized by the tensile yielding of vertical reinforcement, the formation of a plastic hinge zone and, eventually, crushing of the masonry at the critical wall section. This mechanism is generally the preferred failure mode, as it is ductile and is effective in dissipating energy by yielding of reinforcement.

Shear failure is characterized by diagonal tension cracking or shear slip along bed joints. Wall panels that fail in a predominantly shear mode exhibit more brittle behaviour and more rapid strength degradation after the maximum strength is developed as illustrated in Fig. 1.1. Research conducted on shear walls indicates that the controlling mechanism mainly depends on several properties of the wall such as height to length ratio (aspect ratio), the level of applied axial load, and the amount of horizontal and vertical reinforcement. Shear deformations tend to govern the behaviour of low aspect ratio walls, whereas, for relatively high aspect ratio, the response is most likely to be flexural.
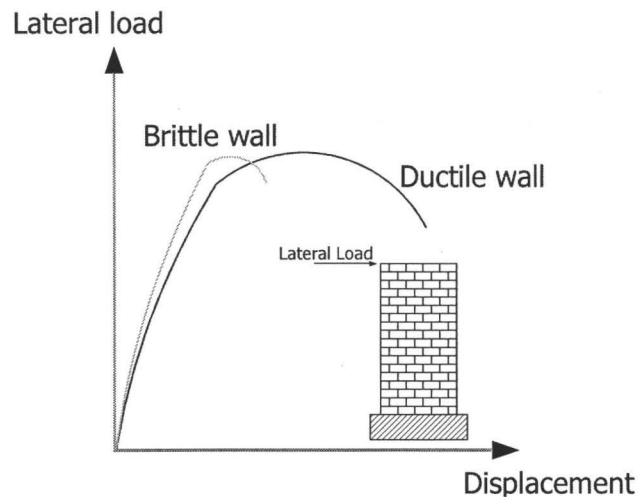
Fig. 1. 1: Load-displacement relationships for reinforced masonry shear walls

In regions where strong earthquake ground motions are anticipated, it is not economically feasible to design a structural wall to remain elastic during a severe earthquake as the design force will be very high. The economical design of masonry to withstand seismic loading requires development of ductility in masonry shear walls as a strategy to reduce the level of force attracted by the

building during the earthquake. The ductile behaviour is achieved by developing flexural plastic hinges at the base of the building for the case of shear walls and by allowing inelastic deformations to occur. Inelastic deformations perform a fuse-like function to limit actions on other structural elements and can provide significant damping.

1.2   Problem statement

Flexural plastic hinging of reinforced masonry shear walls is not well quantified yet is a critical aspect of the seismic response of shear walls. Paulay and Priestley (1992) indicated that the plastic hinge length cannot be defined with great precision. They also indicated that its length is affected primarily by the length of the wall, the moment gradient at the base, and the axial load intensity. To date, data related to these subjects is scarce as is evident in widely different and changing expectations regarding plastic hinge length, which will be presented in the literature review. [Paulay and Priestley (1992) suggest plastic hinge length, l_p of 0.3 to 0.8 time the wall length, l_w. CSA S304.1 (2004) recommends $l_p = l_w/2$ or $h_w/6$ but up to l_w for moderate ductility, whereas IBC (2000) recommends $l_p = l_w/2$]. Guidance for designers in codes tends to incorporate limitations as a result of lack of sufficient information and to ensure safety.

The plastic hinge length has a significant effect on the ductility of structural elements and, subsequently, on the force modification factor for the building. Relationships based on the equal energy principle for the force

modification factor and the displacement ductility, μ_Δ, defined as the ratio of the ultimate and the yield displacement, are presented in Appendix C. Equations relating the plastic hinge length to displacement ductility are presented in Appendix D. Using the equations presented in Appendix D shows that an increase of the plastic hinge length, l_p, results in a significant increase of the displacement ductility of the wall as indicated in Fig. 1.2. This increase in displacement ductility will then affect the force modification factor for the structure.
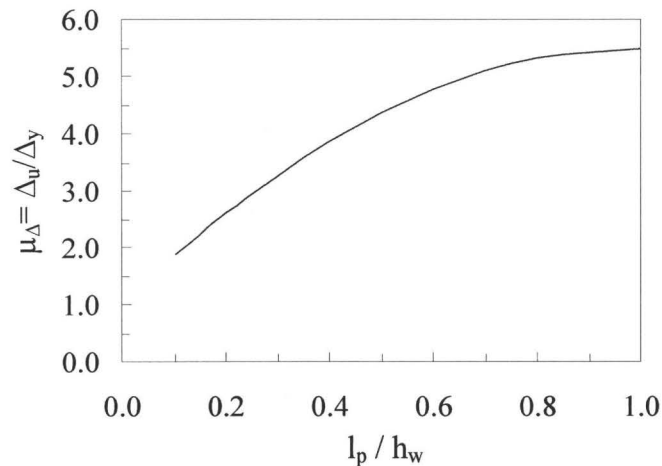
Fig. 1. 2: Effect of plastic hinge length on displacement ductility
(for a constant curvature ductility, see details in Appendix D)

Structures resist earthquake loading either by elastic or inelastic behaviour. Structures designed for immediate occupation after severe earthquake loading must behave almost elastically which results in high seismic design forces and limited displacements. Structures designed for life safety are allowed to behave inelastically which results in lower seismic design forces and higher displacements. Allowing the structure to deform and exhibit higher displacement

ductility will result in higher force reduction, as shown in Fig. 1.3 (see Appendices C and D for review of definition and calculation of displacement ductility and force modification value). The three curves in Fig. 1.3 represent three different responses of structures subjected to lateral loading. Following the principle of equal energy, the areas under the three load-displacement curves, representing the total energy, are equal, which indicates that these three structures having different behaviour will safely resist the lateral loading. The levels of damage are expected to increase with increased inelastic displacement.
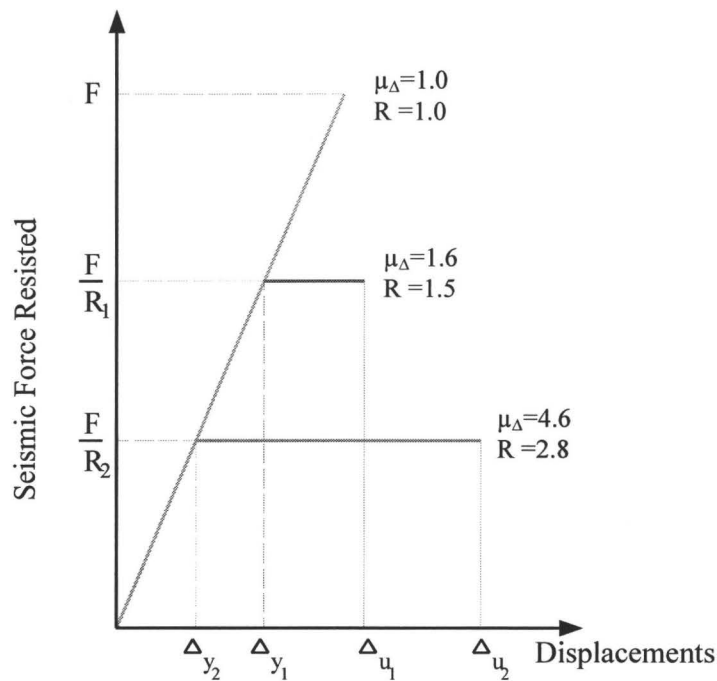
Fig. 1. 3: General structural response (Appendix C)

A good estimation of the length of the plastic hinge is required to calculate wall ductility with reasonable accuracy. A current problem is that the plastic hinge length should be better defined and its effect more accurately predicted in

order not to over-design structures, which may result in stiffer buildings that may introduce a compounding effect of attracting more forces during earthquakes.

1.3   Research significance and objectives

This study addresses the flexural response of ductile reinforced masonry shear walls up to large post-peak displacements corresponding to significant strength degradation. The primary objective of the research is to explore and document the effects of several parameters affecting the plastic hinge length under cyclic reversed loading. The results of the study are intended to provide a step forward towards a better prediction of ductility levels for reinforced masonry shear walls. Another objective of this research is to compare the observed experimental wall performance with the design requirements of the CSA S304.1 (2004) and the force modification factors for ductile reinforced masonry shear walls.

1.4   Scope

In order to achieve the research objectives, a testing program consisting of six reinforced masonry shear walls was chosen. It was thought that this would be a sufficient number to permit study of the effect of amount and distribution of vertical reinforcement as well as the effect of level of axial load on the response of reinforced masonry walls. Study of the length of the plastic hinge zone is also an important objective as also is ductility and energy dissipation related to evaluation of force modification factors.

It was decided that all walls would be tested under cyclic lateral loading and that all walls should exhibit ductile flexural failure. Measurements of the applied loads, vertical and horizontal displacements as well as strains in the reinforcing bars were identified as necessary for analysis of the behaviour of the walls. Also, from these measurements, other quantities to be used in the analysis would be developed, including displacement ductilities, curvature profiles, energy dissipation and equivalent plastic hinge length.

1.5   Literature review

1.5.1 Introduction

Early investigations of masonry shear walls started by the late 1950's (Benjamin and Williams (1958), Schneider (1956) and Scrivener (1966)), but it was not until the beginning of the 1970's that available research facilities enabled studying the seismic behaviour of masonry shear walls under reversed cyclic loading (Williams (1971) and Meli (1972)). Most of the recent studies on seismic behaviour of reinforced masonry shear walls include the effect of wall aspect ratio, amount of horizontal and vertical reinforcement, and level of applied axial load. The following sections present a brief review of the available studies focusing on the in-plane behaviour of reinforced masonry shear walls. It is not the intent here to cover every study conducted, but rather to report the information most directly related to this research. Sections 1.5.2 and 1.5.3 contain reviews of previous work conducted on shear and flexural behaviour of reinforced concrete masonry shear

walls. Reviews on flexural behaviour of reinforced concrete walls, related studies on in-plane loading, background to force modification factors, and reviews of code provisions are included in Sections 1.5.4 to 1.5.7, respectively.

1.5.2 Study of shear-dominated masonry wall behaviour

The shear cracking mechanism in masonry shear walls, as will be explained below, has been investigated by many researchers in the past. As will be discussed, the shear strength of masonry walls has been shown to depend on masonry compressive strength, applied axial load, aggregate interlock, and the amounts of horizontal and vertical reinforcement.

Failures of shear-dominated walls are mainly characterized by diagonal tension cracking. This type of crack forms when the principal diagonal stress exceeds the masonry tensile strength. Shing et al. (1989) indicated that before diagonal tension cracking, shear strength of masonry walls mainly relies on the tensile strength of the masonry as well as the applied axial load. Up to the formation of the first crack, the horizontal reinforcement carries almost zero force. However, once diagonal cracks occur, the shear resistance is distributed between the horizontal steel, the aggregate interlock mechanism, the uncracked masonry zone at the compression toe of the wall, and dowel action of the vertical steel.

Shing et al (1989) also indicated that the applied axial load significantly increases aggregate interlock which in turns increases the shear resistance of the

wall. With the enhancement of aggregate interlock due to the increase of the applied axial load, they indicated that the post-cracking shear resistance increases as well as the ductility for the shear-dominated walls. They also indicated that the influence of the amount of horizontal reinforcement on shear strength is not consistent, but a shear wall with an increased amount of vertical or horizontal reinforcement exhibits better ductility and energy dissipation capabilities. They concluded that reinforced masonry shear walls (with shear controlled capacity) can exhibit a certain extent of ductility and energy dissipation capabilities under cyclic displacement reversals and are, therefore, suitable for seismic resistance provided that proper reinforcement guidelines are followed.

The sequence of formation of major diagonal cracks was explained with the aid of a monotonic test on specimens, with aspect ratio of one, where horizontal steel was carefully instrumented with strain gauges in the vicinity of the diagonal crack (Shing et al. (1990)). A diagonal strut was formed to sustain the vertical and lateral load after two major diagonal cracks had formed (see Fig. 1.4) and at this stage, the horizontal steel is in compression rather than in tension. After the formation of the third major crack, extending from one corner of the square wall to the other corner along the main diagonal, the strut is no longer effective and at this stage the shear resistance is taken by the residual strength of masonry and by the horizontal steel that is subjected to high tension in the vicinity of the crack. Shing et al. (1990) concluded in this study that the overall shear stiffness prior to major diagonal cracking tends to be proportional to the axial

compressive stress and that the ductility of shear-dominated walls is relatively low unless a large amount of horizontal reinforcement is introduced.
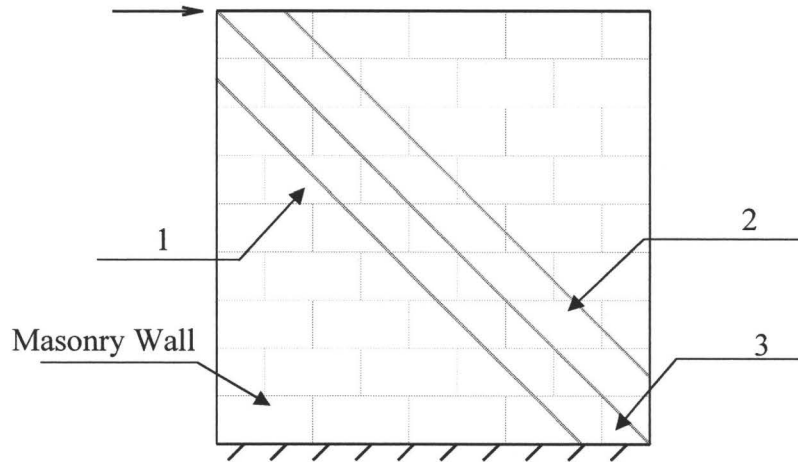
Fig. 1.4: Diagonal cracks sequence (Shing et al. (1990))

Sucuoglu and McNiven (1991) studied the effect of the amount of horizontal reinforcement on the behaviour of reinforced masonry walls from the results of 18 single pier specimens, having an aspect ratio of one. They concluded that the amount of horizontal steel had a significant influence on the hysteretic shear behaviour while the distribution of vertical reinforcement had a negligible effect. They indicated that the horizontal reinforcement was effective in inhibiting the opening of the diagonal shear cracks, but, as the amount of reinforcement increased, its relative effect diminished. They explained this phenomenon as a function of the failure mode indicating that, when the horizontal steel yields, a ductile shear failure can be obtained where diagonal cracks do not open excessively but are distributed evenly over the wall height. On the other hand, higher amounts of horizontal steel restrain the post-cracking deformation

capacity, because the steel remains in the elastic range and does not contribute much to the overall lateral deformation of the wall.

The effect of the aspect ratio on shear behaviour of masonry walls was investigated by Brunner and Shing (1996). They tested three squat masonry shear walls, with aspect ratio (h/L) varying from 0.96 to 0.60, the walls were heavily reinforced (vertically) in order to promote the desired shear failure mechanism. The tests showed that walls with lower aspect ratios had higher stiffness and reached their maximum resistance at smaller displacements. They based prediction of the shear failure mode for walls with aspect ratio less than one (h/L<1) on geometry and they specified two types of shear resistance mechanism. The first type occurs in walls with aspect ratio slightly less than one, where the diagonal crack intersects the base in the compression zone. They suggested that part of the vertical force is transferred directly from the wall to the base at the compression toe while the remaining portion is transmitted across the diagonal crack, which leads to high aggregate interlock forces that add to the shear resistance of the wall. The second type of failure mechanism is for walls that are sufficiently squat where the diagonal crack intersects the base outside the compression zone. In this case, the entire area bounded by the compression block is effective in providing shear resistance at the compression toe and, assuming that the normal compression across the diagonal crack is small, the aggregate interlock forced are therefore minor.

Suter and Ibrahim (1999) investigated the effect of axial load, amount of vertical steel, and wall aspect ratio on the ductility of reinforced masonry shear

walls. They tested three 1.4 m high squat walls with aspect ratio of 0.64 to study the effects of different amounts of the vertical reinforcement and the magnitude of applied axial load on the lateral shear resistance of reinforced masonry shear walls. Two additional 1.4 m high squat walls with aspect ratios of 1.0 and 0.46 were tested to study the effect of aspect ratio on the shear behaviour of reinforced masonry walls. The experimental results indicated that even with increased wall length and increased vertical axial stress, various walls, having the same height, experienced first major diagonal cracks at almost the same lateral displacement. On the other hand, the post-cracking shear behaviour depended mainly on the amount of horizontal and vertical reinforcement and on the level of applied axial load. Test results indicated a reduction in the ductility of the walls with decreases in the aspect ratio. They also indicated that ductility tends to increase with increasing amount of vertical reinforcement and increasing level of axial load for shear-dominated walls. Suter and Ibrahim suggested that the reason for the increase of ductility due to the increase of the vertical reinforcement may be that it adds more confinement to the masonry and in turns improve its post-cracking performance. They also suggested that an increase in the axial load likely enhances the aggregate interlock forces which improve the post-cracking behaviour of the shear dominated walls.

Voon and Ingham (2004) tested ten single storey concrete masonry shear walls to investigate the effects of the amount and distribution of shear reinforcement, level of axial compressive stress, type of grout, and wall aspect

ratio on the shear strength of masonry walls under in-plane loading. Eight walls were 1.8 m long having an aspect ratio of one, one wall with aspect ratio of two had the same length, and the final wall was 3 m long with an aspect ratio of 0.6. The results of the tests indicated a benefit of distributing shear reinforcement throughout the height of the wall, as well as the beneficial effect of axial compressive load on the behaviour of masonry walls. The study also illustrated that masonry shear strength increases with a decrease of the aspect ratio. This finding also was indicated previously by Paulay (1980). The foregoing conclusions confirmed most of the previous research work conducted on shear walls. Voon and Ingham (2004) also investigated the effect of grouting on the behaviour of walls and concluded that partially grouted masonry walls had about the same maximum shear strength as fully grouted masonry walls when the net area shear stress is considered.

This section summarized the behaviour of shear dominated masonry walls under in-plane loading and presented different factors affecting the shear strength of masonry shear walls extracted from previous research. The following section covers some research related to flexural behaviour of masonry shear walls.

1.5.3 Study on flexure-dominated masonry walls

Flexure-dominated shear walls are characterized by flexural yielding of tensile reinforcement and toe crushing of the extreme compressive fibre. Flexural failure, at the end of the wall under compression, is typically initiated by vertical

cracking of the end blocks under compression. This is followed by block crushing, face shell spalling, grout crumbling, and buckling of vertical reinforcements at the ends of the wall.

Flexural behaviour of masonry shear walls is assumed to be less complicated than shear behaviour. Applying simple flexural theory based on the assumption that plane sections remain plane after bending, Shing et al. (1989) were able to predict the flexural strengths of the walls with good accuracy. They indicated that slender walls with high aspect ratio tended to fail in flexure and are more ductile than those that failed in shear.

Shing et al. (1989) investigated the effect of applied axial load on the behaviour of reinforced masonry shear walls. They indicated that the flexural capacity and stiffness of reinforced masonry shear walls increase with increasing axial compression load which may be attributed to the fact that the opening of the flexural cracks is significantly reduced by application of axial load. They concluded that the axial load may have more significant influence on the flexure strength than on the shear strength based on test results showing that the axial load can change the behaviour of the walls from a mixed flexure/shear mode to a brittle mode. On the other hand, they indicated that the increase of flexure capacity and stiffness due to the increase of axial load may not be a desirable factor in seismic resistance design as this was associated with a reduction of the flexural ductility. The delayed yielding of the tensile reinforcement as well as reaching compression failure at lower curvatures tend to reduce the flexural ductility of reinforced masonry shear

walls subjected to axial load. Also, they suggested that severe and accelerated toe spalling along with the higher tendency of the reinforcing bars to buckle under higher axial load tend to reduce the flexure ductility.

Based on the experimental results of testing more than 20 reinforced masonry shear walls, having aspect ratio of one, under in-plane loading, Shing et al. (1990) indicated that the strain profile measured at the base of a typical wall tends to be linear. However, for wall panels subjected to axial load, this profile deviates slightly from the plane section assumption of simple flexure theory. They indicated that this slight deviation will result in only minor redistribution of the tensile stresses in the flexure steel, and therefore will not lead to a significant change of the flexure strength. Shing et al. (1990) indicated that the average EI of the test walls tended to increase with increasing axial load, whereas, the ultimate curvature and displacements tended to decrease. The plastic hinge length was measured for the flexural dominated walls in this study, having an aspect ratio of one. Based on the measured curvature profile over the wall height, the plastic hinge length was estimated to be equal to 0.15 times the wall length.

Inelastic deformations of cantilever masonry walls tend to be more concentrated at the base of the wall. Within this plastic hinge length, large curvatures must act to satisfy displacement demand. The plastic hinge zone is characterized by high inelastic curvatures and plastic yielding of the vertical reinforcement. Although, the moment variation over the height of a cantilever wall is linear, the actual curvature profile over the wall height is not linear and

16

large inelastic curvatures occur at the base. In order to idealize the actual curvature profile, Paulay and Priestley (1992) suggested representing it by an elastic region and a plastic region (within length l_p). They considered the plastic rotation to act at mid-height of the equivalent plastic hinge length (see Appendix D) and presented relationships between curvature ductility, displacement ductility, and equivalent plastic hinge length that were used to determine yield and ultimate displacements in concrete and masonry walls (see Eq. 1.1). The deflection, moment, and curvature relationships for a cantilever masonry shear wall are shown in Appendix D.

$$\mu_\Delta = 1 + 3 \text{ x } (\mu_\varphi - 1) \text{ x } \frac{l_p}{h_w} \text{ x } (1 - 0.5 \text{ x } \frac{l_p}{h_w}) \qquad \text{Eq. 1.1}$$

where :
h_w = Wall height;
μ_φ = Curvature ductility;
μ_Δ = Displacement ductility; and
l_p = Equivalent plastic hinge length

Based on integration of the curvature distribution along the wall height, theoretical values for the equivalent plastic hinge length, l_p, would be proportional to the wall height. They suggested that the plastic hinge length for reinforced masonry shear walls varies between 0.3 to 0.8 times the wall length. The theoretical values for estimating the plastic hinge length did not match well with experimental measured lengths as described by Paulay and Priestley (1992) and they justified this discrepancy as being due to tensile strain penetration inside the footing which is neglected in the theoretical approach. They indicated that the tensile strain penetration, which is the elongation of tensile flexural bars into the

footing, produces additional rotation and deflection. Paulay and Priestley (1992) also suggested a second reason for this discrepancy which was the increased spread of plasticity resulting from inclined flexure-shear cracking. These cracks result in higher steel strains above the base than predicted by the bending moment at that level. An estimation of the plastic hinge length was suggested based on the wall height and the size of the reinforcement as shown in Equation 1.2.

$$l_p = 0.08 \, h_w + 0.022 \, d_b \, f_y \qquad\qquad \text{Eq. 1.2}$$

where : d_b = The bar diameter in mm;
f_y = The yield stress of the reinforcement in MPa;
h_w = Wall height;
l_p = Equivalent plastic hinge length.

Studying the stability of ductile structural walls, Paulay and Priestley (1993) demonstrated that the major source of instability of the compression zone of the wall section within the plastic hinge region is the inelastic tensile steel strains imposed by preceding earthquake-induced displacement, rather than excessive compression strains. The potential for out-of-plane buckling of thin sections of ductile walls depends more on the magnitude of the inelastic tensile strains imposed on a region of the wall that is subjected to compression during the reverse cycle. During unloading of the wall corresponding to a change in direction of response displacements, tensile stresses in the bars are reduced to zero, while the crack width remains large, as a result of plastic tensile strains that developed in the bars. Until the cracks close, the internal compression force within the wall section must be resisted solely by the vertical reinforcement. In the case of masonry walls, with a single layer of reinforcement, there is no apparent stability

provided by the reinforcement until the crack closes on one side of the wall. Crack closure on one side results in out-of-plane curvature. Magnitudes of inelastic tensile strains within the plastic hinge region in a wall will depend on the deformations caused by severe earthquake. Paulay and Priestley (1993) suggested that a conservative plastic hinge length can be estimated using Eq. 1.3. The length given by this equation is assumed to be a reasonable approximation of the potential height of the wall over which out-of-plane buckling may occur.

$$l_p = (0.20 + 0.044\ A_r)\ l_w \hspace{3cm} \text{Eq. 1.3}$$

where: A_r = Aspect ratio of the wall
        l_w = Wall length

Priestley et al. (1993) conducted a total of 75 tests on a 5 storey full scale reinforced masonry building as a part of the U.S. – Japan Coordinated Program for Masonry Building Research. It was the first time that a stiff shear wall type 5-storey structure had been tested from beginning to end utilizing simulated seismic load input rather than predetermined fixed lateral load patterns. During the test, stable and ductile flexural hinges developed in each of the five floor slabs in the door way region between the two shear walls and no brittle failure occurred in the slabs. Inelastic deformation was limited to the desired location of the first storey walls, with yielding of vertical reinforcement extending up to the base of the third floor during the final test stage. The distributed cracks monitored at the end of the experimental test confirmed the development of ductile yield mechanisms. Priestley et al. concluded that masonry buildings in seismic zones can be designed with

ductile performance characteristics well in excess of the required design ductility without any loss of lateral load carrying capacity.

1.5.4 Study of reinforced concrete walls

A ductile response of a shear walls under strong seismic ground motions can be achieved through the development of a flexural plastic hinge at the base, and by resisting the anticipated horizontal shear forces over the height of the wall. The strategy aims at developing a plastic hinge at the base of the wall and ensuring that no shear failure develops prior to the attainment of the probable flexural resistance of the wall in that hinge. In order to achieve the specified length of plastic hinge, detailing requirement should include limits on the depth of the neutral axis, minimum wall thickness to prevent instability, and minimum horizontal and vertical reinforcement as recommended by Tremblay et al. (2001).

Zhang and Wang (2000) investigated the effect of high axial loading on the failure mechanism and ductility of reinforced concrete shear walls. Four isolated cantilever walls (aspect ratio of 2.5) were built and tested under combined action of constant axial load and horizontal load reversals. They indicated that high axial load restrained the development of major inclined cracks in the webs of the walls. This was due to the reduction of the principle tensile stress as a result of the applied axial compression. A flexural plastic hinge region approximately equal to 0.6 times the wall length was formed near the base of the wall. They indicated that the measured strengths for specimens subjected to high

axial load were larger than the predictions which may be attributed to the enhanced concrete strength due to confinement from surrounding concrete under high axial load. The experimental results indicated that walls subjected to high levels of axial load will fail in an undesirable out-of-plane buckling failure mode in the post-yielding stage, and thus, result in low ductility. On the other hand, walls subjected to lower axial load ratios exhibited a relatively high ductility associated with the more favourable crushing failure mode at the ends of the wall.

Investigating the cyclic behaviour of reinforced concrete cantilever walls, Pilakoutas and Elnashai (1995) tested and analysed six walls with aspect ratio of two. They found that the shear stiffness of specimens was not affected by shear reinforcement in excess of the amount required for shear strength purposes. An informative discussion on the deformation before and after yielding of vertical reinforcement was presented. Comparing the vertical deflection at the top of the wall versus deflection at quarter height, they indicated that, during the early stages of loading prior to yielding of the flexural reinforcement, the increment of vertical deformation over the top three quarters of the wall was significantly higher than at the quarter height. The aforementioned result indicated that elongation along the tension face varies more uniformly during the early loading stages where the development of cracks is likely to occur rather than plastic yielding. However, the permanent extension of the wall was almost identical at the top and at the quarter height in the post-yield cycles which indicated that almost all the vertical plastic extension took place within the lower quarter of the wall. They indicated that

significant extension of the walls in the vertical direction took place following yield due to the accumulation of irrecoverable strains mainly within the plastic zone.

Experimental research, conducted by Thomsen and Wallace (2004), involved the testing of six, approximately quarter-scale, wall specimens with rectangular and T-shape cross sections. The experimental results indicated that the inelastic shear response was limited primarily to the bottom third of the wall and that the measurements at the middle third were essentially elastic whereas they were almost constant over the top third of the wall. Thomsen and Wallace noted that the variation of the yield curvature, estimated between $0.0025/l_w$ and $0.004/l_w$, does not change the ultimate curvature estimates for drift levels between 1% and 2% by more than a few percent for wall with aspect ratio of 3. They also noted that the strain profiles depend only on the yield curvature, plastic hinge length, the design (target) displacement, the wall length and height, and the neutral axis depth. Given that design (target) displacement, wall height, and wall length are specified, and that ultimate curvature (thus the strain profile) is insensitive to the assumed yield curvature, the predicted strain profile for a given wall depends primarily on the assumed plastic hinge length. Naturally, shorter plastic hinge lengths make it necessary to achieve greater curvatures and, thus, higher magnitudes of strain along the wall. They also indicated that the depth of the neutral axis is relatively insensitive to changes in the extreme fibre strain once yielding of boundary longitudinal reinforcement occurs. They indicated that the

use of plastic hinge length of between 0.33 to 0.5 times the wall length results in very good agreement between the predicted and measured strain profiles, with better agreement obtained for the rectangular wall with a hinge length of 0.33 times the wall length.

1.5.5 Related studies

Khattab and Drysdale (1993) investigated the effect of horizontal and vertical reinforcement on the shear response of grouted concrete masonry wall panels. The biaxial testing technique used in this study provided an opportunity to investigate the behaviour of reinforced masonry assemblage under a state of pure shear stress without any interference from flexural and axial stresses. They concluded that relating the effectiveness of shear reinforcement only to its percentage is incorrect and that shear reinforcement can only improve shear strength and ductility when adequate detailing and distribution of shear reinforcement between the horizontal and vertical direction is involved. Kattab and Drysdale indicated that it is important to distribute the shear reinforcement between the vertical and horizontal directions to be able to resist part of the excess of forces that cannot be carried by masonry after the formation of diagonal cracks. Tests results proved that total percentages of shear reinforcement higher than 0.2% to 0.3% helped to avoid brittle shear failure and improved both strength and ductility of reinforced masonry assemblage.

Tikalsky et al. (1995) investigated the effect of lateral tension stresses on the compressive strength of reinforced masonry. Vertical tensile cracking was

found to reduce the compressive strength of walls in the direction normal to the tensile strain. Given the significant differences in material and material behaviour between reinforced concrete and reinforced masonry, they indicated that the use of the modified compression field theory formulated by Vecchio and Collins (1986) may be inappropriate. The authors tested full size specimens under transverse tension and orthogonal compression. The test results showed a consistent behavioural pattern that was different from that of reinforced concrete. They indicated that the decrease of compressive strength of reinforced masonry under lateral tension is not as significant as for reinforced concrete. The results showed that for large lateral tensile strains, the compressive strength deterioration of masonry is nearly linear with respect to increase of lateral tension.

Kenji Kikuchi et al. (1999) conducted an interesting investigation on the seismic behaviour of reinforced fully grouted concrete masonry walls. Eight different bearing walls, comprised of both reinforced masonry and reinforced concrete, were tested under reversed cyclic loading simulating an earthquake. Experimental results obtained from this study indicated that grouted masonry walls have almost the same seismic resistant capacity as the reinforced concrete walls having the same overall dimensions. Tests also indicated that reinforced fully grouted masonry walls had similar initial stiffness, ultimate strength, deformation capacity and failure mode as the reinforced concrete walls having the same thickness and reinforcement.

1.5.6 Force modification factor

The effects of earthquakes on structures have been studied for many decades. Natural period, soil condition, type of lateral force resisting system, intensity of the earthquake, and distance to the earthquake epicentre were found to affect seismic induced inertia forces on the structure. In order to simplify representation of the earthquake induced forces on structures, an equivalent static load approach is a common option used in many seismic codes and standards including the NBCC (2005).

Moreover, and because it is usually not economical to design a structure to remain elastic, equivalent static design forces are typically lower than the lateral strength required to maintain a structure in the elastic range in the event of strong earthquake. Reduction from the elastic strength demand is commonly accounted for through the use of force modification factor(s) (R). Modification factors prescribed in seismic codes are intended to account for ductility, and expected over-strength of various structure systems. These factors are based, in large part, on observation of the performance of different structural systems in previous strong earthquakes.

Although no all encompassing research has been done on identifying all parameters affecting R, by studying the data from performance of structures during earthquakes, laboratory test results, and analytical studies, it appears that the R factor(s) depends primarily on ductility, over-strength, period of vibration and redundancy in the system (ATC, 1995).

In the current NBCC (2005), the R values are expressed in terms of ductility (R_d) and over-strength (R_o). The recommended values of R_d are only dependent on the type of lateral load resisting system (that is, ductile frames, shear walls, etc.). The Canadian Standards Association CSA S304.1 (2004) specifies, for reinforced masonry walls, a ductility modification factor R_d equal to 1.5 or 2.0 based on specified limits to the length of the compression zone and limits on the wall height to thickness ratio. In the NBCC (2005), the R_d values are independent of the period of the structure.

Ductility factor R_d

Many research programs conducted in the past aimed at establishing relationships between force modification factors and displacement ductility. The component of the force modification factor, known as R_d, is used to reduce the lateral strength demand as the result of inelastic behaviour in the structure. In general, for structures allowed to behave in an inelastic manner during earthquakes, inelastic deformations increase as the lateral yield strength of the structure decreases.

Many studies [Elghadamsi and Mohraz (1987), Miranda (1993), Riddell and Newmark (1979), Newmark and Hall (1973), Nassar and Krawinkler (1991), Riddell et al. (1989), and Vidic et al. (1992)] were conducted to quantify the effect of the previously mentioned parameters on R_d. Based on these studies, the force modification factor, R_d, was found to be highly dependent on the period of vibration and the level of inelastic behaviour.

Paulay and Priestley (1992), Chopra (1995) and Drysdale et al. (1999) also indicate that the calculation of the force modification factor R_d resulting from inelastic behaviour of structures is primarily dependent on the period of the structure. For very rigid structures, having a very low period of vibration, the system will behave almost elastically resulting in the same magnitude of force for elastic and inelastic systems (equal acceleration principle) and thus will have a force modification factor equivalent to unity ($R_d = \mu_\Delta = 1$). For systems having a high period of vibration, an elastic and an inelastic system will have approximately the same displacement where an equal displacement principle is used to determine the relationship between displacement ductility and force modification factor ($R_d = \mu_\Delta > 1$). Whereas, for structures with low or moderate periods of vibration, the principle of conservation of energy can be used in which case the monotonic load-deformation diagram of the elastic system up to maximum deformation is the same as that of an elasto-perfectly plastic system subjected to the same excitation ($R_d = \sqrt{(2 \mu_\Delta - 1)}$).

It is clear from the previous discussion that it is essential to understand the behaviour of the structure and to identify characteristics such as the period and the ductility in order to determine the appropriate level of design force reduction. Since assigning a high R_d value adequate for long period structures will result in an unsafe design for structures having shorter periods. The opposite of assigning a low R_d value adequate for short period structures will lead to an uneconomical design for structures having longer periods. Moreover, since the period of the structures is inversely related to the square root of the stiffness indicates that any

decrease in the stiffness of a structure subjected to earthquake loading will lead to an increase in the period of the structure. This increase in period may result in shifting the structure from the zone of low or moderate period of vibration to the zone of high period of vibration. This can lead to the use of a different approach in calculating the force modification factor for the structure.

1.5.7 Codes and Standards

In seismic design of masonry structures, the MSJC (2005) divides reinforced masonry shear walls in three categories based on ductility requirements and level of seismic risk. The basic information on these categories is summarized in Table 1.1. **Ordinary reinforced masonry shear walls** are permitted in areas of both low and moderate seismic risk. The response modification factor, R, assigned for this category is 2.0. The required level of performance is deemed to be achieved by creating conditions to achieve a strain gradient corresponding to a strain in the extreme reinforcement equal to 1.5 times the yield strain and maximum compressive strain in the masonry. **Intermediate reinforced masonry shear walls** are allowed to be used in the same low and moderate seismic areas as indicated for the pre-mentioned type, but have a response modification factor, R, equal to 3.5. In this case, the strain in the extreme reinforcement should be equal to 3.0 times the yield strain when extreme fibre strain in masonry reaches the maximum compressive strain. Only **special reinforced masonry shear walls** are allowed in all seismic risk areas. This category of walls has an R value of 5.0 and a strain gradient corresponding to a strain in the extreme reinforcement equal to 4.0 times the yield strain and maximum compressive strain in the masonry.

Guidelines on amount of vertical and horizontal reinforcement as well as the spacing between bars are presented in the code in order to achieve these prescribed strain profiles as summarized in Table 1.2.

Table 1. 1: Walls categories in MSJC (2005)
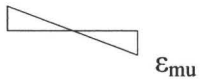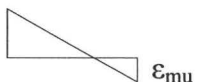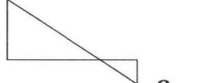
Type	Seismic risk area	Reduction factor (R)	Strain gradient
Ordinary	Low and Moderate	2.0	$1.5\ \varepsilon_y$ — ε_{mu}
Intermediate	Low and moderate	3.5	$3.0\ \varepsilon_y$ — ε_{mu}
Special	All	5.0	$4.0\ \varepsilon_y$ — ε_{mu}

Table 1. 2: Guidelines in MSJC (2005)

Type	Reinforcement Requirements			
	Horizontal		Vertical	
	Min. amount	Max. spacing	Min. amount	Max. spacing
Ordinary	$130\ mm^2$ in Bond Beam	3.0 m	$130\ mm^2$	3.0 m
	or 2 W1.7 wire as joint Reinforcement	0.4 m		
Intermediate	$130\ mm^2$ in Bond Beam	3.0 m	$130\ mm^2$	1.2 m
	or 2 W1.7 wire as joint Reinforcement	0.4 m		
Special	$130\ mm^2$ in Bond Beam	Lesser of: 1.2 m or 1/3H or 1/3L	1/3 of required shear Reinforcement	Lesser of: 1.2 m or 1/3H or 1/3L
	or 2 W1.7 wire as joint Reinforcement	0.4 m		

The Canadian standards, CSA S304.1 (2004), also specifies three categories of reinforced masonry shear walls when designing for seismic loading.

Shear walls of conventional construction are reinforced masonry designed for seismic loadings corresponding to $R_d = 1.5$ and should not exceed the height restrictions for masonry shear walls in accordance with Part 4 of the National Building Code of Canada. **Shear walls with limited ductility** are walls with height to length ratio greater than one, capable of limited ductility and are designed for seismic loadings corresponding to R_d equals to 1.5. The limiting strain requirement associated with this type of wall is deemed to be satisfied when the length of compression block at the ultimate limit state, c, is less than $0.2\ l_w$. This category is applicable for walls with aspect ratio less than 6.0 and maximum compressive strain in masonry not exceeding 0.0025.

Shear walls with moderate ductility are walls with height to length ratio greater than or equal to one, capable of moderate ductility and are designed for seismic loadings corresponding to R_d equal to 2.0. The limiting strain requirement assigned for this type of wall is deemed to be satisfied when the length of compression block, c, is less than $0.2\ l_w$ for walls with aspect ratio less than 4.0 and for c less than $0.15\ l_w$ for walls with aspect ratio less than 8.0 with the same masonry maximum strain as previously mentioned. A comparison between the two types of ductile flexural shear walls addressed in the design standard (Cl. 10.17) is presented in Table 1.3. A variation of the latter category is for **Squat shear walls with moderate ductility.** These walls, with height to length ratio less

than one, should have unsupported heights that satisfy height to thickness (h/(t+10) ratio of less than 20. These squat walls are capable of moderate ductility and are designed for seismic loadings corresponding to R_d equal to 2.0; this level of ductility is deemed to be achieved by specifying ranges for horizontal and vertical amount of reinforcement.

Table 1. 3: Guidelines in CSA S304.1 (2004)

	Limited ductile shear walls	Moderately ductile shear wall
Aspect ratio (A_r)	> 1.0	> 1.0
h/(t+10)	< 18	< 14
R	1.5	2.0
l_p	greater of: l_w or $h_w/6$	greater of: l_w or $h_w/6$
c	< 0.2 l_w, for A_r < 6.0	< 0.2 l_w, for A_r < 4.0 < 0.15 l_w, for A_r < 8.0
Compressive strain	< 0.0025	< 0.0025
Horizontal reinforcement	Max spacing lesser of 1200 mm or ½ l_w	Max spacing lesser of 1200 mm or ½ l_w and should have 180° hooks around the outmost vertical bar

Where: h   = the unsupported height of the wall that contains the plastic hinge
     t   = thickness of the wall
    l_p = plastic hinge length
    c   = length of compression block
    l_w = length of the wall
    h_w = height of the wall

For reinforced concrete shear walls designed and detailed according to CSA. A23.3, the corresponding force modification factor is higher than for reinforced masonry shear walls. R_d values of 3.5 and 2.0 are assigned to ductile and moderately

ductile reinforced concrete shear walls, respectively. Whereas, for reinforced concrete shear walls designed and detailed according to MSJC (2005), the corresponding response modification factor is similar to reinforced masonry shear walls. R values of 5.0 and 4.0 are assigned to special and ordinary reinforced concrete shear walls, respectively. Compared to the American approach that assigns nearly same reduction factors for reinforced concrete and reinforced masonry, the Canadian seismic reduction factor, R, underestimates the ability of reinforced masonry to dissipate energy and to resist seismic loads. The result is a higher seismic loads and more expensive reinforced masonry buildings.

1.6   Conclusion

The wide range of plastic hinge lengths found in the previous work conducted on reinforced concrete and masonry shear walls indicate that more research should be conducted on this point in order to better predict and analyse components and structures under lateral loads. Factors such as amount of reinforcement, level of axial load, aspect ratio and moment gradient should be investigated in order to study the influence of each on the plastic hinge length.

Previous work conducted on reinforced masonry shear wall indicates that ductile behaviour can be achieved when shear walls are properly designed and detailed. Ductility needs to be better quantified in order to compare the corresponding force modification factors with the values specified in CSA S304.1 (2004).

Previous work indicated that reinforced masonry shear walls can be used in seismic zones as they are capable of dissipating energy through inelastic deformation of masonry and yielding of vertical reinforcements. The survey of the research literature indicates that more research is needed to better evaluate the energy dissipated through hysteretic behaviour in reinforced masonry shear walls.

CHAPTER 2
EXPERIMENTAL PROGRAM

2.1   Introduction

The experimental program presented herein was designed to investigate the cyclic flexural response of concrete masonry shear walls. A matrix of six test specimens was set to study the effects of axial load and the amount and distribution of vertical reinforcement along the wall on the plastic hinge length and on the inelastic response of reinforced concrete block masonry shear walls. Because of a construction fault discussed later, an additional wall was added to complete the test matrix. Monitoring the propagation of plasticization into the base was also an objective to assess the impact of this suggested phenomenon (Paulay and Priestley (1992)) on overall wall ductility.

This chapter includes seven additional sections starting with design and construction of the shear wall test specimens. This is followed by details of each test specimen and the results of auxiliary tests on masonry assemblage and the constituent materials. The test setup is described in Section 2.5 followed by a section on measurements and instrumentation. The chapter concludes with documentation of test procedure and final comments.

2.2   Design and construction of shear wall test specimens

This section describes the steps and criteria used in developing the test matrix as well as selecting the construction process.

2.2.1 Selection of shear wall dimensions

In order to achieve flexure dominated behaviour with distinct regions of plastic hinging, it was decided that the aspect ratio of the test walls (height/length) needed to be greater than one. Based on previous work conducted on shear walls with low aspect ratio at McMaster University (Miller et al. (2005)), an aspect ratio of two was chosen to achieve the aforementioned goals while not requiring greater construction and testing effort associated with larger aspect ratios. The idea of testing a wall having a compression zone length greater than one cell long was an important criterion in dimension selection. Also, to realistically represent actual shear wall behaviour, the possibility of having several vertical reinforcing bars in the wall was also a controlling condition in selection of the wall dimensions. Based on simple beam theory, it was found that the minimum satisfactory wall length should be 1.6 m or longer. As a practical minimum, the wall length was selected to be 1.8 m which allows for several symmetrical distributions of vertical reinforcement in the wall such as every cell, every other cell, and every fourth cell. The chosen wall length of 1.8 m resulted in a height of 3.6 m for this research and accommodated future extension of the current research to include shear walls with higher aspect ratios up to h/L = 5 for h = 9 m.

2.2.2 Choice of concrete block

The standard 2-cell hollow 20 cm concrete block (190 x 190 x 390 mm) widely used in Canada was selected for construction of the test walls. Although

available, smaller blocks were not selected because they are not easily reinforced and filled with grout. Also the potential for inelastic out-of-plane buckling addressed by Paulay and Priestley (1993) depends on the unsupported wall height to thickness ratio and use of 20 cm block reduced the potential of this problem so that tests could proceed without requiring intermediate support.

Each course of the 1.8 m long wall was constructed using four and half concrete blocks. Splitter and half splitter units were placed at both wall ends to have flat ends without any frogs, while the three middle units were standard stretchers as shown in Fig. 2.1. Having all walls horizontally reinforced with No. 10 bars, rather than using bed joint reinforcement, created the need for bond beams to accommodate this shear reinforcement. The webs of the blocks in courses containing horizontal reinforcement were saw cut then knocked-out to a depth of 90 mm forming a large continuous horizontal cell that accommodated the continuous bars and provided full embedment of the bar in grout. This type of block is commonly called a knock-out web block and is suitable for construction with horizontal reinforcing bars. Blocks with and without knock-out webs are shown in Fig. 2.2.
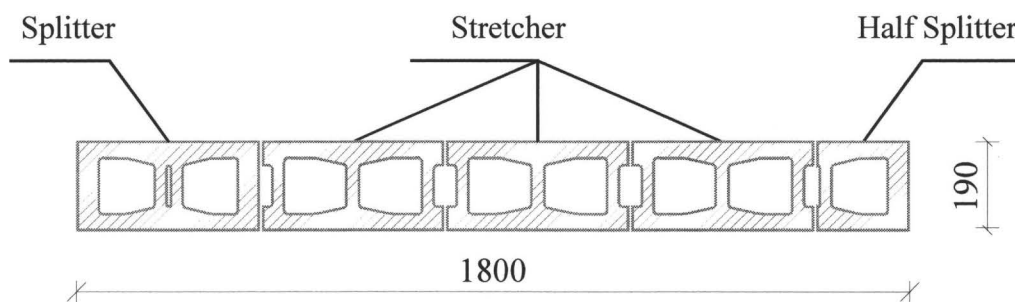
Fig. 2. 1: Section in a standard wall

a) Splitter unit   b) Stretcher unit   c) Half Splitter unit
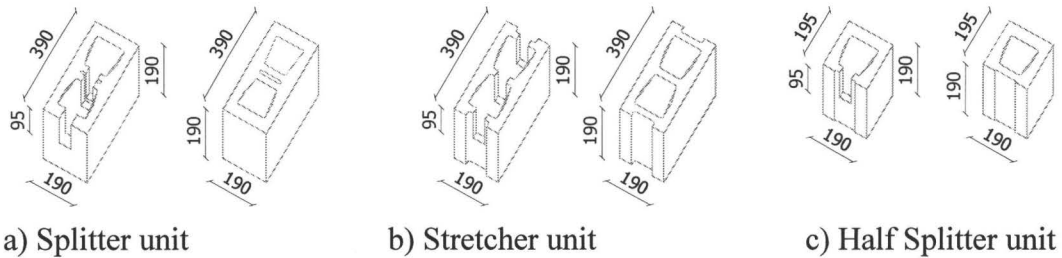
Fig. 2. 2: Blocks with and without knock-out webs

2.2.3 Shear wall construction

The construction of the test walls was divided into three stages starting with building the bases and followed by constructing the walls then filling the cells with grout.

2.2.3.1 Base beam construction

Reinforced concrete base beams were designed to provide fixed ends at the bottom of the walls. These base beams were designed to remain uncracked during testing and had dimensions of 2300 mm long x 500 mm wide x 600 mm deep. To provide a fixed base for the walls, the vertical reinforcement was anchored in the reinforced concrete base beam as shown in Fig. 2.3. The bars terminated in a 90° bend and were tied to the longitudinal bars in the base beam to help maintain accurate bar position during placing of the concrete. The concrete was placed in the forms for the base beams with the vertical reinforcement for the walls extending up for the complete height of the wall to avoid splicing the reinforcement. (The presence of splices in the plastic hinge region would introduce a complication not included in the planning for this initial phase of shear wall research.)
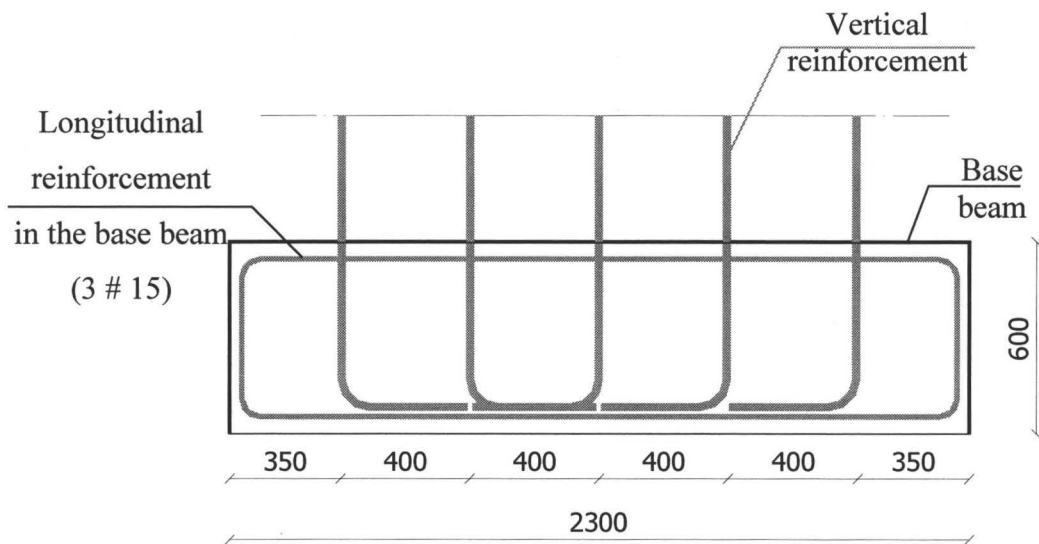
Fig. 2. 3: Details of wall reinforcement in the base beam

As shown in Fig. 2.4, a temporary wooden frame was constructed to hold the vertical steel bars in place during placing of the concrete for the base beams. Ten vertical plastic tubes (50 mm diameter) were placed in each base beam to accommodate the post-tensioning rods that were used to fasten the base beam of the shear wall specimen onto a reusable concrete floor slab used in the testing. Four horizontal plastic tubes (32 mm diameter) were also positioned to create access for horizontal post-tensioning of the base beams. This post-tensioning was added to provide confinement that increased the margin of safety against development of vertical cracks due to the pull up forces from the vertical bars during plastic hinging. Figure 2.5 shows the dimensions and details of the concrete base beams with locations of the vertical and horizontal tubes. All tubes were carefully fixed inside the wooden forms prior to concrete pouring in order to maintain their location and avoid filling with concrete.

Fig. 2. 4: Temporary support of vertical steel during concreting of base beam
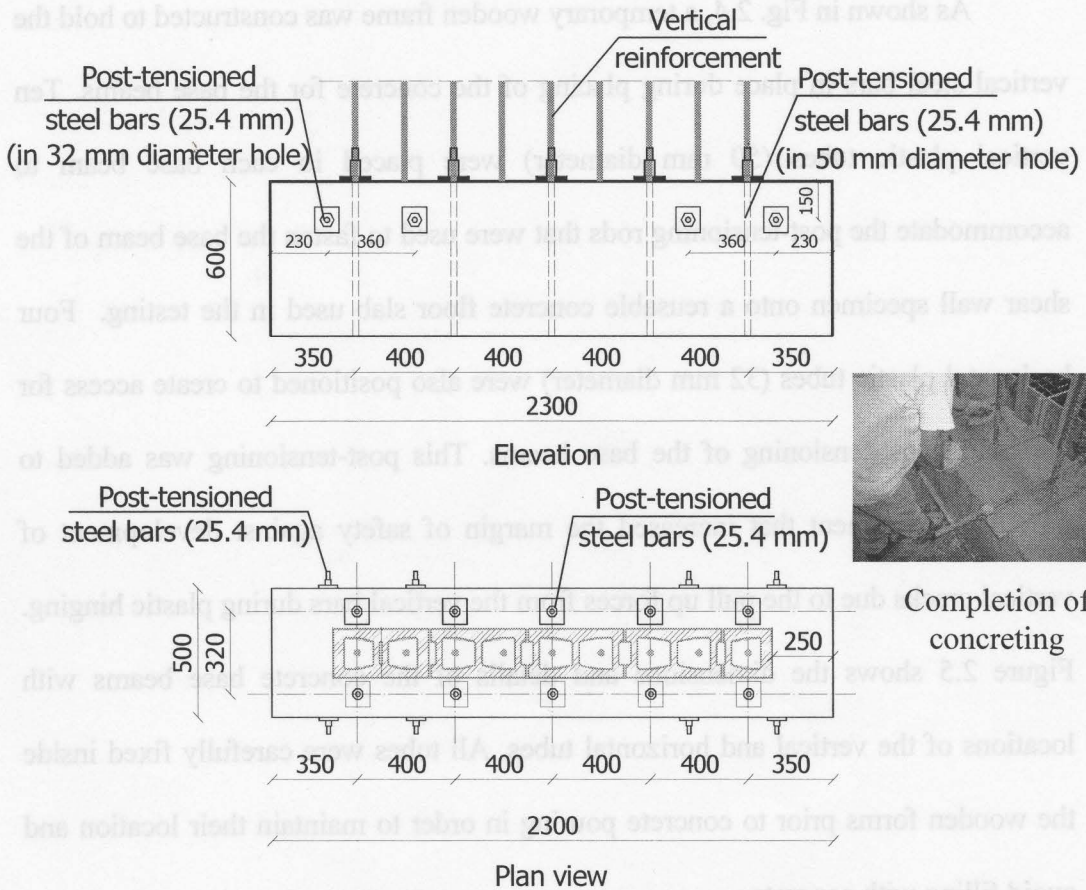
Fig. 2. 5: Details of reinforced concrete base beam and location of test wall

2.2.3.2 Wall construction

The second phase in construction of the shear wall specimens was difficult because all of the concrete blocks and horizontal reinforcement had to be threaded over the vertical reinforcing bars that extended to 3.6 m above the base beams. The blocks were lowered down to a consistent distance above the previous course to allow the mason to build the wall. An experienced mason constructed all of the shear walls in a running bond pattern with the hollow concrete masonry units using face shell mortar bedding and 10 mm mortar joint. Quality control for the mortar used during construction was achieved by drying the sand and weighting the constituent materials. Flow tests on each mortar batch provided a measure of the workability and served as an indicator of any differences in mix proportions. The horizontal reinforcement formed 180° hooks around the outmost vertical reinforcement. The 300 mm return leg of the hook extended to the second last cell as shown in Fig. 2.6 to provide adequate development length.
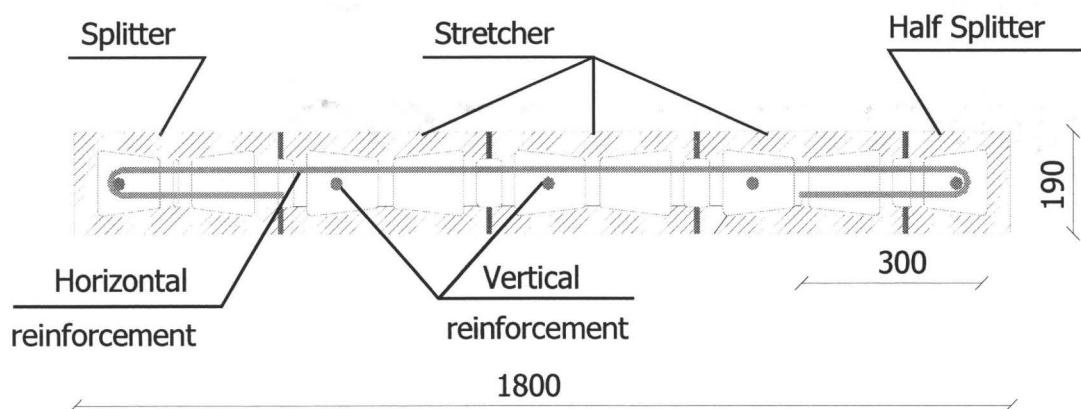
Fig. 2. 6: Details of horizontal reinforcement in a wall

2.2.3.3 Grouting

Grouting of the walls, which was the last phase of construction, was accomplished using fine grout having a 254 mm average slump, as shown in Fig. 2.7. The ready-mix grout was pumped using a 100 mm diameter hose. The high workability as well as the continuous vibration of the vertical reinforcement, as shown in Fig. 2.8, was required to fill the cells and cavities of the 3.6 m high walls. The knock-out webs along the wall length permitted the horizontal reinforcement to be fully encased in grout. As will be discussed later, some cavities and empty cells were discovered in the heavily reinforced walls and their presence was found to be due to hardened mortar dropping on the horizontal reinforcement especially at the ends of the walls where the 180° hairpin shaped hooks of the horizontal bars existed.
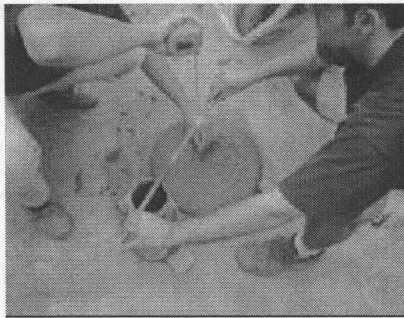
Fig. 2. 7: Slump test of grout   Fig. 2. 8: Placing and vibration of grout
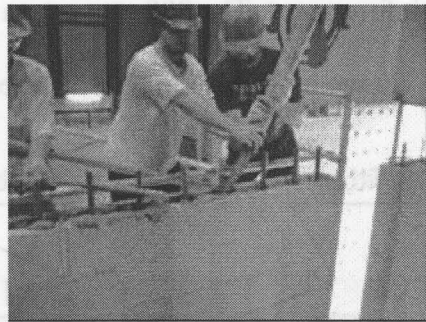
2.3   Details of shear wall test specimen

This section provides details of each test specimen and explains the test matrix used in this research. The predicted flexural and shear strengths of all walls are also presented as well as the wall deflection at the top.

2.3.1 Details of wall reinforcement

The test matrix consisted of six reinforced masonry walls that were built to be tested under in-plane lateral cyclic reversed displacement. Details of the reinforcement for all of the walls are shown in Fig. 2.9. A seventh wall was built during the testing as a duplication of the first wall tested. This was necessary due to incomplete grouting as will be discussed later. All walls had the prescribed aspect ratio of two and were designed to ensure that elastic and inelastic deformations would be dominated by flexure as previously mentioned.

Each wall was constructed with 81 concrete blocks in single wythe construction and was built on the previously described reinforced concrete base beam. All specimens were fully grouted and contained uniformly distributed vertical and horizontal reinforcement.

The horizontal reinforcements were placed in the 'knock-out' notch cut through the webs of the blocks. The presence of this notch significantly enhanced the continuity of the grout by forming a bond beam as was visible after removal of the face shells following testing. All walls, except Wall 3 and Wall 5, had a vertical reinforcing bar in every cell with spacing of 200 mm. Walls 3 and 5 were reinforced vertically in every other cell with spacing of 400 mm.

A summary of the test wall reinforcement ratios, number of bars, and level of applied axial stress is given in Table 2.1. The level of axial stress was calculated as a percent of the compressive strength of the assembly (f'_m). The areas of the vertical and horizontal reinforcement shown in Fig. 2.9 are also described as percentages of the gross area of the masonry cross section.

(a) Wall 5

(b) Wall 3

(c) Wall 4

(d) Walls 1,2,6, and 7
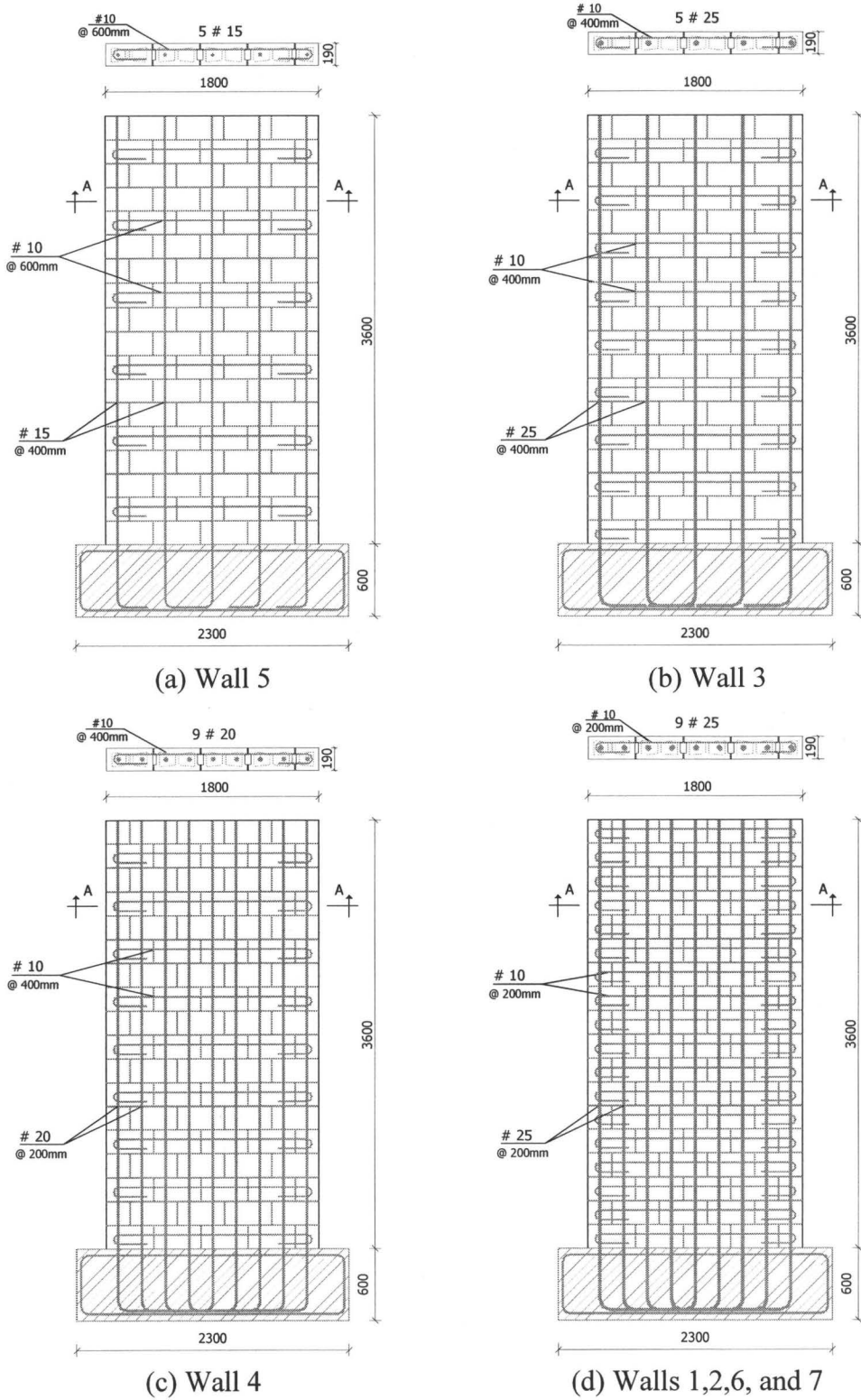
Fig. 2. 9: Reinforcement details for all test specimens

Walls 5, 4, and 2 had vertical steel ratios of 0.29%, 0.78% and 1.31% respectively. These walls were designed to illustrate the effect of amount of flexural reinforcement on the plastic hinge behaviour. Comparing the test results from Walls 3 and 4 having vertical steel ratios of 0.73% and 0.78%; respectively, will show the effect on the plastic hinge behaviour of nearly the same amount but different distributions of reinforcement. Walls 6, and 7 were duplicates of Wall 2, but were built to study the effect of externally applied axial compressive stress of about 5% and 10% of f'$_m$, respectively, (0.75 MPa and 1.5 MPa). Wall 2 was a replication of Wall 1 that, during testing, was found to be poorly grouted.

Table 2. 1: Matrix of test walls

Specimen designation	Wall dimensions	Vertical reinforcement		Horizontal reinforcement		Axial stress (MPa)
		Number of bars and bar size	ρ_v (%)	#10 bars @	ρ_h (%)	
W5		5 # 15	0.29	600 mm	0.08	0
W3		5 # 25	0.73	400 mm	0.13	0
W4	1800 mm x 3600 mm Length x height	9 # 20	0.78	400 mm	0.13	0
W1, W2		9 # 25	1.31	200 mm	0.26	0
W6		9 # 25	1.31	200 mm	0.26	0.75
W7		9 # 25	1.31	200 mm	0.26	1.50

2.3.2 Design of test specimen

This section contains explanation of how walls were designed for bending and checked for shear capacity and how deflections at the top of the walls were

predicted. During this phase, all walls were designed to fail in flexure with a safe margin for shear capacity.

2.3.2.1 Design for flexure

All walls were designed to exhibit ductile failure. The amount of reinforcement was selected based on a predetermined strain profile at failure following the MSJC (2005). In these initial calculations, the MSJC (2005) was used as it is more conservative than CSA S304.1 (2004). The strain profile depends on the ultimate tensile strain in the reinforcing steel when the extreme fibre compressive strain in the masonry reaches its maximum ($\varepsilon_m = 0.0025$). Except for Wall 5, the shear walls were designed to have steel strains ranging from 1.0 to 3.0 times the yield strain when the masonry reached its limiting compressive strain. Wall 5 was included in the test matrix to evaluate the effect of a low amount of steel on the plastic hinge length.

Several assumptions, such as calculating the compression force in the masonry using an equivalent rectangular stress block and including the contribution of vertical reinforcement in compression, were adopted during the design process. All calculations were based on yield strength of 500 MPa for vertical reinforcement, yield strength of 400 MPa for horizontal reinforcement, f'_m of 15 MPa, and self weight of 4.0 kN/m^2. All equations used to predict flexure strength are presented in Appendix A.

Table 2.2 contains the calculated flexural failure load and the corresponding strain profile for each wall. The axial load (P_t) indicated in the

following table is the total axial load at the base of the wall which includes the self weight of the wall in addition to the applied external axial load (P) expressed as an axial stress in term of compressive strength, f'_m.

Table 2. 2: Predicted flexural strength and strain profile

	W5	W3	W4	W1,W2	W6	W7
Steel bars	5 # 15	5 # 25	9 # 20	9 # 25	9 # 25	9 # 25
ρ_v	0.29	0.73	0.78	1.31	1.31	1.31
P_t (kN)	26	26	26	26	282	539
P/A (% f'm)	0	0	0	0	5	10
Q (kN) ($\varepsilon_m = 0.0025$)	118	256	260	382	402	459
Q (kN) ($\varepsilon_m = 0.003$)	119	262	268	399	424	482
Strain x ε_y	7.28	3.57	3.510	2.22	1.90	1.22

2.3.2.2 Design for shear

Walls were designed to have shear capacities much larger than the shear forces corresponding to the predicted flexural strengths. In order to ensure the desired flexural failure mechanism, several shear capacity formulas were investigated and the shear reinforcement was designed using the most conservative value. The shear equation in CSA S304.1 (2004) as well as equations reported by Paulay and Priestley (1992) were used to calculate the amount of horizontal reinforcement needed in walls. Paulay and Priestley (1992) presented two equations for calculating shear strength of masonry shear walls; one for inside the plastic hinge region and the other applied elsewhere. All equations presented in Appendix B were investigated and compared in Table 2.3.

Factors that account for variability in construction and in response were removed for these calculations.

Table 2. 3: Predicted shear strength

Specimen	Maximum axial stress (MPa)	CSA S304.1 (2004)					Paulay and Priestley (1992)				
			Outside plastic hinge zone		Inside plastic hinge zone			Outside plastic hinge zone		Inside plastic hinge zone	
		V_s	V_m	V_u^s	V_m^*	V_u^{s*}	V_s	V_m	V_m	V_m^*	V_u^{s*}
		(kN)	(kN)	(kN)	(kN)	(kN)	(kN)	(kN)	(kN)	(kN)	(kN)
W5	0	80	170	250	85	165	120	180	300	53	173
W3	0	120	170	290	85	205	180	180	360	53	233
W4	0	120	170	290	85	205	180	180	360	53	233
W2	0	240	170	410	85	325	360	180	540	53	413
W6	0.75	240	221	461	110	352	360	242	602	53	413
W7	1.50	240	272	512	136	376	360	303	657	53	413

V_s is the shear strength carried by the horizontal reinforcement

V_m is the shear strength carried by the masonry

V_m^* is the shear strength carried by the masonry inside the plastic hinge region

V_u^s is the maximum shear strength of the wall

$V_u^{s\,*}$ is the maximum shear strength of the wall inside the plastic hinge region

From the previous tabulated values, it can be concluded that the equation given in CSA S304.1 (2004) is more conservative than the one given by Paulay and Priestley (1992) for regions both within and outside of the plastic hinge zone. The shear strength achieved by the horizontal reinforcement and the masonry itself using the CSA S304.1 (2004) equation for all test wall was much greater

than the shear corresponding to flexural capacity. The values for shear strength in the plastic hinge regions were lower than the anticipated shears corresponding to flexural failure but these were assumed to be conservative and were not relied upon for design of horizontal reinforcement.

2.3.2.3 Deflection prediction at the top of the wall

When designing the walls, deflections at initial yielding of tension reinforcement and at ultimate conditions were predicted using simple flexural theory and applying the concept of plane sections remaining plane. Based on the equal energy principle, the relationship between ductility and force modification factor, using the displacement predictions, is explained in Appendix C. Plastic hinge length was assumed to be equal to half the length of the wall for all specimens (l_p = 900 mm) to provide this initial insight into plastic hinge behaviour.

2.4   Material properties

2.4.1 Steel properties

The four different sizes of steel reinforcing bars used were tested in tension to determine yield stress and elastic modulus. For each bar size used, three tensile specimens, 600 mm long, were tested. The results of the tensile tests are summarized in Table 2.4. Based on nominal area of bar, all reinforcing bars had yield strength close to 500 MPa except for the reinforcement used in Wall 7, constructed separately, where the yield strength was 25 % higher.

Table 2. 4: Steel properties

Specimen	Yield strength (MPa)			
	# 10 (100 mm^2)	# 15 (200 mm^2)	# 20 (300 mm^2)	# 25 (500 mm^2)
A	489	500	508	501
B	493	502	500	506
C	491	496	504	503
Average yield strength (C.O.V.) (%)	491 (0.41)	499 (0.61)	504 (0.79)	503 (0.59)

2.4.2 Properties of concrete in the base beams

Three cylinders were tested to evaluate the properties of the concrete used in the base beams for the walls. Average compressive strength after four months for the three cylinders was 39.8 MPa. This strength is somewhat higher than is likely to be used in footing in real construction. The concrete strength will influence bond slip that, in turn, may affect the extent of plasticization and effective hinge length inside the base.

2.4.3 Mortar properties

In order to achieve consistency during the construction process, a target mortar flow of 120 mm was selected. The mix proportions employed to attain this value are presented in Table 2.5. Compressive tests were conducted on mortar cubes in order to evaluate their strength and to ensure consistency of all component material used during construction. Forty batches, weighting 49.7 kg

each, were prepared during the construction of the six walls and the twenty seven prisms. For each batch, one flow test was conducted and three mortar cubes were taken in order to provide quality control during the whole construction process. Although standards specify a damp condition for sand for site use, dry sand was used in the mixes prepared in the laboratory for better quality control. Average flow tests resulted in mortar flow value of 125 mm and a C.O.V. of 27.3 %. Twenty randomly chosen mortar cubes (50 mm x 50 mm) were tested and resulted in an average compressive strength of 27.7 MPa and a C.O.V. of 11.6 %.

Table 2. 5: Mortar mix proportions

	kg/ batch	Parts by weight
Cement	7.65 kg	1.00
Lime	1.57 kg	0.20
Dry Sand	27 kg	3.53
Water	13.5 kg	1.76
Total	49.7 kg	6.49

2.4.4 Grout properties

Fine grout commercially available from a ready-mix company was pumped into the full 3.6 m wall height. The high workability of the grout, having 254 mm slump, resulted in filling of most of the cavities in the walls. Four block moulded prisms and two cylinders of grout were taken to determine the grout properties. Two of the grout prisms were block moulded with dimensions of 95

mm x 95 mm x 190 mm and two were poured inside the cells of the same type of blocks used in the walls as shown in Fig. 2.10. Grout prisms with same dimensions were cut later from the blocks. The grout was air cured in the mould consistent with curing of the grout in the walls. Compression tests conducted on the grout prisms and cylinders resulted in the compressive strengths shown in Table 2.6.

Problems with the pumping equipment and with achieving a sufficiently fluid grout resulted in some problems while grouting the first two walls. The high workability was reached by using additives and plasticizers. Because filling of the first two walls was conducted in two stages over the 3.6 m height, rapid hardening of the grout occurred over the hardened mortar droppings at several locations on the hairpin shaped hooks of the horizontal reinforcement. This resulted in some ungrouted regions in these two walls. The remaining walls were grouted in one 3.6 m lift height and showed good filling resulting in almost no empty or partially filled cells.
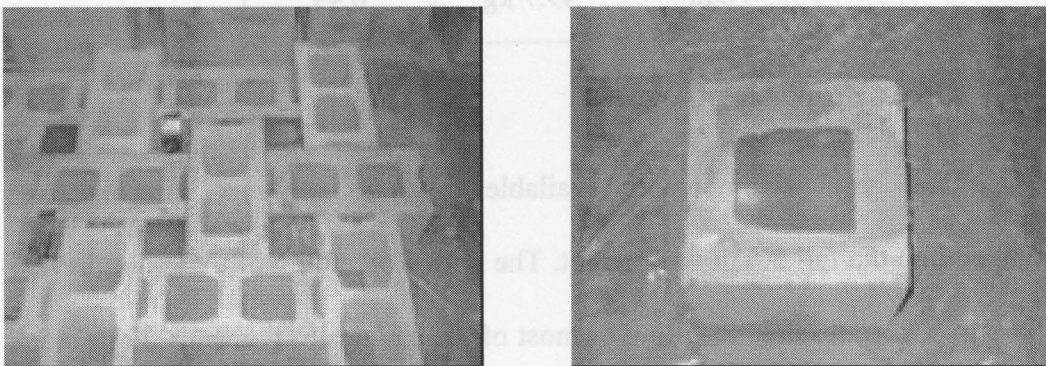
Fig. 2. 10: Block moulded grout prisms

Table 2. 6: Grout properties

Specimen	Grout strength (f'$_g$) (MPa)		
	Block moulded prism	Inside cells prism	Cylinders
1	37.7	36.3	39.2
2	35.3	37.5	36.3
Average	36.3	36.9	37.8

2.4.5 Block properties

Compression tests were conducted on six hollow concrete masonry units. Three stretchers and three splitters were tested in accordance with the CSA A165.1 using hard capping and 120 mm thick loading plates. Compressive strength for concrete masonry blocks, based on net area, is reported in Table 2.7.

Table 2. 7: Block compressive strength

Specimen	Stretcher unit		Splitter unit	
	Failure load (kN)	Strength (MPa)	Failure load (kN)	Strength (MPa)
A	1076	25.32	899	19.65
B	1006	23.69	915	19.98
C	1079	25.41	1001	21.86
Average (C.O.V.)	1054 (3.89)	24.81 (3.89)	938 (5.80)	20.49 (5.80)

Note: Areas used to calculate strength were: 45800 mm^2 for Splitter units and 42500 mm^2 for Stretcher units.

2.4.6 Prism properties

Twenty seven grouted masonry prisms, comprising sets of three prisms in nine groups, were tested to determine the compressive strength of the masonry

assemblage as well as the ultimate strain. As a part of the study, the effect of knock-out webs on the behaviour of the walls was investigated by comparing results from tests of prisms constructed with the different types of block.

The prisms were four blocks high by one block long (790 mm high x 390 mm long). Prism compressive strengths (f'_m) and strains (ε_0) at ultimate strength are reported in Table 2.8. The different configurations of prisms that were tested are shown in Fig. 2.11. Groups 1, 2 and 3 formed Type I of the tested prisms, (Fig 2.11(a)), and were constructed using splitter units in the first and third courses and half splitter in the second and fourth courses. These prisms represented the 200 mm region at both ends of the walls. Groups 4, 5 and 6 formed Type II, (Fig 2.11(b)), and were constructed with half splitter and half stretcher units in alternating courses and represented the second 200 mm region from the ends of the walls. Type III, (Fig 2.11(c)), consisting of Groups 7, 8 and 9 were constructed using stretchers cut into a quarter and three quarter unit in running bond in all of the four courses and represented a typical section at mid-length of the wall.

The twenty seven prisms were constructed by the same experience mason just after wall construction ended. The face shells as well as the end webs for all prisms were mortared. The grouting of the prisms was conducted on the same day as the grouting of the walls using the same ready-mix grout. Vibrators were used to ensure good filling and compaction of the grout inside the prisms.

Table 2. 8: Prisms Test Results

		Age (months)	f'$_m$ (MPa)	Average f'$_m$ (MPa) [C.O.V.] (%)	Strain at max stress (ε_0)	Average ε_0 [C.O.V.] (%)
Type I	G1	6	15.41	14.35 (7.25)	0.0017	0.00180 (9.62)
		7	14.30		0.0020	
		7	13.33		0.0017	
	G2	6	15.25	14.64 (----)	0.0018	0.00185 (---)
		8	14.02		0.0019	
		N/A	N/A		N/A	
	G3	6	16.19	16.04 (5.08)	0.0016	0.00173 (8.81)
		8	15.16		0.0017	
		8	16.77		0.0019	
Type II	G4	6	13.94	13.58 (---)	0.0019	0.00185 (---)
		7	13.23		0.0018	
		N/A	N/A		N/A	
	G5	6	13.72	14.16 (2.72)	0.0017	0.00180 (5.56)
		7	14.42		0.0019	
		7	14.35		0.0018	
	G6	6	15.81	--- (---)	0.0015	--- (---)
		N/A	N/A		N/A	
		N/A	N/A		N/A	
Type III	G7	6	15.78	16.10 (1.77)	0.0018	0.00187 (6.19)
		7	16.33		0.0020	
		8	16.18		0.0018	
	G8	8	17.23	16.81 (---)	0.0022	0.00210 (---)
		8	16.38		0.0020	
		N/A	N/A		N/A	
	G9	6	12.94	13.18 (---)	0.0019	0.00195 (---)
		8	13.41		0.0020	
		N/A	N/A		N/A	
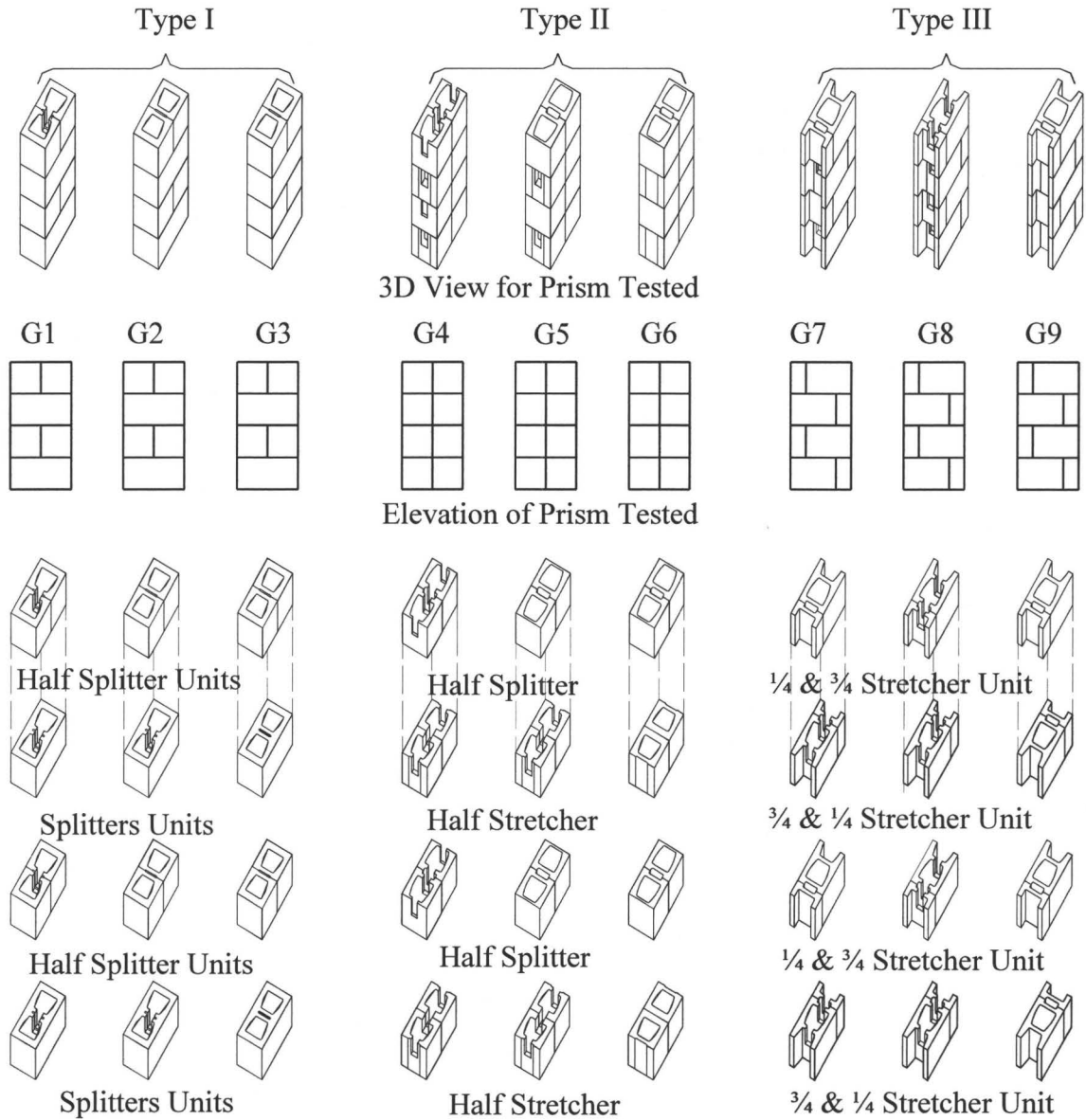
(a) Splitter Blocks (b) Alternating Splitter and Stretcher Blocks (c) Stretcher Blocks

Fig. 2. 11: Prism configurations

Vertical wood boards were attached to the ends of the prisms during grouting to prevent escape of grout from the knock-out webs. The quarter and three quarter pattern for stretcher units prisms (Type III) were used to avoid problems with grouting the frogged ends of stretcher units and were shown

(Hallucha (2002)) to provide the same strength as found from whole and half unit arrangements. The prisms were air cured exactly as the walls.

The comparison conducted between the three groups of the same type were intended to show the effect of knock-out webs for every course and every other course on the behaviour compared to results for the regular prisms (see Appendix G).

Prisms testing began at age of six month coinciding with testing of Wall 2, the third wall to be tested. Even though it was expected that at this age that there would be little influence of age, the prism ages are recorded in Table 2.8. The second stage of prism testing was done just after the fourth wall was tested (Wall 4) and the final stage was completed just after testing the last wall (Wall 7). Three additional prisms, Group 3 of Type 1, were built with Wall 7 but were tested for compressive strength only. These prisms were included because laboratory batched grout was used and confirmation of strength was required. Unfortunately, several prisms were broken during handling prior to grouting and have a notation of N/A in the table as they were not tested.

2.5   Shear wall test setup

The test rig was designed to test full scale shear walls up to three meters long under cyclic loading (Miller, 2006). As shown in Fig. 2.12, the rig consisted of a 4200 mm long x 1100 mm wide x 600 mm deep reusable concrete floor slab that was clamped to the strong floor with the aid of ten, 63 mm diameter, post-

tensioned steel bolts spaced at 920 mm in both the longitudinal and transversal directions. Sixteen 25.4 mm diameter steel prestressing bars were anchored in the reusable floor slab and, after positioning the test wall, were post-tensioned to clamp the base beam of the specimen to the reusable floor slab in order to prevent rotation of the wall base beam during testing. These prestressing bars were spaced at 400 mm in the longitudinal direction and at 320 mm in the transverse direction.

Axial load was applied to the top of the wall by means of four 25.4 mm diameter Dywidag prestressing bars that could be threaded into Dywidag nuts anchored at the base of vertical holes in the reusable concrete slab. Each pair of bars pivoted on a roller oriented along the length of the wall as shown in Fig. 2.13. Load was applied by a manually operated hydraulic jack on one side of each pair of prestressing bars (see Fig. 2.13). Load was distributed along the wall length through the top steel loading beam.

The lateral cyclic load was applied using an MTS hydraulic actuator with a maximum capacity of 1000 kN in the pull direction and 1400 kN in the push direction. The lateral load applied to the wall was positioned to coincide with the top of the wall in order to create a zero moment condition at the top of the wall. The actuator was attached to the stiff steel loading beam on the top of the walls to which the extensions of the vertical reinforcement were welded. This arrangement was chosen to simulate the transmission of the earthquake load along the length of the shear wall through the connection of vertical reinforcement to the horizontal diaphragm.
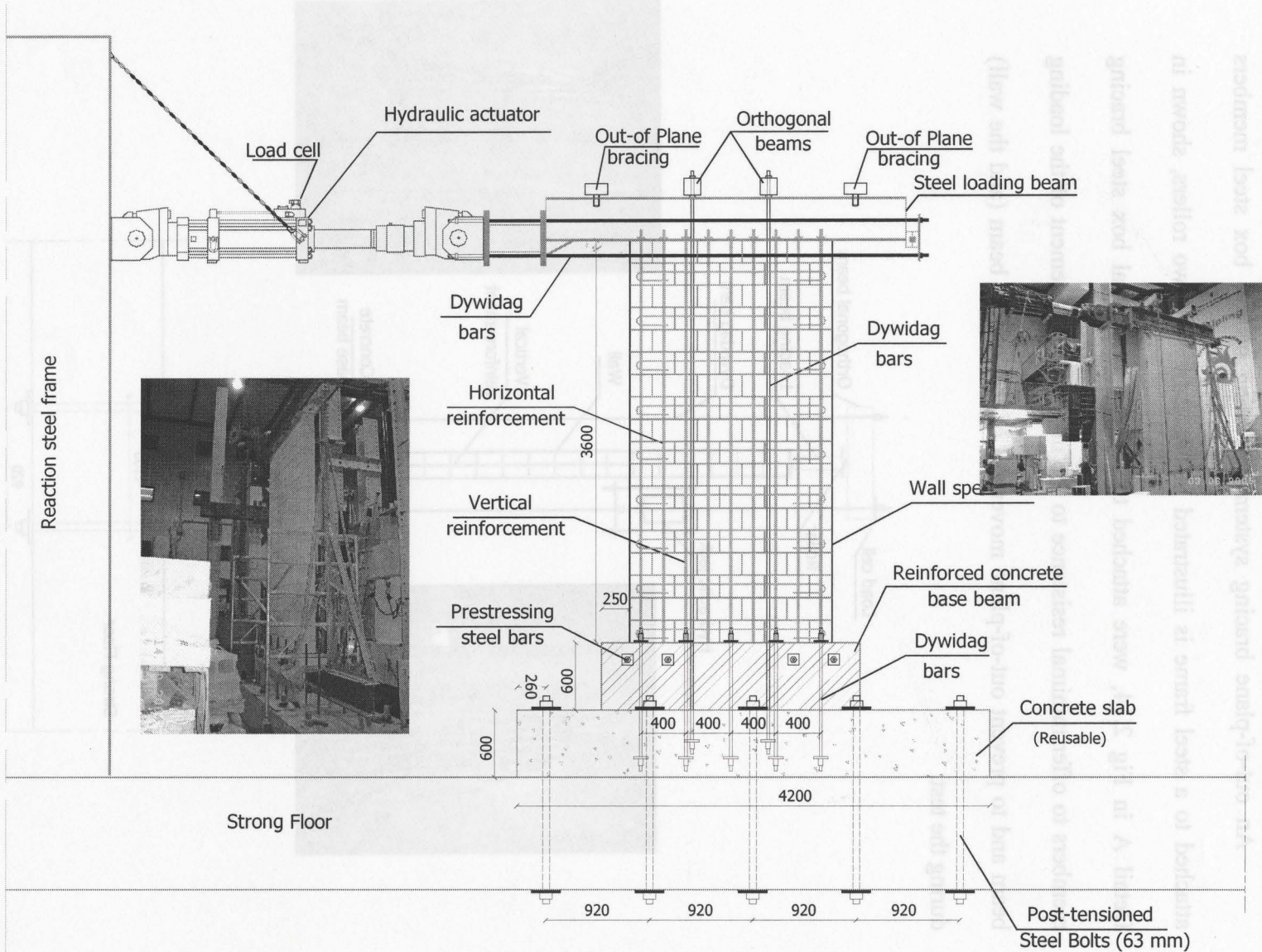
Fig. 2. 12: Test setup (Face view)

An out-of-plane bracing system consisting of two box steel members attached to a steel frame is illustrated in Fig. 2.14. The two rollers, shown in Detail A in Fig 2.14, were attached to the two horizontal box steel bracing members to offer minimal resistance to the in-plane displacement of the loading beam and to prevent out-of-plane movement of the loading beam (and the wall) during the test.
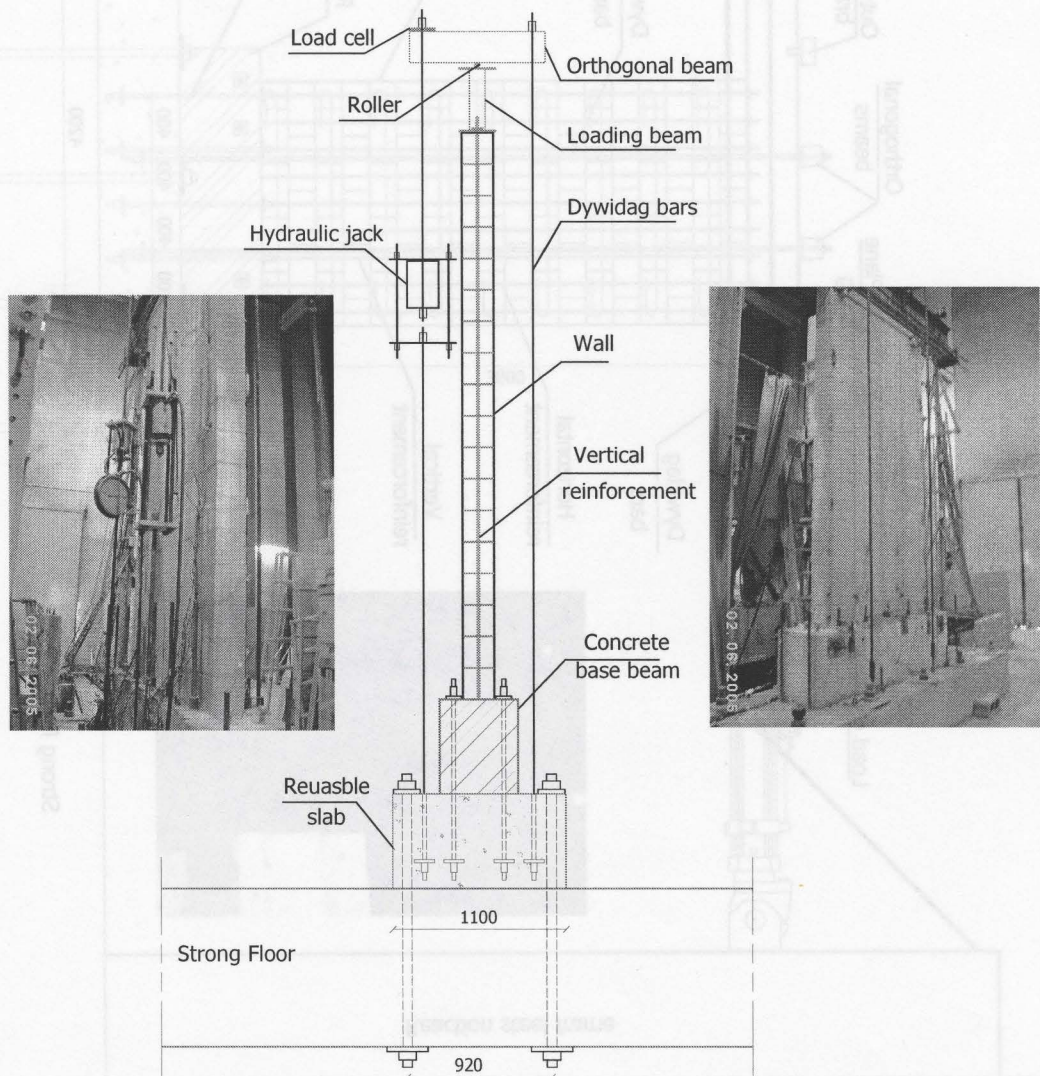
Fig. 2. 13: Axial load setup (End view)
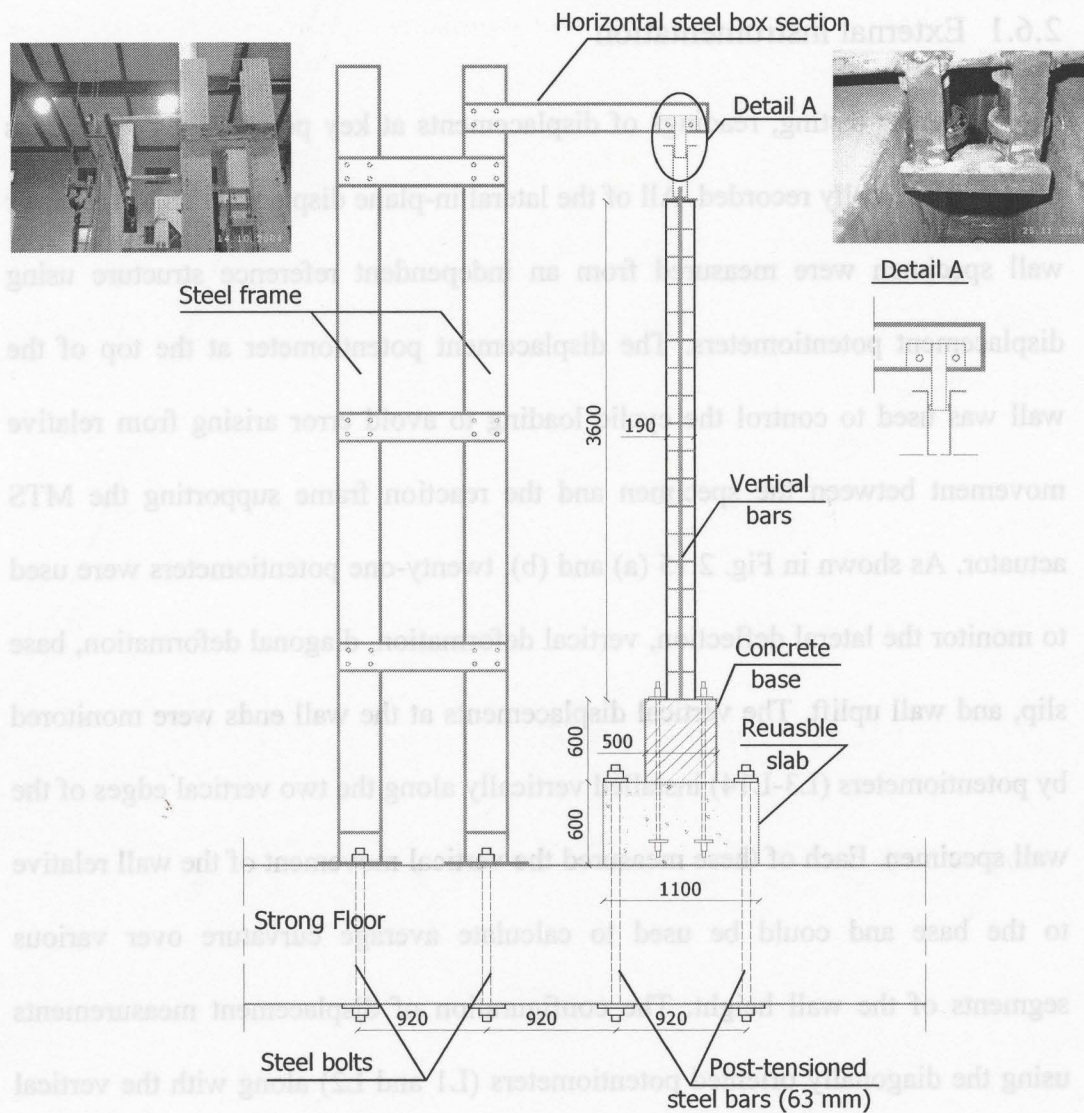
Fig. 2. 14: Out–of-plane bracing system

2.6   Measurements

During testing, loads, deflections and strains were measured to monitor the behaviour of the shear wall. A 60-channel data acquisition system was used to record 41 deformation readings at 7 second intervals.

2.6.1 External instrumentation

During testing, readings of displacements at key points along specimens were electronically recorded. All of the lateral in-plane displacements of the shear wall specimen were measured from an independent reference structure using displacement potentiometers. The displacement potentiometer at the top of the wall was used to control the cyclic loading to avoid error arising from relative movement between the specimen and the reaction frame supporting the MTS actuator. As shown in Fig. 2.15 (a) and (b), twenty-one potentiometers were used to monitor the lateral deflection, vertical deformation, diagonal deformation, base slip, and wall uplift. The vertical displacements at the wall ends were monitored by potentiometers (L3-L14) installed vertically along the two vertical edges of the wall specimen. Each of these measured the vertical movement of the wall relative to the base and could be used to calculate average curvature over various segments of the wall height. The configuration of displacement measurements using the diagonally oriented potentiometers (L1 and L2) along with the vertical potentiometers (L3 and L9) created a strain rosette required to distinguish between shear and flexural deformations.

The strain profile in the lower part of the wall was calculated from readings of potentiometers (L7, L8 and L13-L18) mounted vertically throughout the length of the shear wall specimen. The lateral displacements of the wall at different heights were measured by eight horizontally positioned potentiometers (L20-L25, L28 and L29) attached to a truss supported on a steel beam

cantilevered from the reinforced concrete base beam of each specimen as shown in Fig. 2.15. This configuration allowed recording of displacement of the wall relative to the base beam without the need to make any correction due to rotation or sliding of the base beam relative to the floor slab. [Note: No relative movement between the wall base beam and the floor beam was observed at any stage of testing, whereas the reaction frame for horizontal loading did experience movement.] Uplift of the wall from the concrete base beam was monitored by the vertical potentiometers (L26 and L27) that were attached at mid-height of the first masonry course at each end of the wall. A linear potentiometer (L19) was mounted horizontally on the base beam to measure any horizontal slip that might occur between the wall and the concrete base beam. All potentiometers were attached to a steel bracket at the base beam level, as shown in Detail A in Fig. 2.15 (c), in order not to lose all readings due to damage associated with toe crushing of the wall.

2.6.2 Internal instrumentation

In addition to the potentiometers used externally, ten electrical strain gauges were epoxied to the reinforcing steel bars prior to wall construction. Proper surface preparation of the reinforcing steel required removing bar ribs with an electrical grinder prior to bonding which resulted in a slight reduction of the area of the bar. The foil gauges were protected with a clean sealer coating for waterproofing. A butyl sealer and black tape were added for protection from

physical damage (see Fig. 2.16 (a)) during the grouting process as well as during wall construction. As shown in Fig. 2.16 (b), the gauges were located within the most highly stressed region to monitor initial yielding, extent of yielding over the wall height, and penetration of the bar yielding inside the base beam. Strain gauges S1 to S10 were attached to the outermost vertical reinforcing bars in a typical wall specimen. Each bar was fitted with five strain gauges distributed along the length of the bar according to a defined scheme. One electrical strain gauge was installed at the interface between the wall and the base to detect the initial yielding (see Fig. 2.16 (c)). Two strain gauges were attached on the steel bar inside the base beam at depths of 150 mm and 300 mm (see Fig. 2.16 (d)). The other two gauges were installed at heights of 500 mm and 900 mm above the base beam.

2.6.3 Loading

The lateral cyclic load was applied using an MTS hydraulic actuator that contained a built-in load cell used for monitoring the horizontal force and an internal LVDT for monitoring its horizontal displacement. Applied axial loads were measured from the load cell attached to the hydraulic jacks. The load cells were calibrated prior to conducting the tests and were found to give consistent measurements. The axial stress on specimens was held within 4 % during testing by increasing or decreasing the load depending on the direction of the vertical displacement of the wall.

(a) Instrumentation layout

(b) Photograph of external instrumentation

(c) Detail A
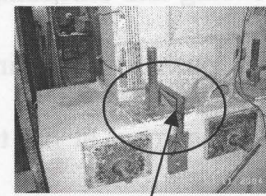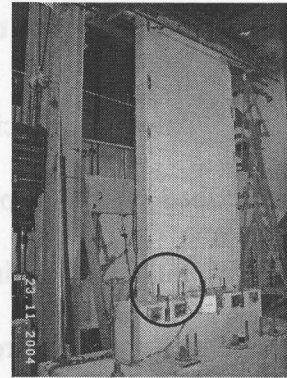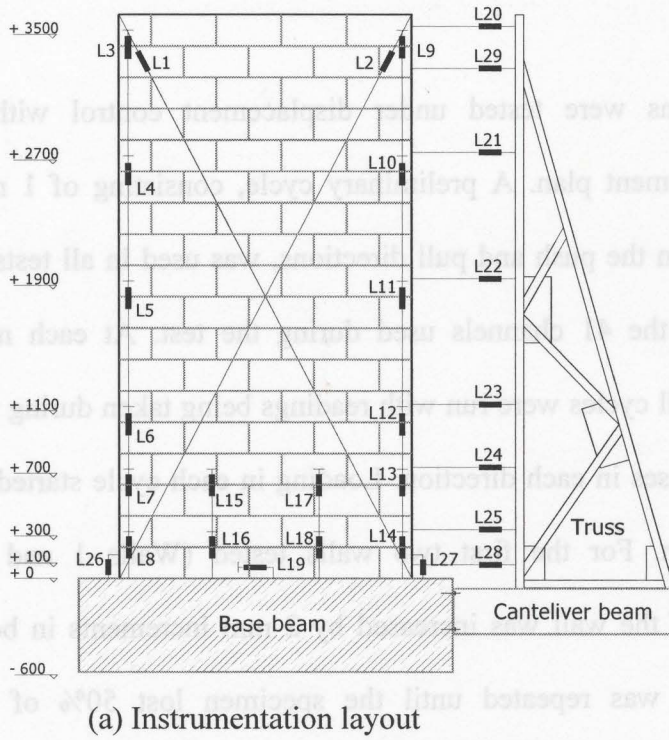
Fig. 2. 15: External instrumentation

(a) Protection for a strain gauge

(b) Layout of strain gauge in a typical wall

(c) Strain gauge at interface

(d) Strain gauges in the base beam
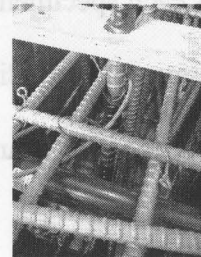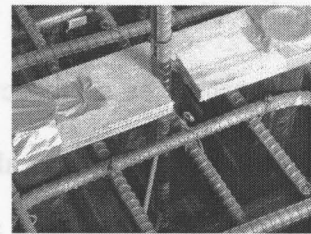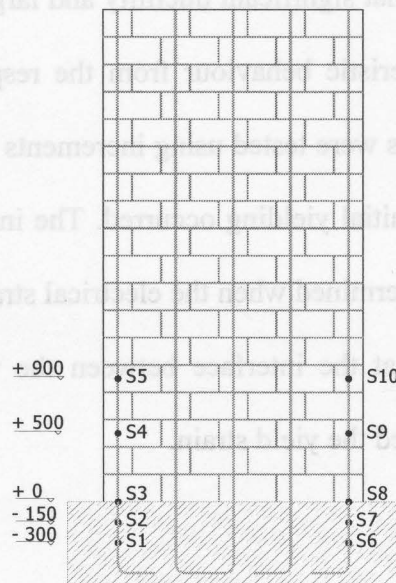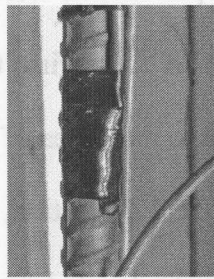
Fig. 2. 16: Internal instrumentation

2.7   Test procedure

All wall specimens were tested under displacement control with a prescribed lateral displacement plan. A preliminary cycle, consisting of 1 mm displacement for loading in the push and pull directions, was used in all tests to check the readings from the 41 channels used during the test. At each new displacement level, two full cycles were run with readings being taken during the loading and unloading phases in each direction. Loading in each cycle started in the push (West) direction. For the first two walls tested (Walls 1 and 3) displacement at the top of the wall was increased by 2 mm increments in both directions. The sequence was repeated until the specimen lost 50% of its maximum lateral load resistance which was considered the failure criteria in this study. After establishing that significant ductility and large displacements were to be expected as a characteristic behaviour from the response of these first two walls tested, all other walls were tested using increments equal to multiples of the yield displacement after initial yielding occurred. The initial yield deflection, Δ_y, for each specimen was determined when the electrical strain gauge, located on the outmost longitudinal bar at the interface between the wall and the reinforced concrete base beam, reached the yield strain.

2.8   Closure

The selection of dimensions for the test walls and the criteria used in developing the test matrix were presented. Construction of the shear walls from

base beam construction to final grouting the walls was described. The details of reinforcements of the shear walls in this study ensured flexure dominated wall behaviour with a safe margin against shear failure. All auxiliary tests for the masonry assemblage and their constituent materials were reported in this chapter. Details of the setup used for testing the shear walls in this study as well as measurements and instrumentation used for recording displacements of the test specimens were presented. The procedure adopted for testing the shear walls was also provided.

CHAPTER 3

TEST RESULTS

3.1   Introduction

The results for the wall tests are presented in this chapter. For each specimen, details are presented followed by observations of cracking and progressive failure during the test. Load-displacement response of the wall is discussed and hysteresis loops are presented for each wall. In addition, the extent of yielding of reinforcement in the wall and its penetration inside the base beam are reported. The deflection and drift profile along the wall height are presented at different displacement levels. Also, the curvature profile over the height of the wall and the strain profile along the wall length are presented.

At the beginning of each discussion, the main characteristics of the test wall are listed. For ease of reference, these are repeated in the lower right corner of the figure containing the hysteresis response of the wall. The hysteresis loops from the recorded load versus displacement data during successive push – pull cycles of loading are used as reference for other aspects of behaviour. Except for Wall 1, again for ease of reference, data on displacement and lateral load resistance for both the push and pull cycles corresponding to conditions of initial yield of tension reinforcement, the maximum load, and 1 percent drift are shown in the upper left corner of the figure containing the hysteresis data.

Photographs and descriptions are provided to document stages of cracking and eventual deterioration of the compression zones in relation to wall displacement. Deflection profiles over the height of the wall were plotted for key points in the hysteresis loading using the eight measurement locations. Although these deflection profiles provide some indication of relative curvature over the wall height, a better indication is obtained from plots of average curvatures over segments of the wall height.

Average curvatures over the wall height were determined based on strain profiles. A representation of a strain profile for a cross section is shown in Fig. 3.1. Average curvature, Φ, for a given gauge length h_{gauge} was calculated using Eq. 3.1. Curvature profiles along the wall height were similar for loading in the push and pull directions for all walls except for Wall 1 where defects were discovered in the wall during the test as will be discussed later.
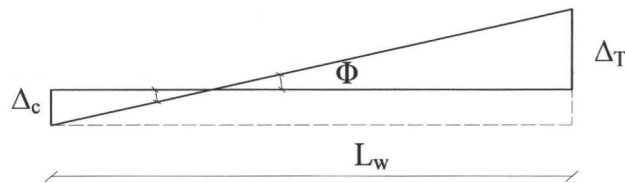
Fig. 3. 1: Strain profile used for curvature calculation

$$\Phi = \frac{\dfrac{\Delta_T}{h_{gauge}} + \dfrac{\Delta_c}{h_{gauge}}}{L_w} \qquad \text{Eq. 3. 1}$$

Where: Φ is the average curvature over a given segment along the wall height. Δ_c and Δ_T, shown in Fig. 3.1, are the net displacement readings obtained by the linear potentiometers at the edges of the wall over a given segment height. h_{gauge} is the segment height corresponding to the measured Δ_c and Δ_T

70

3.2   Wall 1

3.2.1 Details of Wall 1

Wall 1 was the first specimen to be tested. This wall was reinforced with No. 25 vertical bars in every cell ($\rho_v = 1.31\%$) and No. 10 horizontal bars in every course ($\rho_h = 0.26\%$), and was not subjected to any superimposed axial load during the test.

The hysteresis loops for cyclic loading up to maximum load are shown in Fig. 3.2 for loading in the push and pull directions. As is explained later, testing problems led to the decision to continue cyclic loading in the post-peak range with a constant minor push cycle and an incrementally increasing pull cycle. The results are shown in Fig. 3.3 (a). The envelope of the load-displacement data for loading in the pull direction is provided in Fig. 3.3 (b).
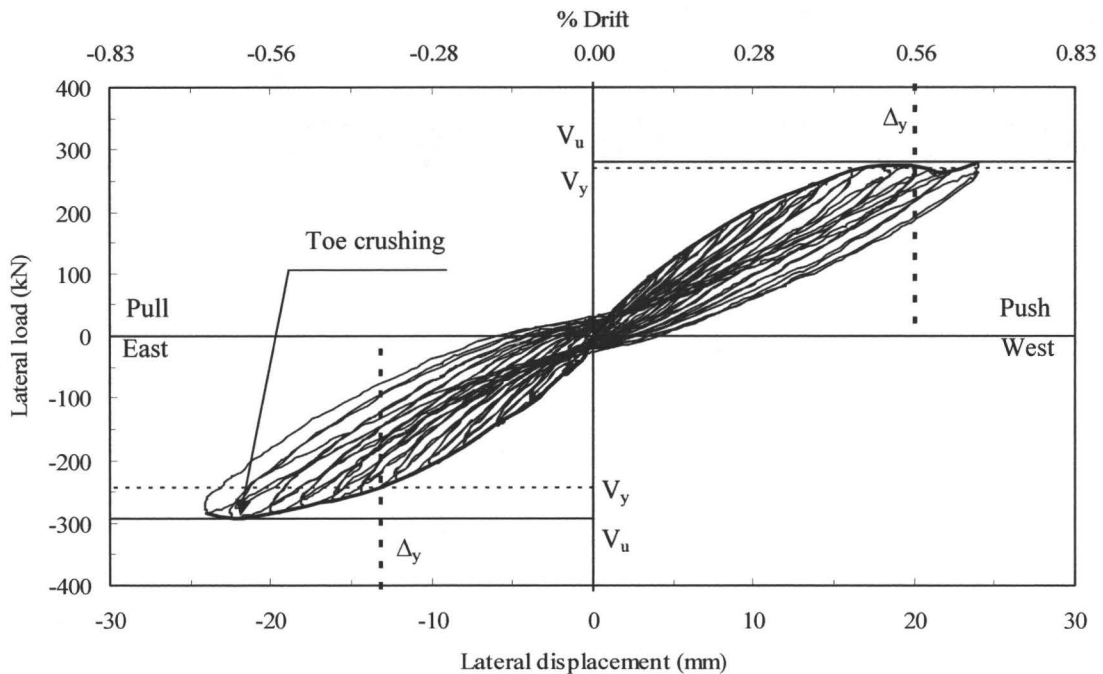
Fig. 3. 2: Hysteresis loops up to maximum load (Wall 1)

71
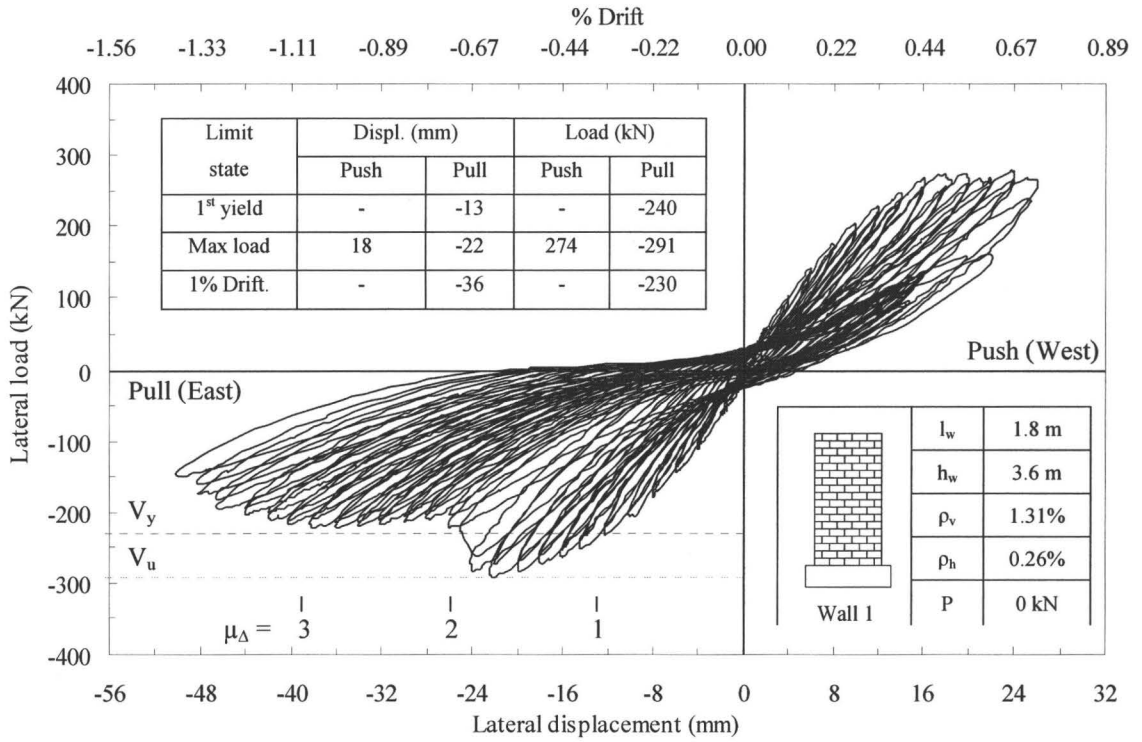
(a) Hysteresis loops (Wall 1)
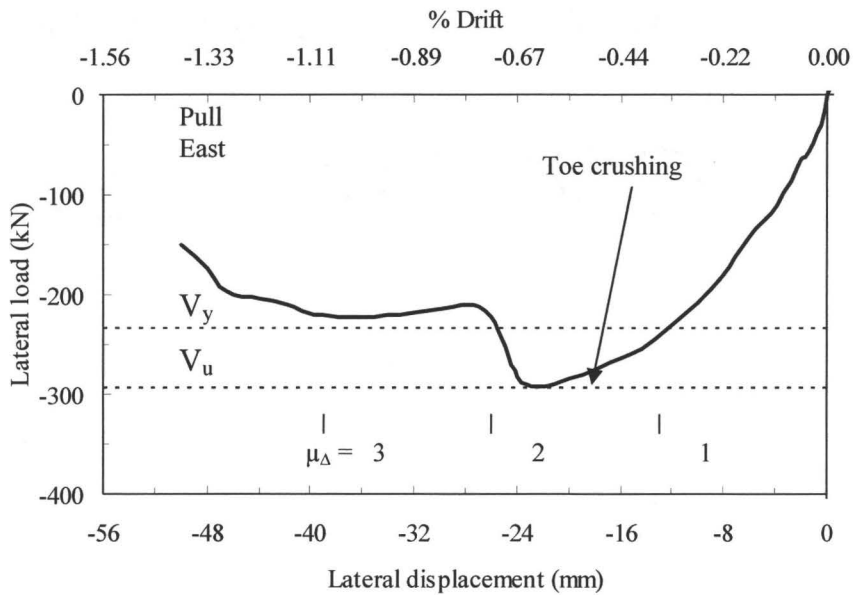
(b) Envelope of load-displacement for Wall 1 (Pull direction)

Fig. 3. 3: Loading behaviour of Wall 1

3.2.2 General observations

Wall behaviour during the whole test was dominated by flexural response which was indicated by the dominance of horizontal cracks along the bed joints that started to form during the 4 mm loading cycle. As shown in Fig. 3.4, these cracks increased in width following yielding of the vertical reinforcement. They became longer and wider with increasing displacement levels. Minor diagonal cracks formed in a stepped pattern during the 10 mm displacement cycle and developed over the full height of the wall after maximum load was reached. The wall exhibited reasonably symmetric response for loading in the push and pull directions up to maximum load (see Fig. 3.2), which corresponded to failure of the West toe at a load of 270 kN and a deflection of 20 mm. Spalling of face shells at the West toe up to the fourth course occurred during the 20 mm displacement cycle, with no sign of buckling of the outermost bar as shown in Fig. 3.5. During the 22 mm push displacement, the roller in the out-of-plane bracing system broke and testing was temporarily stopped while it was replaced.
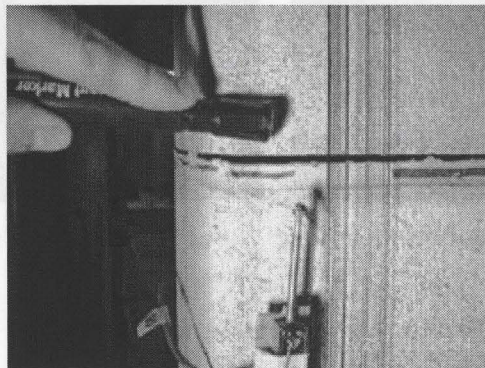
Fig. 3. 4: Wide horizontal cracks   Fig. 3. 5: Spalling of face shells
East end (Wall 1)   at 20 mm displacement (Wall 1)
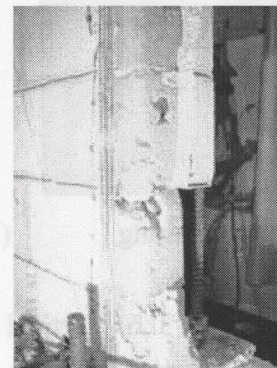
Some cracking pattern differences between the East and West ends of the wall were observed before reaching the maximum load. A vertical crack, at 200 mm from the East wall end, extended alternatively through head joints and blocks from the tenth course to the first course (see Fig. 3.6 (a) and (b)). At 18 mm displacement in the pull direction, this vertical crack extended between the tenth course and the third course and at 22 mm pull displacement, it propagated down to the first course. The East toe then began failing at an applied lateral load of 283 kN at 24 mm displacement in the pull direction. At the same time as the East toe crushed, the lateral displacement increased abruptly from 24 mm to 25 mm, the block in the first course crushed, and the East 200 mm of the wall separated from the rest of the wall up to the tenth course following the previously indicated vertical crack (see Fig. 3.6 (c)).

(a) Extending along the height   (b) Reaching bottom course   (c) Separation of the end cell
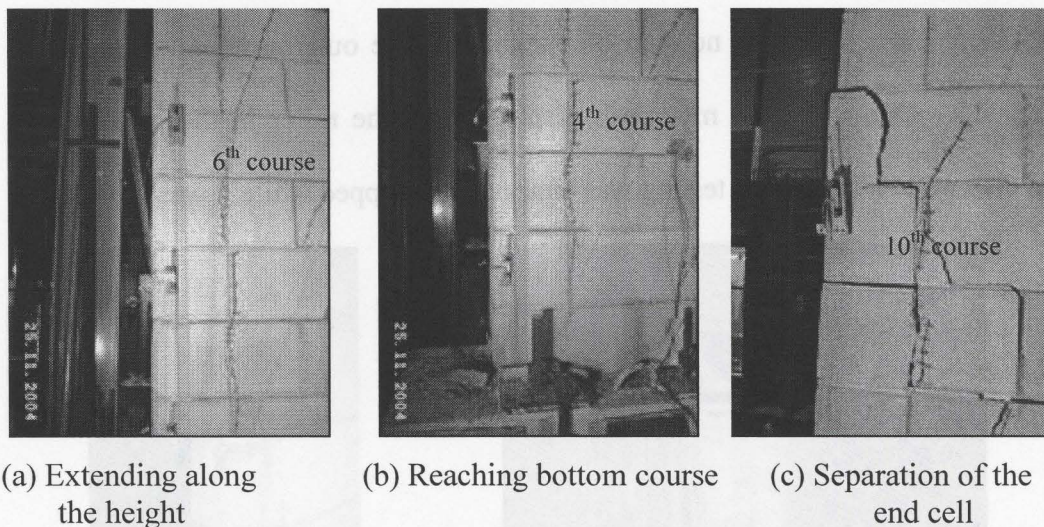
Fig. 3. 6: Vertical crack at 200 mm from the East end (Wall 1)

The explanation for this behaviour was not clear until later during the test. After both toes had failed, the wall lost a significant amount of its out-of-plane

resistance which led to out-of-plane force on the bracing system. Due to a slight misalignment between the actuator and the wall, one bearing in the bracing system failed during the initial loading to a target deflection of 26 mm in the push direction. After failure of the out-of-plane bracing system, the wall tended to deflect out-of-plane during loading in the push direction and caused concern for safety and for accuracy of the in-plane loads and displacements. Visual inspection, during loading in the push direction after toe crushing, indicated that the wall started to deflect out-of-plane at 16 mm top wall deflection. It was decided to continue with the test but only incrementally increasing the pull cycle displacement while limiting deflection to 16 mm for each loading cycle in the push direction; the tensile force in the actuator during loading in the pull direction tended to keep the wall in line.

Cyclic loading was continued as described above and it was observed that the load dropped significantly from 291 kN to 221 kN during the first 26 mm displacement cycle in the pull direction following toe failure (see Fig. 3.3). The sudden drop in the load, during the cycle following maximum load, corresponded to the complete separation of the 200 mm wide vertical strip of wall containing the extreme East cells. By examining this strip during the test after spalling of face shells, it was found that the grout had not filled this region leaving the reinforcing bar unbonded to the wall. This provided an explanation for the previously noted unsymmetric hysteretic behaviour after toe crushing and for the separation of the 200 mm wide vertical strip of wall.

The cyclic loading was continued and, as can be seen in Fig. 3.3 (a), the wall did not experience any additional major degradation in strength; as the top deflection of the wall in the pull direction increased from 26 mm to 46 mm, the corresponding decrease in resistance was from 221 kN to 195 kN. When the wall was pulled to 48 mm top deflection, diagonal cracks started to appear in the plastic hinge region up to one metre from the bottom of the wall as shown in Fig 3.7. Subsequently, the lateral resistance dropped to 175 kN. At 50 mm displacement in the pull direction, the resistance of the wall had decreased to 150 kN corresponding to approximately 50% strength degradation and, in the second cycle at the same displacement, the resistance of the wall dropped to 110 kN. The testing was terminated at this point.
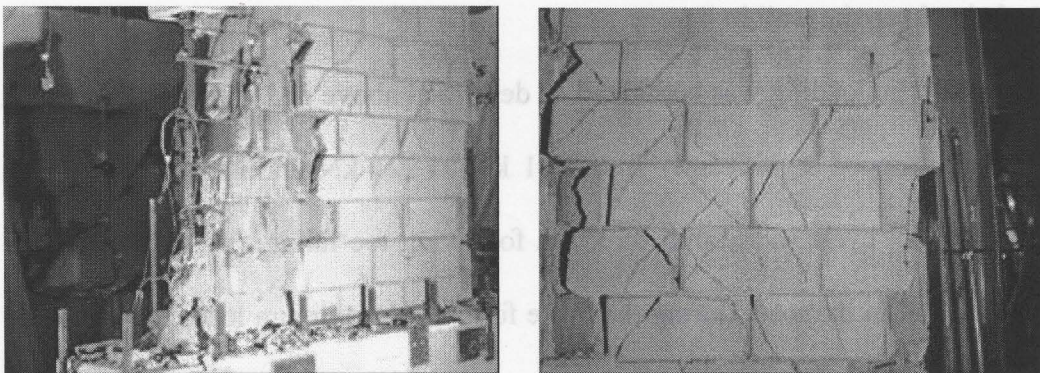
a) Major damage at the East end   b) Minor damage at the West end

Fig. 3. 7: Diagonal cracks in plastic hinge zone (Wall 1)

The tested wall was dismantled so that all of the empty cells could be located (see Fig. 3.8). The reason for all of the empty cells found in the wall appeared to be due to mortar dropping during wall construction and their hardening over the hooks in the horizontal reinforcement at the ends of the wall.

The hardening of the mortar droppings made the opening in the cells, through which the grout should flow, very narrow especially at the end of the wall where splitter block units, having smaller cells, were used.

(a) Ungrouted zone up to 10th course (East end)

(b) Ungrouted zone up to 3rd course (East end)

East end

Empty cells

Major crack

1800

10th course

7th course

4th course

3600

600

2300

(c) Elevation of Wall 1
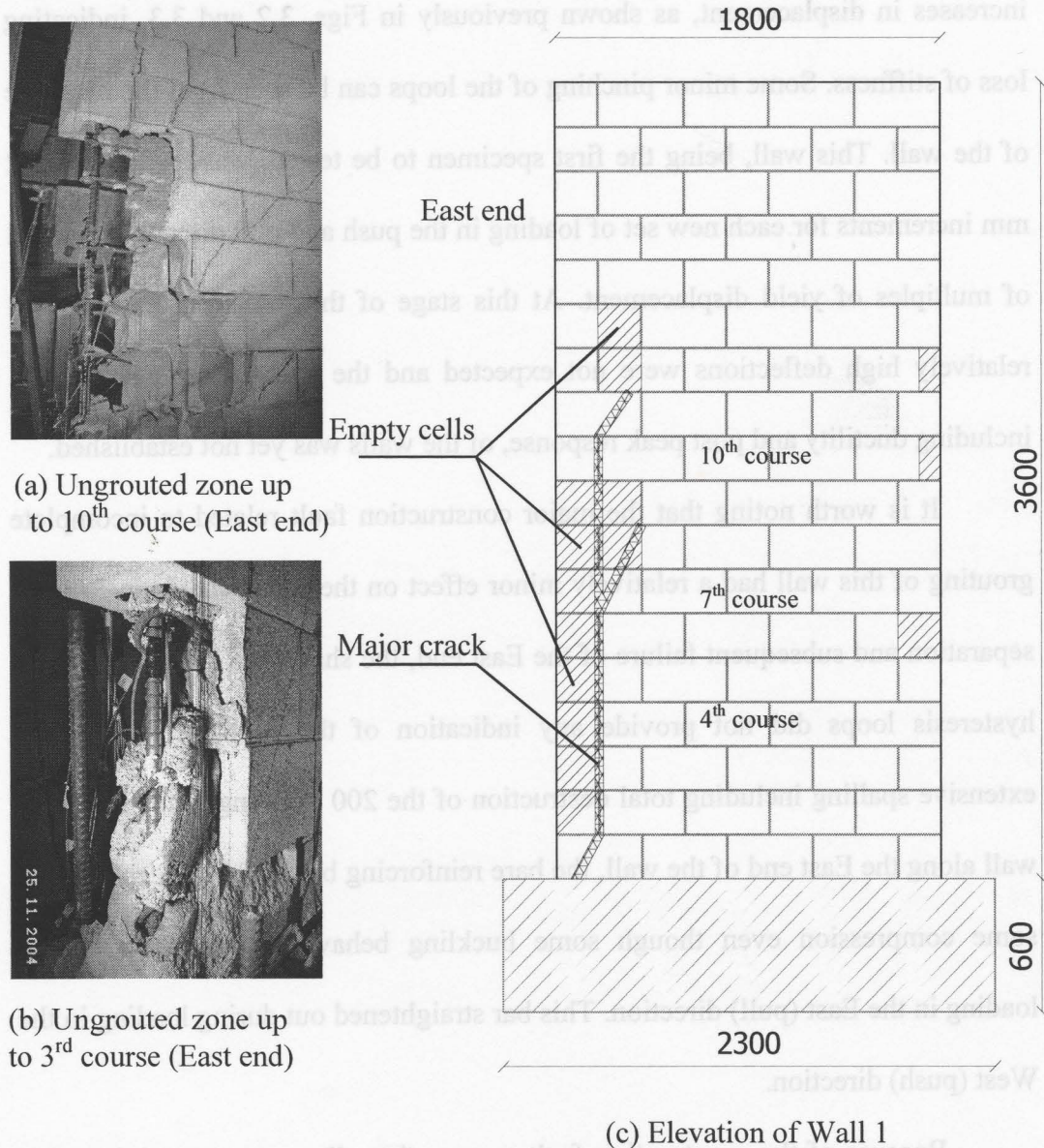
Fig. 3. 8: Location of empty cells and major crack (Wall 1)

77

3.2.3 Load-displacement response

The hysteresis loops indicated stable response for the wall despite existence of the major defect. The slopes of the loops decreased gradually with increases in displacement, as shown previously in Figs. 3.2 and 3.3, indicating loss of stiffness. Some minor pinching of the loops can be seen from the response of the wall. This wall, being the first specimen to be tested, was loaded using 2 mm increments for each new set of loading in the push and pull directions instead of multiples of yield displacement. At this stage of the research, the observed relatively high deflections were not expected and the characteristic behaviour, including ductility and post peak response, of the walls was yet not established.

It is worth noting that the major construction fault related to incomplete grouting of this wall had a relatively minor effect on the wall behaviour. Prior to separation and subsequent failure of the East end, the shape and symmetry of the hysteresis loops did not provide any indication of the problem. Even after extensive spalling including total destruction of the 200 mm ungrouted length of wall along the East end of the wall, the bare reinforcing bar could be seen to resist some compression even though some buckling behaviour was observed for loading in the East (pull) direction. This bar straightened out during loading in the West (push) direction.

Because of the construction fault, a seventh wall was constructed so that the complete test matrix would be followed. However, the results from testing

Wall 1 have been included as interesting documentation of the effect of a major flaw.

3.2.4 Extent of yielding of reinforcement

Yielding of the outermost bars was monitored using five electrical strain gauges attached at different heights on the reinforcing bars. The two gauges inside the base beam did not show any sign of yielding but the one at the interface between the wall and the base beam as well as the other two attached at 500 mm and 900 mm heights from the base beam indicated yielding. Table 3.1 shows the extent of yielding in the outermost West reinforcement for Wall 1. The readings from the strain gauges attached to the bar located in the East end, which was under tension during loading in the West (push) direction, did not show consistency. As was noticed from the measurements, the strain gauge located at 500 mm height indicated that the East bar had yielded at 16 mm displacement for loading in the West (push) direction while the gauge at the interface between the wall and the base beam indicated yielding at 18 mm displacement for loading in the same direction. Having this bar unbonded and fixed at the second and tenth course resulted in its greatest elongation occurring between these two fixation points. Then, after toe crushing, the bottom fixation point moved to the base instead of the second course and the strain gauge at the interface showed higher values.

Table 3. 1: Extent of yielding of the outermost West bar (Wall 1)

Strain gauge location	Initial yielding condition			Strain at max. load	Strain $(x\ \varepsilon_y)$
	Load	Displacement	% Drift		
Interface	- 240 kN	13.3 mm	0.36	0.0092	3.68
500 mm	- 267 kN	18.4 mm	0.51	0.0025	1.00
900 mm	N/A	N/A	N/A	0.0023	0.92

3.2.5 Wall deformation and drift

In-plane lateral displacements were measured at eight points over the height of the wall using potentiometers attached at the West end of the wall. However, the three lower potentiometers became ineffective when the anchors attaching them to the wall failed due to major cracking and spalling extending up to the fourth course at the West toe, as was shown previously in Fig. 3.5. This resulted in losing all subsequent deflection readings at these locations. The recorded in-plane lateral displacements over the height of the wall, for loading in the pull direction, are presented in Fig. 3.9 for key loading conditions related to yielding of reinforcement. Concentration of bending over the lower 1.2 m of the wall height is evident while the top 2.4 m of the wall appears to be relatively straight.
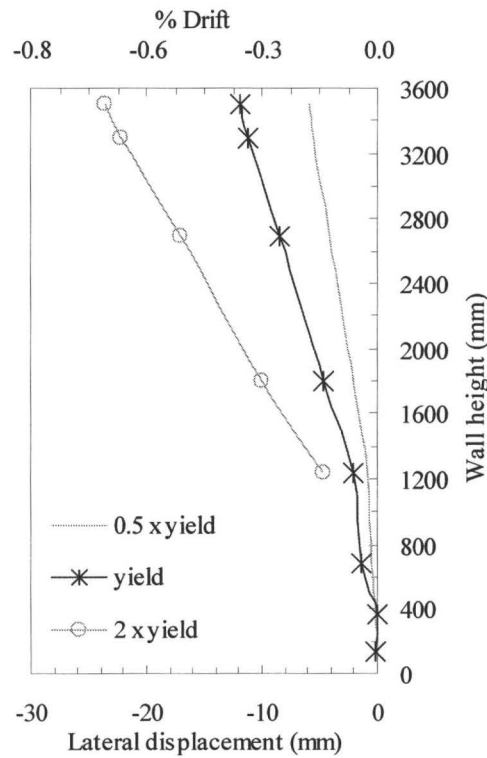
Fig. 3. 9: Total in-plane lateral deflection for loading in pull direction (Wall 1)

3.2.6 Wall curvature

Average curvatures over segments of the height of Wall 1 at different lateral displacements stages are presented in Fig. 3.10. Average curvatures were calculated for seven segments over the wall height using the displacement readings recorded from the fourteen vertical potentiometers; seven located at each end of the wall. Average curvatures reached their maximum values near the base of the wall as shown from the curves corresponding to different displacement levels. The extensive block spalling and subsequent loss of potentiometer attachment anchors made it impossible to obtain measurements at high deflections after loss of the face shells at the East end of the wall.
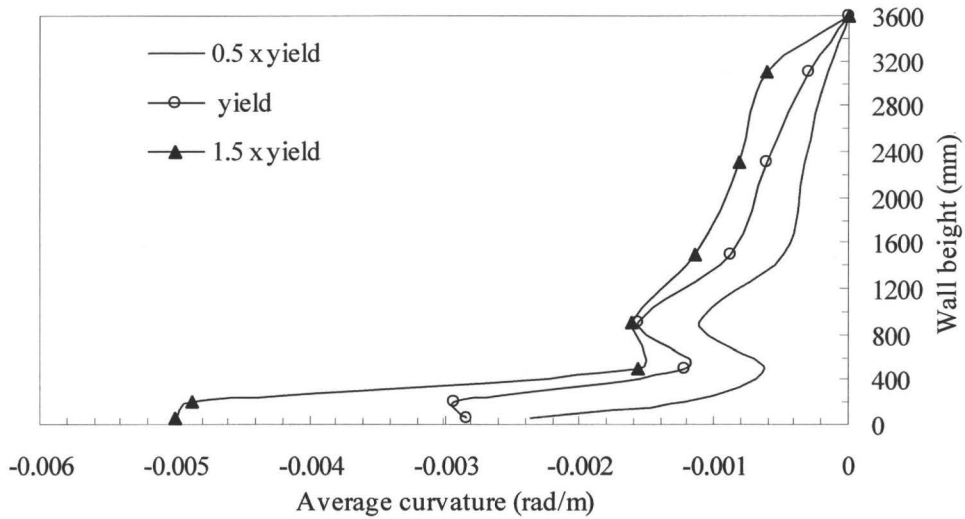
Fig. 3. 10: Average curvature along wall height for loading in pull direction (Wall 1)

3.2.7 Strain profile

The strain profiles along the wall length calculated using the displacement readings of the two sets of four linear potentiometers located at heights of 300 mm and 700 mm above the base beam are presented in Fig. 3.11 for loading in the pull direction. The profiles of average strain between the base beam and 300 mm above the base beam, shown in Fig. 3.11 (a), indicate that the lengths of the compression zone are about 600 mm long with maximum compressive strains of 2 $x10^{-3}$ and 3.7 $x10^{-3}$ at yield displacement and at one and a half times the yield displacement, respectively. The figure also shows nonlinear strain profiles along the length of the wall. The profiles of average strain between 300 mm and 700 mm above the base beam, shown in Fig. 3.11 (b), indicate that the lengths of the compression zone are about 750 mm and 650 mm long with maximum compressive strains of 0.4 $x10^{-3}$ and 0.5 $x10^{-3}$ at initial yield displacement and at one and a half times the initial yield displacement, respectively. The figure also

82

indicated a reasonable linear strain profile along the portion of the wall under tension.
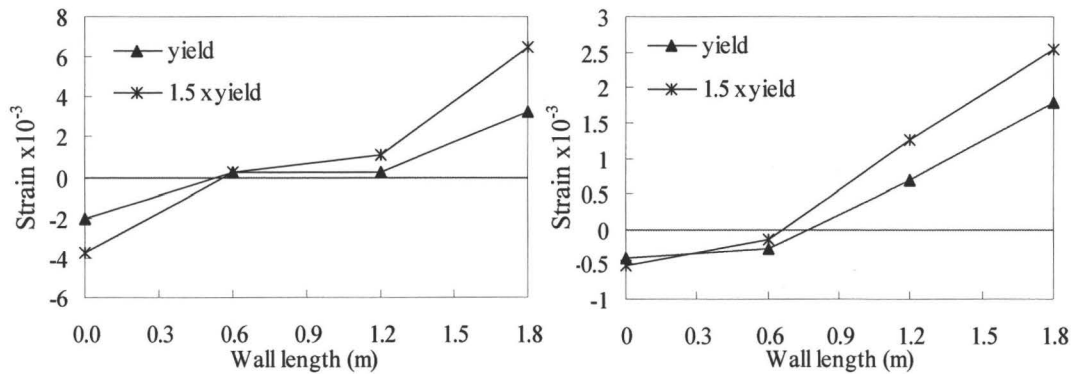
(a) 0 – 300 mm above the base beam   (b) 300 – 700 mm above the base beam

Fig. 3. 11: Profile of average strain along wall length for pull direction
of loading (Wall 1)

3.3 Wall 2

Wall 2 was actually the third wall to be tested and at this stage a new loading pattern was adopted.

3.3.1 Details of Wall 2

Wall 2 was a duplicate of Wall 1 that had been incompletely grouted. This wall was reinforced with No. 25 vertical bars in every cell (ρ_v = 1.31%) and No. 10 horizontal bars in every course (ρ_h = 0.26%), and it was not subjected to any superimposed axial load during the test. No ungrouted spaces were found before or after the test in this wall.

The hysteresis loops for Wall 2 for cyclic loading are shown in Fig. 3.12 for loading in the push and pull directions.

Limit	Displ. (mm)		Load (kN)	
state	Push	Pull	Push	Pull
1st yield	15	-15	296	-292
Max load	30	-30	360	-380
1% Drift	36	-36	352	-346

l_w	1.8 m	
h_w	3.6 m	
ρ_v	1.31%	
ρ_h	0.26 %	
Wall 2	P	0 kN
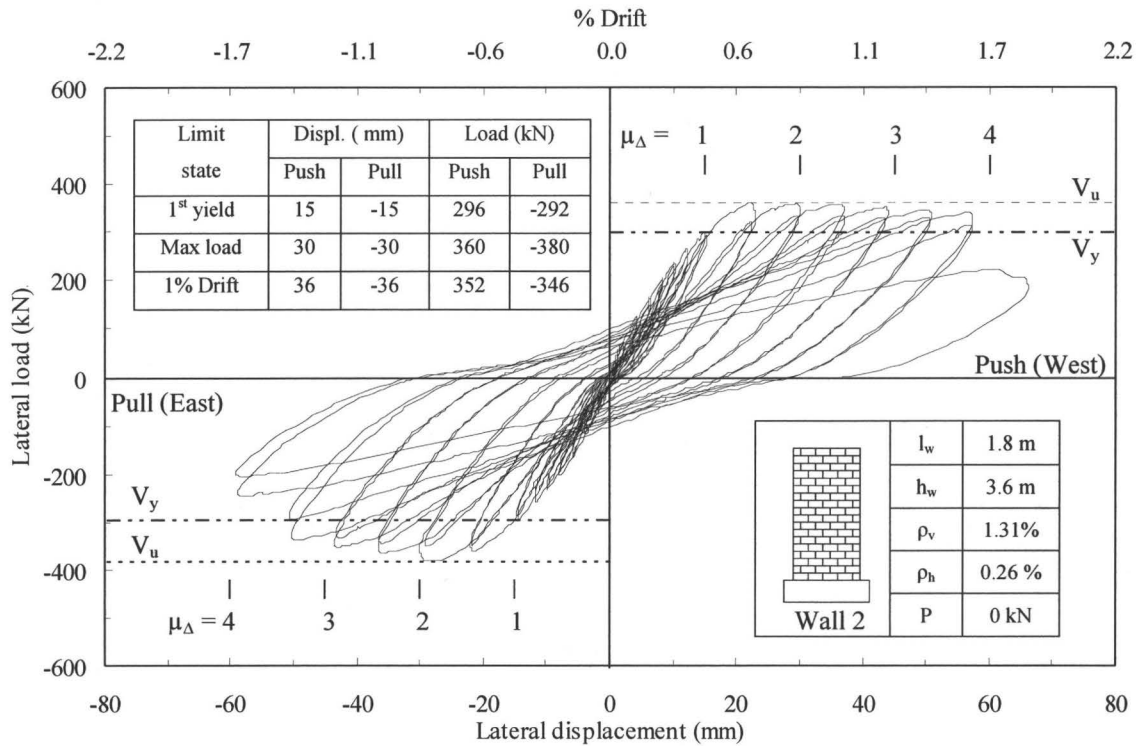
Fig. 3. 12: Hysteresis loops (Wall 2)

3.3.2 General Observations

The strains recorded in the outermost end reinforcing bars were monitored during the test and once one of these bars reached the yield strain, the loading step was stopped to avoid plastic strain in the extreme tension bar. Then, when the lateral force was reversed, yielding of the other end bar would be expected at or near the same lateral deflection.

The observed crack pattern was similar to the previous wall indicating flexure dominated response. Horizontal bed joint cracking was seen up to the sixth course during the 6 mm displacement cycle (see Fig. 3.13). During the 12 mm displacement cycle, stepped cracks started to form between the fourth and the

eleventh courses and elongations of the horizontal cracks were observed. Figure 3.14 illustrates the symmetry of cracking pattern for loading in the push and pull directions. Stepped cracks reached the top of the wall at 37 mm displacement. The hysteresis loops for Wall 2 for loading in the push and pull directions were almost symmetric.

East
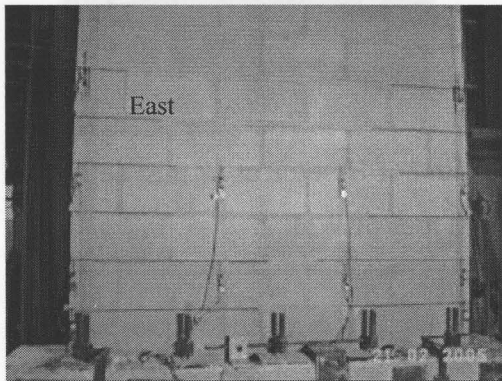
West

Fig. 3. 13: Horizontal cracks corresponding   Fig. 3. 14: Stepped cracks corresponding
to 6 mm top deflection (Wall 2)   to 12 mm top deflection (Wall 2)

Vertical cracks in the West toe, shown in Fig. 3.15 (a), started to form during the 22 mm displacement cycle for loading in the West (push) direction while similar cracks in the East toe were noticed at 30 mm displacement for loading in the East (pull) direction. These extended to the second course above the base at 37 mm displacement (see Fig. 3.15 (b)). Cracking of the face shells in the West toe occurred, and along with the vertical crack in the end web, led to deterioration of parts of the end block at the West end of the wall during the 30 mm displacement cycle (see Fig. 3.16 (a)). Diagonal cracks propagated through the first course during the second cycle of the same displacement level (see Fig. 3.16 (b)).

85
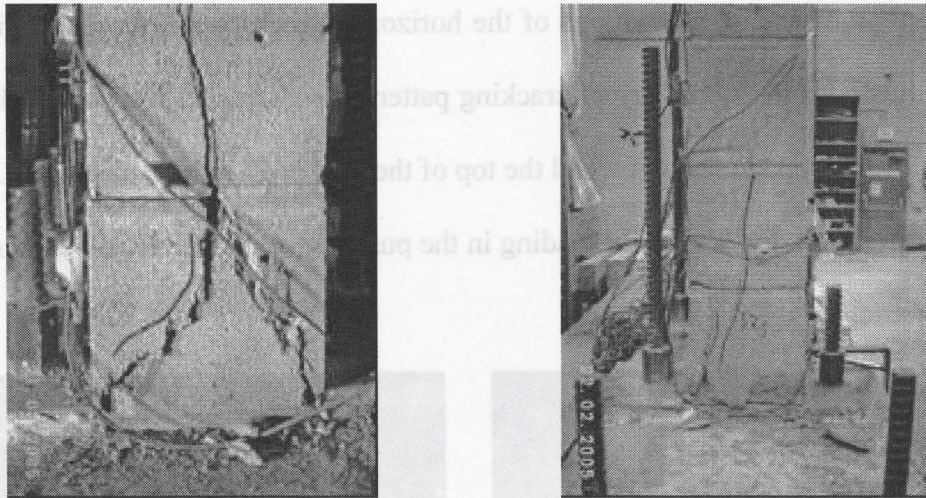
(a) End of West toe at 22 mm deflection (b) End of East toe at 37 mm deflection

Fig. 3. 15: Cracks in both toes of Wall 2
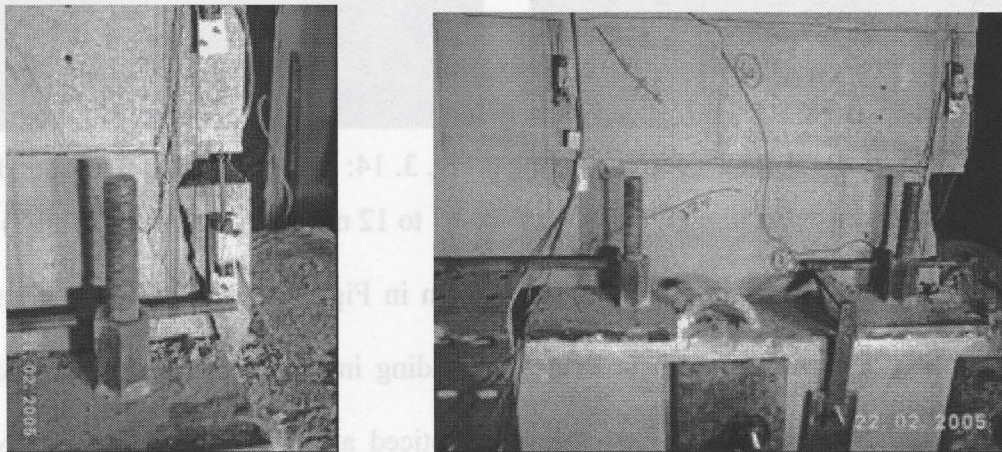
(a) Spalling of end West web (b) Diagonal cracks along wall length reaching first course (West end)

Fig. 3. 16: Spalling and cracking at 30 mm top deflection (Wall 2)

The maximum load for loading in the West (push) direction was 360 kN at 30 mm displacement and 380 kN at the same displacement for loading in the East (pull) direction. Following toe crushing, the wall degraded faster for loading in the East (pull) direction than for loading in the West (push) direction. After major spalling of face shells at the East and West toes had occurred during the second

cycle of the 37 mm displacement, the outermost grout columns could be seen (see Fig. 3.17 (a) and (b)). Cracking of the East and West grout columns, as shown in Fig. 3.18 (a) and (b), occurred at 45 mm and 52 mm displacements, respectively.
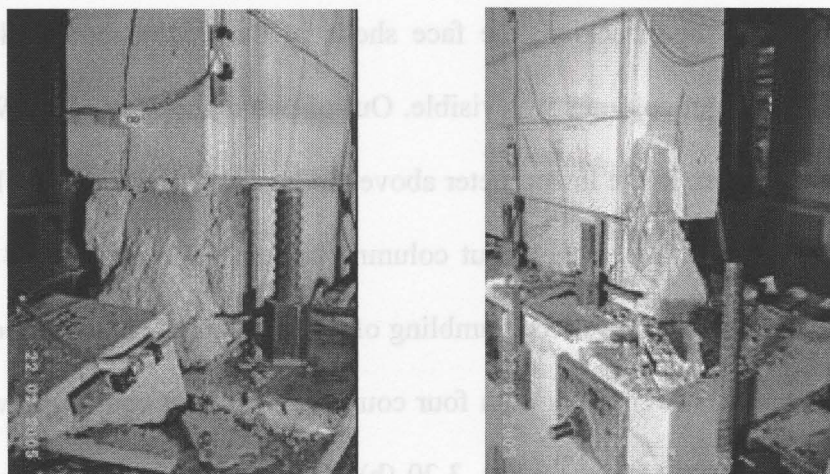
(a) East end   (b) West end

Fig. 3. 17: Spalling at both ends at 37 mm top deflection (Wall 2)
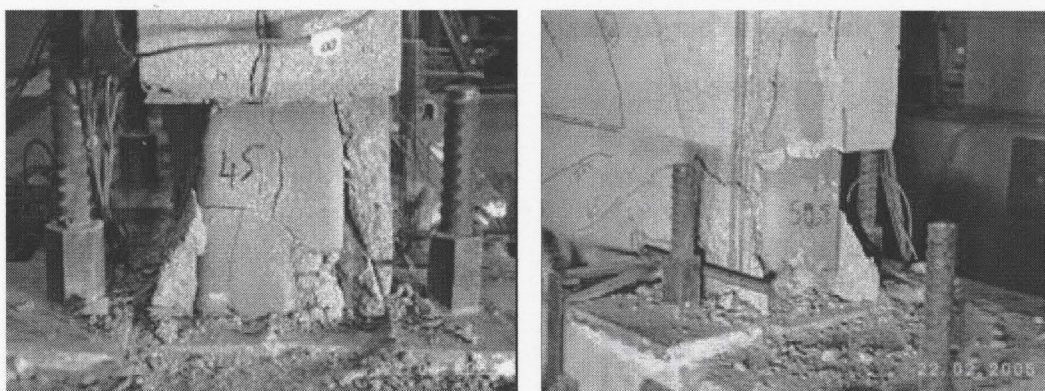
(a) East toe at 45 mm top deflection   (b) West toe at 52 mm top deflection

Fig. 3. 18: Cracking of outermost grout columns (Wall 2)

During the second cycle of the 52 mm displacement for loading in the East (pull) direction, a dramatic increase of crack width in the end webs of the bottom three courses of block along with splitting of the grout column and buckling of the outermost East bar were observed (see Fig. 3.19 (a)). After compression buckling

of the East end reinforcing bar had occurred during the second 52 mm displacement cycle for loading in the East (pull) direction, the resistance of the wall decreased significantly. At the end of the test, the extreme two East compression bars had buckled, the face shells in this region had spalled, and splitting of the grout columns was visible. Out-of-plane buckling of the West end of the wall was seen in the lower meter above the base with neither local buckling of the bars nor splitting of the grout columns being visible (see Fig. 3.19 (b)). Spalling of face shells as well as crumbling of grout columns could be seen in the outermost two cells over the bottom four courses at the East end of the wall (see Fig. 3.20 (a)). While as seen in Fig. 3.20 (b), deterioration in the West end was limited to face shell spalling with no major crumbling of grout in the outermost two cells over the bottom four courses.
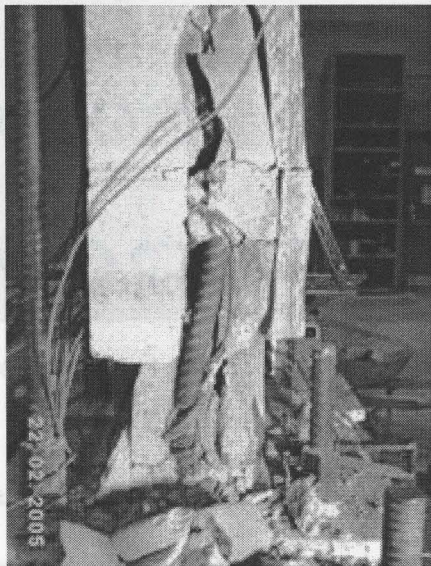
(a) Splitting of East grout column   (b) Out-of-plane buckling at West end

Fig. 3. 19: Failure mechanism at both ends of Wall 2 (at 52 mm top deflection)

(a) East end   (b) West end
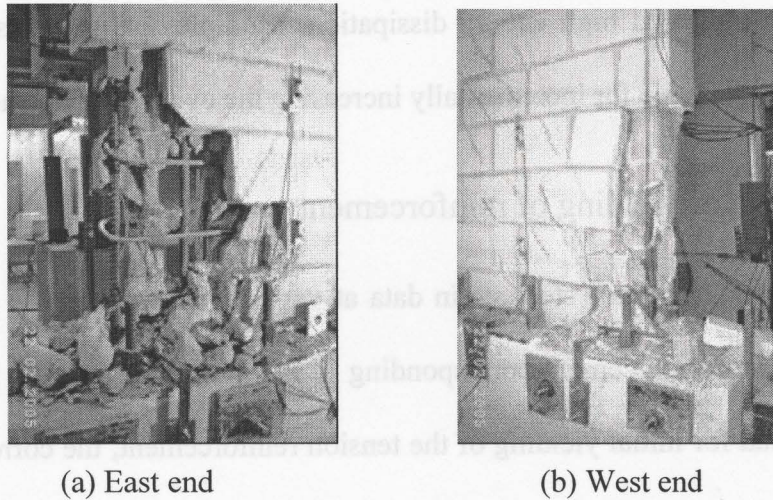
Fig. 3. 20: Damage of Wall 2 at the end of the test at 60 mm top deflection

3.3.3 Load-displacement response

The load-displacement hysteresis loops for Wall 2 shown in Fig. 3.12 indicate a symmetric response. The slopes of the loops decreased gradually with increases in displacement indicating loss of stiffness. As shown from the hysteresis loops, Wall 2 lost 20% of its strength at about four times the yield displacement for loading in the West (push) direction and at about three and a half times the yield displacement for loading in the East (pull) direction. The wall strength degraded to about 50% of its maximum capacity at four times the yield displacement for loading in the East (pull) direction and indicated the same loss for loading in the West (push) direction at four and a half times the yield displacement, at which point the test was terminated.

The response of the wall was almost linear elastic up to initial yielding of the end bar which resulted in generation of thin loops and low energy dissipation during these cycles. At high displacement levels, the loops started to become

fatter which indicated high energy dissipation. Multiples of yield displacement were used as the basis for incrementally increasing the cyclic displacements.

3.3.4 Extent of yielding of reinforcement

Table 3.2 presents steel strain data at various locations on the outermost East and West reinforcement corresponding to the yield load and the maximum load. The load for initial yielding of the tension reinforcement, the corresponding lateral displacement and percent drift are shown. Also, at maximum load, the strain and the strain as a multiple of yield strain, ε_y, are provided. During this test, the readings recorded from the strain gauges, at the interface between the wall and the base beam on the two outermost end reinforcing bars, were carefully monitored. When one of these readings indicated the yield strain, the loading was stopped and the lateral force was reversed to avoid having plastic deformation in the bar prior to reaching yield strain for this reverse loading. As a result, and unlike Wall 3 which will be presented later, the yield displacements for Wall 2 were the same for loading in the push and pull directions. This facilitated interpretation and tracking of the stresses and forces in the reinforcing bars. Initial yielding of the outermost East bar occurred during the 15 mm displacement cycle at 296 kN. The West bar yielded at 292 kN during the same loading cycle. After yielding was recorded, the West strain gauge located at the interface between the wall and the base beam began to give inconsistent readings and was thereafter ignored. The strains recorded at maximum load from the strain gauges located

150 mm and 300 mm below the interface between the wall and the base beam were about $0.92 \times \varepsilon_y$ and $0.32 \times \varepsilon_y$, respectively for the push loading direction, and $0.83 \times \varepsilon_y$ and $0.43 \times \varepsilon_y$, respectively for the pull loading direction, which shows some elongation of the bar inside the base beam. The maximum strains recorded from the strain gauges located 150 mm and 300 mm below the interface between the wall and the base beam were about $1.1 \times \varepsilon_y$ and $0.44 \times \varepsilon_y$, respectively for the push loading direction (corresponding to 6% strength degradation). The corresponding strains were $0.97 \times \varepsilon_y$ and $0.58 \times \varepsilon_y$, respectively, for the pull loading direction (corresponding to 37% strength degradation). Both occurred during the 60 mm displacement cycle.

Table 3. 2: Extent of yielding of reinforcement (Wall 2)

Strain gauge location	Wall end	Initial yielding condition			Strain at max. load	Strain $(\times \varepsilon_y)$
		Load	Displacement	% Drift		
Interface	West	- 292 kN	15 mm	0.41	----	----
500 mm		- 281 kN	15 mm	0.41	2.84×10^{-3}	1.13
900 mm		- 245 kN	58 mm	1.61	2.17×10^{-3}	0.87
Interface	East	296 kN	15 mm	0.41	10.12×10^{-3}	4.04
500 mm		312 kN	16 mm	0.44	2.71×10^{-3}	1.08
900 mm		320 kN	17 mm	0.47	2.63×10^{-3}	1.05

3.3.5 Wall deformation and drift

In-plane lateral displacements were measured at eight points over the height of the West end of the wall as in previous walls. Moving the anchors from the end webs to the face shells for the three lower measurement points delayed the loss of the attachment points to the wall and reduced the number of locations

where measurements were lost. The recorded in-plane lateral displacements over the height of the wall, for loading in both directions, are presented in Fig. 3.21 for key loading conditions related to yielding of reinforcement. A concentration of bending over the lower 0.7 m of the wall height is evident while the top 2.9 m of the wall tends to be relatively straight.
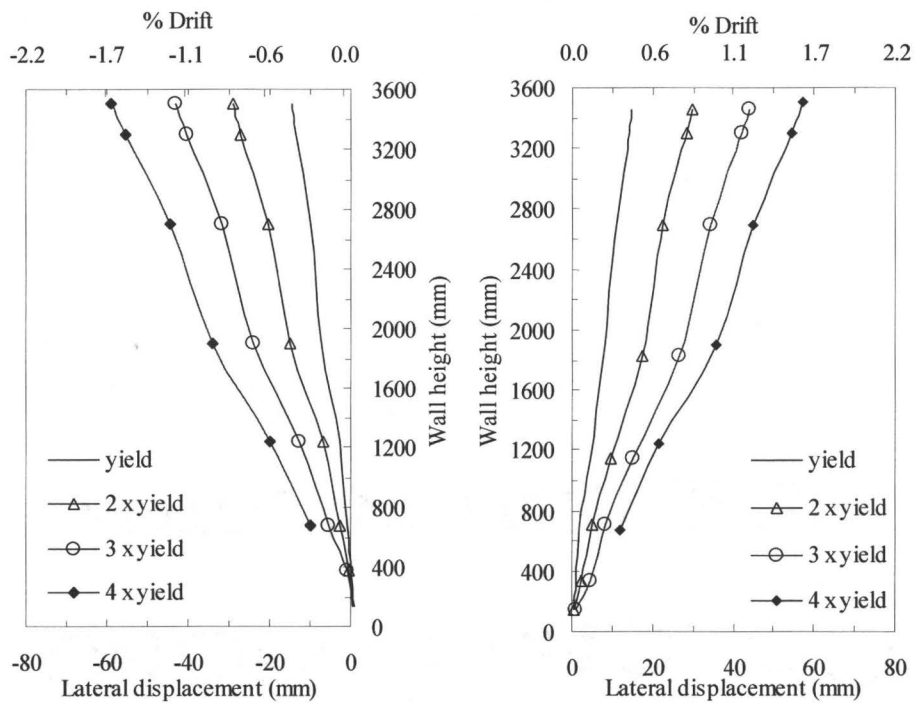
(a) Loading in East (pull) direction   (b) Loading in West (push) direction

Fig. 3. 21: Total in-plane lateral deflection (Wall 2)

3.3.6 Wall curvature

Average curvatures over segments of the height of Wall 2 at different lateral displacements stages are presented in Fig. 3.22 for loading in both directions. Average curvatures were calculated as explained previously and showed good symmetry for the push and pull loading directions. The early crushing of the West toe subjected to compression during loading in the push

direction resulted in slightly higher curvatures compared to loading in the pull direction (see Figs. 3.15 to 3.17). Average curvatures over the bottom 300 mm of the wall reached an average value of 0.0185 rad/m at a top displacement equivalent to three times the yield displacement of the wall. Block spalling and subsequent loss of potentiometer attachment anchors made it impossible to obtain measurements at higher deflections. High average curvatures were measured over the bottom 900 mm of Wall 2 and were relatively low and almost unchanged over the remainder of the wall for increased displacement.
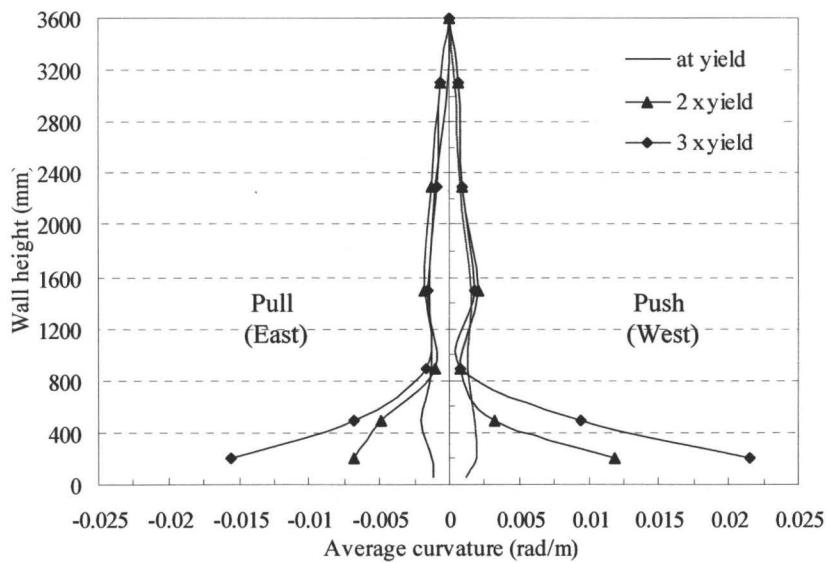
Fig. 3. 22: Average curvature along wall height for loading in both directions (Wall 2)

3.3.7 Strain profile

The strain profiles along the wall length were calculated as discussed previously and are presented in Fig. 3.23 for loading in both directions. The average strain profiles for the push and pull loading directions showed similar patterns as shown in Figs. 3.23 (a) to (d). The profiles of average strain between

the base beam and 300 mm above it, shown in Fig. 3.23 (a), indicate that the lengths of the compression zone are about 500 mm and 400 mm with maximum compressive strains of 1.2 x10^{-3} and 2.6 x10^{-3} at initial yield displacement and at two times the initial yield displacement, respectively. The figure also shows a fairly linear strain profile along the whole length of the wall at two times the initial yield displacement.

(a) 0 – 300 mm above the base beam   (b) 300 – 700 mm above the base beam

(c) 0 – 300 mm above the base beam   (d) 300 – 700 mm above the base beam
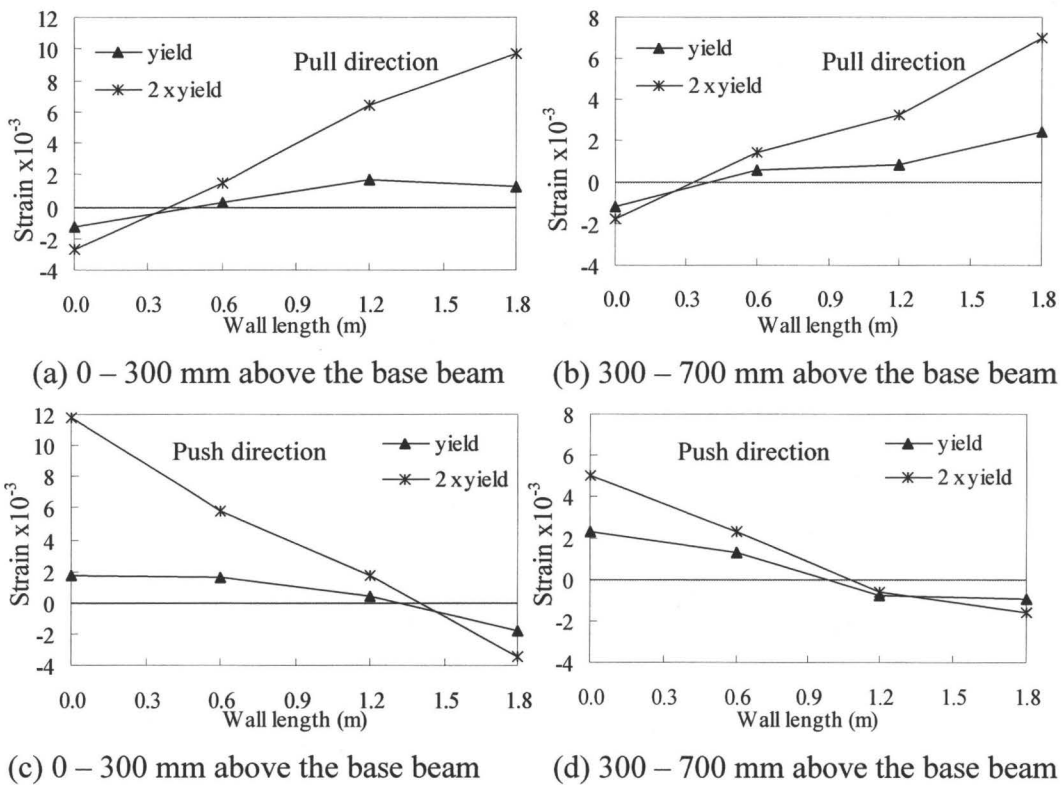
Fig. 3. 23: Profile of average strain along wall length for loading in both directions (Wall 2)

The profiles of average strain between 300 mm and 700 mm above the base beam, shown in Fig. 3.23 (b), indicate that the lengths of the compression zone are about 400 mm and 300 mm with maximum compressive strains of 1.18 x10^{-3} and 1.75 x10^{-3} at initial yield displacement and at two times the initial yield

displacement, respectively. The figure shows a fairly linear strain profile along the portion of the wall under tension.

3.4   Wall 3

Wall 3 was actually the second wall to be tested and therefore the loading pattern followed closely that of Wall 1.

3.4.1 Details of Wall 3

Wall 3 was reinforced with No. 25 vertical bars in every other cell (ρ_v = 0.73%) and No. 10 horizontal bars in every other course (ρ_h = 0.13%) starting with the first course. It was not subjected to any superimposed axial load during the test. After discovering empty cells in Wall 1, this wall was checked to locate any defective regions and, if required, to repair the wall before testing. Figure 3.24 indicates the locations of empty cells discovered by drilling into this wall.

The repair technique adopted to fill the empty cells of the wall with grout is shown in Fig. 3.25. A 25 mm diameter hole was drilled at the bottom course of the wall (Fig. 3. 25 (a)), and a hand pump was used to inject the grout through a hose inserted into the hole. Inspection holes were also drilled in order to ensure filling of all empty cells (Fig. 3. 25 (b)). After filling four courses, another 25 mm diameter hole was drilled at the fifth course in order to continue grouting and not to exceed the pressure capacity of the pump.

The hysteresis loops for Wall 3 for cyclic loading are shown in Fig. 3.26 for loading in the push and pull directions.
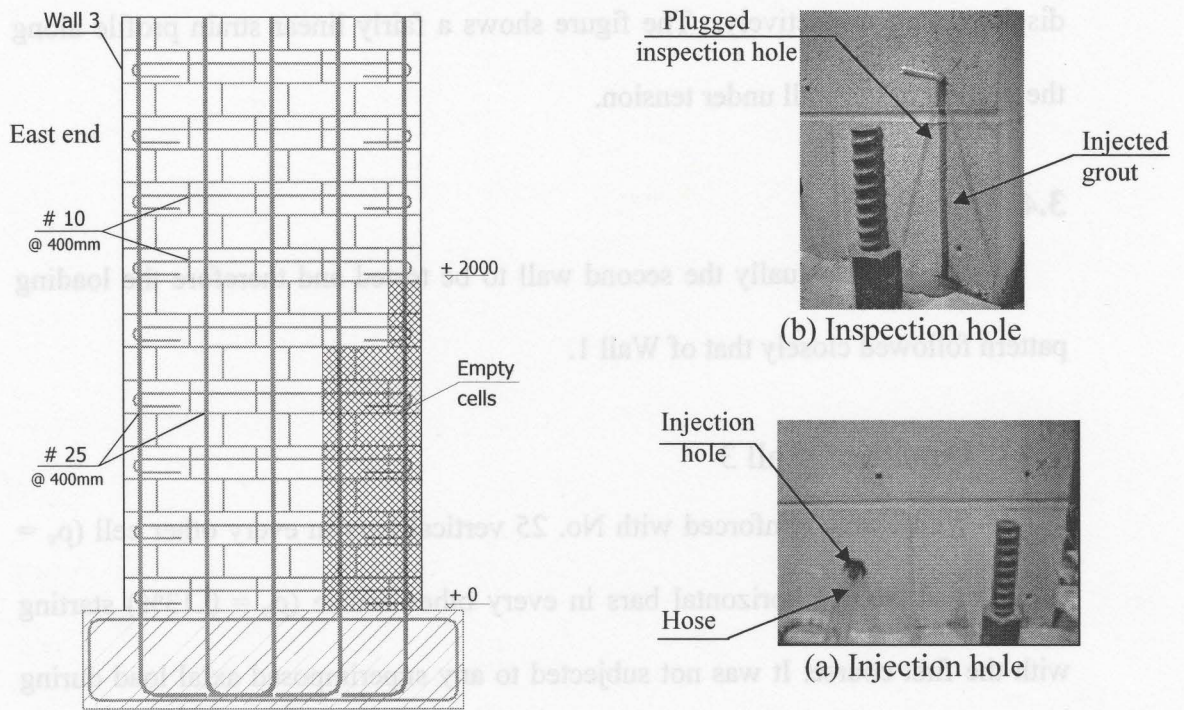
Fig. 3. 24: Location of empty cells (Wall 3)

(b) Inspection hole

(a) Injection hole

Fig. 3. 25: Repair technique (Wall 3)
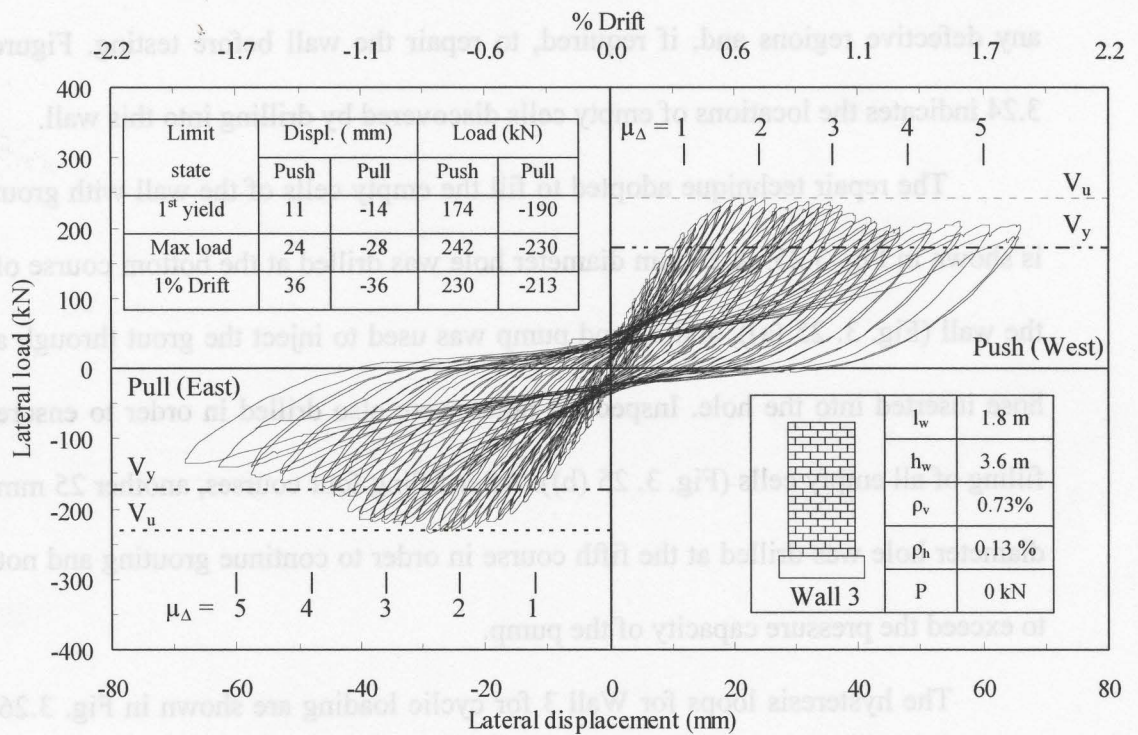
Fig. 3. 26: Hysteresis loops (Wall 3)

3.4.2 General observations

The cracking pattern was similar to those for the previous walls and indicated flexure dominated response. Bed joint cracks were visible during the 4 mm displacement cycle; cracks were seen in the first three courses above the base beam and were symmetric at both ends of the wall. Horizontal bed joint cracks were visible up to the eighth course during the 8 mm displacement cycle and extended for an average of 600 mm from both ends of the wall. Stepped cracks became visible during the 10 mm displacement cycle and were concentrated between the sixth and the fifteenth course as indicated in Fig. 3.27 (a). The stepped cracks extended down to the second course above the base beam during the 12 mm displacement cycle (see Fig. 3.27 (b)) and, with increasing wall deflection, the stepped cracks started to pass through the blocks. The diagonal cracks were visible over the entire height of the wall reaching the top loading beam during the 28 mm displacement cycle as shown for the top half of Wall 3 in Fig. 3.27 (c). The horizontal cracks became wider rather than increasing in length with further increases of wall displacement.

The repaired wall displayed good symmetry for loading in the push and pull directions up to about 40 mm displacements, but some differences in compression zone damage for higher displacements led to greater degradation of wall resistance for loading in the East (pull) direction. [For loading in the pull direction, the compression zone was not at the West end grout injection repair zone]. The crack between the wall and the base beam extended to the whole

97

length of the wall during the 24 mm displacement cycle and the maximum width of this crack, at the East end, was found to be about 5.3 mm, as shown in Fig. 3.28, during the 42 mm displacement cycle for loading in the West (push) direction.
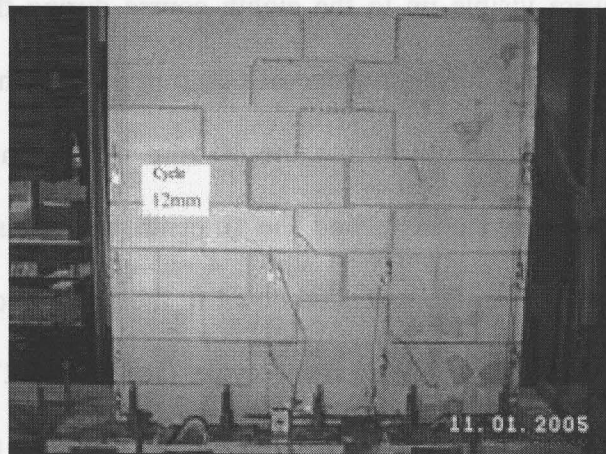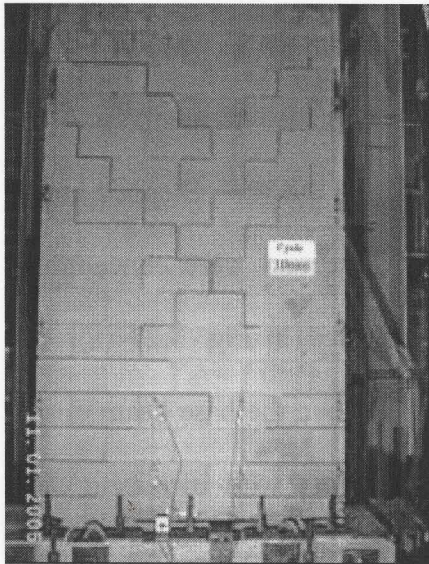
(a) Cracks at 10 mm top deflection

(b) Cracks at 12 mm top deflection
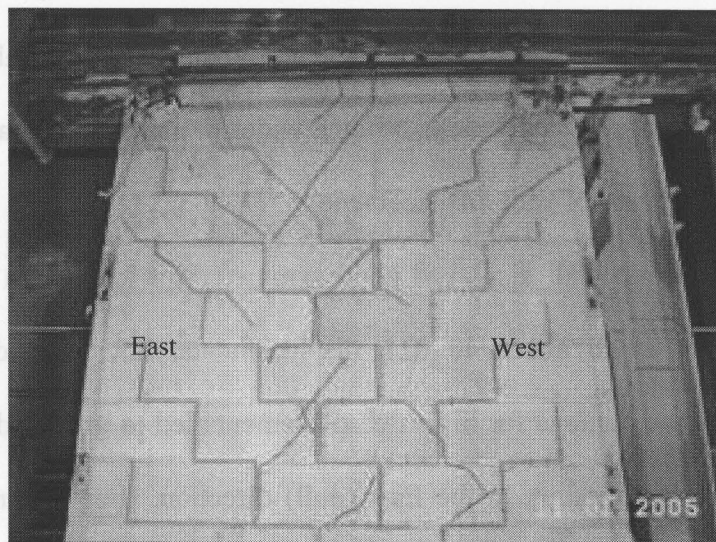
(c) Cracks at 28 mm top deflection

Fig. 3. 27: Cracking progress in Wall 3
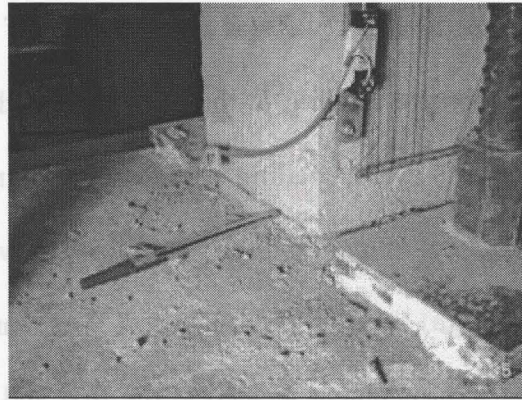
Fig. 3. 28: Wide crack at base level of Wall 3 at 42 mm top deflection

Vertical cracks started to appear in the East and West toes of the wall at 34 mm top wall deflection while maximum loads of 242 kN and 235 kN were reached during the 24 mm and 28 mm displacement cycles for loading in the push and pull directions, respectively. At 38 mm top deflection, vertical cracks in the East and West toes extended to the second course above the base beam, as seen in Fig. 3.29 (a) and (b). At the same displacement level, very wide horizontal and diagonal cracks were noticed and light could be seen through bed joints located at midlength of the wall at the fourth course above the base beam.
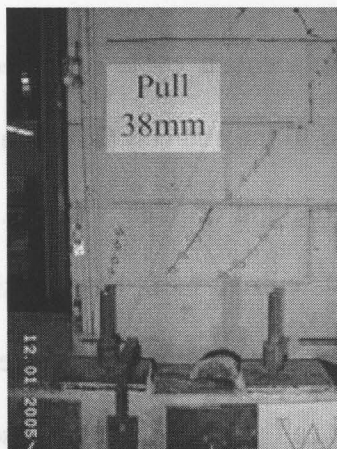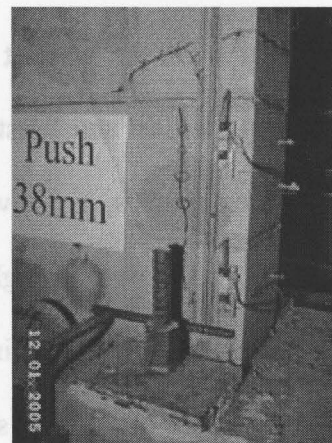
(a) Cracks at East toe　　　　　　　　　　　　(b) Cracks at West toe

Fig. 3. 29: Cracking at toes of Wall 3 at 38 mm loading cycle

Major cracking of the block webs at the West end of the wall occurred at 42 mm top wall deflection for loading in the West (push) direction. During the second 42 mm displacement cycle, spalling of the end webs up to the third course and deterioration of grout column around the outermost bar were seen at the West toe, as shown in Fig. 3.30 (a) and (b). The outermost West bar was seen to buckle between the horizontal reinforcement located at the first and third course during the 44 mm displacement cycle for loading in the West (push) direction, as shown in Fig. 3.30 (c), and this bar straightened during the reverse cycle of loading.

Spalling of the East toe and cracking of the outermost grout column occurred during the 44 mm displacement cycle for loading in the East (pull) direction, as indicated in Fig. 3.31 (a). At about 46 mm displacement, the column of grout around the outermost East bar deteriorated and buckling of this bar was also seen between the horizontal reinforcement located at the first and third course, as shown in Fig. 3.31 (b) and (c). This bar also straightened in tension during the reverse cycle of loading.

Inspection of the wall at the 50 mm displacement cycle indicated that deterioration at the East and West toes was limited to the end cell (200 mm) over the bottom three courses, as shown from the photograph of Wall 3 in Fig. 3.32. Cyclic loading of the wall to higher displacements caused more deterioration to the East toe resulting in crumbling of the grout columns around the outermost East bar and spalling of the face shells in the next cell up to the third course (see Fig. 3.33 (a)). The West end experienced less damage consisting of only

crumbling of the grout column around the outermost West bar up to the second

course and spalling of the end webs up to the fourth course (see Fig. 3.33 (b)).

(a) Major cracking   (b) Spalling around the bar at (c) Buckling of the bar at
at 42 mm top displacement   42 mm top displacement   44 mm top displacement

Fig. 3. 30: Progressive deterioration at the West toe for Wall 3
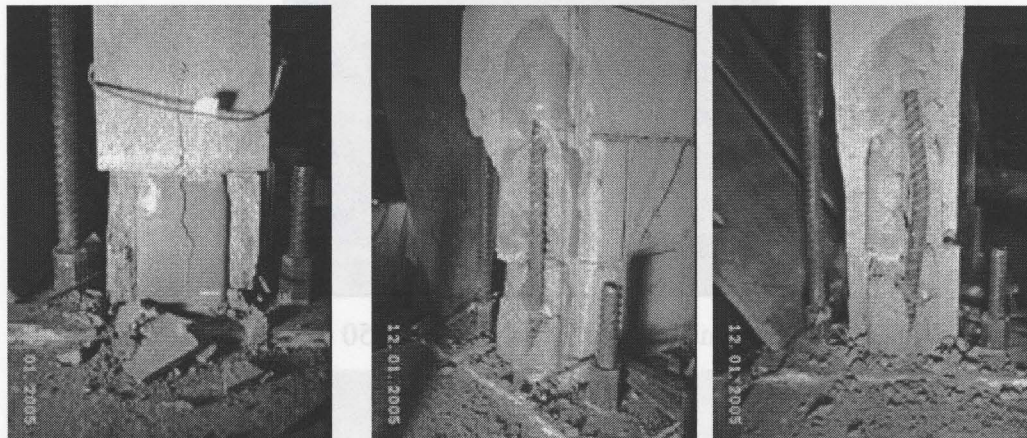
(a) Cracking in grout column   (b) Spalling around the bar   (c) Buckling of the East bar
at 44 mm top displacement   at 46 mm top displacement   at 46 mm top displacement

Fig. 3. 31: Progressive deterioration at the East toe for Wall 3

Inspection of the wall at the 50 mm displacement cycle indicated that

deterioration at the East and West toes was limited to the end cell (200 mm) over

the bottom three courses, as shown from the photograph of Wall 3 in Fig. 3.32.

Cyclic loading of the wall to higher displacements caused more deterioration to

the East toe resulting in crumbling of the grout columns around the outermost East bar and spalling of the face shells in the next cell up to the third course (see Fig. 3.33 (a)). The West end experienced less damage consisting of only crumbling of the grout column around the outermost West bar up to the second course and spalling of the end webs up to the fourth course (see Fig. 3.33 (b)).

Fig. 3. 32: Deformation profile of Wall 3 at 50 mm top deflection
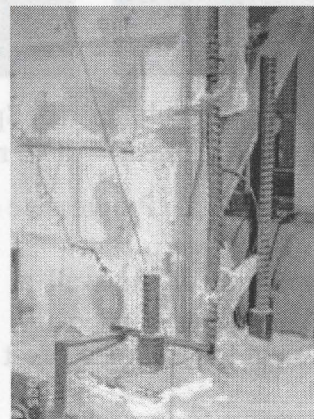
(a) East end   (b) West end

Fig. 3. 33: Damage at both ends of Wall 3 at 55 mm top deflection

The wall did not experience severe degradation in strength during loading in the West (push) direction unlike for loading in the reverse direction as mentioned earlier. Significant buckling of the East two end reinforcing bars was observed close to the termination of the test (see Fig. 3.34), and face shell spalling extended from the East end to about midlength of the wall (see Fig. 3.35). Deterioration at the West end was limited to the end cells and buckling of the bars in the West end of the wall was limited to the outermost bar only as shown previously. At the beginning of the second 75 mm displacement for loading in the West (push) direction, the East reinforcing bar broke (see Fig. 3.36), and the wall lost significant strength leading to the test being terminated. The bar failure may have been related to fatigue stresses resulting from the high number of loading cycles under post-yield conditions.
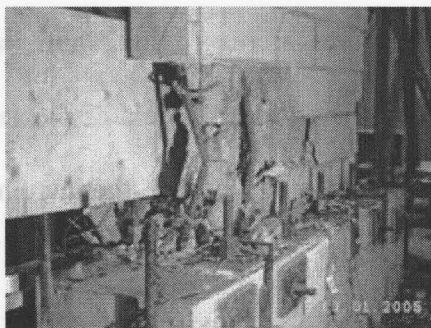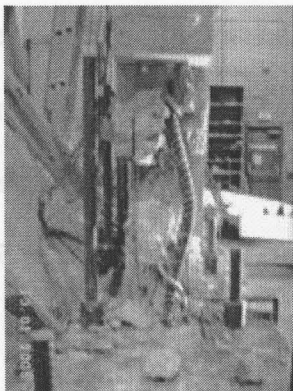
Fig. 3. 34: Major buckling   Fig. 3. 35: Deterioration at the   Fig. 3. 36: East bar
of East bar in Wall 3   East end of Wall 3   broken in Wall 3

3.4.3 Load-displacement response

The load-displacement hysteresis loops, shown in Fig. 3.26 for Wall 3, indicate a stable and symmetric response for the repaired wall. The slopes of the

loops decreased gradually with increases in displacements indicating loss of stiffness. As shown from the hysteresis loops, Wall 3 lost 20% of its strength at a displacement of about six times the displacement at initial yield for loading in the West (push) direction. A similar loss occurred at about four and a half times the initial yield displacement for loading in the East (pull) direction. The wall resistance degraded for loading in the East (pull) direction to about 50% of its maximum capacity at the end of the test but did not show a similar loss in strength during the push loading cycles.

The response of the wall was almost linear elastic up to first yielding of the tension reinforcement; this generated thin hysteresis loops and low energy dissipation during these loading cycles. At high displacement levels, the hysteresis loops started to become fatter and minor pinching could be seen due to incrementally cycling the wall in both directions. As was the case for Wall 1, the cyclic loading of this wall was increased in 2 mm increments up to 50 mm displacement instead of using multiples of yield displacement. After getting some confidence related to the response of the wall, the increments were increased to 5 mm for the remainder of the test.

3.4.4 Extent of yielding of reinforcement

During loading in the West (push) direction causing initial yielding in the East bar, displacement was not stopped quickly enough to avoid some yield deformation. As a result of the plastic deformation, the yield displacement for loading in the East (pull) direction was slightly higher. The yield displacement for

loading in the West (push) direction was recorded to be 11 mm at a load of 174 kN compared to 14 mm at 190 kN for loading in the East (pull) direction. The outermost bars at both wall ends experienced yielding as recorded from the strain gauges on the reinforcement at the interface between the wall and the base beam and at 500 mm above the base beam.

The yielding eventually extended up to 900 mm for the West bar while the East bar did not experience yielding at that height. No yielding was recorded from the strain gauges inside the base beam. At maximum load, the strains recorded from the strain gauges located 150 mm and 300 mm below the interface between the wall and the base beam were about $0.82 \times \varepsilon_y$ and $0.5 \times \varepsilon_y$, respectively, for the push loading direction, and $0.80 \times \varepsilon_y$ and $0.36 \times \varepsilon_y$, respectively, for the pull loading direction, which shows some elongation of the bar inside the base beam. The maximum strains recorded from the strain gauges located 150 mm and 300 mm below the interface between the wall and the base beam were about $0.92 \times \varepsilon_y$ and $0.65 \times \varepsilon_y$, respectively, for the push loading direction (corresponding to 13% strength degradation). The corresponding strains were $0.90 \times \varepsilon_y$ and $0.50 \times \varepsilon_y$, respectively, for the pull loading direction (corresponding to 34% strength degradation). Both occurred during the 60 mm displacement cycle.

As indicated in Table 3.3, at maximum load, the tensile strain in the West outermost bar in the repaired zone was lower than for the East outermost bar at the interface between the wall and the base beam. However, the reverse condition was observed at 500 mm above the base beam.

Table 3. 3: Extent of yielding of reinforcement (Wall 3)

Strain gauge location	Wall end	Initial yielding condition			Strain at max. load	Strain $(x\ \varepsilon_y)$
		Load	Displacement	% Drift		
Interface	West	- 190 kN	14 mm	0.38	$6.28\ x10^{-3}$	2.51
500 mm		- 229 kN	26 mm	0.72	$6.29\ x10^{-3}$	2.51
900 mm		- 229 kN	26 mm	0.72	$2.54\ x10^{-3}$	1.01
Interface	East	174 kN	11 mm	0.30	$17.91\ x10^{-3}$	7.18
500 mm		202 kN	16 mm	0.44	$2.78\ x10^{-3}$	1.11
900 mm		208 kN	17 mm	0.47	$2.16\ x10^{-3}$	0.86

3.4.5 Wall deformation and drift

In-plane lateral displacement was measured at eight points over the height of the West end of the wall, as was done for Wall 1. However, the three lower wire potentiometers became ineffective, as also was the case for Wall 1, when the anchors attaching them to the wall failed due to major cracking and face shell spalling extending up to the fifth course at the West toe. This resulted in losing all subsequent readings at these locations. The recorded in-plane lateral displacements over the height of the wall, for loading in both directions, are presented in Fig. 3.37 (a) and (b) for key loading conditions related to yielding of reinforcement. A concentration of bending over the lower 0.8 m of the wall height is evident while the top 2.8 m of the wall appears to remain relatively straight.
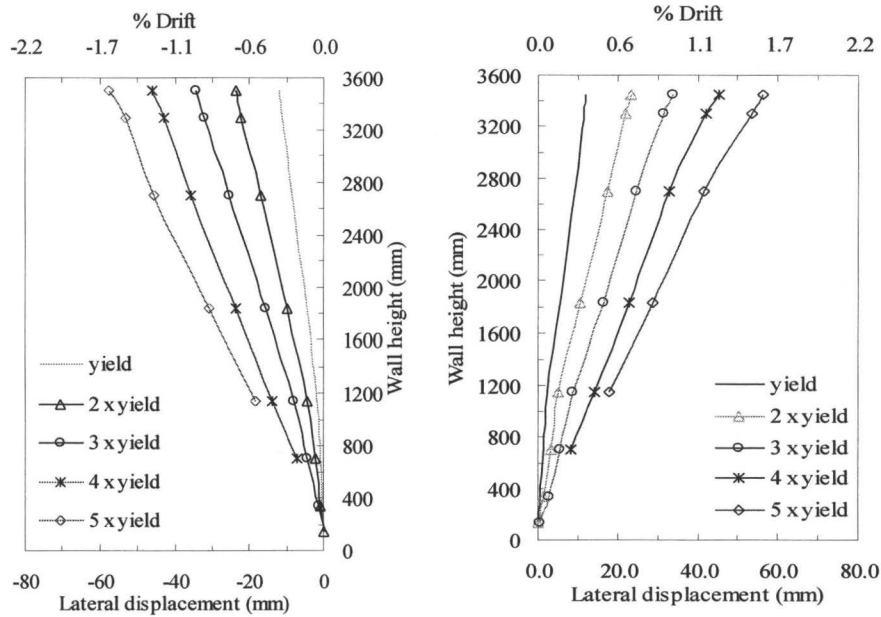
(a) Loading in East (pull) direction   (b) Loading in West (push) direction

Fig. 3. 37: Total in-plane lateral deflection (Wall 3)

3.4.6 Wall curvature

Average curvatures over segments of the height of Wall 3 at different lateral displacements stages are presented in Fig. 3.38 for loading in both directions. Average curvatures were calculated as previously described and showed good symmetry for loading in the push and pull directions. Average curvatures over the bottom 100 mm of the wall reached a value of 0.019 rad/m at a top displacement equivalent to three times the yield displacement of the wall. Block spalling at the West end and subsequent loss of potentiometer attachment anchors made it impossible to obtain measurements at higher deflections. High average curvatures were recorded over the bottom 900 mm of Wall 3 and were relatively low and unchanging with increased deflection over the remainder of the wall height.

107
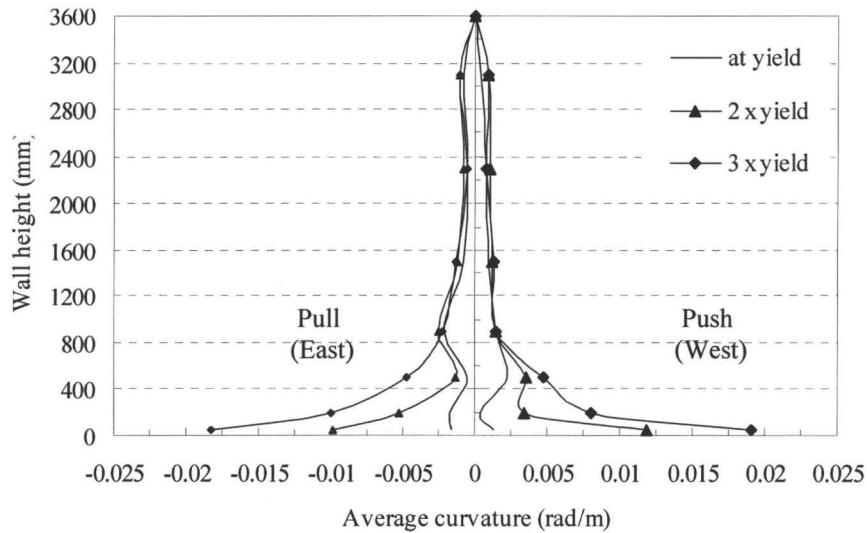
Fig. 3. 38: Average curvature along wall height for loading in both directions (Wall 3)

3.4.7 Strain profile

The strain profiles along the wall length were calculated as explained for Wall 1 and are presented in Fig. 3.39 for loading in both directions. The average strain profiles for loading in the push and pull directions showed some discrepancies due to having different damage levels at the ends of the repaired wall. The profiles of average strain between the base beam and 300 mm above the base beam, shown in Fig. 3.39 (a), indicate that the lengths of the compression zone are about 450 mm and 200 mm with maximum compressive strains of 1.4 $x10^{-3}$ and 3.1 $x10^{-3}$ at yield displacement and at three times the yield displacement, respectively. The figure also shows a fairly linear strain profile along the length of the wall under tension for low displacement levels.

The profiles of average strain between 300 mm and 700 mm above the base beam, shown in Fig. 3.39 (b), indicate that the length of the compression zone is very small at yield displacement and almost no compression zone was

recorded within this segment at three times the yield displacement. The explanation of this behaviour can be due to the cumulative plastic deformation in the reinforcement over the bottom part of the wall which prevented the cracks from closing during the reverse part of the load cycle. The figure also shows a fairly linear strain profile along the portion of the wall under tension. Figures 3.39 (c) and (d) show the strain profile for the wall during the push loading cycle where the grout used in repair was under compression. The compression strain values recorded during the push direction of loading seemed to be inconsistent as higher strain was calculated for regions at greater height above the base beam.

(a) 0 – 300 mm above the base beam   (b) 300 – 700 mm above the base beam

(c) 0 – 300 mm above the base beam   (d) 300 – 700 mm above the base beam
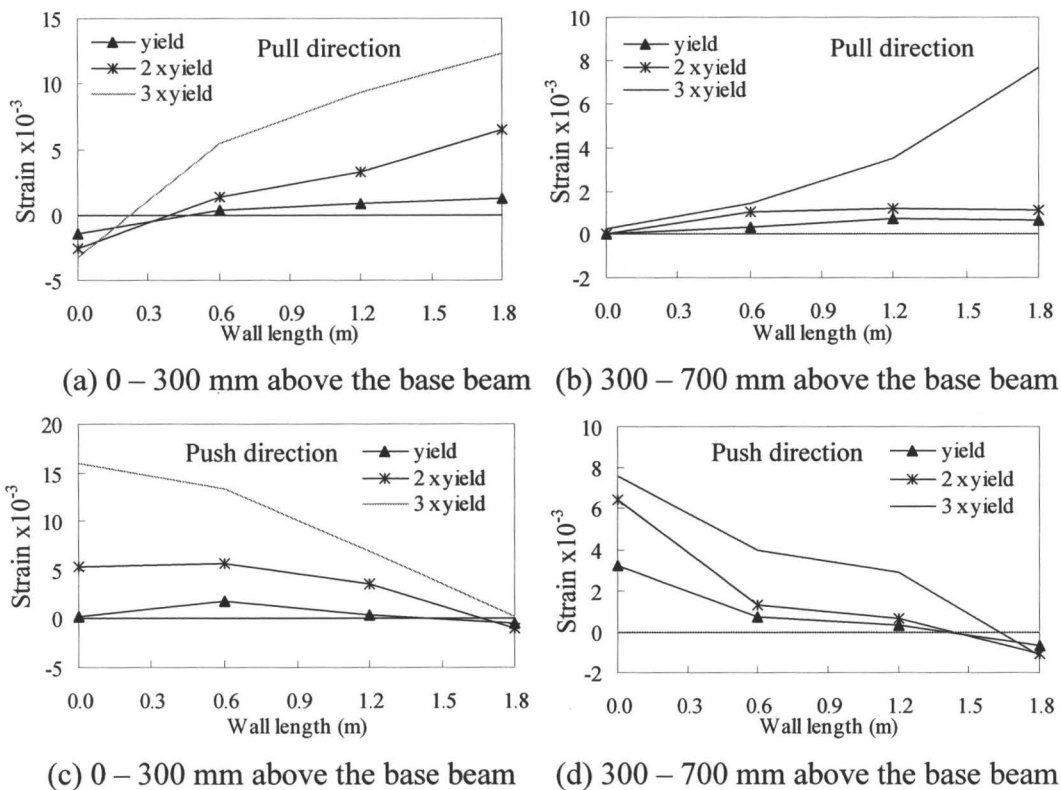
Fig. 3. 39: Profile of average strain along wall length for loading in both directions (Wall 3)

3.5   Wall 4

3.5.1 Details of Wall 4

Wall 4 was reinforced with No. 20 vertical bars in every cell (ρ_v = 0.78%) and No. 10 horizontal bars in every other course (ρ_h = 0.13%) starting with the first course. It was not subjected to any superimposed axial load during the test.

The hysteresis loops for Wall 4 for cyclic loading are shown in Fig. 3.40 for loading in the push and pull directions. The displacement increments used in this test were multiple of yield displacement similar to those used for Wall 2.
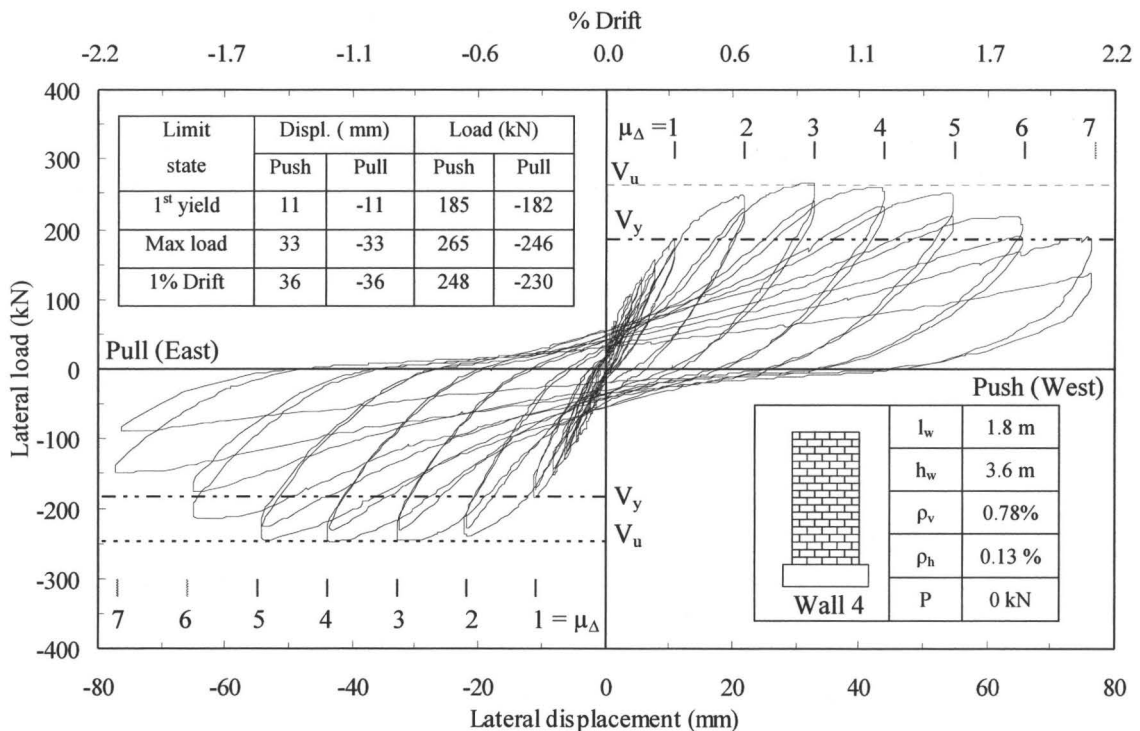
Fig. 3. 40: Hysteresis loops (Wall 4)

3.5.2 General observations

The observed crack pattern was similar to those of the previously discussed walls indicating flexure dominated response. Horizontal bed joints cracks were first detected during the 4 mm displacement cycle and extended up to the sixth course. Stepped cracks appeared between the fourth and the ninth courses during the 11 mm displacement cycle (see Fig. 3.41 (a)), and during the 22 mm displacement cycle, diagonal cracks formed and extended over the wall height as shown in Fig. 3.41 (b). The wall resisted a maximum load of 265 kN for loading in the West (push) direction and 246 kN for loading in the East (pull) direction during the 33 mm displacement cycle for both loading directions.
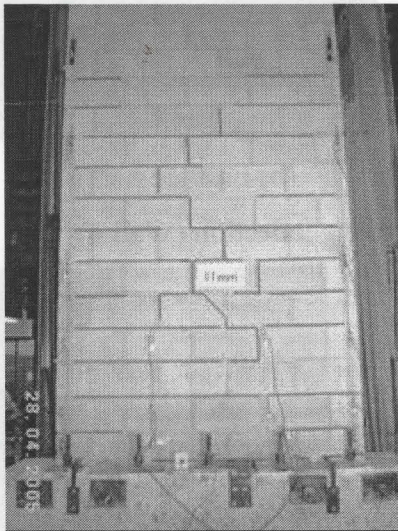
(a) At 11 mm top wall deflection   (b) At 22 mm top wall deflection
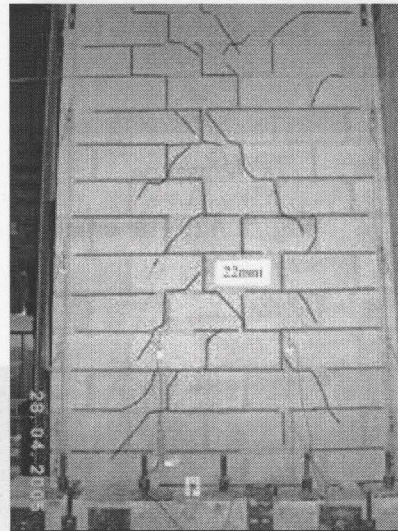
Fig. 3. 41: Cracking in Wall 4

Vertical cracks in the East and West toes also started to form during the 33 mm displacement cycle and some minor spalling of the webs of the end blocks in the second course was observed in the West toe during the second loading cycle

(see Fig. 3.42 (a) and (b)). Spalling of the end blocks started to occur during the 44 mm displacement cycle and at 55 mm top deflection, it extended to the second course (see Fig. 3.43 (a) and (b)). During the same displacement cycle, diagonal cracks were observed over the bottom meter of the wall (see Fig. 3.44) causing about 10% reduction in strength.
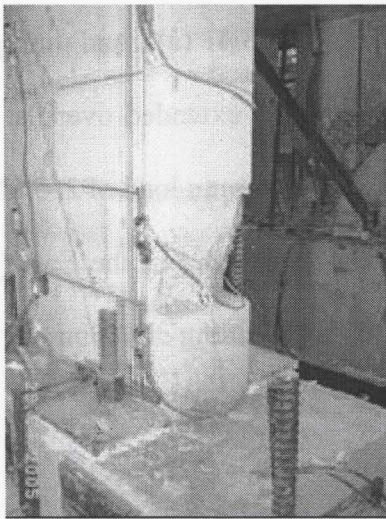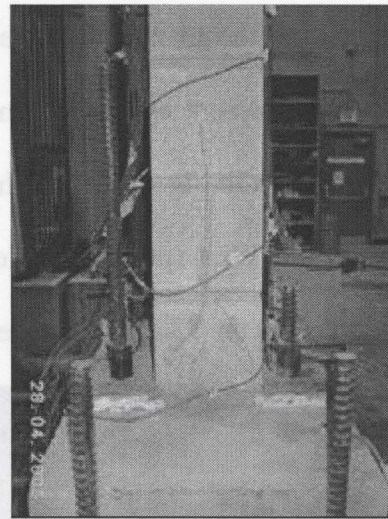
| (a) West toe | (b) East toe |

Fig. 3. 42: Toe cracking at 33 mm top deflection (Wall 4)
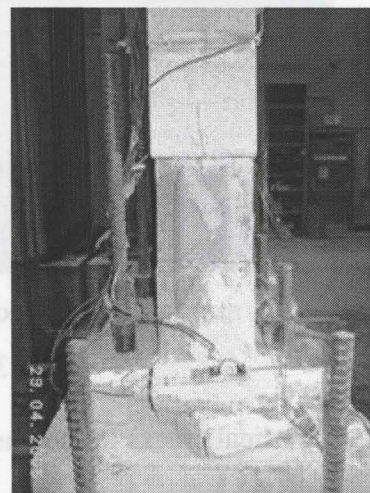
| (a) West toe | (b) East toe |

Fig. 3. 43: Toe spalling at 55 mm top deflection (Wall 4)
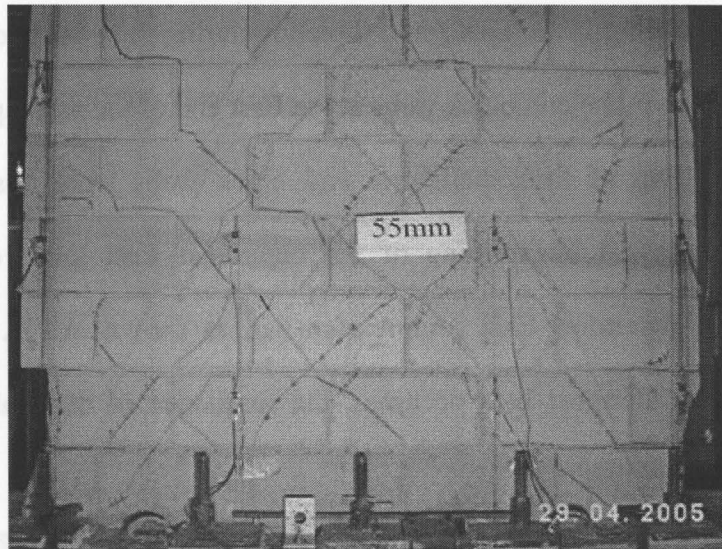
Fig. 3. 44: Cracking within the bottom meter at 55 mm top deflection (Wall 4)

At 66 mm displacement for loading in the West (push) direction, wide cracks in the face shells at the West end of the wall up to the third course and spalling of face shells and end webs were observed. The strength decreased by an additional 9%. These were followed by deterioration of the outermost West grout column and buckling of the outermost West compression bar, as shown in Fig. 3.45.
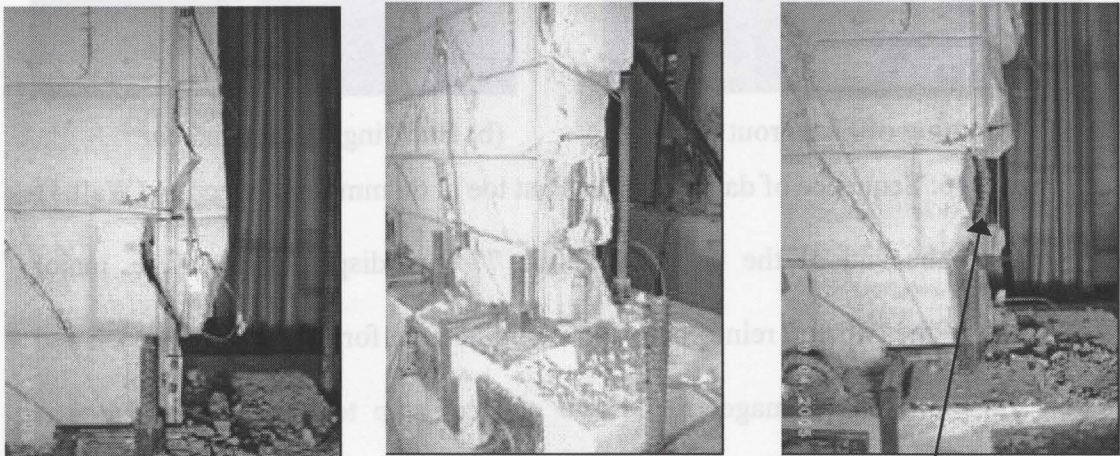
(a) Cracking of end blocks   (b) Deterioration of grout column (c) Buckling of end bar

Fig. 3. 45: Sequence of damage at the West toe at 66 mm top deflection (Wall 4)

113

During loading in the East (pull) direction during the 66 mm displacement cycle, wide cracks in the end block webs at the East end of the wall up to the third course and spalling of face shells and end block webs were observed. This damage was followed by splitting of the outermost East grout column and buckling of the outermost East compression bar, as shown in Fig. 3.46. After buckling of the outermost bars occurred, the resistance of the wall decreased significantly.
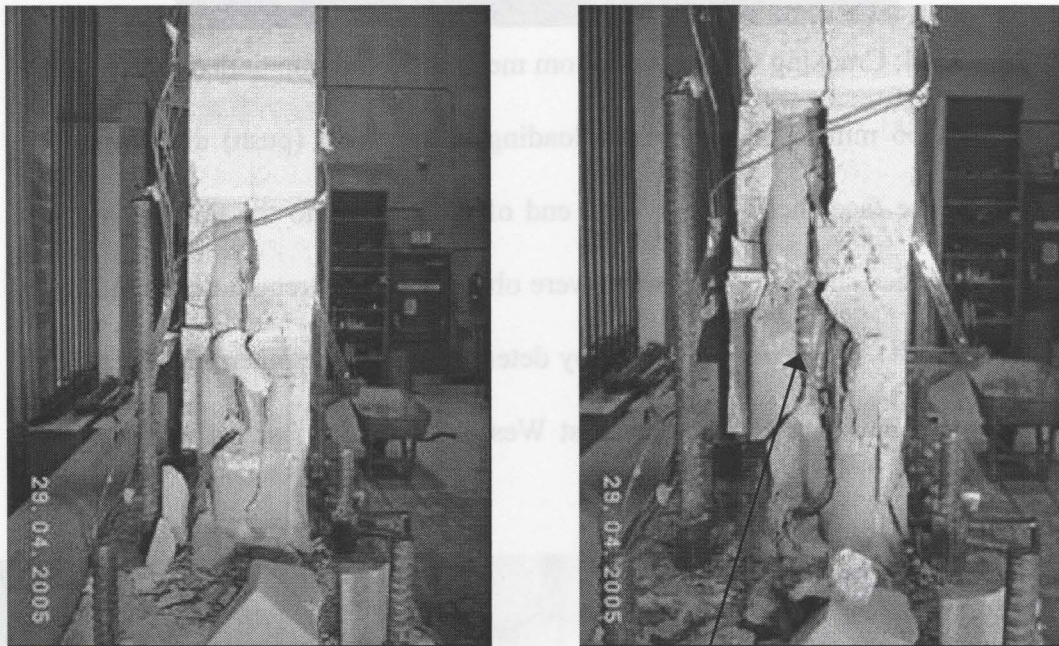
(a) Splitting of East grout column   (b) Buckling of East end bar

Fig. 3. 46: Sequence of damage at the East toe at 66 mm top deflection (Wall 4)

At the end of the test, during the 77 mm displacement cycle, major buckling of the two end reinforcing bars could be seen for loading in the push and pull directions and damage of the two end cells up to the third course was significant (see Fig. 3.47 (a), (b) and (c)).
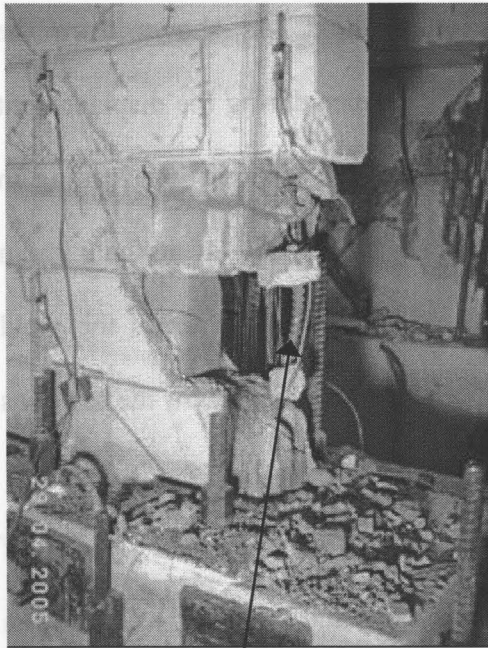
(a) Major buckling of West bar   (b) Major buckling of East bar
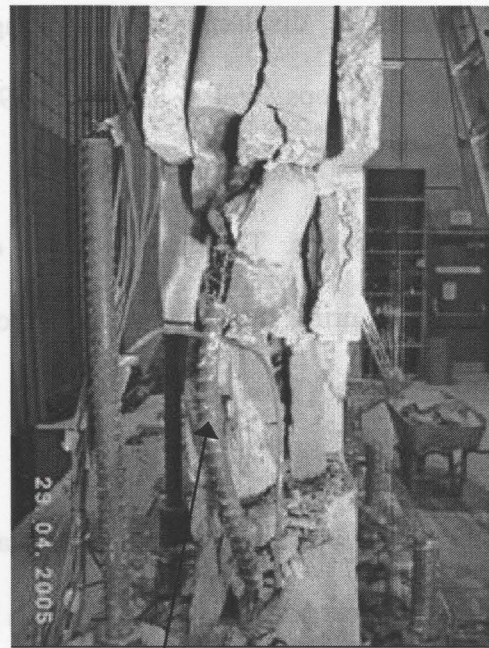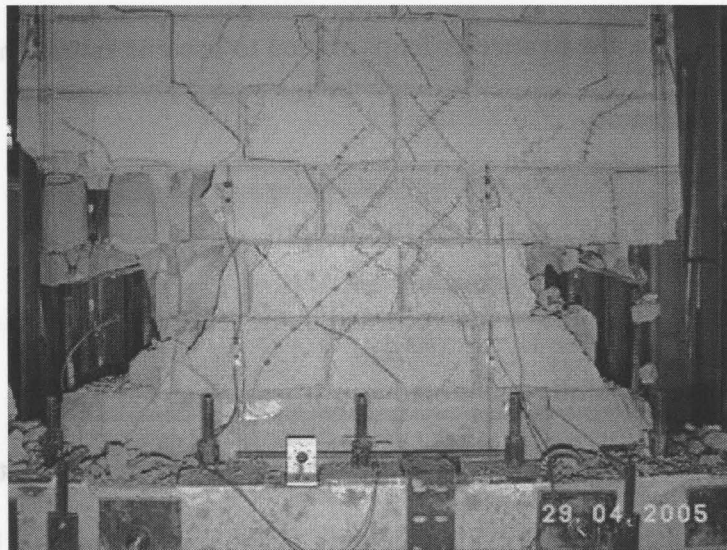
(c) Damage level in the bottom meter of the wall

Fig. 3. 47: Wall 4 at the end of the test (at 77 mm top deflection)

3.5.3 Load-displacement response

The load-displacement hysteresis loops for Wall 4, shown in Fig. 3.40, indicate a symmetric response. The slopes of the loops decreased gradually with

increases in displacement indicating loss of stiffness. As shown from the hysteresis loops, Wall 4 lost about 19% of its resistance during the displacement cycle corresponding to six times the yield displacement (66 mm) for loading in both directions. The wall strength degraded to about 50% of its maximum capacity during the displacement cycle corresponding to seven times the yield displacement (77 mm) for loading in both directions at which point the test was terminated.

The response of the wall was almost linear elastic up to initial yielding of the outermost bar. This generated thin hysteresis loops and low energy dissipation during the cycles as was the case for the previously discussed walls. At high displacement levels, the hysteresis loops started to become fatter which indicated high energy dissipation.

3.5.4 Extent of yielding of reinforcement

During this test, the strains recorded in the reinforcing bars at the two ends of the walls were carefully monitored and it was observed that the strain in the outermost West bar became much larger than in the outermost East bar starting with the 6 mm displacement cycle. Yielding of the outermost West bar occurred at 141 kN at 7.8 mm deflection whereas the strain reading for the East bar indicated that it was not close to yielding. At this point, a quick calculation was performed and, based on the increase of load from the previous cycle for both strain gauges, it was concluded that the reading from the West strain gauge at the

interface between the wall and the base beam was not consistent and that the reading from the East strain gauge was more reasonable.

The test was continued assuming that no yielding had occurred yet. During the 11 mm loading cycle, the lateral load reached 185 kN and the East strain gauge showed initial yielding for loading in the West (push) direction. During the same displacement cycle but for loading in the East (pull) direction, the lateral load reached 182 kN, which was assumed to represent the initial yielding state. This load was consistent with the predicted load from hand calculations which are presented later. The extent of yielding of reinforcement for Wall 4 is presented in Table 3.4. No yielding was recorded from the strain gauges inside the base beam. The strains recorded at maximum load from the strain gauges located 150 mm and 300 mm below the interface between the wall and the base beam were about 0.52 x ε_y and 0.08 x ε_y, respectively for the push loading direction, and 0.66 x ε_y and 0.26 x ε_y, respectively for the pull loading direction, which shows some elongation of the bar inside the base beam. The maximum strains recorded from the strain gauges located 150 mm and 300 mm below the interface between the wall and the base beam were about 0.68 x ε_y and 0.15 x ε_y, respectively, for the push loading direction (corresponding to 21% strength degradation). The corresponding strains were 0.75 x ε_y and 0.42 x ε_y, respectively, for the pull loading direction (corresponding to 14% strength degradation). Both occurred during the 60 mm displacement cycle. The West strain gauge located at 300 mm

below the interface between the wall and the base beam recorded much lower readings which can be due to error in the gauge or in its connection.

Table 3. 4: Extent of yielding of reinforcement (Wall 4)

Strain gauge location	Wall end	Initial yielding condition			Strain at max load	Strain ($x\ \varepsilon_y$)
		Load	Displacement	% Drift		
Interface	West	-182 kN[*]	11 mm[*]	---	---	---
500 mm		-193 kN	13 mm	0.36	9.45×10^{-3}	3.78
900 mm		-212 kN	16 mm	0.44	3.81×10^{-3}	1.52
Interface	East	185 kN	11 mm	0.30	11.58×10^{-3}	4.63
500 mm		204 kN	13 mm	0.36	8.60×10^{-3}	3.44
900 mm		225 kN	16 mm	0.44	6.15×10^{-3}	2.46

* Assumed to represent initial yielding

3.5.5 Wall deformation and drift

In-plane lateral displacement was measured at eight points over the height of the West end of the wall as indicated previously. Compared to previous tests, the relatively minor damage to the West end of the wall allowed the deformation profile of the wall to be measured up to high levels of displacement. The recorded in-plane lateral displacements over the wall height, for loading in both directions, are presented in Fig. 3.48 (a) and (b) for key loading conditions related to yielding of reinforcement. A concentration of bending over the lower 0.8 m of the wall height is evident while the top 2.8 m of the wall tends to be relatively straight.

(a) Loading in East (pull) direction   (b) Loading in West (push) direction
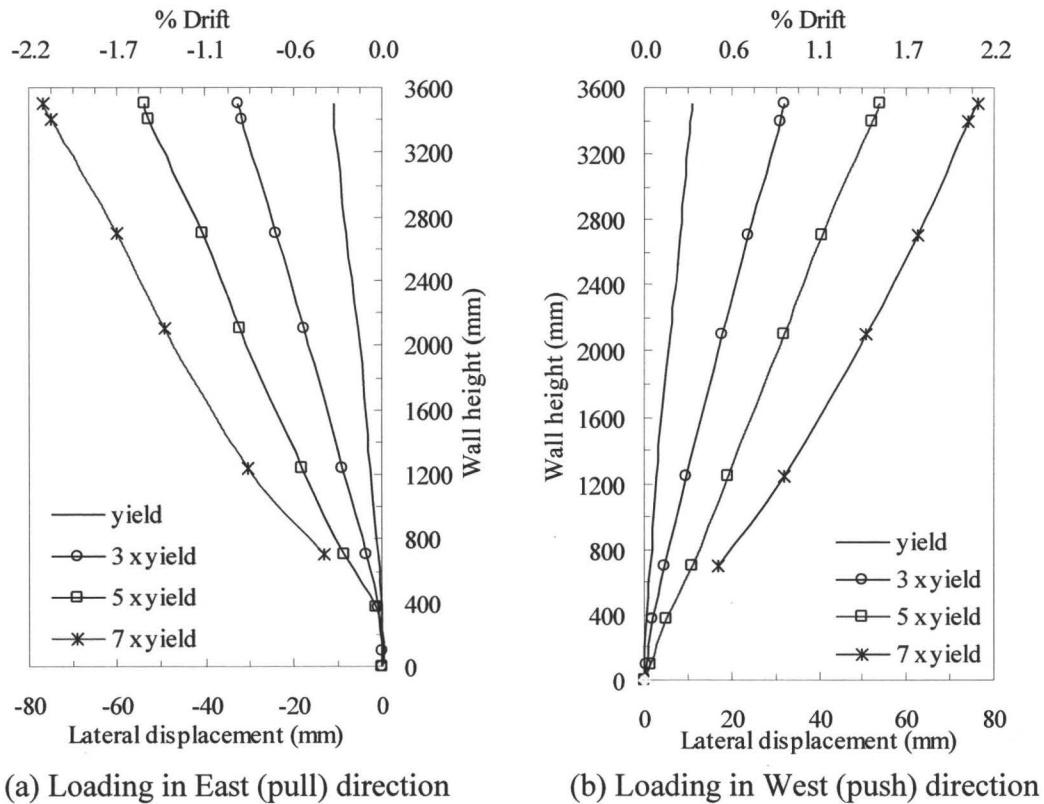
Fig. 3. 48: Total in-plane lateral deflection (Wall 4)

3.5.6 Wall curvature

Average curvatures over segments of the height of Wall 4 at different lateral displacements stages are presented in Fig. 3.49 for loading in both directions. Average curvatures were calculated as explained previously and showed good symmetry for the push and pull loading directions. Average curvatures over the bottom 100 mm of the wall reached a value of 0.015 rad/m at a top displacement equivalent to three times the initial yield displacement of the wall. High average curvatures were measured over the bottom 1000 mm of Wall 4 and were relatively low over the remainder of the wall height.
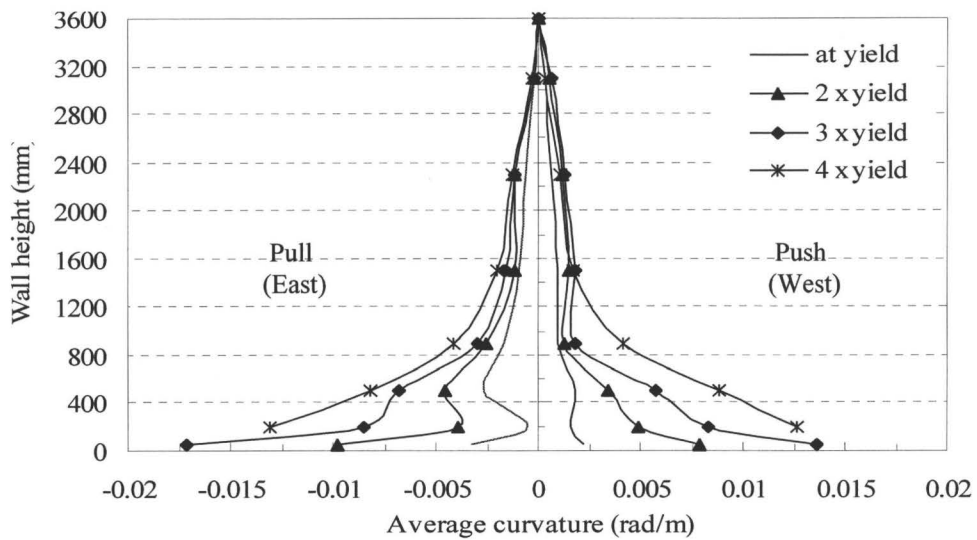
Fig. 3. 49: Average curvature along wall height for loading in both directions (Wall 4)

3.5.7 Strain profile

The strains along the wall length were calculated as discussed previously and are presented in Fig. 3.50 for loading in both directions. The average strain profiles for loading in the push and pull directions had similar patterns. The profiles of average strain between the base beam and 300 mm above the base beam, shown in Fig. 3.50 (a), indicate that the lengths of the compression zone are about 350 mm and 300 mm with maximum compressive strains of 1.7×10^{-3} and 5.1×10^{-3} at yield displacement and at four times the yield displacement, respectively. The figure also shows a fairly linear strain profile along the wall length under tension for low displacement levels.

The profiles of average strain between 300 mm and 700 mm above the base, shown in Fig. 3.50 (b), indicate that the length of the compression zone is very small at yield displacement and almost no compression zone was recorded within this segment at four times the yield displacement. The explanation of this

behaviour again can be due to the cumulative plastic deformation in the reinforcement over the bottom part of the wall which prevented the cracks from closing during the reverse part of the load cycle. The figure also shows a fairly linear strain profile along the wall length. The strain profiles in the push cycles, presented in Figs. 3.50 (c) and (d), are similar to those for the pull direction of loading with some minor differences in the length of the compression zone in the region between 300 mm and 700 mm above the base beam. This discrepancy may be due to the accuracy of the measuring devices given that the measured displacements are relatively small.

(a) 0 – 300 mm above the base beam   (b) 300 – 700 mm above the base beam

(c) 0 – 300 mm above the base beam   (d) 300 – 700 mm above the base beam
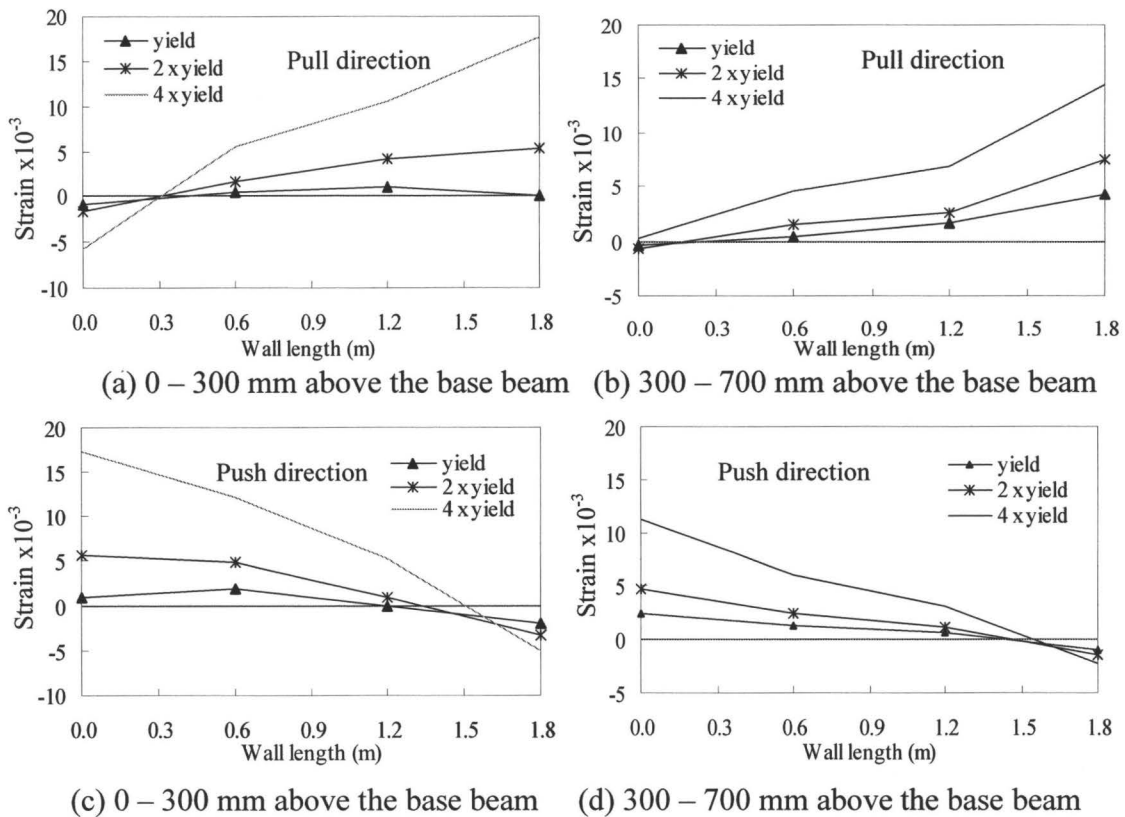
Fig. 3. 50: Profile of average strain along wall length for loading in

both directions (Wall 4)

3.6   Wall 5

3.6.1 Details of Wall 5

Wall 5 was reinforced with No. 15 vertical bars in every other cell (ρ_v = 0.29%) and No. 10 horizontal bars in every third course (ρ_h = 0.08%) starting with the second course above the base beam. It was not subjected to any superimposed axial load during the test.

The hysteresis loops for Wall 5 for cyclic loading are shown in Fig. 3.51 for loading in the push and pull directions. The displacement increments used in this test were multiples of yield displacement similar to those used for Wall 2. The wall displayed reasonable symmetry for load-displacement for loading in the push and pull directions over the full range of testing.
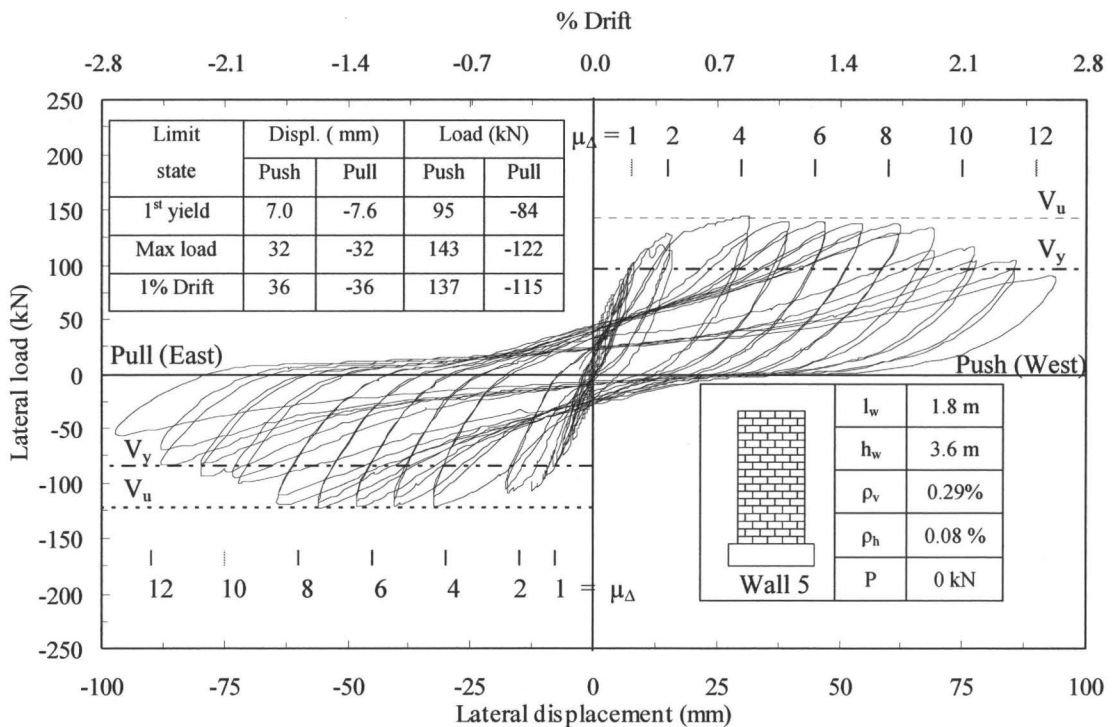
Fig. 3. 51: Hysteresis loops (Wall 5)

3.6.2 General observations

The observed crack pattern was similar to the previously discussed walls indicating flexure dominated response. Flexural horizontal bed joint cracking was first observed during the 2 mm displacement cycle and propagated along the length of the wall up to the 16 mm displacement cycle when minor stepped cracks were first observed (see Fig. 3.52). At 12 mm displacement in the East (pull) direction, the top beam sheared the five No. 15 bars that were welded to it and the wall returned suddenly to its initial position. After inspection, it was found that the bars failed at the weld location which indicated that they were overheated during welding and were weakened. The top beam was then removed from the wall and seven, one and a half courses deep, holes were drilled into the top of the wall into which No. 20 bars were epoxy anchored to serve as dowels. The new dowels were then welded to the top beam and the test was continued without any subsequent problems. At 32 mm displacement, almost symmetric stepped cracks were observed during loading in the push and pull directions and these cracks extended from the first course above the base beam up to midheight of the wall (see Fig. 3.53).

Maximum load was 143 kN at 32 mm displacement, for loading in the West (push) direction, compared to 122 kN at the same displacement level in the opposite direction of loading. At 48 mm displacement, a vertical crack along the end face shells over the bottom two courses was observed in the West toe during loading in the West (push) direction. Also, at the same displacement level in the

opposite direction of loading, vertical cracks in the block web at the East end of

the wall were observed in the second course above the base beam and developed

into splitting failure during the second loading cycle at this displacement (see Fig.

3.54 (a) and (b)).
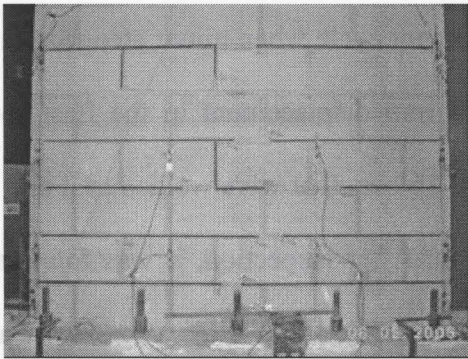
Fig. 3. 52: Cracks in Wall 5
at 16 mm top deflection
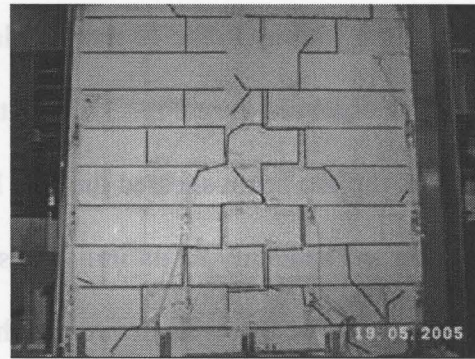
Fig. 3. 53: Cracks in Wall 5
at 32 mm top deflection
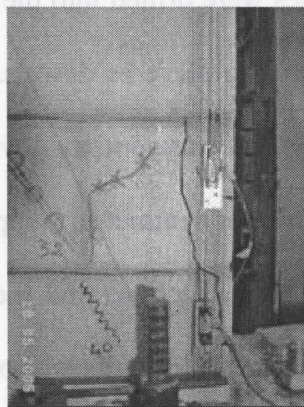
(a) West toe
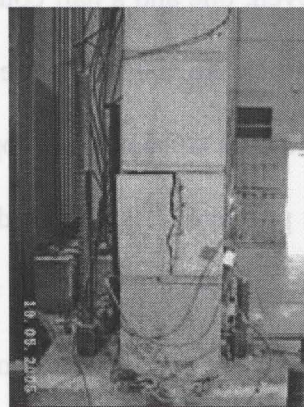
(b) East toe

Fig. 3. 54: Cracking at wall ends at 48 mm top deflection (Wall 5)

At 64 mm displacement, significant opening of the crack occurred in the

end face shells at the West end of the wall for loading in the West (push) direction

and, during the second loading cycle at the same displacement the cracking

extended to the fourth course (see Fig. 3.55 (a) and (b)). The end block webs fell

away when the compression force was removed during the reverse cycle (see Fig. 3.55 (c)). The sequence of deterioration at the East toe was similar to the West toe during the 64 mm displacement cycle, but after spalling of the end webs at the East bottom two blocks, buckling of the end East reinforcement between horizontal bars occurred. This was followed by separation of the end cells of the wall in the third and fourth course and by deterioration of the outermost grout column, as shown in Fig. 3.56 (a), (b) and (c).
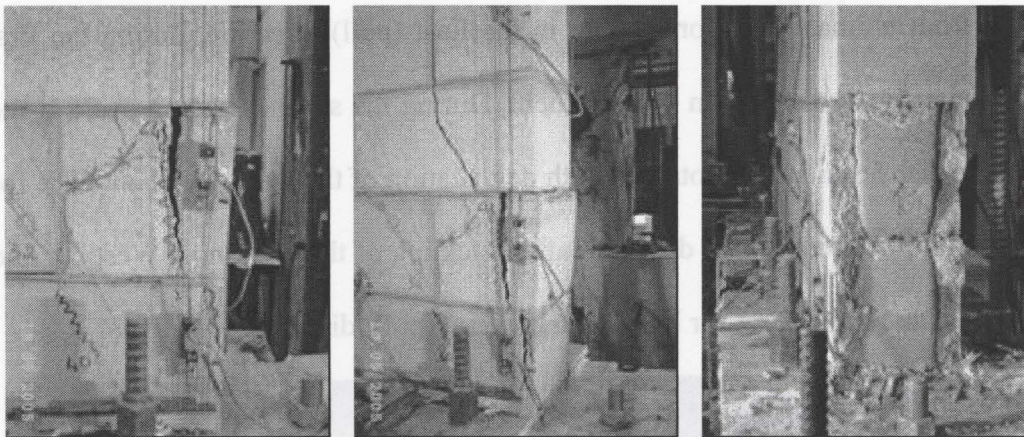
(a) Major opening of crack   (b) Extent of cracking   (c) Spalling of end webs

Fig. 3. 55: Progress of damage at the West toe at 64 mm top deflection (Wall 5)
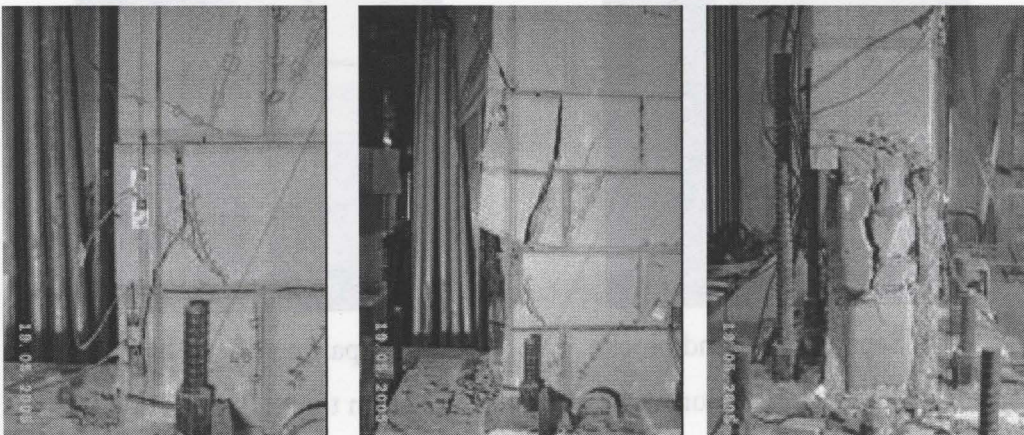
(a) Major opening of crack (b) Separation of end blocks (c) Deterioration of grout

Fig. 3. 56: Progress of damage at the East toe at 64 mm top deflection (Wall 5)

During the first loading cycle at the 72 mm displacement, the end cell at the West end of the wall separated up to the sixth course and buckling of the outermost West bar was observed (see Fig. 3.57 (a)). Then the resistance of the wall decreased by about 9% from ultimate load for loading in the West (push) direction. Sections of the West end block fell away as compression was removed when loading in the East direction (see Fig. 3.57 (b)). After buckling of the outermost East bar had occurred, the resistance of the wall had decreased by about 18% from ultimate load for loading in the East (pull) direction, during the first loading cycle at the 72 mm displacement. During the second loading cycle at the 72 mm displacement, the total strength degradation of the wall was about 23% for loading in the West (push) direction after buckling of the outermost West bar had occurred and about 26% for loading in the East (pull) direction.
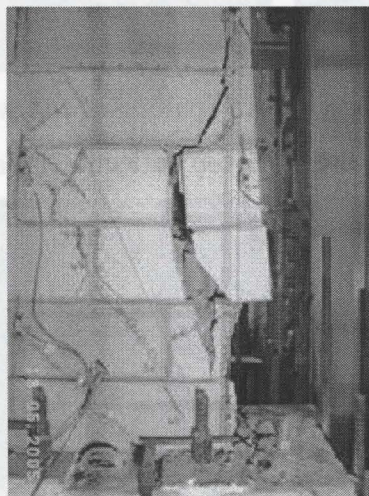
(a) Separation of end blocks   (b) Spalling of end blocks

Fig. 3. 57: Deterioration at the West toe at 72 mm top deflection (Wall 5)

During the 80 mm displacement cycle, local buckling of the East bar occurred (see Fig. 3.58 (a)), while in-plane buckling of the West outermost bar

was observed between the horizontal bars located in the second and fifth course (see Fig. 3.58 (b)). The deformation of the wall at 80 mm displacement for loading in the West (push) direction, presented in Fig. 3.59, shows that the wall tended to be relatively straight between the fifth course above the base beam and the top of the wall. At the same displacement level, bulging of two face shells at mid-length of the wall at the fourth course was seen and after spalling of these face shells at 88 mm displacement, vertical cracks could be seen in the grout columns but no buckling of vertical reinforcement at this location was observed, as shown in Fig. 3.60.
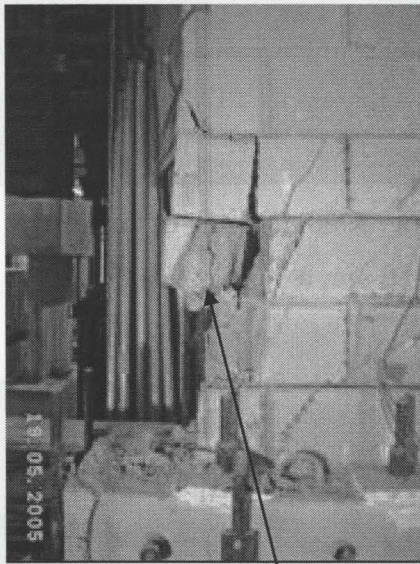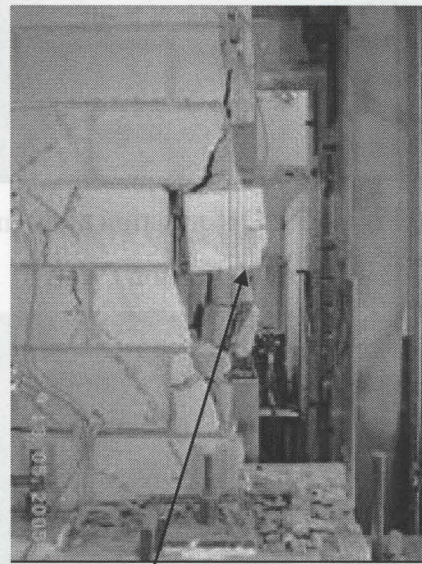
(a) East bar buckling   (b) West bar buckling

Fig. 3. 58: Buckling of outermost bars at 80 mm top deflection (Wall 5)

At the end of the test, significant buckling of the outermost bars was observed (see Fig. 3.61 (a) and (b)). Also deterioration of grout columns and spalling of face shells was seen over the four lower courses extending to one and a half blocks from each end of the wall (see Fig. 3.62). The East outermost bar

broke during the second cycle of the 96 mm displacement, and the test was terminated.
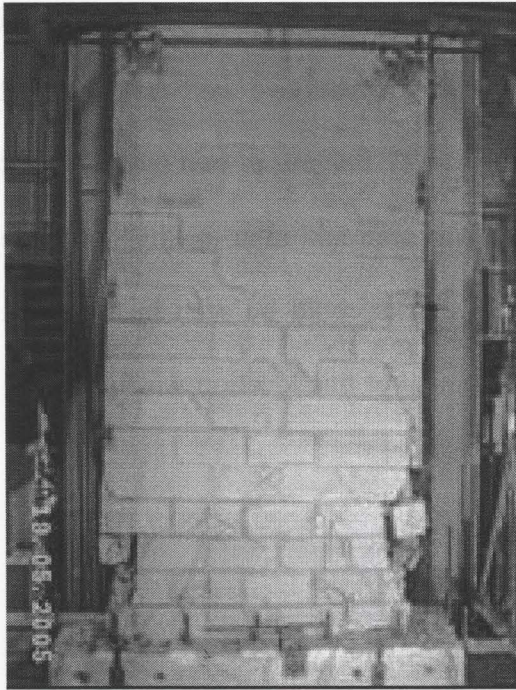
Fig. 3. 59: Deformation at 80 mm
top wall deflection (Wall 5)
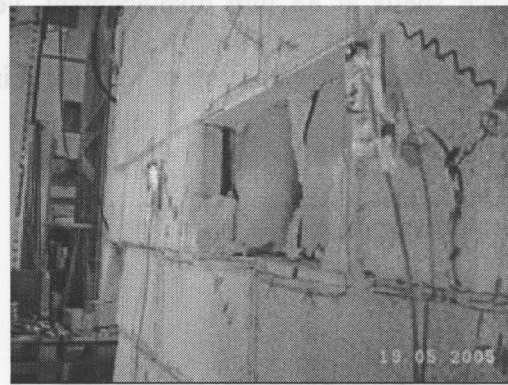
Fig. 3. 60: Bulging of face shells
at 88 mm top deflection (Wall 5)

(a) East bar

(b) West bar
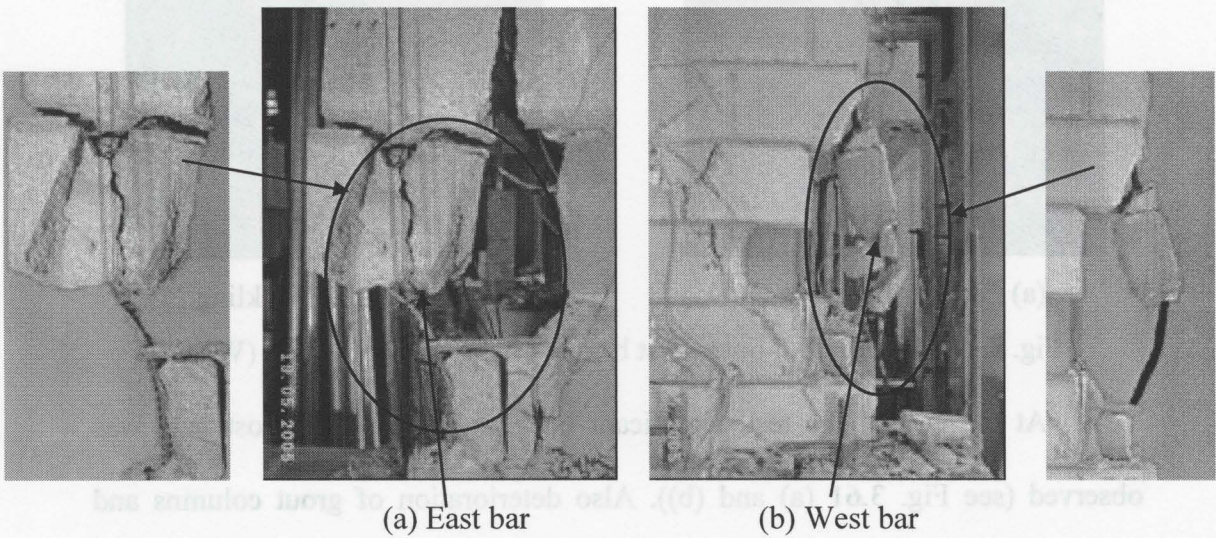
Fig. 3. 61: Buckling of outermost bars at 88 mm top deflection (Wall 5)
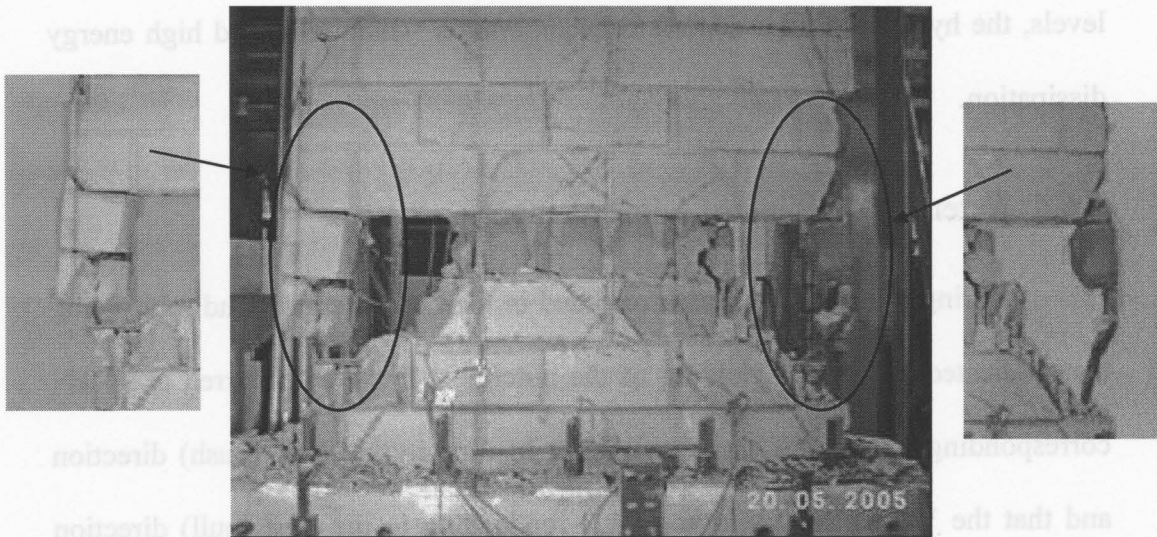
Fig. 3. 62: Damage level at the end of the test at 96 mm top deflection (Wall 5)

3.6.3 Load-displacement response

The load-displacement hysteresis loops for Wall 5, shown in Fig. 3.51, indicate a symmetric response. The slopes of the loops decreased gradually with increases in displacement indicating loss of stiffness which is similar to previously discussed walls. As shown from the hysteresis loops, Wall 5 had lost about 15% of its resistance at a displacement corresponding to nine times the yield displacement for loading in the push and pull directions. The wall strength had degraded to about 50% of its maximum capacity at a displacement corresponding to twelve times the initial yield displacement for loading in the push and pull directions at which point the test was terminated.

The response of the wall was almost linear elastic up to initial yielding. This resulted in thin hysteresis loops and low energy dissipation during these cycles as was the case for the previously discussed walls. At high displacement

levels, the hysteresis loops started to become fatter which indicated high energy dissipation.

3.6.4 Extent of yielding of reinforcement

During this test, the strains recorded in the two outermost end reinforcing bars indicated that initial yielding of the outermost East bar occurred at 95 kN corresponding to 7.0 mm displacement for loading in the West (push) direction and that the West bar yielded at 84 kN for loading in the East (pull) direction during the same displacement cycle. The readings from the West strain gauges at the interface between the wall and the base beam as well as at 500 mm above the base were not consistent after the sudden movement of the wall at failure of the bars welded to the top beam and were then ignored.

The extent of yielding of reinforcement for Wall 5 is presented in Table 3.5. No yielding was recorded from the strain gauges inside the base beam. The strains recorded at maximum load from the strain gauges located 150 mm and 300 mm below the interface between the wall and the base beam were about $0.56 \times \varepsilon_y$ and $0.08 \times \varepsilon_y$, respectively, respectively for the push loading direction, and $0.56 \times \varepsilon_y$ and $0.06 \times \varepsilon_y$, respectively for the pull loading direction, which shows some elongation of the bar inside the base beam. The maximum strains recorded from the strain gauges located 150 mm and 300 mm below the interface between the wall and the base beam were about $0.87 \times \varepsilon_y$ and $0.21 \times \varepsilon_y$, respectively, for the push loading direction (corresponding to 8% strength degradation). The

corresponding strains were 0.80 x ε_y and 0.20 x ε_y, respectively, for the pull

loading direction (corresponding to 18% strength degradation). Both occurred

during the 72 mm displacement cycle.

Table 3. 5: Extent of yielding of reinforcement (Wall 5)

Strain gauge location	Wall end	Initial yielding condition			Strain at max. load	Strain (x ε_y)
		Load	Displacement	% Drift		
Interface	West	-84 kN	7.6 mm	0.21	----	----
500 mm		-84 kN	7.6 mm	0.21	---	---
900 mm		-93 kN	9.0 mm	0.25	17.61×10^{-3}	7.04
Interface	East	95 kN	7.0 mm	0.19	18.21×10^{-3}	7.28
500 mm		106 kN	9.0 mm	0.25	13.80×10^{-3}	5.52
900 mm		106 kN	9.0 mm	0.25	13.18×10^{-3}	5.27

3.6.5 Wall deformation and drift

In-plane lateral displacements were measured at eight points over the

height of the West end of the wall as indicated previously. Because of only minor

damage at the West end of the wall, measurement of the deflection profile of the

wall up to high levels of displacement was possible. The recorded in-plane lateral

displacements over the height of the wall, for loading in both directions, are

presented in Fig. 3.63 (a) and (b) for key loading conditions related to yielding of

reinforcement. A concentration of bending over the lower 1.1 m of the wall height

is evident while the top 2.5 m of the wall tended to remain relatively straight.
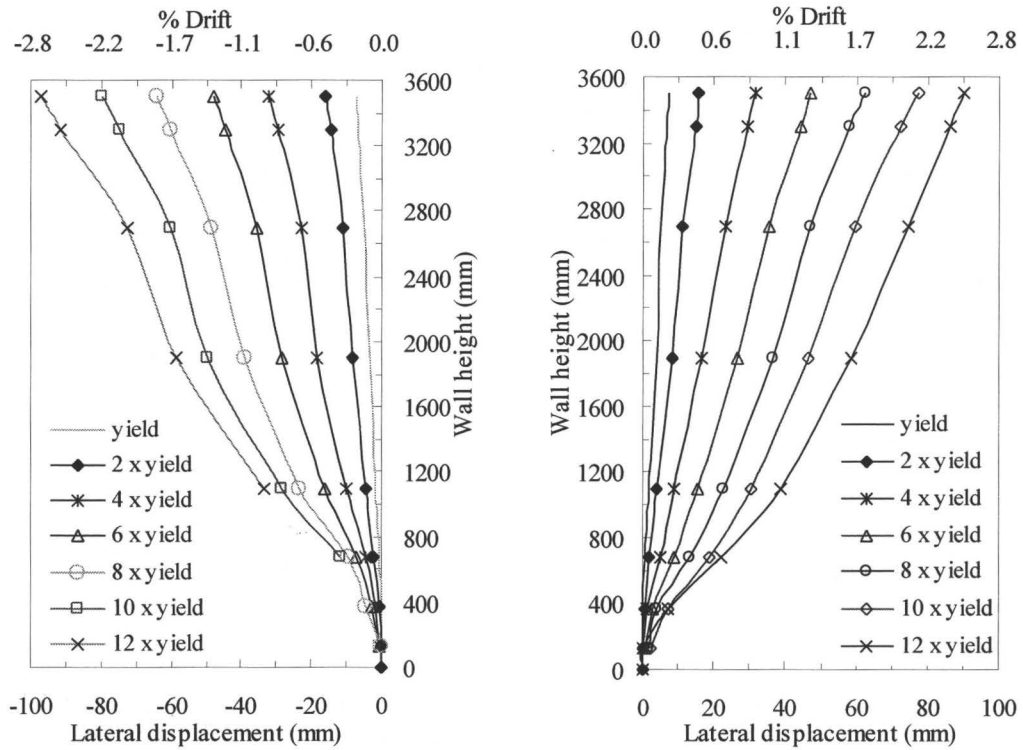
(a) Loading in East (pull) direction   (b) Loading in West (push) direction

Fig. 3. 63: Total in-plane lateral deflection (Wall 5)

3.6.6 Wall curvature

Average curvatures over segments of the height of Wall 5 at different lateral displacements stages are presented in Fig. 3.64 for loading in both directions. Average curvatures were calculated as explained previously and showed good symmetry for loading in both directions. Average curvatures over the bottom 300 mm of the wall reached a value of 0.014 rad/m at a top displacement equivalent to six times the initial yield displacement of the wall. High average curvatures (corresponding to those greater than yield curvatures) were measured over the bottom 1500 mm of Wall 5 and were relatively low over the remainder of the wall height.
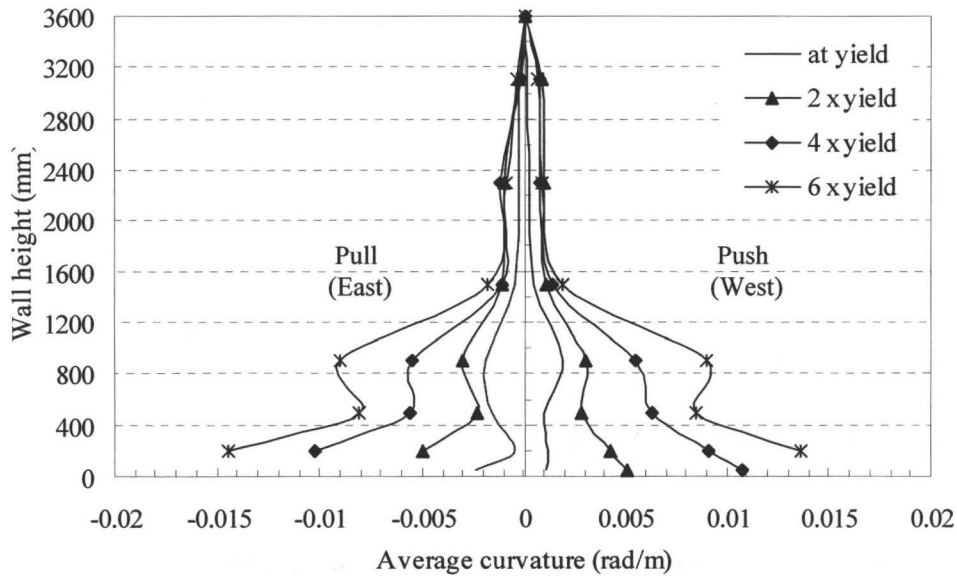
Fig. 3. 64: Average curvature along wall height for loading in both directions (Wall 5)

3.6.7 Strain profile

The strain profiles along the wall length were calculated as discussed previously and are presented in Fig. 3.65 for loading in both directions. The average strain profiles for loading in the push and pull directions had similar patterns. The profiles of average strain between the base beam and 300 mm above the base beam, shown in Fig. 3.65 (a) and between 300 mm and 700 mm above the base, shown in Fig. 3.65 (b), indicate that the length of the compression zone is very small which can be due to the significant plastic extension of the outermost bars during the cyclic loading of the wall. The figures also show reasonably linear strain profiles along the wall length. Figures 3.65 (c) and (d) show the strain profiles for loading in the push direction.

(a) 0 – 300 mm above the base beam   (b) 300 – 700 mm above the base beam

(c) 0 – 300 mm above the base beam   (d) 300 – 700 mm above the base beam
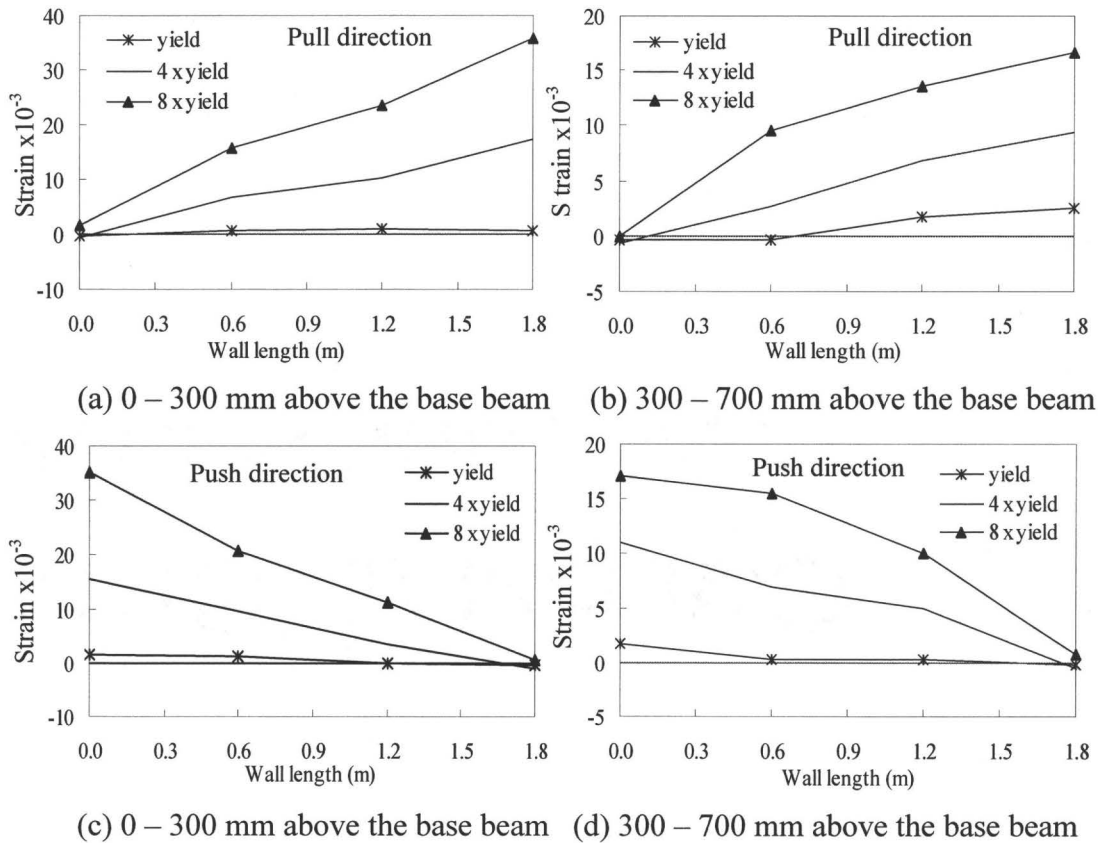
Fig. 3. 65: Profile of average strain along wall length for loading in
both directions (Wall 5)

3.7   Wall 6

3.7.1 Details of Wall 6

Wall 6 was reinforced with No. 25 vertical bars in every cell ($\rho_v = 1.31\%$)
and No. 10 horizontal bars in every course ($\rho_h = 0.26\%$), and it was subjected to a
superimposed axial load of 260 kN during the test which was equivalent to 0.75
MPa compression (about 5% of f'_m). Empty cells were discovered at the West
end of the wall between the first and the fourth course prior to testing (see the
hatched area of the wall at the bottom right side of Fig. 3.66). The wall was
repaired using the same technique as applied for repair of Wall 3.

134

The hysteresis loops for Wall 6 for cyclic loading are shown in Fig. 3.66 for both the push and pull loading cycles. The displacement increments used in this test were multiples of yield displacement similar to those used for Wall 2. The wall displayed reasonable symmetry for load- displacement in the push and pull directions during most of the test but showed more strength for loading in the East (pull) direction.
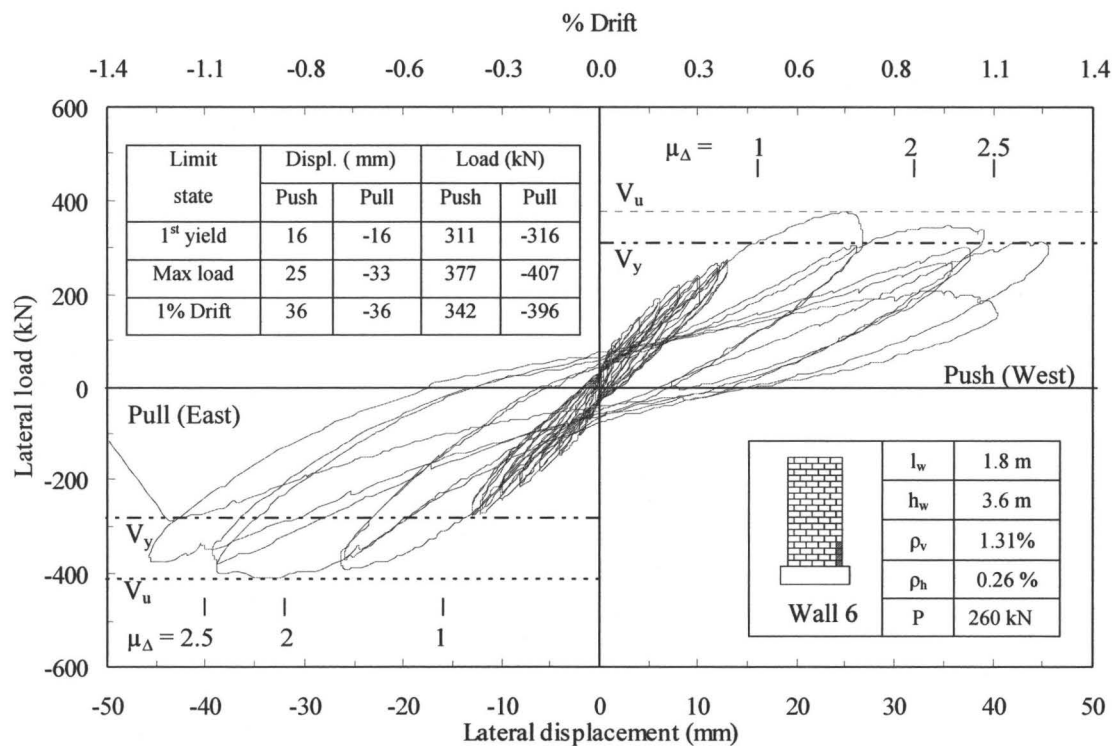
Fig. 3. 66: Hysteresis loops (Wall 6)

3.7.2 General observations

The observed crack pattern was similar to those for the previously discussed walls indicating flexure dominated response. At 8 mm displacement, horizontal bed joint cracks were observed over the bottom seven courses of the wall, as shown in Fig. 3.67. Stepped cracks were seen during the 10 mm

displacement cycle and spread between the third and the eleventh course above

the base beam (see Fig. 3.68). Maximum load was not reached at the same

displacement level for loading in the push and pull directions. The wall reached

377 kN lateral load capacity for loading in the West (push) direction at 24 mm top

deflection compared to 407 kN capacity for loading in the East (pull) direction at

32 mm top deflection.
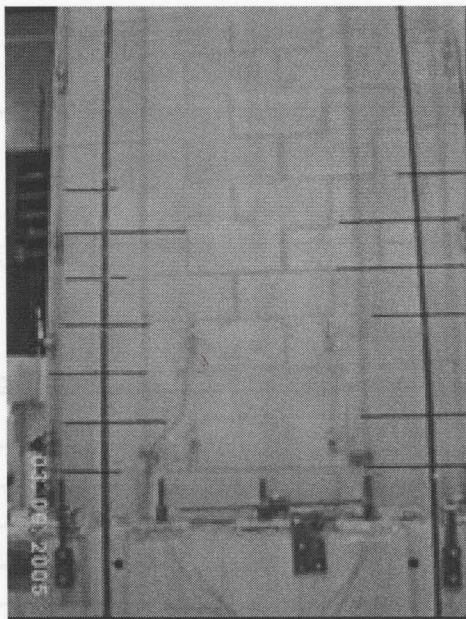
| Fig. 3. 67: Cracks at 8 mm (Wall 6) | Fig. 3. 68: Cracks at 10 mm (Wall 6) |
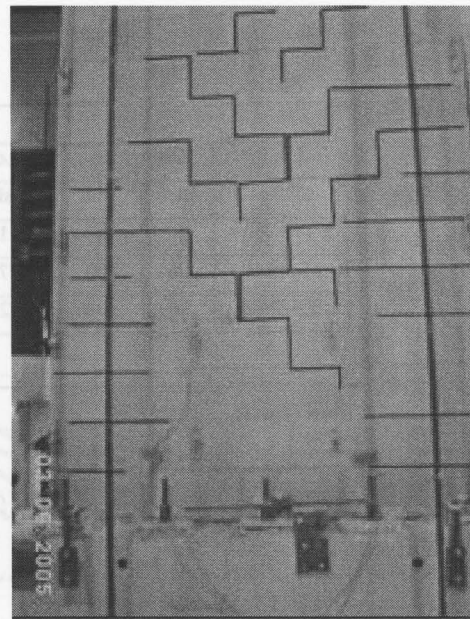
Vertical cracks appeared in both toes during the 26 mm displacement

cycle and crushing of the West toe began at this stage. The vertical crack

extended from the bottom course to the fifth course at the West toe while at the

East toe a similar crack developed from the second course and up to the fifth

course (see Fig. 3.69 (a) and (b)). During the 39 mm displacement cycle, spalling

of face shells occurred at the West toe up to the fifth course and web spalling of

the end blocks at the second and third course occurred at the East toe revealing a

vertical crack in the grout column (see Fig. 3.70 (a) and (b)). More deterioration occurred at the East toe during the same cycle (see Fig. 3.71 (a) and (b)), and consisted of face shell spalling and grout column splitting.
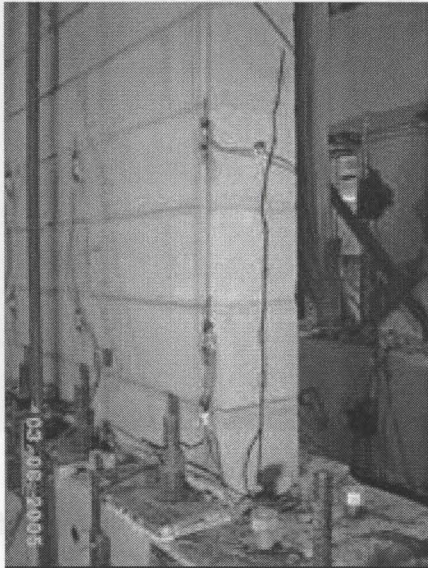
(a) West toe cracking   (b) East toe cracking

Fig. 3. 69: Toe cracking at 26 mm top deflection (Wall 6)
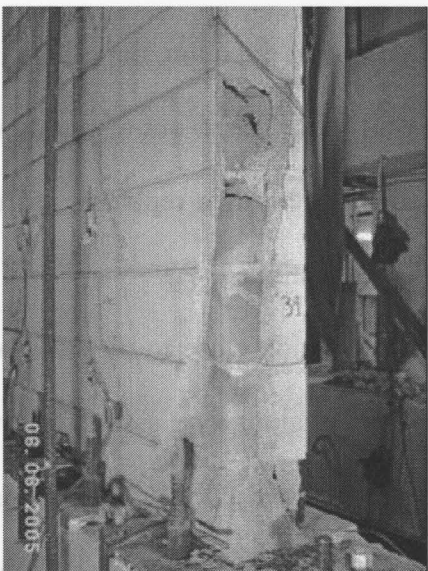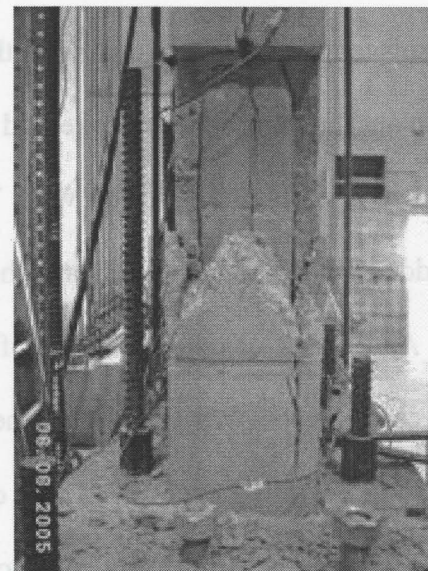
(a) West end spalling   (b) East end spalling

Fig. 3. 70: Spalling at both ends of Wall 6 at 39 mm top deflection
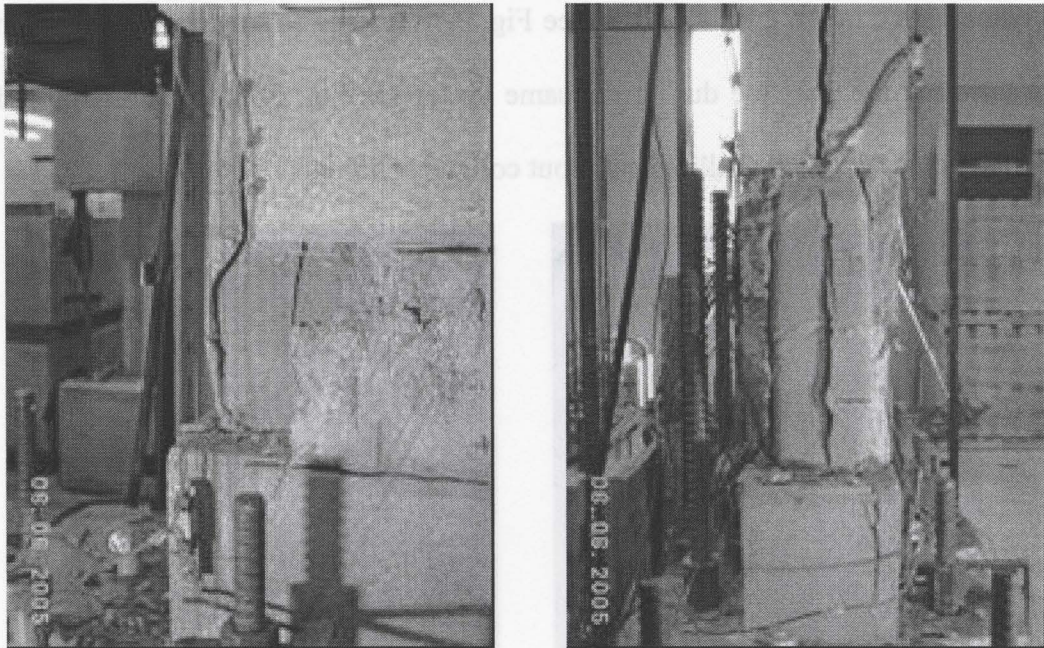
(a) Face shell spalling   (b) Grout column splitting

Fig. 3. 71: Continued deterioration at the East end of Wall 6 at 39 mm top deflection

Additional spalling occurred in the West toe as can be seen in Fig. 3.72 which also shows significant overall distortion of the wall. During the second 39 mm displacement cycle for loading in the West (push) direction, the rollers in the out-of-plane bracing system broke and the wall was pushed out-of-plane which resulted in a visible twist in the wall. The rollers were then replaced, stiffeners were added to the bracing system and the test was continued.

As a result of the visible out-of-plane deflection close to the base beam, higher compression was created on the face shells along one side of the wall. After the first loading cycle at 45 mm displacement, one side of the wall lost all face shells from the third to the sixth course along the wall length, as shown in Fig. 3.73. During the second 45 mm displacement loading cycle, the load started

to decrease simultaneously with increases in displacement. The load decreased from 206 kN at 35 mm top deflection to 160 kN at 41 mm top deflection during the same loading cycle and out-of-plane buckling of the wall and the end West bar, starting from the third course, were clearly visible (see Fig. 3.74 (a) and (b)). The West (push) loading cycle was stopped and the wall was pulled towards the target 45 mm displacement in the East direction. At 45 mm top deflection, major out-of-plane deflection occurred at the third course at the East end of the wall (see Fig. 3.74 (c)), and the lateral load dropped abruptly from 287 kN to 118 kN to end the test. The extent of deterioration of the wall at the end of the test can be seen in Fig. 3.75.
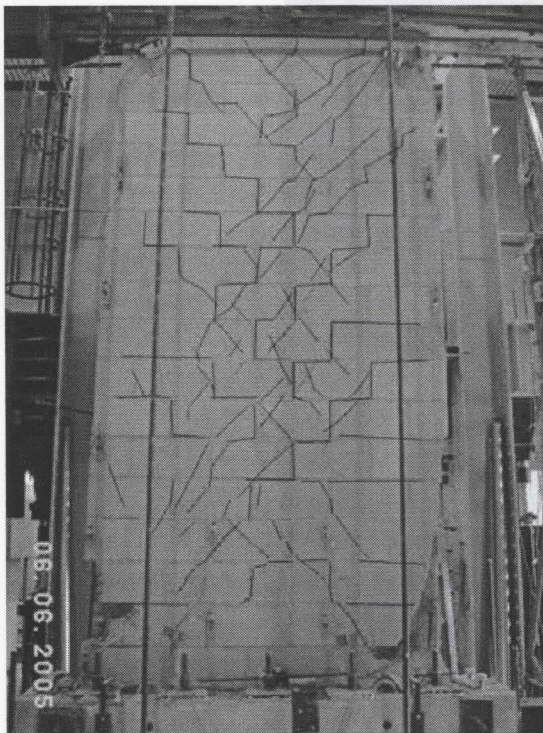
Fig. 3. 72: Deformation at 39 mm top deflection (Wall 6)
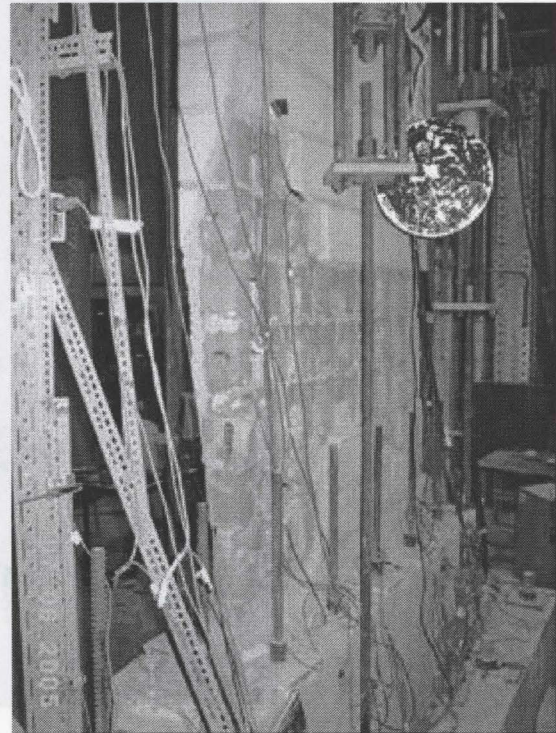
Fig. 3. 73: Spalling of face shells along one side of Wall 6 at 45 mm top deflection
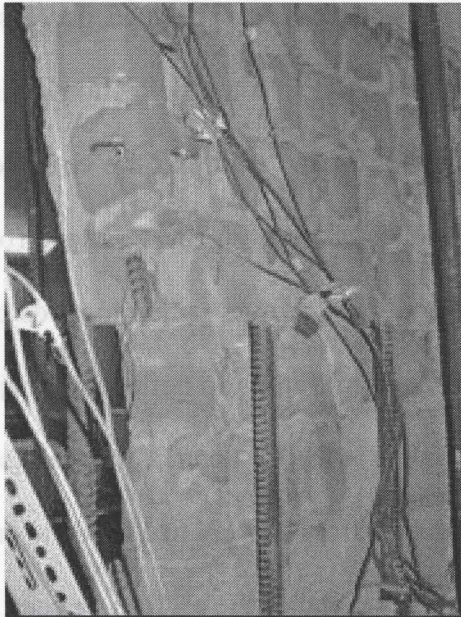
(a) Wall buckling (West)
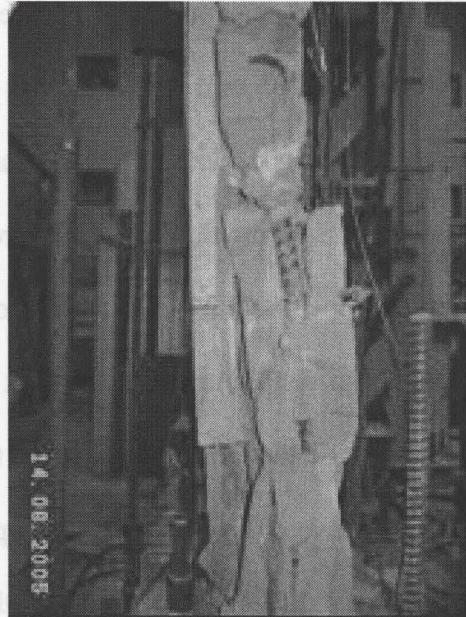
(b) Bar buckling (West)
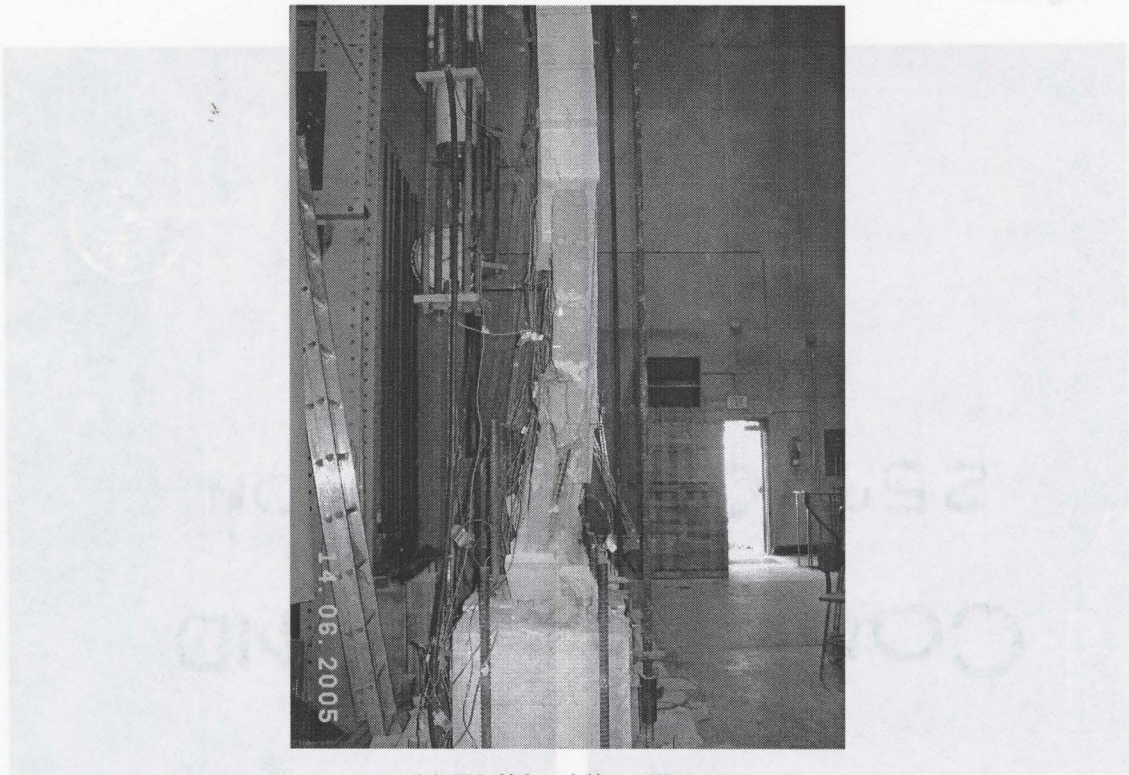
(c) Wall buckling (East)

Fig. 3. 74: Buckling of the wall and the outermost bars at 45 mm
top deflection (Wall 6)
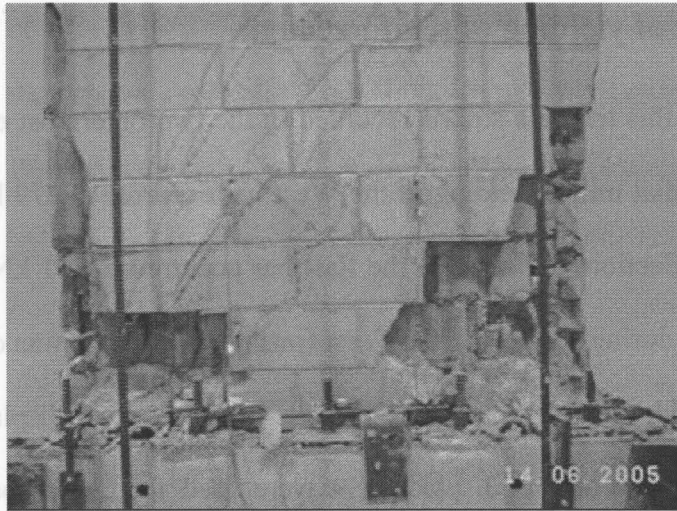
Fig. 3. 75: Damage level at the end of the test at 45 mm top deflection (Wall 6)

3.7.3 Load-displacement response

The load-displacement hysteresis loops for Wall 6, shown in Fig. 3.66, indicate a reasonably symmetric response. The slopes of the loops decreased gradually with increasing displacement indicating loss of stiffness similar to previously discussed walls. As shown from the hysteresis loops, Wall 6 had lost about 15% of its resistance at a displacement of about two and a half times the displacement at initial yielding for loading in both directions. An abrupt decrease in strength was observed during the 45 mm displacement cycle coinciding with spalling of face shells and significant out-of-plane deflection of the wall during the test.

The response of the wall was almost linear elastic up to first yielding of the reinforcement. This generated thin hysteresis loops and low energy dissipation which was consistent with previous discussions. At high displacement levels, the hysteresis loops started to become fatter which indicated high energy dissipation.

3.7.4 Extent of yielding of reinforcement

During this test, the strains recorded in the two outermost end reinforcing bars indicated that initial yielding of the West bar occurred at 279 kN lateral load and 13 mm deflection. Yielding of the East bar occurred at 311 kN and about 16 mm deflection during loading in the West (push) direction. It was decided during the test to consider the 13 mm deflection to be the initial yield displacement of the wall, and multiples of this displacement were used for cyclic loading. Further analysis conducted later indicated that the 16 mm displacement corresponding to 311 kN is more likely to have been the initial yield displacement.

Even though there may be some concern for the reliability of some of the electronic strain gauges on the steel bars, the extent of yielding of reinforcement obtained from the strain gauge readings for Wall 6 is presented in Table 3.6. No yielding was recorded from the strain gauges inside the base beam. The strains recorded at maximum load from the strain gauges located 150 mm and 300 mm below the interface between the wall and the base beam were about $0.72 \times \varepsilon_y$ and $0.40 \times \varepsilon_y$, respectively, for the push loading direction, and $0.75 \times \varepsilon_y$ and $0.46 \times \varepsilon_y$, respectively, for the pull loading direction, which shows some elongation of the bars inside the base beam. The maximum strains recorded from the strain gauges located 150 mm and 300 mm below the interface between the wall and the base beam were about $0.79 \times \varepsilon_y$ and $0.54 \times \varepsilon_y$, respectively, for the push loading direction (corresponding to 8% strength degradation). The corresponding strains were $0.88 \times \varepsilon_y$ and $0.56 \times \varepsilon_y$, respectively, for the pull loading direction

(corresponding to 18% strength degradation). Both occured during the 72 mm displacement cycle.

Table 3. 6: Extent of yielding of reinforcement (Wall 6)

Strain gauge location	Wall end	Initial yielding condition			Strain at max. load	Strain $(x\ \varepsilon_y)$
		Load	Displacement	% Drift		
Interface	West	-316 kN	16 mm	0.36	$9.76\ x10^{-3}$	3.90
500 mm	West	-327 kN	17 mm	0.47	$5.88\ x10^{-3}$	2.35
900 mm	West	-346 kN	24 mm	0.66	$4.25\ x10^{-3}$	1.70
Interface	East	311 kN	16 mm	0.44	$7.35\ x10^{-3}$	2.94
500 mm	East	341 kN	19 mm	0.52	$2.95\ x10^{-3}$	1.18
900 mm	East	283 kN	34 mm	0.94	$2.33\ x10^{-3}$	0.93

3.7.5 Wall deformation and drift

In-plane lateral displacement was measured at eight points over the height of the West end of the wall as indicated previously. Extensive damage at the West end of the wall resulted in disconnection of the potentiometers at the lower heights above the base beam at levels of displacement greater than two and a half times the displacement at initial yield. The recorded in-plane lateral displacements over the wall height, for loading in both directions, are presented in Fig. 3.76 (a) and (b) for key loading conditions related to yielding of reinforcement. A concentration of bending over the lower 0.7 m of the wall height is evident while the top 2.9 m of the wall tended to be relatively straight.
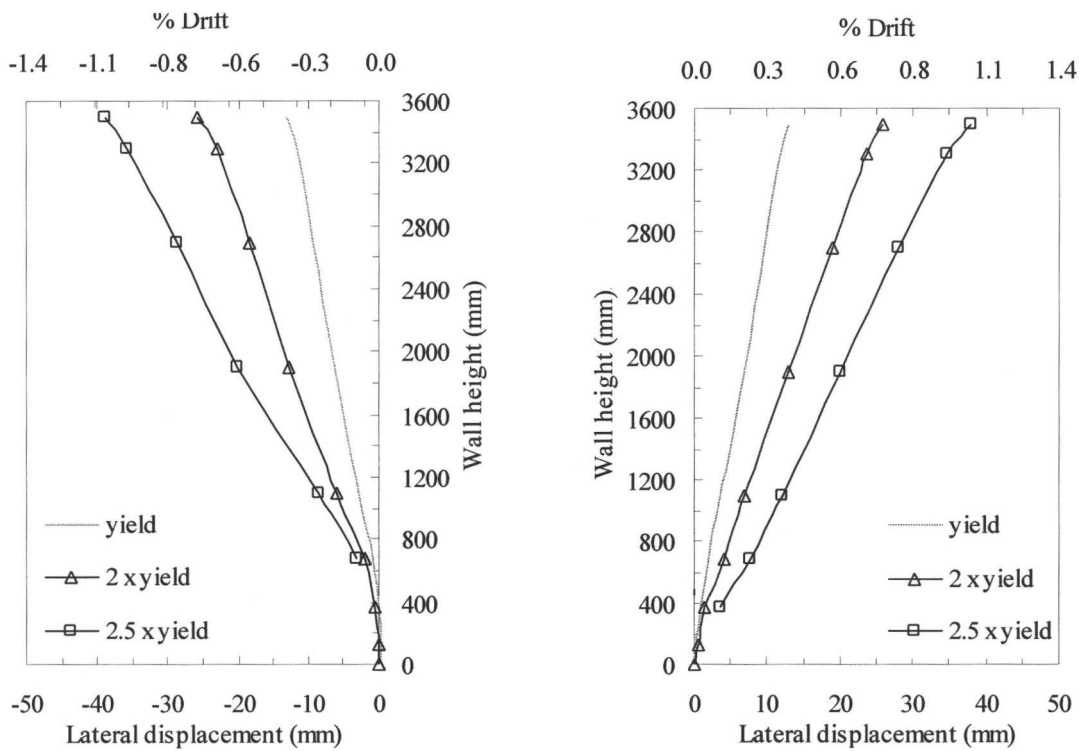
(a) Loading in East (pull) direction   (b) Loading in West (push) direction

Fig. 3. 76: Total in-plane lateral deflection (Wall 6)

3.7.6 Wall curvature

Average curvatures over segments of the height of Wall 6 at different lateral displacements stages are presented in Fig. 3.77 for loading in both directions. The average curvatures were calculated as explained previously and showed good symmetry for the push and pull loading directions. It was only possible to calculate average curvatures over the wall height for low levels of displacement because loss of face shells at high displacement levels ended reading of the vertical displacement readings for lower wall heights. Relatively high curvatures, compared to the remainder of the wall height, were recorded over the lower 800 mm of the wall.
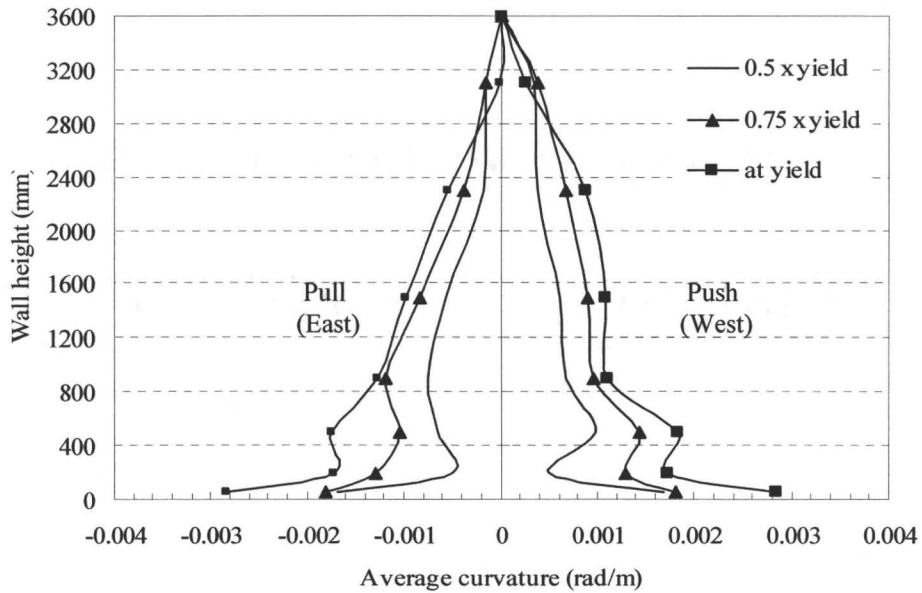
Fig. 3. 77: Average curvature along wall height for loading in both directions (Wall 6)

3.7.7 Strain profile

The extensive spalling of face shells during the early stages of this test limited availability of measurements to those obtained at low displacement levels. The profiles of average strain were not presented for this wall.

3.8   Wall 7

3.8.1 Details of Wall 7

Wall 7 was reinforced with No. 25 vertical bars in every cell ($\rho_v = 1.31\%$) and No. 10 horizontal bars in every course ($\rho_h = 0.26\%$), and it was subjected to a superimposed axial load of 520 kN during the test which was equivalent to 1.50 MPa compressive stress (about 10% of f'$_m$). This wall was built separately after the six previous walls had been built but had a similar masonry compressive

strength (f'$_m$ of about 15 MPa). However, the vertical reinforcement had a higher yield strength compared to the other shear walls (f$_y$ = 625 MPa).

The hysteresis loops for Wall 7 for cyclic loading are shown in Fig. 3.78 for both the push and pull loading directions. The displacement increments used in this test were similar to those used for Wall 2. The wall displayed reasonable symmetry of the load-displacement loops for the push and pull cycles of loading.
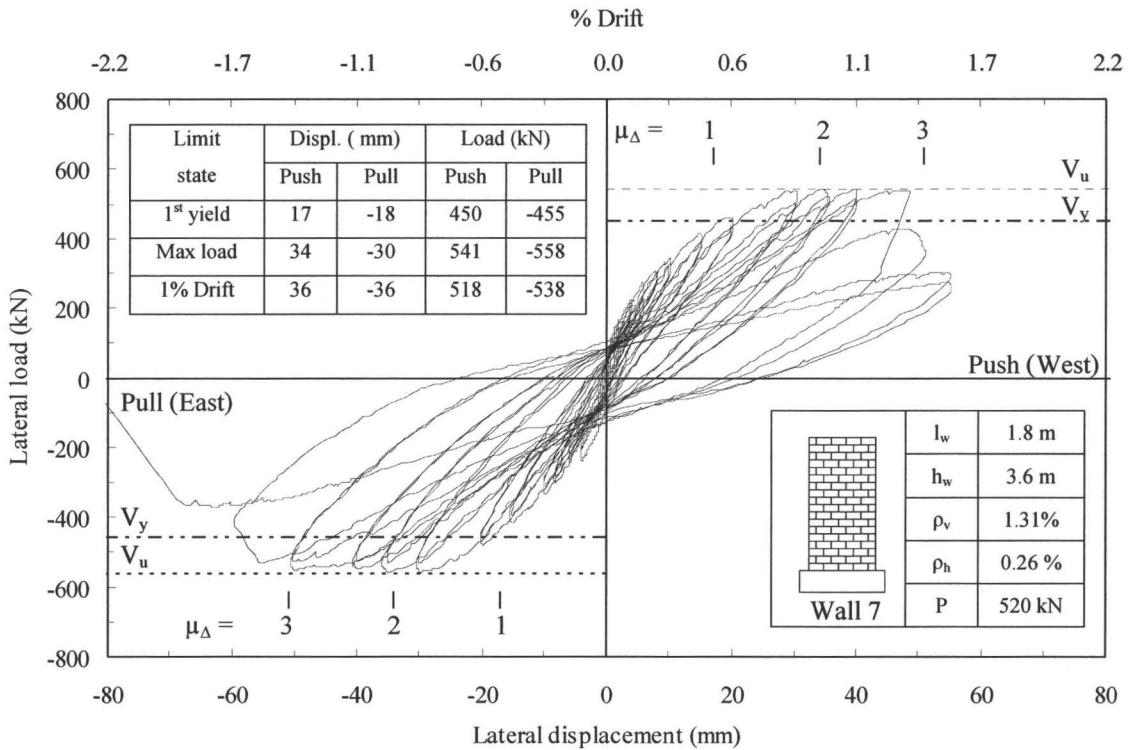
Fig. 3. 78: Hysteresis loops (Wall 7)

3.8.2 General observations

The observed crack pattern was similar to those for the previously discussed walls indicating flexure dominated response. Flexural horizontal bed joint cracking was observed at 6 mm displacement and diagonal cracks passing

through blocks rather than stepped cracks along mortar joints were observed

between the second course above the base beam and midheight of the wall at 10

mm displacement (see Fig. 3.79 (a)). These diagonal cracks extended over the

wall height at 15 mm displacement (see Fig. 3.79 (b)) and became more closely

spaced over the wall at 30 mm displacement (see Fig. 3.79 (c)).
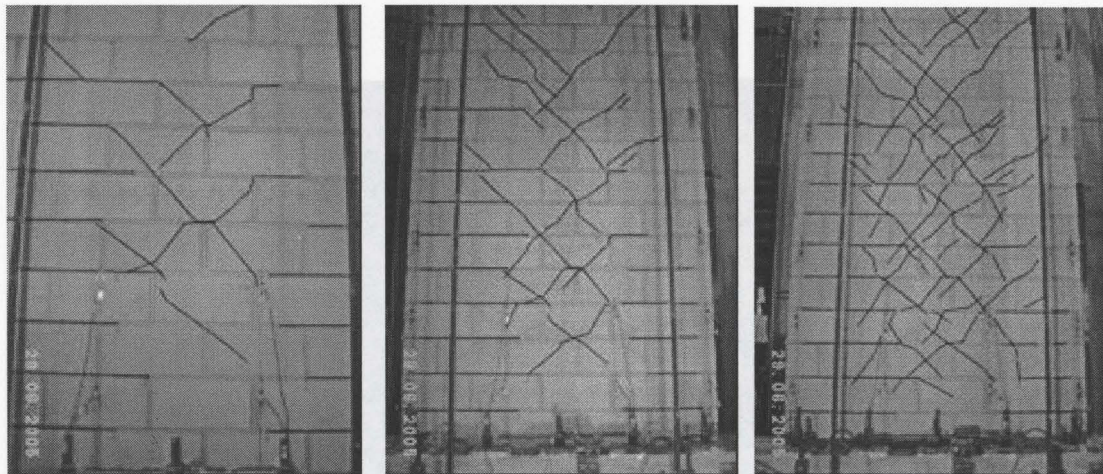
(a) At 10 mm top deflection (b) At 15 mm top deflection (c) At 30 mm top deflection

Fig. 3. 79: Crack progression (Wall 7)

Maximum load of 541 kN was reached at 30 mm displacement for loading

in the West (push) direction compared to 558 kN at the same displacement for

loading in the East (pull) direction. A vertical crack appeared at the East toe at 30

mm displacement and extended to the third course at 35 mm displacement (see

Fig. 3.80 (a)) while vertical and horizontal cracks were observed at the same

displacement at the West toe, as shown in Fig. 3.80 (b). Cracks along the face

shells at the bottom three courses at the East toe at 35 mm displacement are

shown in Fig. 3.81. Spalling of the block web of the first course at the West end

of the wall occurred during the second cycle of the 35 mm displacement whereas

no sign of deterioration was seen at the East toe. At 40 mm displacement, the second course above the base beam at the West end of the wall crushed and vertical cracks extended up to the third course as shown in Fig. 3.82. Spalling up to the third course at the West end (see Fig. 3.83 (a)) and up to the second course at the East end of the wall occurred during the 50 mm displacement cycle (see Fig. 3.83 (b)).
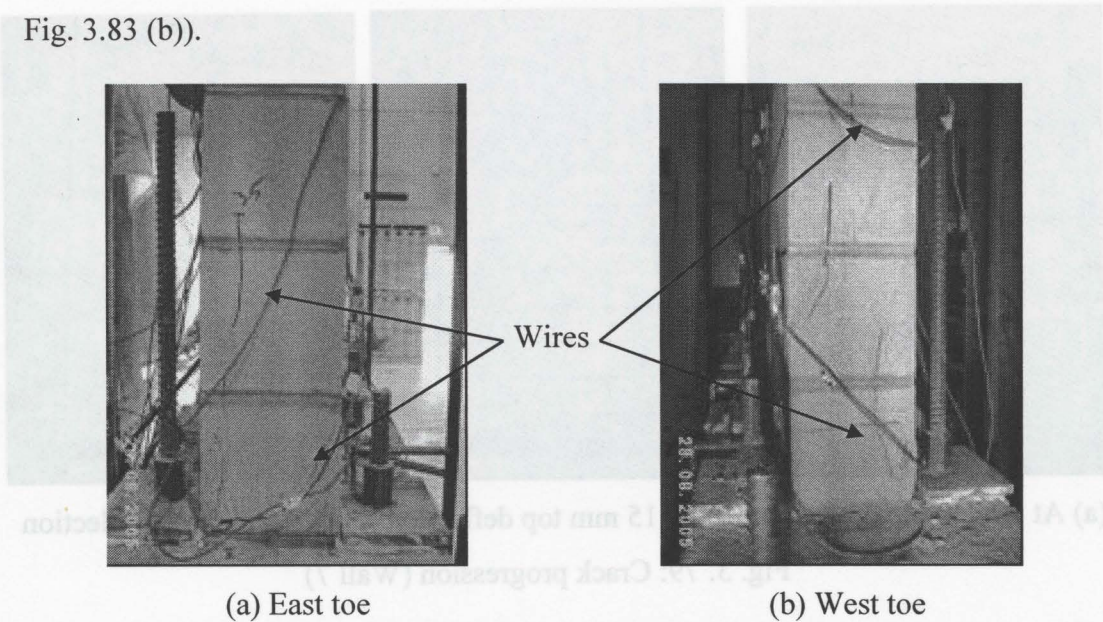
(a) East toe   (b) West toe

Fig. 3. 80: Cracks at both toes at 35 mm top deflection (Wall 7)
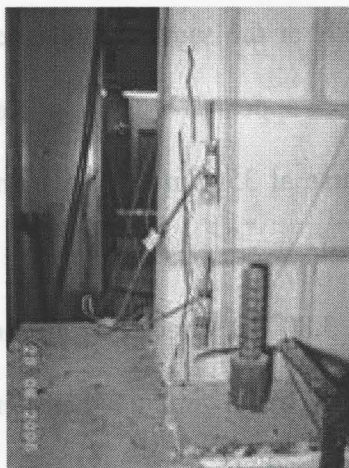
Fig. 3. 81: Face shells cracking at the East toe at 35 mm top deflection (Wall 7)
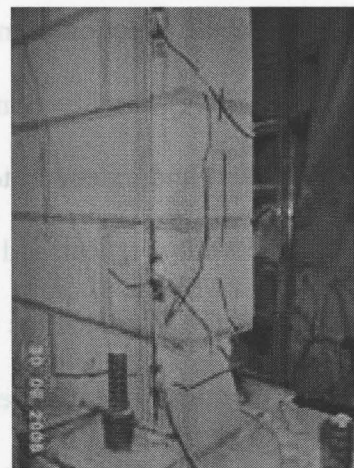
Fig. 3. 82: Crushing of the West toe at 40 mm top deflection (Wall 7)
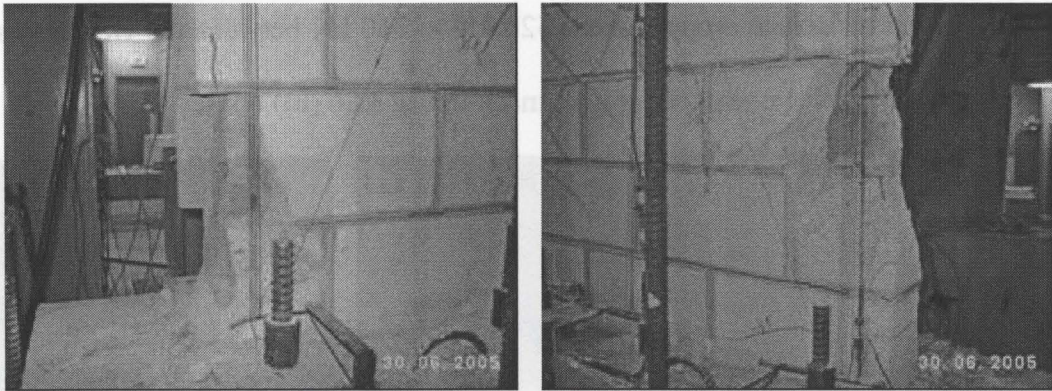
(a) East toe   (b) West toe

Fig. 3. 83: Spalling at both toes at 50 mm top deflection (Wall 7)

The sequence of major deterioration at the West end started with spalling of the end face shells. It was followed by deterioration of the grout column and the beginning of the outermost bar buckling with cracking of the face shells at the third course at the West end of the wall (see Fig. 3.84 (a), (b) and (c)). During the second 50 mm displacement cycle, the outermost West bar buckled and spalling of the face shells at the West end of the wall occurred. The lateral resistance of the wall then decreased from 530 kN to about 400 kN for loading in the West (push) direction.

Major buckling of the outermost West bar was observed during the first 55 mm displacement cycle as shown in Fig. 3.85 (a). Buckling of the second outermost bar was observed during the second 55 mm displacement cycle after crumbling of the outermost two grout columns at the West end of the wall had occurred (see Fig. 3.85 (b)). The resistance of the wall for loading in the West (push) direction decreased to 50% during this loading cycle. Buckling of the East bar occurred during the first 55 mm displacement cycle (see Fig. 3.86 (a)), and the

wall's lateral resistance dropped from 520 kN to 360 kN between the two cycles

of the 55 mm displacement (see wall damage in Fig 3.86 (b)).
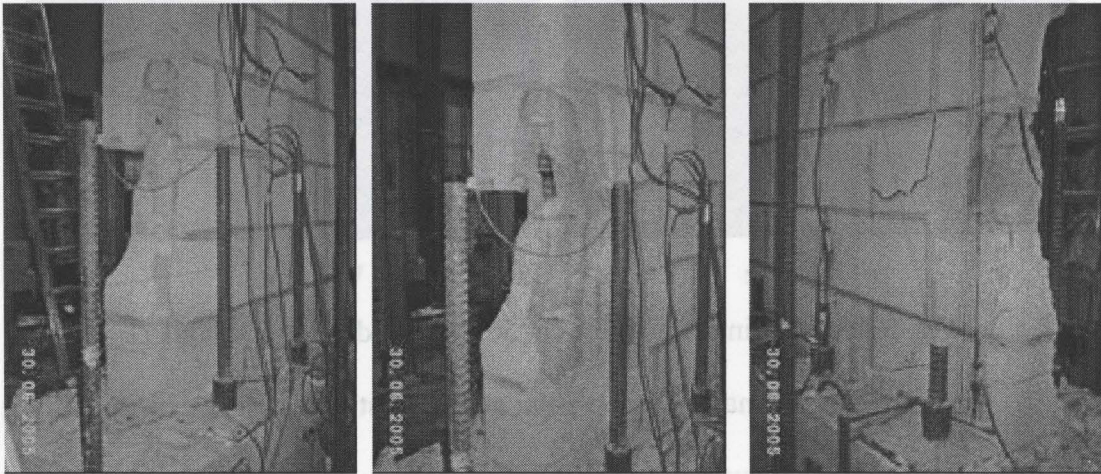
(a) Spalling of blocks   (b) Bar buckling   (c) Cracking of the face shells

Fig. 3. 84: Deterioration progress during the 50 mm displacement cycle

(West end Wall 7)
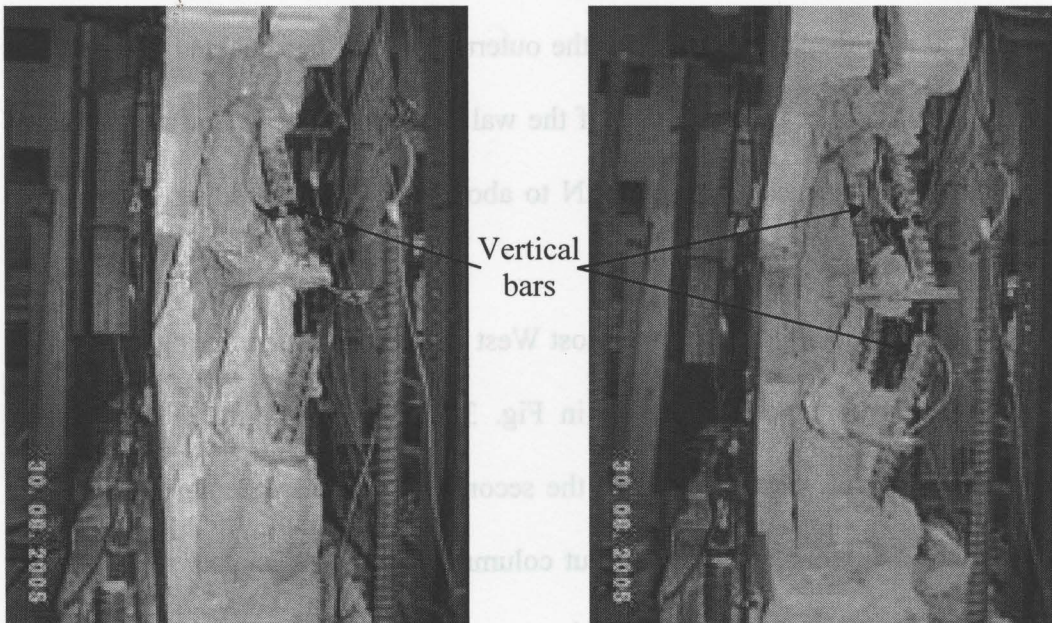
(a) Outermost bar   (b) Outermost two bars

Fig. 3. 85: Buckling of bars at the West toe at 55 mm top deflection (Wall 7)

The wall was then pulled (East direction) an additional 10 mm without any loss in lateral resistance, and at 65 mm displacement in the East direction, the load dropped from 360 kN to 50 kN and combined shear compression failure occurred with significant buckling of the outermost East bar at the second course between the horizontal reinforcements (see Fig. 3.87 (a) and (b)). At the end of the test, buckling of three bars at each end of the wall was observed.
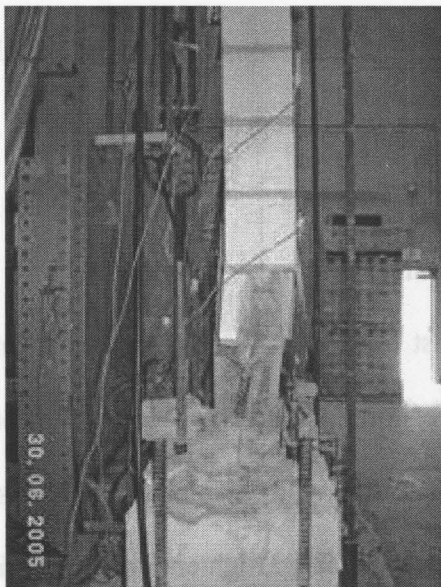
(a) Outermost bar buckling (East)   (b) Wall deformation
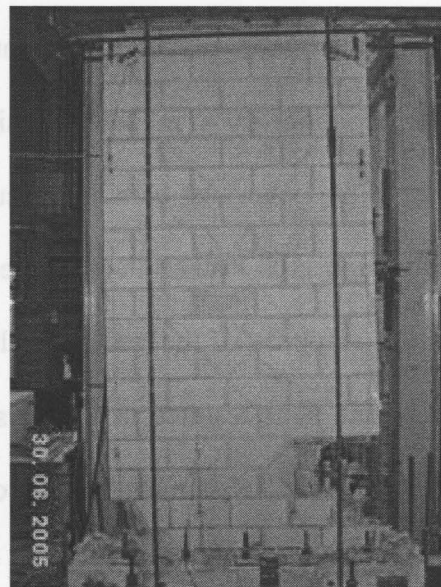
Fig. 3. 86: Wall 7 at 55 mm top deflection for East (pull) loading direction
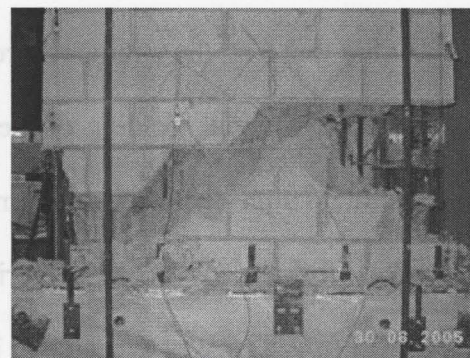
(a) Bar buckling (East)   (b) Shear compression failure

Fig. 3. 87: Wall 7 at failure at 65 mm top wall deflection (East direction)

3.8.3 Load-displacement response

The load-displacement hysteresis loops for Wall 7 shown in Fig. 3.78 indicate a symmetric response. The slopes of the loops decreased gradually with increasing displacement indicating loss of stiffness similar to all other test walls. Wall 7 did not exhibit a significant loss in lateral resistance until buckling of the outermost reinforcement occurred during the displacement cycle corresponding to three times the initial yield displacement for both directions of loading. An abrupt decrease of about 40% in lateral resistance was recorded for the wall once buckling of the outermost bars had occurred. This large decrease may have been due to the high axial load on the damaged wall.

The response of the wall was almost linear elastic up to first yielding of reinforcement. This resulted in thin hysteresis loops and low energy dissipation during these low displacement loading cycles. At higher displacement levels, the hysteresis loops started to become fatter which indicated high energy dissipation

3.8.4 Extent of yielding of reinforcement

During this test, the strains recorded in the two outermost end reinforcing bars indicated that initial yielding of the outermost East bar occurred at 450 kN lateral load at 17 mm displacement compared to 455 kN lateral load at 18 mm displacement for the West bar. During the test, the yield strain of the reinforcement in Wall 7 was expected to be similar to the previous test walls. This resulted in cycling the wall at multiples of 10 mm displacement which would

correspond to the displacement causing initial yielding of the reinforcing bars assuming the yield strength equal to 500 MPa. Prediction of the yield load for Wall 7 using the higher strength steel, reported later in Chapter 4, was similar to the recorded load in the following table. The extent of yielding of reinforcement for Wall 7 is presented in Table 3.7.

Table 3. 7: Extent of yielding of reinforcement (Wall 7)

Strain gauge location	Wall end	Initial yielding condition			Strain at max. load	Strain (x ε_y)
		Load	Displacement	% Drift		
Interface	West	-455 kN	18 mm	0.50	19.35 x10^{-3}	6.28
500 mm		-524 kN	25 mm	0.69	3.18 x10^{-3}	1.03
900 mm		-524 kN	25 mm	0.69	3.19 x10^{-3}	1.03
Interface	East	450 kN	17 mm	0.47	19.97 x10^{-3}	6.48
500 mm		518 kN	24 mm	0.66	3.11 x10^{-3}	1.01
900 mm		518 kN	24 mm	0.66	3.12 x10^{-3}	1.01

3.8.5 Wall deformation and drift

In-plane lateral displacement was measured at eight points over the height of the West end of the wall as indicated previously. The recorded in-plane lateral displacements over the height of the wall, for loading in both directions, are presented in Fig. 3.88 (a) and (b) for key loading conditions related to yielding of reinforcement. A concentration of bending over the lower 0.7 m of wall height is evident while the top 2.9 m of the wall tended to be relatively straight.

(a) Loading in East (pull) direction (b) Loading in West (push) direction
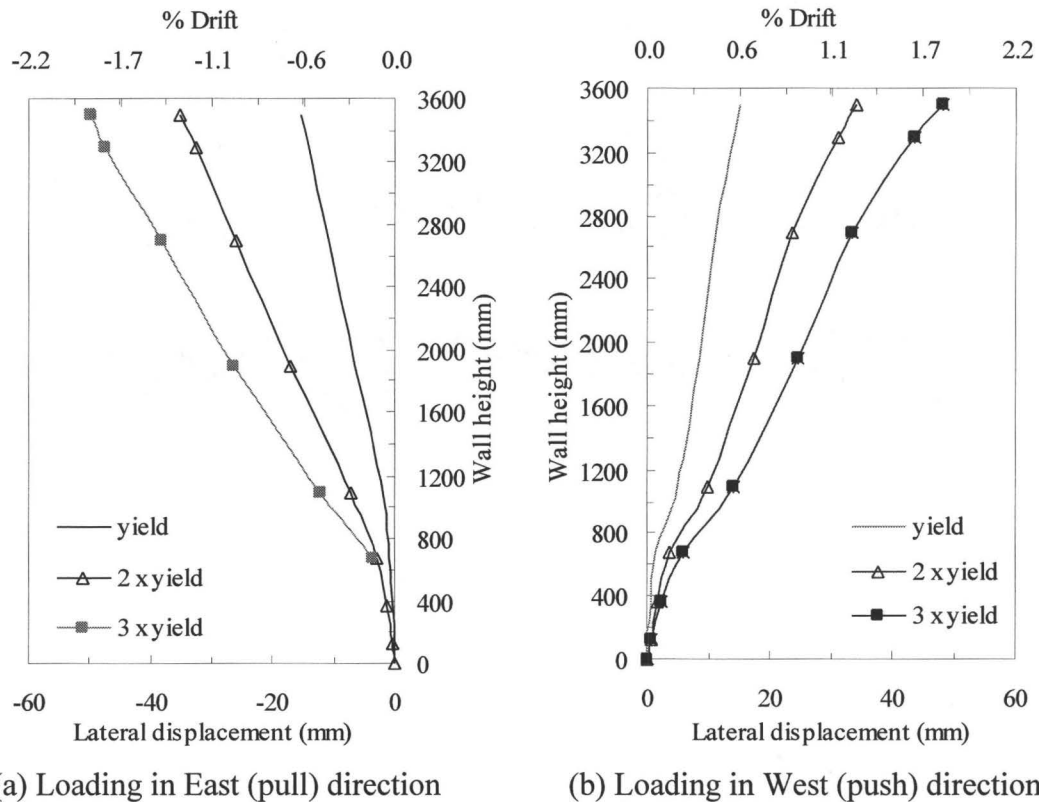
Fig. 3. 88: Total in-plane lateral deflection (Wall 7)

3.8.6 Wall curvature

Average curvatures over segments of the height of Wall 7 at different lateral displacements stages are presented in Fig. 3.89 for loading in both directions. Average curvatures were calculated as explained previously and showed good symmetry for the push and pull loading directions. It was possible to calculate average curvatures over the wall height up to high levels of displacement because relatively minor damage occurred in the face shells up to near failure. Average curvatures over the bottom 300 mm of the wall reached a value of 0.016 rad/m at a top displacement equivalent to three times the initial

yield displacement of the wall. Relatively high average curvatures, compared to the remainder of the wall height, were recorded over the lower 900 mm of the wall height.
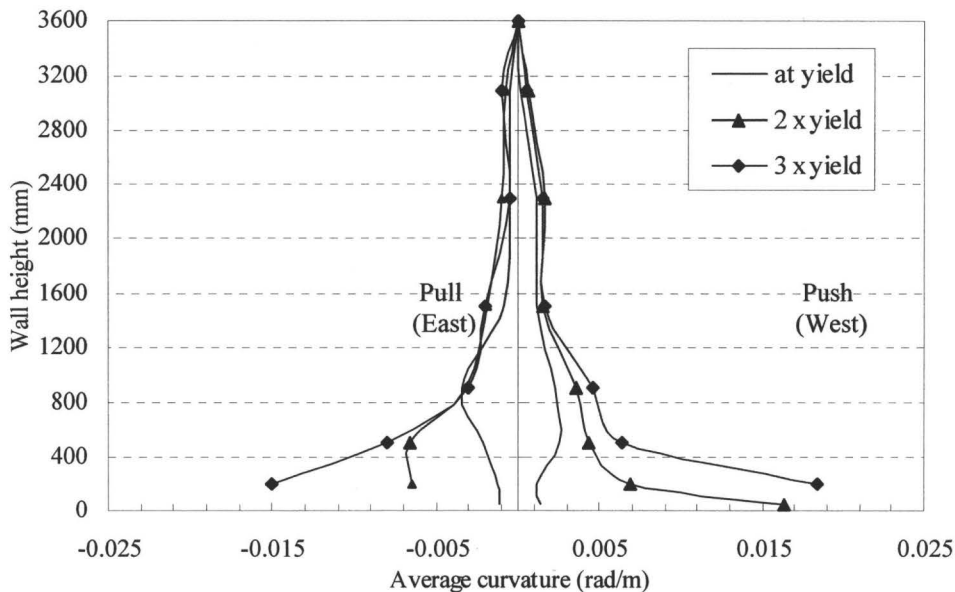
Fig. 3. 89: Average curvature along wall height for loading in both directions (Wall 7)

3.8.7 Strain profile

The strain profiles along the wall length were calculated as discussed previously and are presented in Fig. 3.90 for loading in both directions. The average strain profiles for the push and the pull loading directions followed similar patterns. The profiles of average strain between the base beam and 300 mm above the base beam, shown in Fig. 3.90 (a), indicate that the lengths of the compression zone were about 450 mm and 370 mm with maximum compressive strains of 1.28×10^{-3} and 4.1×10^{-3} at initial yield displacement and at two times the yield displacement, respectively. The profiles of average strains between 300

mm and 700 mm above the base beam, shown in Fig. 3.90 (b), indicate that the lengths of the compression zone were about 600 mm with maximum compressive strains of 0.95 $\times 10^{-3}$ and 2.9 $\times 10^{-3}$ at initial yield displacement and at two times the yield displacement, respectively. The figure also shows a fairly linear strain profile along the wall length at two times the yield displacement between 300 mm and 700 mm above the base beam. Figures 3.90 (c) and (d) show the strain profiles in the push direction of loading.

(a) 0 – 300 mm above the base beam   (b) 300 – 700 mm above the base beam

(c) 0 – 300 mm above the base beam   (d) 300 – 700 mm above the base beam
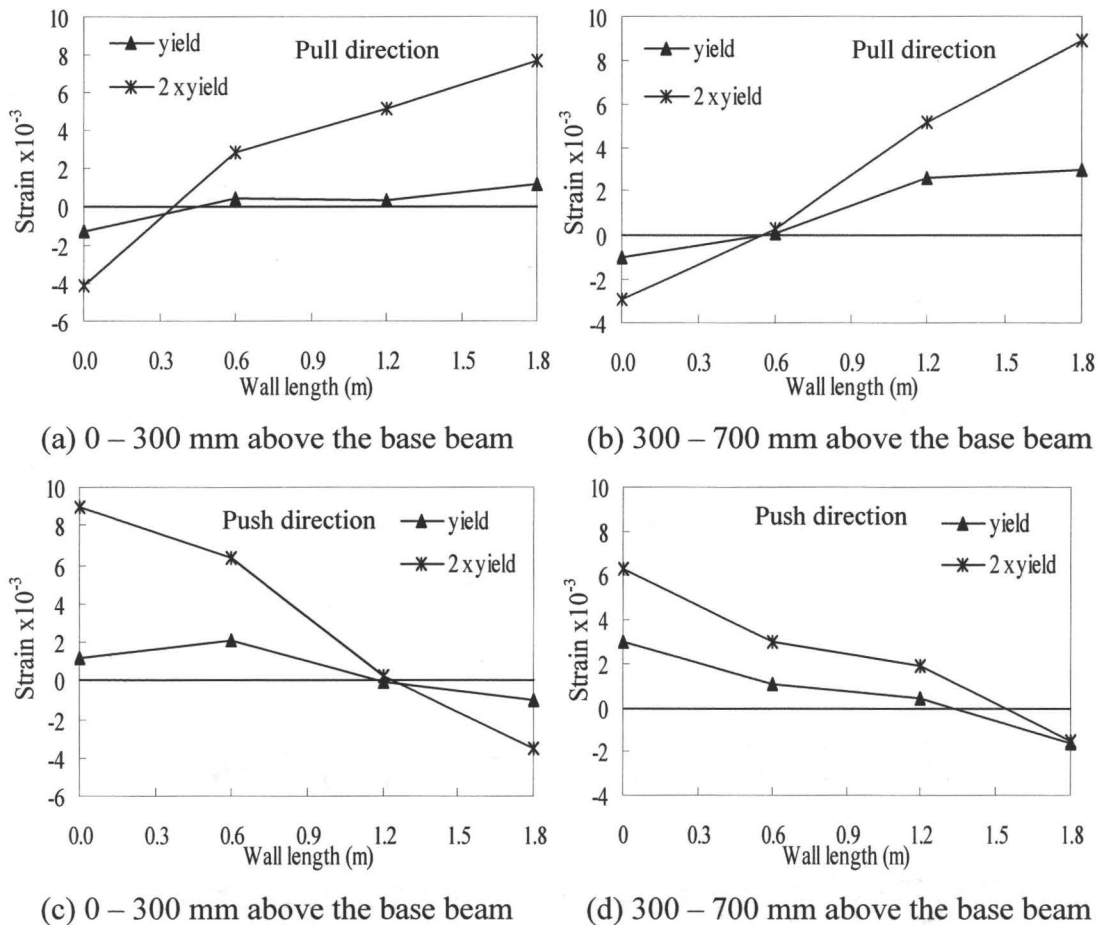
Fig. 3. 90: Profile of average strain along wall length for loading in

Both directions (wall 7)

3.9   Closure

The results of the seven test walls are reported in details in this chapter. Nearly independent reports are presented for each wall. Each report started with a summary of the test observations and the cracking progression up to termination of the test. Hysteresis loops and deformation profiles for all walls were presented followed by calculations of the average curvatures over the wall height and the average strain profiles along the wall length at heights close to the base beam. The extent of yielding in the wall is also presented from the reading of the strain gauges attached to the vertical reinforcement.

Comparisons between the test results for all walls will be presented in Chapter 4 and analysis of these results will be conducted in a comparative way in order to investigate the effects of various test parameters on different walls behaviours. A summary and conclusions will be presented in Chapter 5.

CHAPTER 4

ANALYSIS OF RESULTS

4.1   Introduction

Analysis of the test results presented in detail in Chapter 3 is the main focus of this chapter. The goal is to extract quantitative information by analysing and comparing these test results and identifying the effects of different test parameters on wall behaviour.

A description of the general response of the test walls is provided in Section 4.2. The subsequent sections present analysis for the effects of the test parameters (the amount and distribution of vertical reinforcement, and the applied axial stress) on the response of the test walls.

The seismic performance of shear walls is affected by some basic characteristics of the wall such as stiffness, strength, ductility, energy dissipation, and plastic hinge length. In order to assess the elastic and the inelastic behaviour of structural elements under seismic loads, documentation of these characteristics is one goal of this chapter. Identifying the effects of the different test parameters on these characteristics is the other focus of this chapter.

Natural frequency (period), which is directly related to the wall stiffness, affects the seismic demand or the force attracted by the wall during earthquakes. In addition, depending on the period of the structure and using the concept of equal energy (used for stiff structures) or equal displacements (used for flexible structures),

the relationship between displacement ductility and force modification factor can be established. The effect of the test parameters on the variation of the stiffness is presented and discussed in Section 4.3.

Under seismic loads, the member should have adequate strength (supply) to meet seismic demand. Discussion of wall capacities and the effect of testing parameters on the strength variation of the test walls is presented in Section 4.4.

The displacement ductility which is directly related to the force modification factor is determined by evaluating the lateral displacements of a member at initial yield and at ultimate load. The effects of the test parameters on the lateral displacement and the displacement ductility of the test walls are presented in Sections 4.5 and 4.6, respectively.

Energy dissipation is a very important factor in the seismic performance of structural members as it determines the level of hysteresis damping of the member during seismic loading. Energy dissipation provides higher hysteretic damping and results in lower force to be resisted by the wall. In Section 4.7, the effects of the test parameters on the energy dissipation are discussed.

In shear walls, plastic hinges are zones where high curvatures occur and high amounts of energy are dissipated as a result of steel yielding. The plastic hinges affect the ultimate and post-peak displacements of the members under lateral loading which defines the displacement ductility of the member which, in turn, determines the force modification factor to be applied in design of the structure. In Section 4.8, plastic hinge lengths for different walls are estimated

from the experimental results and compared with available formulations in the literature. Section 4.9 contains a summary of the main conclusion of the chapter.

4.2   General response of walls

The global response of the test walls is summarized using the envelopes of the load-displacement data as shown in Fig. 4.1. In general, the envelopes show ductile behaviour for all walls characterized by relatively little strength degradation with increased displacement after reaching maximum load.

Walls 2, 6 and 7, having the same vertical steel ratio of 1.3% and subjected to axial stresses of 0.00 MPa, 0.75 MPa and 1.50 MPa, respectively, experienced more distinct reduction in lateral load resistance before failure unlike Walls 3, 4, and 5 which had smaller amounts of vertical reinforcements and no applied axial stress.

The envelopes of the load-displacement curves for Wall 1 and its replicate Wall 2 are presented in Fig. 4.2 to illustrate the impact of the accidentally ungrouted region found in Wall 1 on the wall response (see Section 3.2 for details). The diagram shows that the initial behaviour of the two walls was reasonably similar up to 0.25% drift and a difference of only 10% in the lateral load resistance was recorded between the two walls at first yield. When the unsupported bar of Wall 1 was under high compressive stress during the reverse cycle of loading after tension yielding, the difference in behaviour became more significant. The bar in the ungrouted region in Wall 1 started to buckle and therefore offered minor resistance

under compression stresses at an earlier stage compared to the similar bar surrounded with grout in Wall 2.
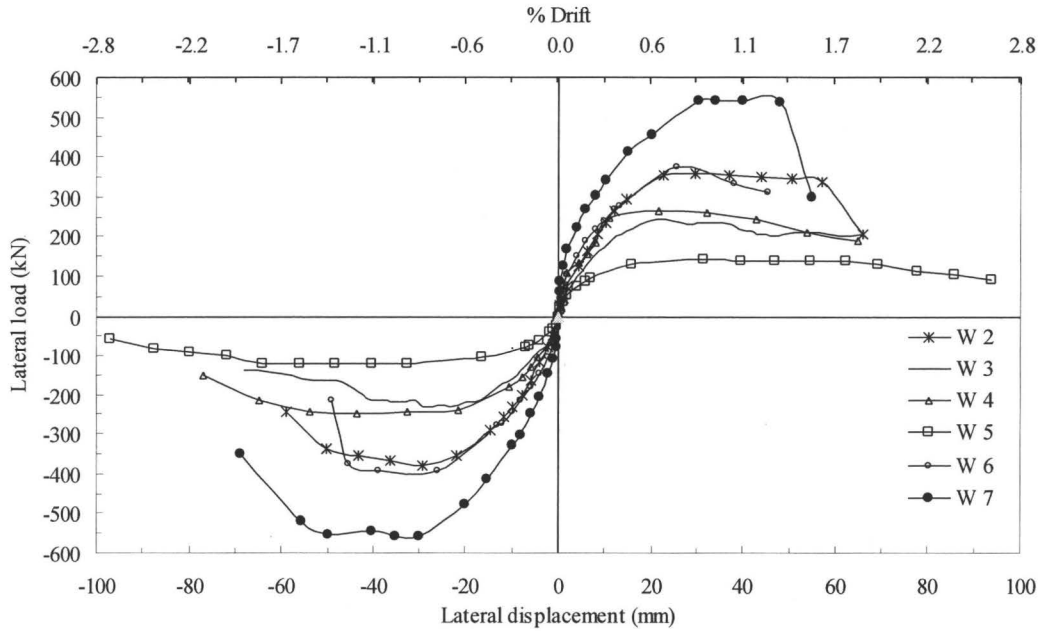
Fig. 4. 1: Load-displacement envelopes for wall test matrix
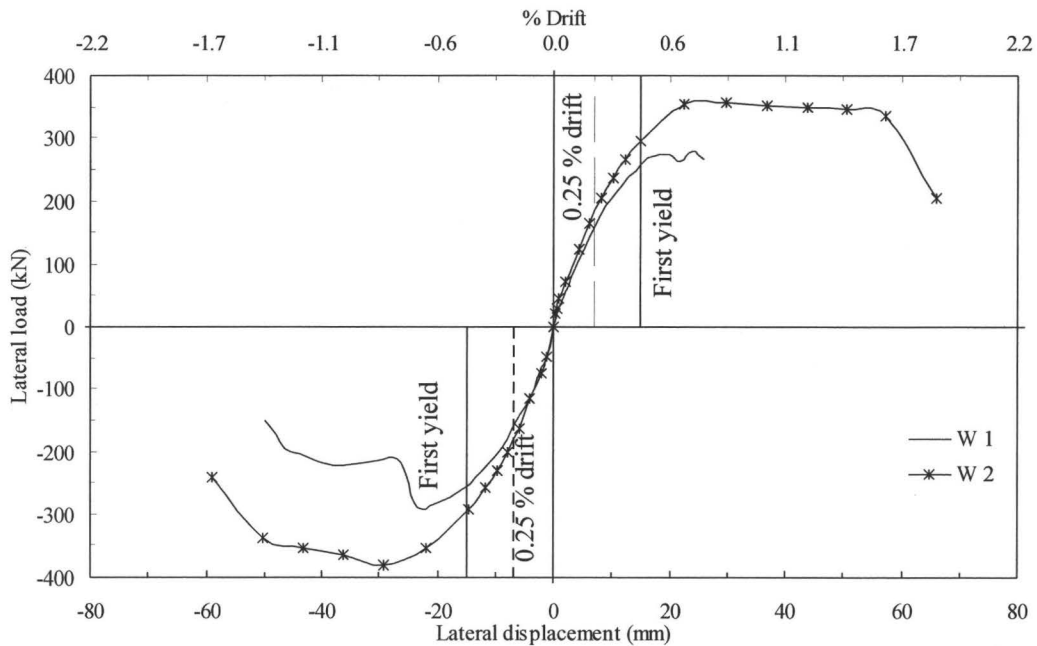
Fig. 4. 2: Load-displacement envelopes (Wall 1 and Wall 2)

4.3   Wall stiffness

To assess variation in the stiffness, the secant stiffness was considered as a useful measure of wall stiffness and was used for all walls. The secant stiffness is defined as the ratio between the lateral resistance and the corresponding wall displacement at the top. The variation in secant stiffness under increasing top displacements is shown in Fig. 4.3(a). The initial stiffness is shown as the first data point for all walls and is defined herein as the secant stiffness measured during the first cycle of loading corresponding to 0.25 mm displacement (0.007% drift).

Comparing the secant stiffness at low levels of displacements for Walls 2, 6 and 7 (see Fig. 4.3(b)) which were subjected to axial stresses equal to 0.00 MPa, 0.75 MPa, and 1.50 MPa, respectively, one can conclude that stiffness increases significantly with increases in the level of applied axial stress. This is consistent with previous research work (Shing et al. 1990) indicating that the overall shear stiffness prior to diagonal cracking tends to be proportional to the axial compression and is considered to be due to the compression enhancement of the masonry shear strength through decreased principal tensile stresses in the wall.

The increase of vertical reinforcement in Walls 4, and 2 (0.78%, and 1.30%, respectively) with respect to Wall 5 (0.30% vertical reinforcement) resulted in increases in initial stiffness. Calculated at 0.11% drift, the increases were 20% and 36%, respectively, with respect to Wall 5, as shown in Fig. 4.3(b). The increase of initial stiffness with increase of steel ratio may be explained, in part, by the increases of the transformed area of the section.
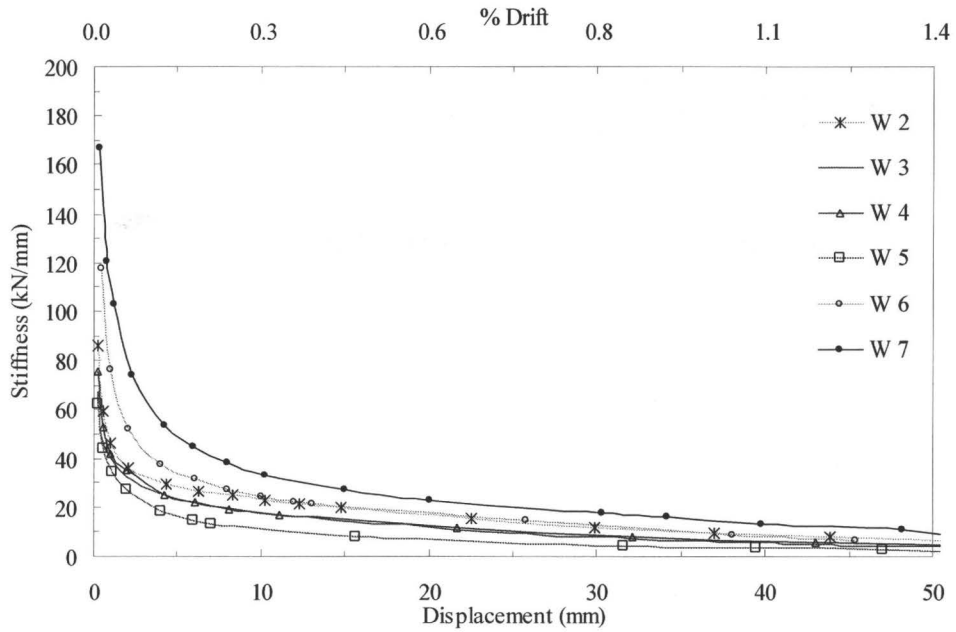
(a) Entire stiffness- displacement range
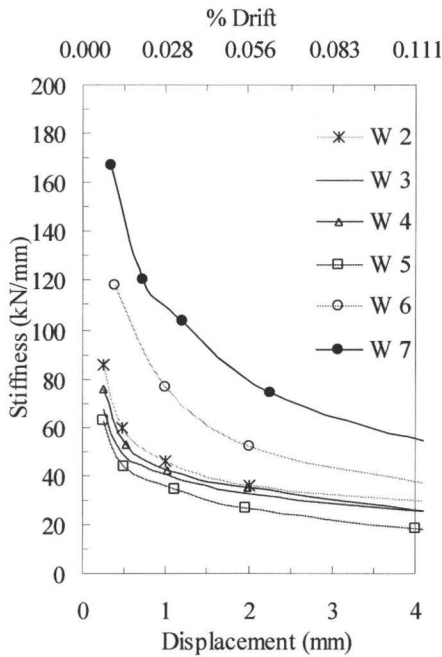
(b) Low displacement range
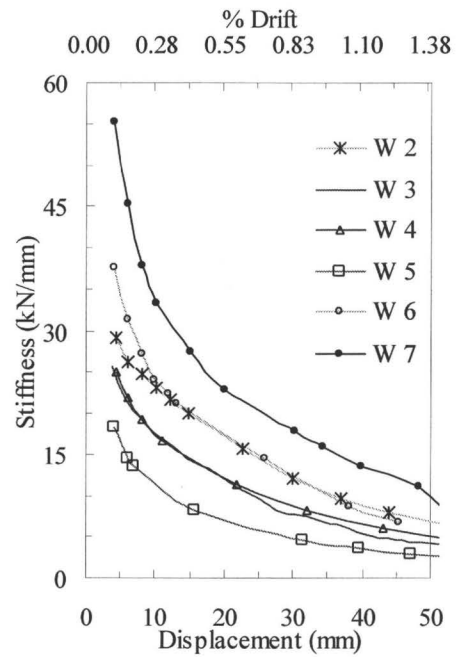
(c) High displacement range

Fig. 4. 3: Stiffness versus top wall deflection

As can be seen in Fig. 4.3 (c), the effect of increasing the amounts of vertical

reinforcement on calculated secant stiffness has a greater effect at larger deflections

corresponding to well developed flexural cracking. For Walls 3 and 4, reinforced with almost the same amount of vertical reinforcement (0.73% and 0.78%, respectively) but with different distributions, it can be seen that Wall 4, with closely spaced vertical reinforcement, had a slightly higher initial stiffness (about 12%) than Wall 3.

In general, the stiffnesses for all walls decreased rapidly to about 30 - 40% of the initial stiffness at very low displacement (drift) levels equal to 4 mm displacement (0.11% drift) as indicated in Fig. 4.3 (b). On an absolute scale, less rapid decreases were observed at higher displacement levels, up to 50 mm (1.38% drift), as indicated in Fig. 4.3 (a) and (c). The stiffness of Wall 6, subjected to 0.75 MPa axial stress, decreased rapidly at high displacement levels and became almost equal to the stiffness of Wall 2, which was identical but not subjected to axial stress (see Fig. 4.3(b)). However, this result may be due to out-of-plane displacement problems that occurred during the test of Wall 6 as discussed in Section 3.7.2. The measured initial stiffness, stiffness corresponding to first yield, and stiffness corresponding to maximum lateral load are presented in Table 4.1.

In order to compare the prediction for the yield stiffness of reinforced masonry shear walls, equations commonly used for stiffness predictions are presented and applied in the following discussion.

The estimated gross stiffness and the cracked stiffness for all walls, presented in Table 4.1, were calculated based on flexure and shear deformations using Eq. 4.1. The moment of inertia and area of the section were calculated using the gross

masonry area, A_g, and the transformed cracked section, A_{cr}, respectively, to determine the initial stiffness, I_g, and the cracked stiffness, I_{cr}, respectively, for the walls. Constant section properties were assumed over the wall height (for calculated values refer to Appendix H).

$$K = 1/ \left(\frac{h^3}{3 \, E_m \, I} + \frac{1.2 \, h}{G_m \, A} \right)$$
Eq.4. 1

where: E_m $= 850 \times f'_m$
       G_m $= 0.4 \times E_m$ for rectangular sections.

Table 4.1: Wall stiffness

Stiffness (kN/mm)	Wall No. (% Vert. Reinf.) [Comp. stress]	Wall 2 (1.3%) [0 MPa]	Wall 3 (0.73%) [0 MPa]	Wall 4 (0.78%) [0 MPa]	Wall 5 (0.3%) [0 MPa]	Wall 6 (1.3%) [0.75 MPa]	Wall 7 (1.3%) [1.50 MPa]
Measured	Initial[1]	85.94	67.57	75.67	62.75	117.93	167.13
Measured	First yield[2]	19.61	16.38	16.79	13.61	19.92	25.63
Measured	Ultimate	11.94	10.45	8.22	4.51	14.51	15.82
Estimated	Initial[3]	73.64	70.41	69.75	66.44	73.64	73.64
Estimated	Cracked[4]	24.36	17.48	17.24	8.81	24.77	25.42
Estimated	Effective[5]	12.75	12.75	12.75	12.75	15.95	16.58
Estimated	Cracked / Initial (%)	33.0	24.8	24.7	13.2	33.6	34.5
Measured	at 0.5% Drift	20.9%	19.5%	17.3%	12.2%	18.3%	10.8%
Measured	at 1.0% Drift	11.1%	9.1%	9.8%	6.5%	7.1%	6.8%
Measured	at 1.5% Drift	7.4%	5.7%	6.0%	4.0%	---	2.5%

[1] Initial stiffness is measured at 0.25 mm displacement for all walls
[2] Yield stiffness is measured at yield displacement for all walls
[3] I_g and A_g are used for initial stiffness calculation
[4] I_{cr} and A_{cr} are used for cracked stiffness calculation
[5] I_{eff} and A_e are used as suggested by Priestley and Hart (1989) using Eq. 4.2

As an alternative to calculations based on fundamental structural mechanics, Priestley and Hart (1989) developed an empirical equation for preliminary prediction

of effective moment of inertia for cracked reinforced masonry sections taking into consideration the effects of cracking, tension stiffening, and axial load. The stiffness of cantilever walls subjected predominantly to flexural deformations may be based on an effective moment of inertia, I_{eff}. This effective moment of inertia is related to the gross moment of inertia of the uncracked section I_g, using Eq. 4.2. They also suggested that the ratio of the effective area, A_e, resisting shear deformation to the gross section area, A_g, is similar to the ratio of the effective moment of inertia to the gross moment of inertia.

$$I_{eff} = \left(\frac{100}{f_y} + \frac{P_u}{f'_m \, A_g} \right) I_g \qquad\qquad Eq.4.2$$

where: f'_m = Masonry compressive strength
 P_u = Axial load on wall.

It can be seen that the approach based on section properties (using Eq. 4.1) gives acceptable estimates of the initial stiffness (15% underestimated) for walls not subjected to axial stress, such as Walls 2, 3, 4, and 5. This difference is acceptable given the accuracy of top displacement measurements at very low displacement levels. However, prediction of the initial stiffness for Walls 6 and 7, subjected to axial stress, significantly underestimated the experimental results. This can be justified as using a constant value for the elastic modulus of masonry, $E_m = 850 \, f'_m$ for the initial stiffness calculation (Eq. 4.1) may result in inconsistent values when axial load is applied (see variation in E_m calculated for prisms in Appendix G). The slopes of the masonry stress-strain curves vary significantly and, for accurate results, values corresponding to different stages should be taken into consideration.

Differences of only 10% were found between the estimated cracked stiffness and the measured stiffness at first yield for Walls 3 and 4 (0.73% and 0.78% vertical reinforcement and no axial stress). The measured stiffness for Wall 5, at first yield, was much higher than the predicted stiffness based on the cracked moment of inertia applied to the whole height of the wall. This may be explained as Wall 5, having the least amount of reinforcement (0.3%), experienced first yielding at low drift and lateral force values compared to the other walls which in turn implies that a large portion of the wall height may have been uncracked. This implies that the effective moment of inertia for the wall could be higher than the assumed cracked moment of inertia over the whole height. The use of the cracked area as the effective area for shear stiffness may lead to underestimating the shear stiffness due to the neglected participation of aggregate interlock forces. This effect would be more significant with narrow cracks associated with the earlier stages of loading.

The opposite result occurred for Wall 2, where the measured stiffness at first yield was much lower than the predicted value. This may be explained by considering that Wall 2, having the largest amount of reinforcement (1.3%), experienced first yielding at higher drift and lateral force values compared to Wall 5, having the least amount of reinforcement (0.3%). At the first yield stage, diagonal and stepped cracking were significant which may have led to a decrease in the effective shear area resulting in lower shear stiffness.

The use of the empirical equation suggested by Priestley and Hart (1989) significantly underestimated the stiffness at first yield of the test walls. Although,

this equation takes into account the effect of axial stress on the stiffness, the fact that it only depends on the yield strength of bars to account for crack width without accounting for the number or size of the reinforcement used may lead to significant errors in estimating the stiffness of the test walls. Another reason for the discrepancy between the estimated values and the measured values at yield may be that this equation was developed for cantilever walls subjected predominately to flexural deformation. As will be discussed later, the shear deformations for the test walls were significant and contributed significantly to the measured lateral deflections.

The secant stiffnesses for the test walls were normalized with respect to the corresponding initial stiffnesses. The variation of normalized wall stiffness with respect to different drift levels is presented in Fig. 4.4 (a). The figure shows a similar trend of stiffness degradation for all of the test walls. Normalized stiffness values are given in Table 4.1 at drift levels of 0.5%, 1.0% and 1.5%. Comparing Wall 2 (1.3% steel) and Wall 5 (0.3% steel) shows that the stiffness degradation for a wall with a higher amount of reinforcement is less significant than for a wall with a lower amount. On the other hand, comparing similarly reinforced Walls 2, 6, and 7 subjected to axial stresses of 0.00 MPa, 0.75 MPa, and 1.50 MPa, respectively, indicates that the relative stiffness degradation is more significant with increase in the level of axial compressive stress.

It can be observed that significant variations in stiffness of reinforced masonry shear walls occur at different drift levels. Such differences will directly affect the period of a shear wall structure and thereby influence the seismic demand

at different drift levels. To provide a general indication of the effect, Eq. 4.3 is a best

fit equation relating the stiffness of the test walls with respect to wall drift.

Stiffness / Initial stiffness (%) = 9.7 x (% drift)$^{-0.5}$ Eq.4. 3
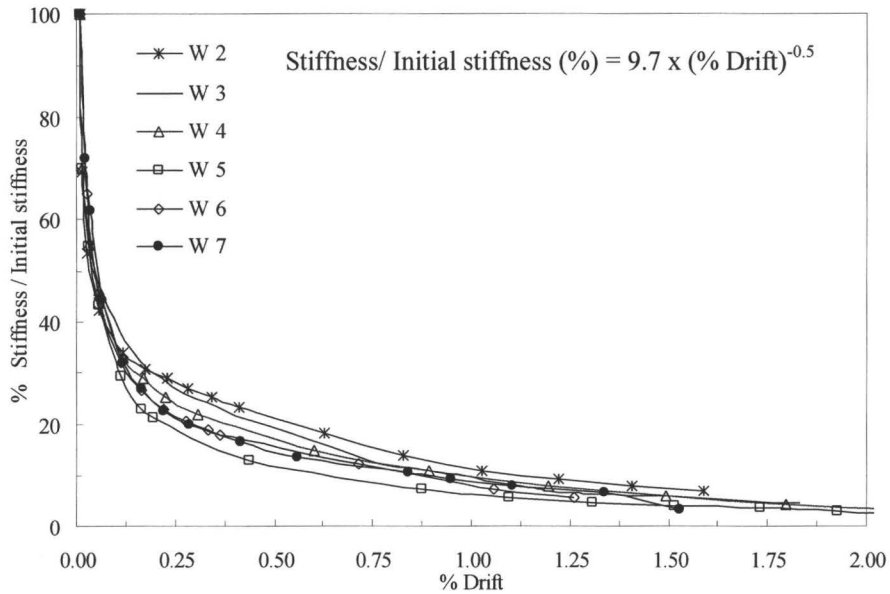
(a) Stiffness versus percent drift
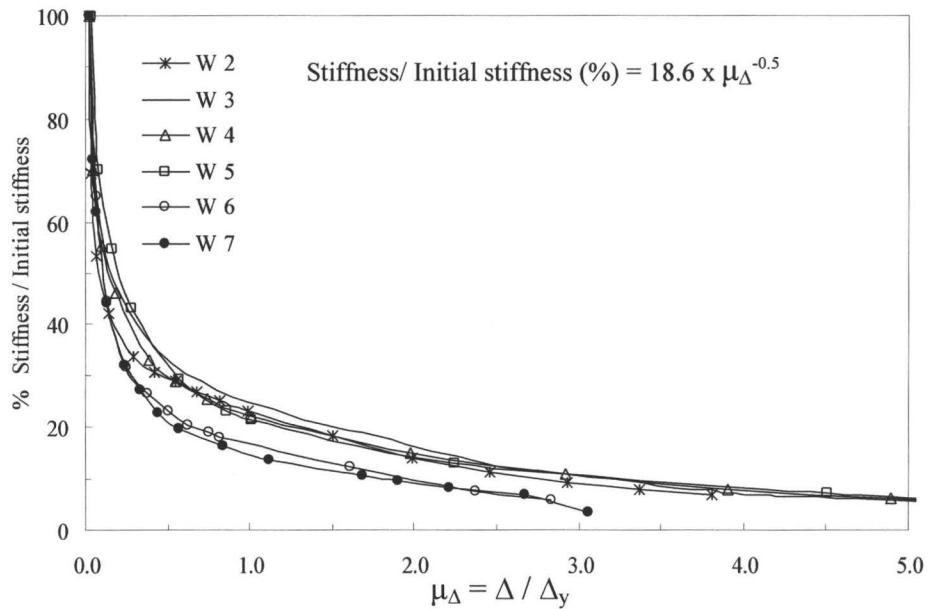
(b) Stiffness versus displacement ductility

Fig. 4. 4: Stiffness relationships

As an alternative indication, normalized wall stiffness with respect to the displacement ductility (Δ / Δ_y) for each wall is presented in Fig. 4.4 (b). The figure shows a similar trend of stiffness degradation for all the test walls. The best fit equation relating wall stiffness to displacement ductility is given by Eq. 4.4.

Stiffness / Initial stiffness (%) = 18.6 x (Displacement ductility)$^{-0.5}$ Eq.4. 4

The results in Fig. 4.4 (b) also indicate that the secant stiffness at initial yield (at μ_Δ =1) for walls without axial stress (Walls 2, 3, 4, and 5) is about 20% of the initial stiffness. The secant stiffness at first yield (at μ_Δ =1) for walls subjected to axial stress was shown to decrease to as little as about 15% of the initial secant stiffness. The stiffness at 1.0% drift (see Table 4.1), which roughly corresponds to the maximum load as indicated later in Section 4.5, is in the order of 50% of the stiffness at first yield (occurring between 0.3% and 0.5% drift).

A point of the above discussion is that using the higher stiffness of the member at first yield may not be appropriate in the context of modern design approaches such as ultimate limit state design or displacement based design. A significant decrease of 50% in the stiffness for masonry structures having periods ranging between 0.4 and 0.8 sec (Drysdale et al. (1999)) will results in an increased period ranging between 0.6 and 1.1 sec. Increases in the period of the structure associated with stiffness degradation may influence the force attracted by the structure during an earthquake. The increase in period may also lead to changing the approach used in calculating the force modification factor for the structure. An equal energy approach is used for structures having a low period whereas equal

displacement is used for structures having a longer period. (For further discussion refer to Appendix I).

4.4   Wall capacity

The capacity for each wall is defined as the maximum lateral load resisted by the wall during the test. Flexure capacity of a reinforced masonry shear wall mainly depends on the masonry compressive strength, the yield strength and the amount and distribution of the vertical reinforcement. The average compressive strength, f'_m, for all test walls was about 14.9 MPa as determined from the masonry prism test results presented in Section 2.4.6. The average yield strength for the vertical reinforcement was about 502 MPa for all walls except for Wall 7 which was constructed separately as explained in Section 2.4.1.

Prediction of wall capacities during the design phase was based on simple beam theory and linear strain distribution for monotonic loading. As presented in Table 4.2, two sets of calculations were done; one including the compression reinforcement and the other neglecting its contribution. Equations used for strength predictions are provided in Appendix A. The ultimate wall capacity under cyclic loading was assumed to be similar to wall capacity when subjected to monotonic loading as shown by Jamison (1997). It should also be noted that flexural strengths are not considered to be dependent on the sequence of loading or even on variation of axial load during the test, but simply on the amount of axial load at the ultimate stage as was addressed by Abrams (1987).

The predicted and measured capacities for the test walls are listed in Table 4.2. Good agreement can be seen between the predicted and measured strength values for walls tested without axial load (within 9% on average). This indicates that the use of simple beam theory for flexural strength predictions is within acceptable accuracy which agrees with previous work conducted by Shing et al. (1989).

Table 4. 2: Predicted and measured lateral loads for flexural behaviour

	Steel ratio % & Axial stress	Yield load Q_y (kN)		Ultimate load Q_u (kN)		
		Predicted (Comp. reinf.)	Measured Push direction (Pull direction)	Predicted (comp. reinf.) ε_u =0.0025	Predicted (comp. reinf.) ε_u =0.003	Measured Push direction (Pull direction)
W1[*]	1.3% 0 MPa	---	--- (231)	---	---	274 (291)
W2	1.3% 0 MPa	284 (291)	296 (292)	338 (382)	352 (399)	360 (380)
W3	0.73% 0 MPa	185 (188)	174 (190)	242 (256)	245 (262)	242[**] (235)
W4	0.78% 0 MPa	184 (186)	185 (182)	246 (260)	253 (268)	265 (246)
W5	0.3% 0 MPa	83 (84)	95 (84)	117 (118)	118 (119)	143 (122)
W6	1.3% 0.75 MPa	321 (330)	311 (316)	347 (402)	365 (424)	377[**] (407)
W7[+]	1.3% 1.5 MPa	---[++] (412)	450 (455)	362 (459)	391 (482)	541 (558)

[*] No predictions are presented for Wall 1 where an ungrouted zone were discovered during the test.

[**] Results when maximum load occurred where repair grout failed in compression.

[+] Predictions based on yield strength of vertical reinforcement = 625 MPa.

[++] No value presented as predictions indicated compression failure before yielding.

For the two directions of cyclic loading, average differences of 2% and 23% were observed between the strengths predicted using compression reinforcement and the measured strengths for Walls 6 and 7 with axial stresses of 0.75 MPa and 1.50 MPa (corresponding to 5% and 10% f'$_m$), respectively. The differences between the

predicted and measured capacities are consistent with the conclusion stated by Zhang and Wang (2000) that strength predictions of shear walls under high axial load using simple beam theory tend to underestimate the actual strengths. High compressive stresses reduce the amount of flexural and shear cracks along the wall height and increase the length of the compression zone.

In an attempt to account for the higher yield strength of the vertical steel in Wall 7, it was decided, for comparison purposes only, to adjust the strength of this particular wall. The ratio between the measured and predicted strength (using 625 MPa steel) was multiplied by the predicted strength using reinforcement with 500 MPA yield strength. This adjustment will minimize the effect of different yield strengths on the comparison between the results.

The measured flexure yield and ultimate capacities for Walls 5, 3, 4 and 2 (with steel ratio of 0.3%, 0.73%, 0.78% and 1.3%, respectively) are presented in Fig. 4.5 (a). The figure illustrates the expected dependency of the wall capacity on the amount of vertical reinforcement. It can be seen from the figure that the flexural strength is very sensitive to the amount of vertical reinforcement, and a fairly linear increase can be observed. Comparing Walls 3 and 4, having almost the same percentage of vertical reinforcement (No. 25 @ 400 mm and No. 20 @ 200 mm, respectively, for a 1.8 m long wall) but a different distribution, indicates that the flexural strength is mainly affected by the amount of reinforcement and is not very sensitive to the different distributions of the bars along the wall length. (Of course, even for Wall 3, the distribution is still quite uniform.) This is consistent with

previous research on masonry shear walls reported by Priestley (1986). Figure 4.5 (b) presents the yield and ultimate capacities for Walls 2, 6, and 7 (adjusted) (with the same steel ratio and subjected to axial compressive stresses of 0.0 MPa, 0.75 MPa, and 1.50 MPa, respectively). The figure indicates that the flexure strength is less sensitive to the increased axial stress compared to increases in reinforcement.
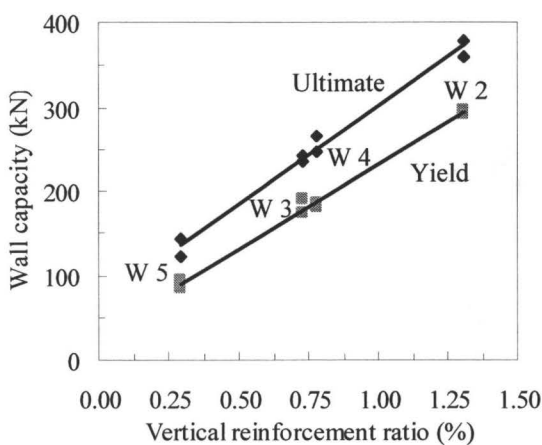
(a) Effect of steel ratio on wall capacity (b) Effect of axial stress on wall capacity
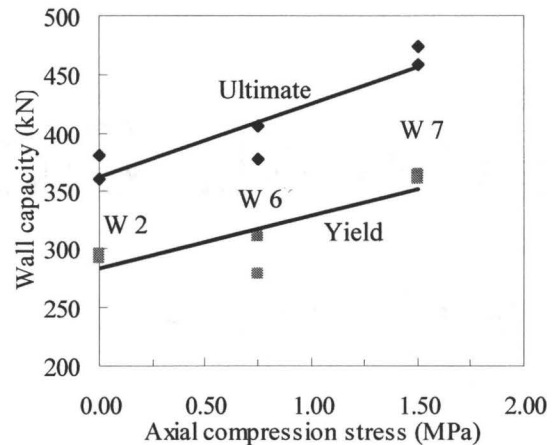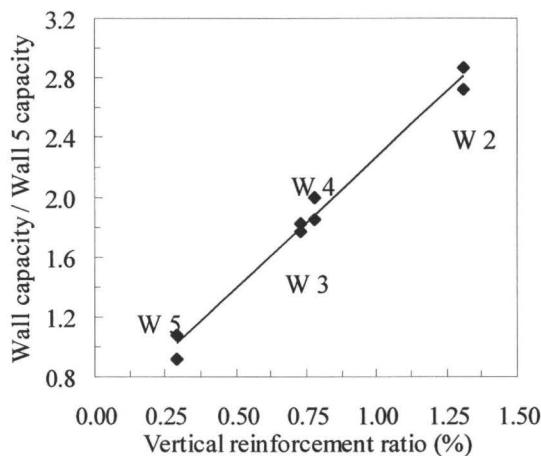
(c) Effect of steel ratio on the
normalized wall capacity
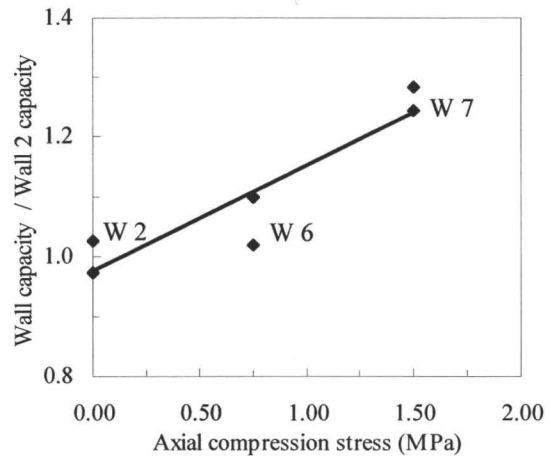
(d) Effect of axial stress on the
normalized wall capacity

Fig. 4. 5: Effect of steel ratio and axial compression stress on wall capacity

The effect of increasing the amount of vertical reinforcement on normalized ultimate capacities is presented in Fig. 4.5 (c), where wall capacities are normalized with respect to the average capacity of Wall 5 with 0.3% vertical reinforcement, (the least amount of vertical reinforcement). It can be observed from the figure that increasing the vertical reinforcement from 0.3% to 1.3% (4.3 times) results in nearly tripling of the wall capacity. This can easily be explained by simple mechanics where increasing the amount of reinforcement led to an increase in the compression zone length to satisfy equilibrium with the increased tension force. This increase in length of the compression zone in turn led to a slight decrease in the moment arm for the section resulting in a less than proportionate increase in total capacity with respect to the increased amount of reinforcement.

The effect of increasing the applied axial stress on the normalized ultimate capacities is presented in Fig. 4.5 (d), where wall capacities are normalized with respect to the capacity of Wall 2 (with no axial stress). If the average values for capacities in the push and pull loading directions are used for comparison, an increase of 22% in the average wall capacity corresponds to an applied axial stress of 1.50 MPa (corresponding to 0.10 f'_m). This increase can be simply explained by looking at the interaction diagram for members subjected to axial compression force and bending. It is known that an increase in axial compression in the tension failure region, where the capacities of these walls are located, is associated with an increase in moment capacity. Alternatively, a reduction in moment capacity with increased compression load occurs in the compression failure region. The

increase associated with Wall 7 with respect to Wall 2 is difficult to analyse. Although an adjustment based on yield strength of reinforcement was made, it may not be accurate as wall strength is dependent on many other parameters besides the strength of the vertical reinforcement.

4.5 Displacements

The ability of a wall to undergo large deformations under lateral loads without losing much of its strength has a major influence on its response during earthquakes. Flexible walls with high displacement capabilities beyond yielding are generally preferable to rigid walls with more limited deflection. However, in practical terms, the shear wall response related to first yield and ultimate displacements must be related to usable drift levels under earthquake loading.

In general, the total in-plane lateral deflection results from three main components, namely: sliding, flexural and shear displacements. Displacement predictions during the design phase for the test program were based on flexural deformation only. At that time, it was expected that the flexural deformation would be dominant and that the shear deformation would be minor for these walls which had an aspect ratio (height/length) of two. Displacements due to sliding were intended to be removed from the total deflection by subtracting the base slip, if any, from the total deflection. Equations used for predicting the yield and the ultimate displacements caused by flexural deformations only are presented in Appendix D using the estimated (calculated) strain profile (curvature) at first yield and at ultimate

loads and assuming a plastic hinge length equal to half the wall length (as suggested by the IBC (2000)). The ultimate masonry compressive strain was set equal to 0.0025. The measured yield and ultimate displacements for all walls along with the corresponding predicted values are listed in Table 4.3. The displacements corresponding to 20% post-peak lateral load degradation are also included in the table for comparison.

Table 4. 3: Predicted and measured displacements

	Predicted displacement without compression reinf. (with compression reinf.)		Measured displacement for Push (Pull) direction		
	Δ_y (mm)	Δ_u (mm)	Δ_y (mm)	Δ_u (mm)	$\Delta^+_{0.80}$ (mm)
W1	----	---	--- (13)	18 (22)	---
W2	9.16 (8.95)	14.66 (16.52)	15	30 (30)	60 (52)
W3	8.48 (8.36)	18.91 (21.92)	11	24[*] (28)	46 (44)
W4	8.53 (8.43)	18.12 (20.01)	11	33 (33)	53 (68)
W5	7.73 (7.69)	33.01 (37.1)	7.0	32 (32)	77 (79)
W6	9.57 (9.32)	13.65 (15.29)	16	25[*] (33)	45 (45)
W7[**]	--- (12.25)	14.26 (15.38)	17	30 (34)	51 (62)

[*] The values of ultimate deflections indicated for Walls 3 and 6 were recorded when the repaired zone containing the new grout failed in compression.
[**] Predictions shown for Wall 7 were based on f_y = 625 MPa.
[+] Post-peak displacement corresponding to 0.80 Q_u.

It can be seen in Fig. 4.6 (a) that the yield displacements, as expected, tend to increase with increases in the amount of vertical reinforcement. The yield displacement almost doubled corresponding to an increase of the amount of reinforcement from 0.3% to 1.3%. The yield displacements also tend to increase

with increase of the applied axial stress as shown in Fig. 4.6 (b). A 12% increase in the yield displacement was recorded corresponding to an increase in axial stress from 0.0 to 1.5 MPa, as indicated from the results of Walls 2 and 7, respectively. The reason for these observations is simply due to the increased curvature associated with the increase of the compression zone length. From geometry of strain distribution, obviously the magnitude of the masonry compressive strain also increased corresponding to the increase of the length of the compression zone.
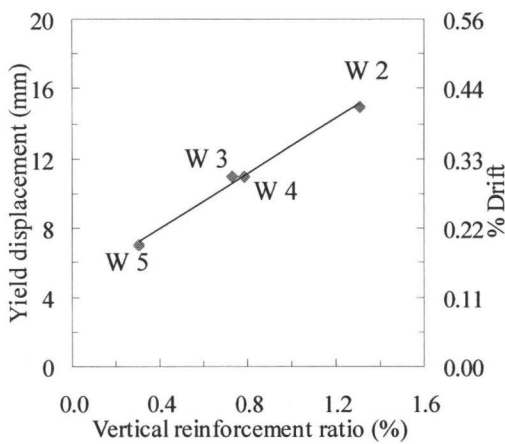
(a) Effect of steel ratio on Δ_y
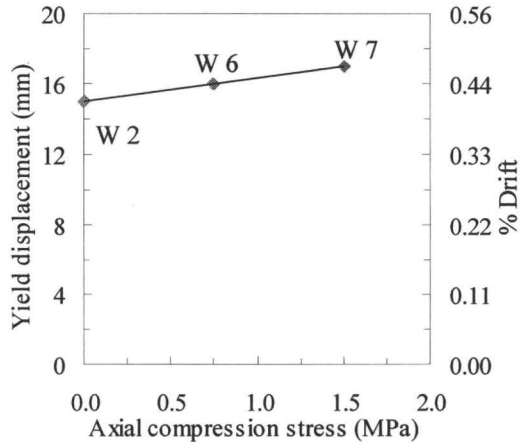
(b) Effect of axial stress on Δ_y
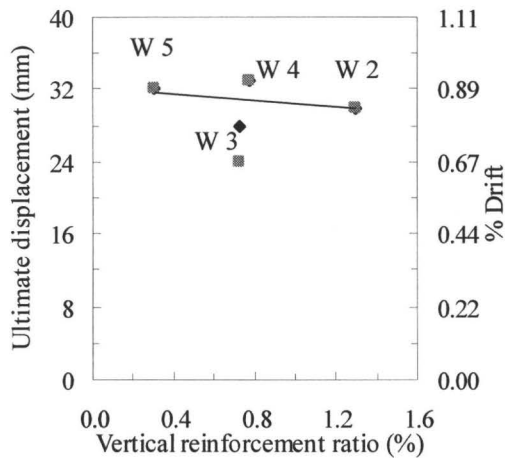
(c) Effect of steel ratio on Δ_u
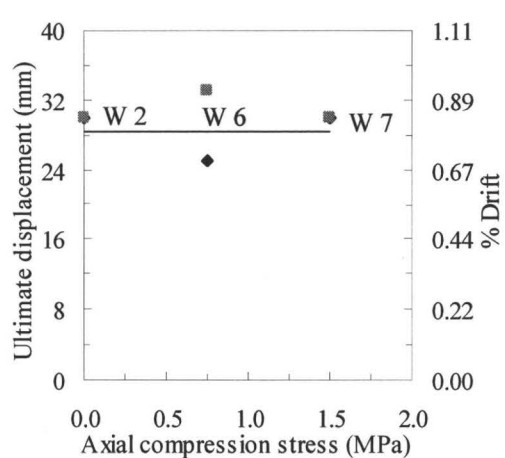
(d) Effect of axial stress on Δ_u

Fig. 4. 6: Effect of steel ratio and axial compression stress on displacements

It can be seen in Fig. 4.6 (c) and (d) that all test walls reached their maximum load at displacements close to 30 mm (0.83% Drift) and that the displacements at ultimate load are not as sensitive to the test parameters as are the yield displacements.

Except for Wall 5 predictions, which were close, all other predictions presented in Table 4.3 for the yield and ultimate deflections underestimated the experimental values. To investigate the discrepancy between the predicted and measured displacement, an attempt was made to subtract the shear deformation. The contributing components of the recorded top deflection needed to be decoupled in order to evaluate the flexural and shear deformations separately.

The method suggested by Massone and Wallace (2004) was used to separate (decouple) the shear and flexure deformations. This method relies on using diagonal and vertical displacements over the full height of the wall to separate the flexure and shear deflection parts of total wall deflection assuming the center of rotation for the wall to be at one third of the height from bottom. The procedure involved is documented in Appendix E.

Figures 4.7 (a) to (f) show the percent contributions of the shear and flexural components to the total deflection at the top of each wall as a function of the total top deflection of the wall using the above-mentioned decoupling method. It can be seen from Fig. 4.7 (a) to (f) that the relative contribution of flexural deformation decreases with increase in total lateral deflection.
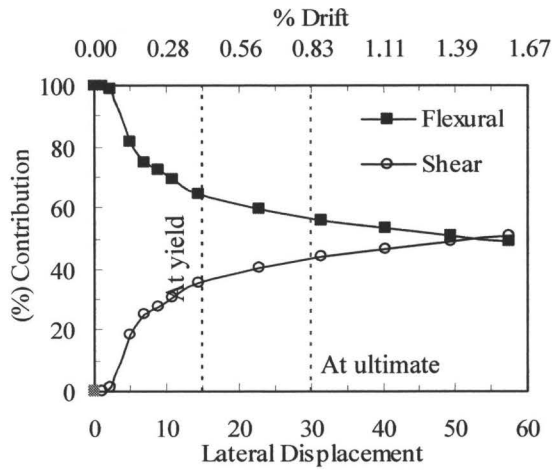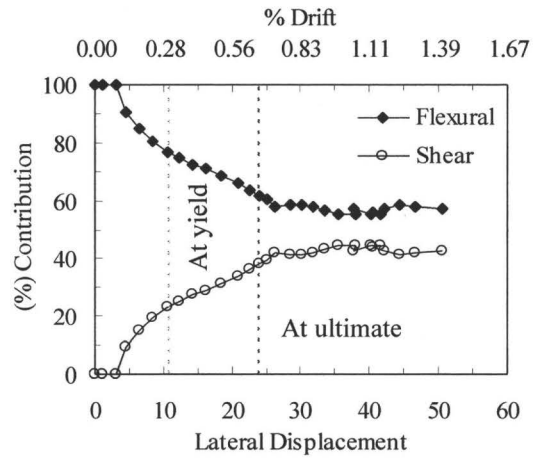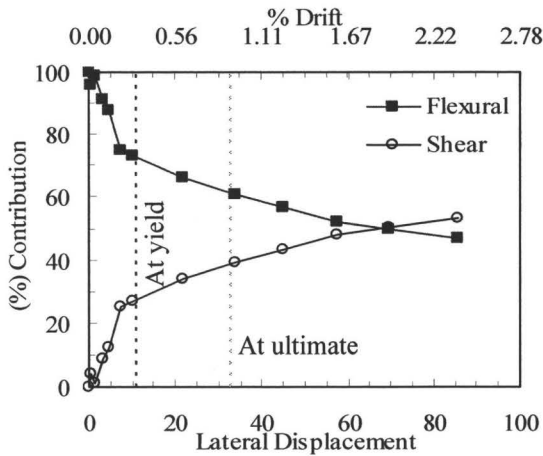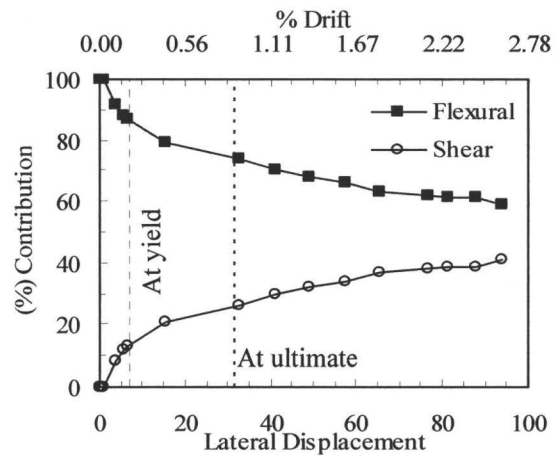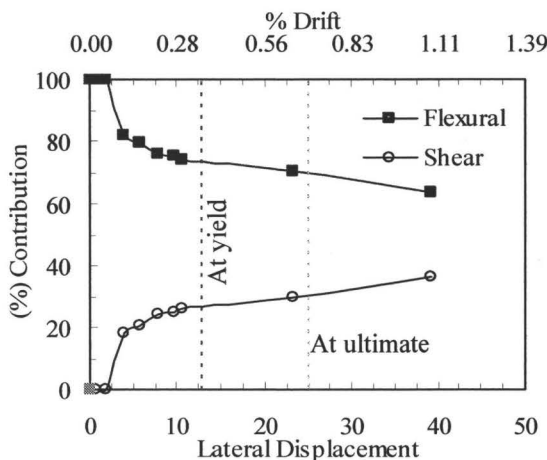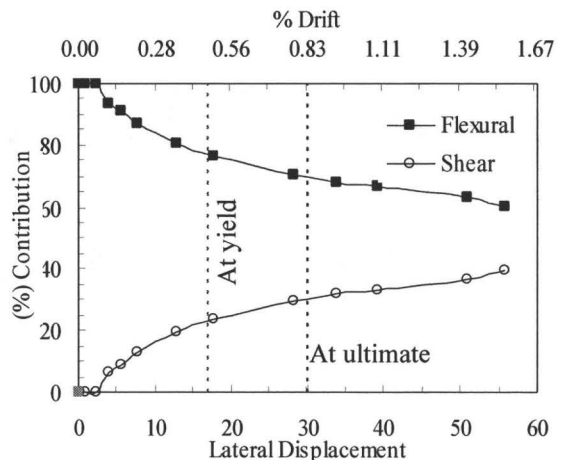
Fig. 4. 7: Relative contribution of flexure and shear deformations to total deflection

The corollary is an increase in the relative shear deflection with increased total wall deflection. The increase in deflection due to shear deformation shown in the diagrams occurred as wall cracks propagated starting with horizontal bed joint cracking, (causing large flexural deformations) and followed by stepped and diagonal cracking at higher displacement levels (causing shear deformation). The flexural deflection contributions as a percentage of the total deflection of the walls at first yield, ultimate load and at 1% drift are listed in Table 4.4.

Based on the decoupled results, it can be concluded that flexural deformation was not completely dominant and that shear deformation would contribute a significant share of the total deflection. Therefore, shear deformations should not be ignored in evaluating the total deflection of walls. In addition, it can be concluded that the percentage of shear deflection is not a fixed value for a specific wall aspect ratio (height/length).

Table 4. 4: Calculated flexural deflection as a percent of total deflection[*]

	Flexure displacement / Total displacement (%)					
	W2	W3	W4	W5	W6	W7
At yield displacement	64	75	72	87	73	77
At ultimate load	56	59	61	74	68	69
At 1% drift	54	55	59	72	65	67

[*] These values are based on the method suggested by Massone and Wallace (2004)

To assess the effect of the different test parameters on the flexural and shear deformation of the walls, diagrams relating the different test parameters to the flexure deflections of the test walls were generated. Figure 4.8 (a) shows the percentage of flexural deflection with respect to the amount of vertical

reinforcement for Walls 5, 4, and 2 with vertical reinforcement ratios of 0.3%, 0.78%, and 1.3%, respectively. The figure shows that the flexural displacement contribution as a percent of the total top displacement decreased with increased vertical reinforcement. This decrease may be explained by increasing amount of vertical reinforcement tending to increase the flexural stiffness of the wall. Also the flexural capacity increases with increases in amount of vertical reinforcement. Higher capacities for the walls imply higher shear forces which will increase the shear deformation.

An increase in the relative flexural deformations with increased applied axial stress can be seen in Fig. 4.8 (b), for Walls 2, 6, and 7 subjected to axial compressive stresses of 0.00 MPa, 0.75 MPa, and 1.50 MPa, respectively. This relative increase may be explained by the applied axial stress enhancing the shear resistance and the shear stiffness of the wall which reduces the shear component of the total deflection.

(a) Effect of steel ratio   (b) Effect of axial compression stress
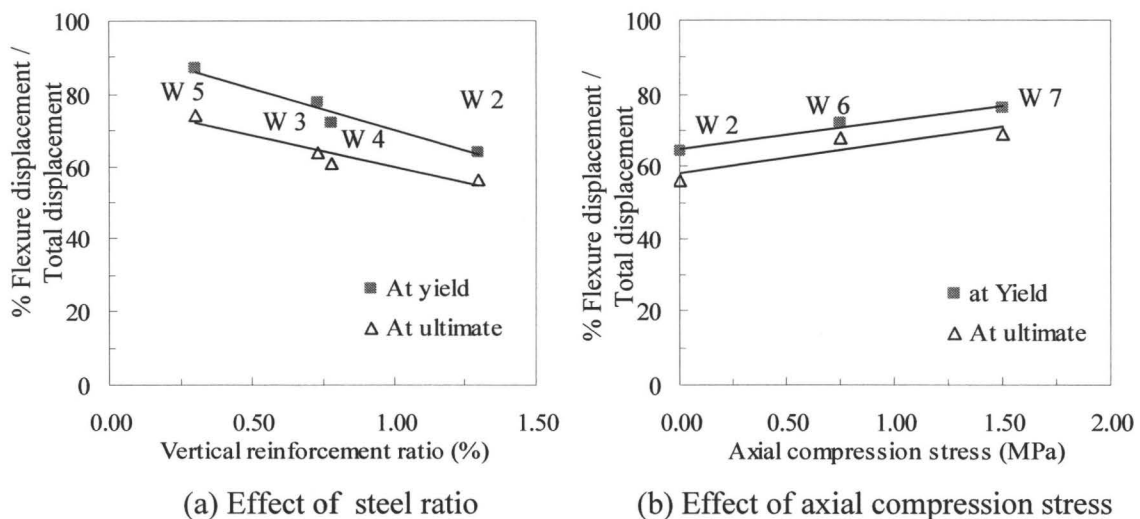
Fig. 4. 8: Effect of steel ratio and axial compression stress on flexural deformation

Based on the method suggested by Massone and Wallace (2004), the flexural component of the total deflection, reported in Table 4.5, were calculated by multiplying the percentage of flexural contribution reported in Table 4.4 by the measured total deflections at first yield and at ultimate load reported in Table 4.3. The predictions of the flexural deflections at first yield and at ultimate load are also included in Table 4.5. The contribution of the vertical reinforcement in compression is neglected in Prediction 1 and included in Prediction 2. Another approach based on integration of the curvature profile along the wall height was used to evaluate the flexural deflections for the walls at first yield and at ultimate load. The results from this latter approach are also presented in Table 4.5.

Table 4. 5: Comparison between measured and predicted flexural deflections

		Flexure deflections (mm)						Avg. Flexural/ Total (%)
		W2	W3	W4	W5	W6	W7	
At first yield	Decoupling[*]	9.6	8.3	7.9	6.1	11.7	13.1	75
	Prediction 1[**]	9.16	8.5	8.5	7.7	9.6	---	77
	Prediction 2[***]	8.9	8.4	8.4	7.6	9.3	12.3	75
	Curvature profile	9.6	7.4	7.6	5.6	9.1	11.9	68
At ultimate load	Decoupling[*]	16.8	14.2	20.1	23.7	17.0	20.7	65
	Prediction 1[**]	14.7	18.9	18.1	33.0	13.7	13.4	64
	Prediction 2[***]	16.5	21.9	20.0	37.1	15.3	15.4	73
	Curvature profile	24.3	20.9	24.2	27.3	---[*v]	21.5	76

[*] These values were based on the decoupling method suggested by Massone and Wallace (2004).

[**] These values were predicted when vertical compression reinforcement was neglected.

[***] These values were predicted when vertical compression reinforcement was included.

[*v] No value calculated due to loss of instrumentation measuring vertical deformations at ultimate load.

It can be seen from the table that predictions of the flexural deflection at first yield are consistent with the experimental results after decoupling and with the deflection resulting from the average curvature profiles (within 1 mm difference which can be due to the accuracy of measurements). Larger differences at ultimate load can be seen between the flexural deflection predictions and the experimental results. The larger deflections calculated from the experimental results can be explained based on the inelastic deformations at ultimate load where the plastic hinge length significantly affects the deflections.

The predictions of flexural deflections when compression reinforcement is included (Prediction 2 in Table 4.5) are lower than the predictions of flexural deflections when neglecting the compression reinforcement (Prediction 1 in Table 4.5) at first yield while the opposite is observed at ultimate load. It is obvious that including compression reinforcement in the strength calculation will reduce the length of the compression zone. At first yield, having the strain in the outermost vertical reinforcement equal to the yield strain, the reduced compression zone length will reduce curvature which will in turn reduce the flexural deflection at first yield. At ultimate load, having the strain at the extreme masonry compression fibres equal to the maximum compressive strain, the reduced compression zone length will cause an increase in the curvature which will in turn increase the flexural deflection.

The calculated flexural deflections from the measured average curvature profiles along the wall height are considered to be the most accurate measure of

flexural deflections at ultimate load based on the following discussion. The other predicted deflections at ultimate load reported in Table 4.3 were based on using a constant value of the equivalent plastic hinge length equal to half the wall length, as suggested by the IBC (2000), over which a constant plastic curvature acts. Using a constant equivalent plastic hinge length, however, turned out to be inconsistent with the test results. The measured values for plastic hinge length for all test walls will be presented later in Section 4.8.

The decoupling method used was based on having the centre of rotation for the walls located at one third of the wall height from the base as was suggested by Massone and Wallace (2004). This can result in an accurate estimation for deflections up to first yield. However, after extensive yielding of reinforcement, inelastic deformations in the masonry and, elongation of the vertical reinforcement in the base beam of the wall, the curvature at the base of the walls becomes very high. The distribution of curvature over the wall height can no longer be approximated as being triangular with the resultant rotation located at the one third height of the wall. Due to the sensitivity of the decoupling method to the location of the resultant rotation of the walls, it can be seen that lowering the location of the resultant rotation of the walls at the inelastic loading stages may result in better estimations of the flexural deflections.

Although the decoupling method underestimated the flexural deflections at ultimate load, it still gave reasonable results taking into account the accuracy of the measurement instrumentations. Based on the decoupling method and the

average curvature profiles, it can be seen that the average flexural deflections for the test walls (with aspect ratio of 2) can be considered to range between 68% and 76% (averaging about 72%) of the total deflection.

Based on the decoupling results, the shear deformations appeared to be significant. The percentages of shear deformation, presented in Table 4.6, were calculated from the experimental results at selected deflection levels presented in term of percent drift. Calculations were based on the suggested method for decoupling of the total deformation. It can be seen from the table that the average amount of shear deformation account for 19% and 38% of the total deflection at 0.2% and 1% drift, respectively.

Table 4. 6: Calculated shear deflection as a percent of the total measured deflections

Drift	Shear deflection* / Total deflection (%)						
	W2	W3	W4	W5	W6	W7	Avg.
0.2 %	25	17	24	14	22	12	19%
0.5 %	38	31	32	21	28	24	29%
1.0 %	46	45	41	28	35	33	38%

* These values are based on the method suggested by Massone and Wallace (2004)

Equation 4.5 is used to calculate shear deformation for a cantilever member subjected to a point load at the top. Given that the shear deformation can be calculated from the previous table, the effective area, A_e, in the following equation can be calculated for an assumed value of the shear modulus, G_m. For ease of reference, the value of the effective shear area will be calculated with respect to the gross area of the walls (i.e: 1800 mm x 190 mm). The effective areas calculated at different drift values are presented in Table 4.7 and shown in Fig. 4.9.

$$\Delta_{shear} = \left(\frac{1.2 \, V.h}{G_m \, A_e} \right)$$ Eq.4. 5

where: V   = Lateral load

A_e = Effective area resisting shear.

G_m = 0.4 E_m for rectangular sections.

h   = Wall height

Table 4. 7: Calculated effective shear area as a percentage of the gross area

Drift	A_e^* / A_g (%)					
	W2	W3	W4	W5	W6	W7
0.2 %	25.3	28.7	20.8	23.1	31.6	49.9
0.5 %	11.7	10.4	9.8	8.5	15.4	24.9
1.0 %	5.2	3.5	4.3	3.4	6.6	11.0

*These values are based on the method suggested by Massone and Wallace (2004)

(a) Effect of steel ratio   (b) Effect of axial compression stress
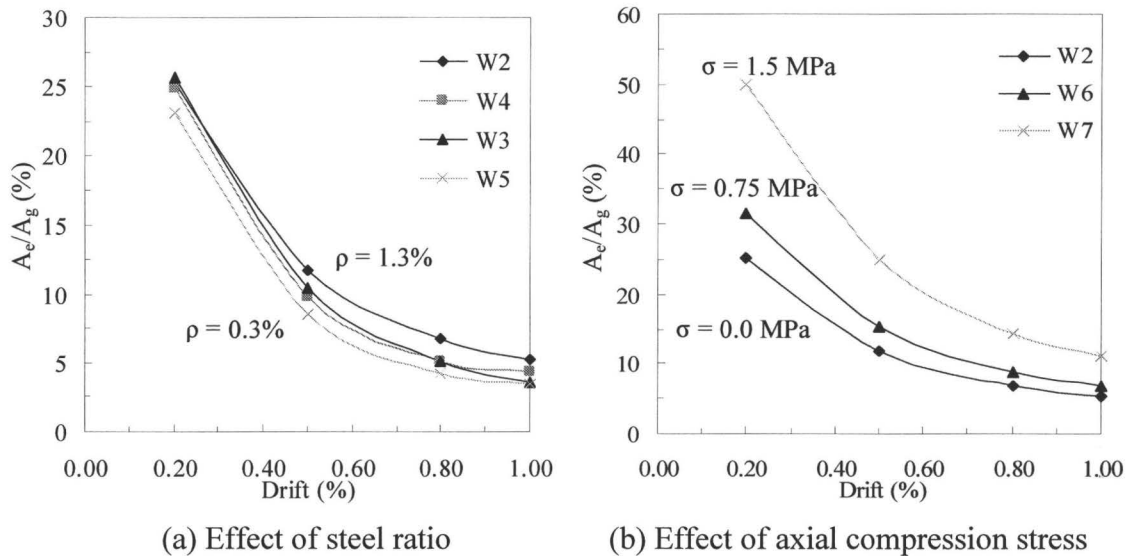
Fig. 4. 9: Effect of steel ratio and axial compression stress on effective shear area

From Fig. 4.9 (a), it can be seen that, as expected, the effective shear area along the wall height decreases significantly with increased top deflection. This is due to the extent of stepped and diagonal cracking over the whole height of walls not subjected to axial stress and, also, to softening of the masonry where G_m is no

longer 0.4 times the original elastic modulus. As shown in Fig. 4.9 (b), axial compression is effective in enhancing the effective shear area, which is consistent with the enhanced shear strength of walls subjected to axial stress.

From an elastic cracked section analysis performed for the test walls, the areas of the uncracked zones of the walls are presented in Table 4.8 as percentages of the gross area of the wall. It can be seen that values of effective shear area calculated in Table 4.7 based on the suggested method at 0.2% drift (also reported in Table 4.8), are close to the uncracked areas estimated from the cracked section analysis (within 20%).

Table 4. 8: Calculated cracked area as a percentage of the gross section area

	A_{cr} / A_g (%)					
	W2	W3	W4	W5	W6	W7
Elastic analysis[*]	27.4	22.7	23.3	16.4	30.1	31.5
0.2 % drift	25.3	28.7	20.8	23.1	31.6	49.9

[*]These values are based on elastic cracked section analysis accounting for axial load

Not withstanding that the effects of dowels and of aggregate interlock forces are neglected in resisting the shear, and a cracked section is assumed for the whole height of the wall, the uncracked masonry area calculated from elastic analysis can give a good estimate of the effective shear area at low drift levels.

4.6   Displacement ductility

Displacement ductility, μ_Δ, is used to calculate the force modification factor and is considered as a measure of the ability of the member to deform after yielding of the tension reinforcement. The displacement ductility is currently defined as the

ratio between the top deflection at ultimate load and the deflection at initial yielding of the outermost tension reinforcing bar in the wall. Alternatively, another measure of ductility could be determined corresponding to deflection at the condition when 20% strength degradation has occurred. The predicted and the measured values of displacement ductility at ultimate load and the measured displacement ductility at 20% degradation in strength are presented in Table 4.9, along with the corresponding drift levels. Displacement ductility corresponding to 1% drift is also included in the same table.

Table 4. 9: Predicted and measured displacement ductility

	Predicted[*]	Measured displacement ductility for Push direction (displacement ductility for Pull direction)				
	At max load	At max load		At 1% Drift	At 20% degradation	
		μ_Δ	Drift (%)		μ_Δ	Drift (%)
W2	1.85	2.0 (2.0)	0.83 (0.83)	2.4	4.0 (3.5)	1.67 (1.46)
W3	2.62	2.2 (2.5)	0.68 (0.78)	3.3	4.2 (4.0)	1.27 (1.21)
W4	2.37	3.0 (3.0)	0.92 (0.92)	3.3	4.8 (6.2)	1.47 (1.89)
W5	4.83	4.6 (4.2)	0.89 (0.89)	5.1	11.0 (11.3)	2.14 (2.20)
W6	1.64	1.6 (2.1)	0.69 (0.90)	2.3	2.8 (2.8)	1.26 (1.26)
W7	1.15	1.8 (1.8)	0.83 (0.94)	2.1	3.0 (3.6)	1.43 (1.70)

[*]Details of calculation to predict ductility are presented in Appendix F.

It can be seen from the table that values of displacement ductility corresponding to 20% strength degradation for Walls 2, 4, 5, and 7 are at high drift levels (near 1.5%) which can lead to stability issues and other P-Δ effect. (IBC (2000) limits the useful drift level to 1%.) In order to conduct an objective

comparison between displacement ductilities for the test walls, the displacement ductilities at maximum load (Fig. 4.10) and at a drift limit of 1% (Fig. 4.11) are used.

As seen in Figs. 4.10 (a) and (b), the displacement ductility tends to decrease with increase of vertical reinforcement. When the vertical reinforcement ratio increased from 0.3% to 1.3%, the displacement ductilities, calculated at maximum load and at 1% drift, decreased to less than 50%, as indicated from the test results corresponding to Walls 5 and 2, respectively. From Figs. 4.10 (a) and 4.11 (a), it can be inferred that displacement ductility is highly dependent on the amount of vertical reinforcement. This can be explained by looking at the yield displacements of the walls which are highly dependent on the amount of reinforcement, as discussed in Section 4.5, whereas, the displacements at ultimate load for all walls were similar.

The displacement ductility of Wall 4, having the same amount but more closely spaced vertical reinforcement (bar every cell) compared to Wall 3 (bar every other cell), is greater than the displacement ductility of Wall 3. This can be explained by the observation that Wall 3 experienced more sliding than Wall 4, as explained in Section 3.4.2 in discussion of Fig. 3.28, where a continuous crack was formed between the base beam and Wall 3. The recorded base slip for Wall 3 during the push loading cycle at ultimate load and at 4 times the yield displacement were 0.1 mm and 0.2 mm, respectively, compared to 0.8 mm and 2.8 mm, respectively, for Wall 4 at the same displacement levels. Sliding displacements associated with significant yielding may be responsible for reduction of ductility as addressed by Paulay et al. (1982).

(a) Effect of steel ratio

(b) Effect of axial compression stress
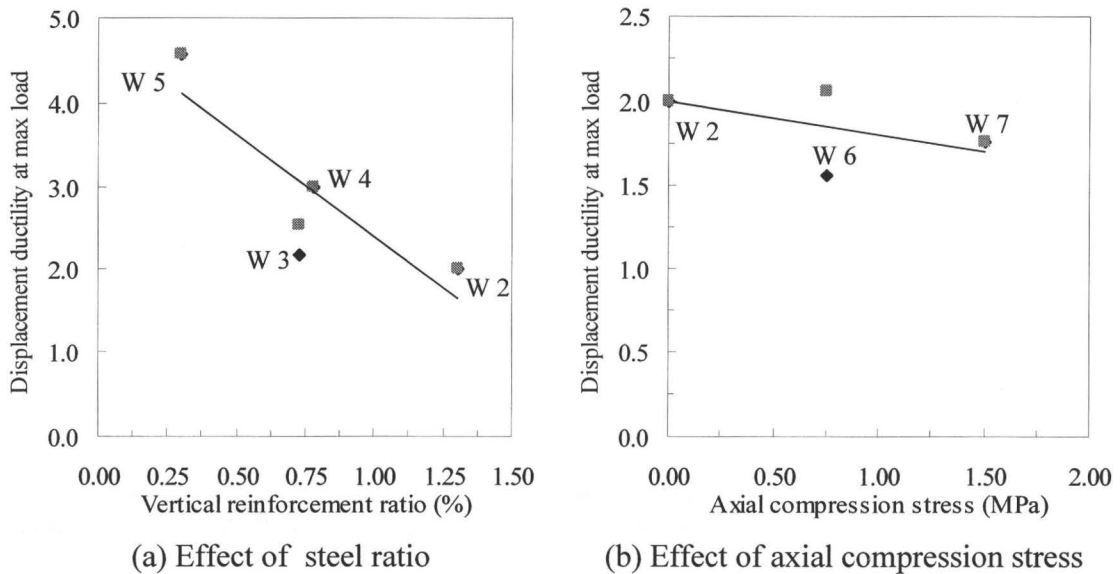
Fig. 4. 10: Effect of steel ratio and axial stress on displacement ductility at maximum load

(a) Effect of steel ratio

(b) Effect of axial compression stress
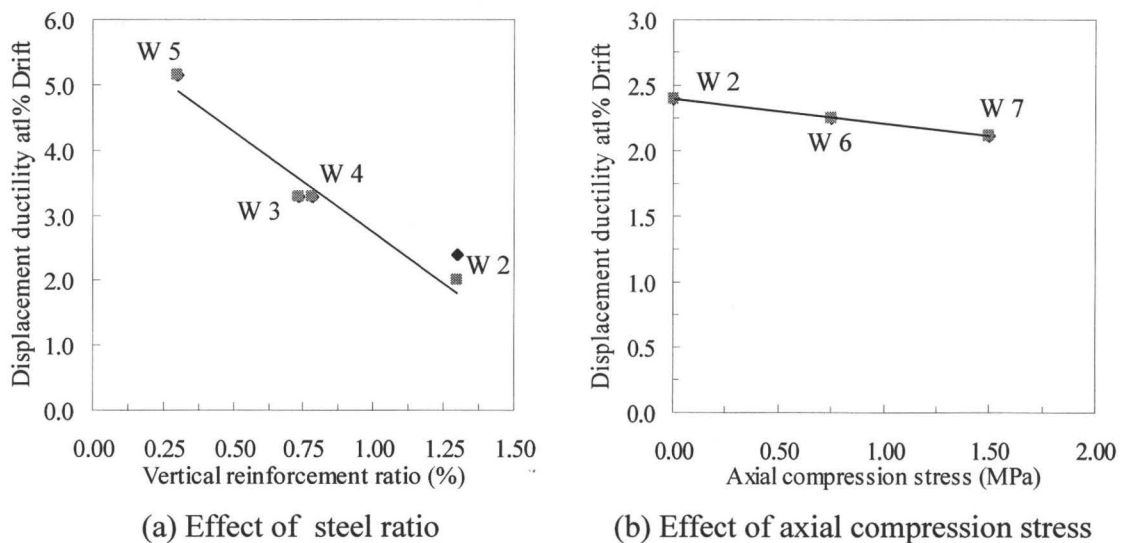
Fig. 4. 11: Effect of steel ratio and axial stress on displacement ductility at 1% drift

The test results presented in Fig. 4.10 (b) and 4.11 (b), show that the displacement ductility decreases slightly with increases in applied axial compression stress. When applied axial stress increased from 0.0 to 1.5 MPa, the displacement ductility, calculated at maximum load and at 1% drift, decreased by 12%, as indicated from the test results for Walls 2 and 7, respectively. As presented in

Section 4.5, the increase of the applied axial compression stress corresponds to a slight increase in the displacements at yield and, given that the displacements at ultimate for all walls are similar, it can be seen that the displacement ductility is slightly dependent on the applied axial stress at relatively low axial stress.

4.7   Energy dissipation

Energy dissipation is an important aspect in seismic design since it reduces the amplitude of the seismic response and, thereby, reduce the ductility and strength demands of the structure.

The envelope of the load-displacement hysteresis loops is insensitive to the imposed displacement increments and to the number of cycles (Jamison (1997)). Given that the displacement history is not identical for all walls as every wall was cycled at multiples of its initial yield displacement, comparing the energy dissipated with respect to a single hysteresis loop at a particular drift level cannot be used as a basis for comparison between walls. Therefore, the energy dissipation will be represented, as suggested by Seible and Hose (2000), by the area enclosed within the inelastic force-displacement curve at each displacement cycle as shown in Fig. 4.12.

The energy dissipation at different displacement levels during the tests of all walls is presented in Fig. 4.13. The figure shows that, as expected, for low displacement levels, the energy dissipation was low which characterized the loading stages before yielding. For higher displacement levels, the energy dissipation increased significantly for different walls with respect to early stages of loading.
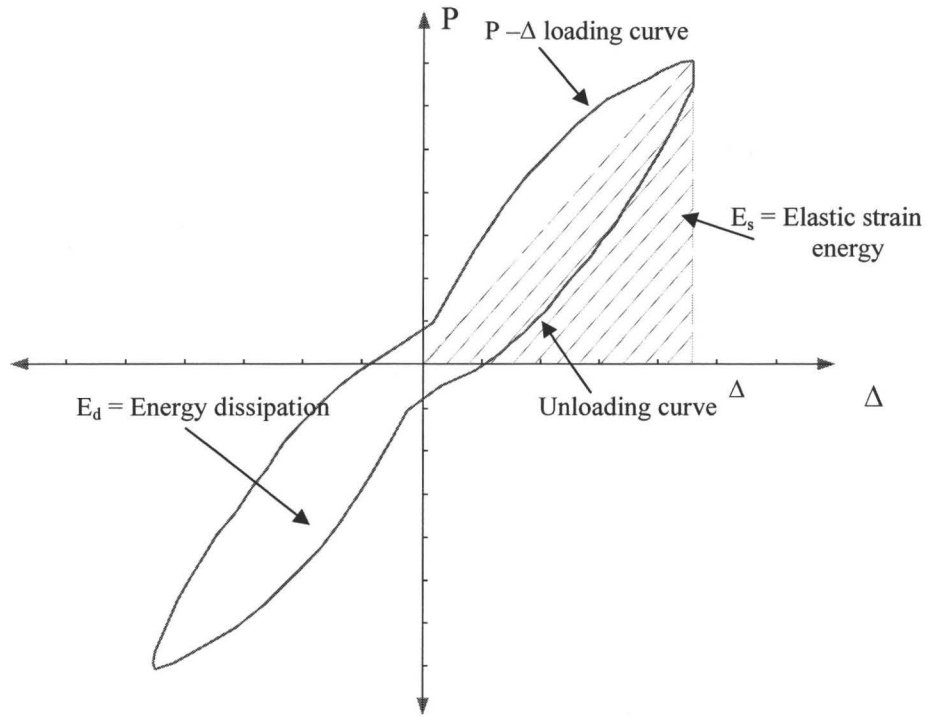
Fig. 4. 12: Calculation of energy dissipation
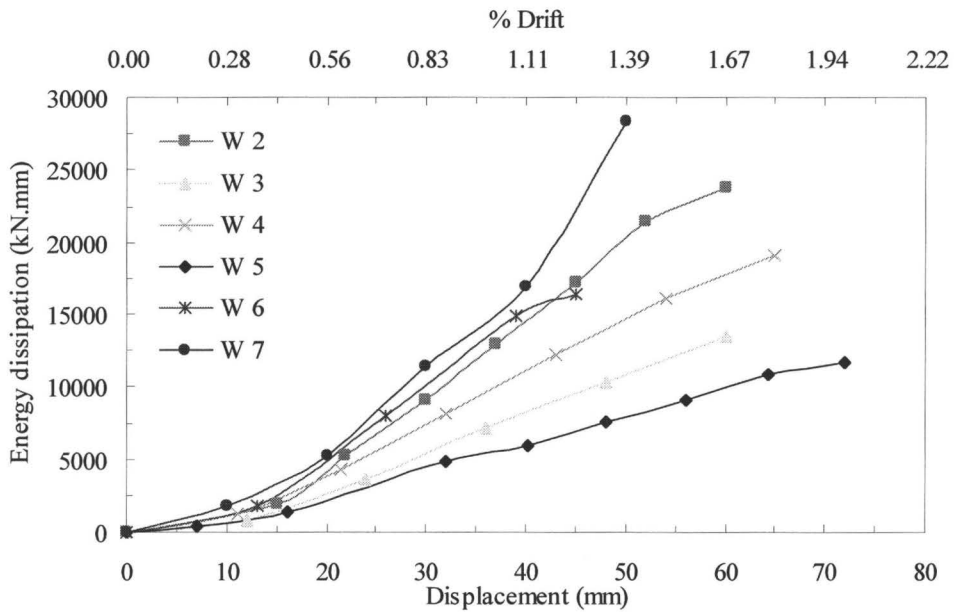
Fig. 4. 13: Energy dissipation for the test walls

The energy dissipation at selected drift levels is presented in Table 4.10 and

plotted in Fig. 4.14. It can be seen that a significant increase in the energy dissipation

occurs in reinforced masonry shear walls at high drift levels. The energy dissipation

for most walls at 1.0% drift was about three times the energy dissipation at 0.5%

drift. At 1.5% drift, this ratio ranged between 4.8 and 6.6 times. No values for energy

dissipation corresponding to 1.5% drift are presented for Walls 6 and 7 as these walls

failed before reaching this drift level. These significant increases are mainly due to

cracking and other inelastic deformations in the masonry at high displacement levels.

Table 4. 10: Energy dissipated corresponding to drift level

	Energy dissipation (kN.mm)		
	0.5% drift	1.0% drift	1.5% drift
W 2	3317	12381	22107
W 3	2220	7175	11906
W 4	3195	9590	16164
W 5	1811	5325	8747
W 6	4133	13243	---[*]
W 7	4496	14716	---[*]

[*] These values are not indicated as Walls 6 and 7 failed at drift level lower than 1.5%
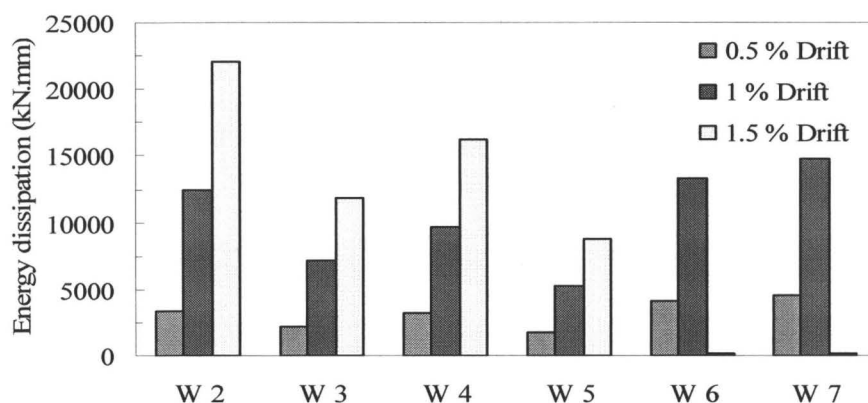
Fig. 4. 14: Energy dissipation for the test walls at different drift levels

The normalized energy dissipation values for all walls were plotted against

the corresponding displacement ductilities in Fig. 4.15. The normalized energy

dissipation for a wall at any displacement level is defined as the ratio between the

energy dissipation at this displacement level and the energy dissipation at first yield. Energy dissipation was normalized for individual walls to monitor the trend of increase of energy dissipation after yielding and to eliminate the effects of different wall capacities and displacement capabilities. Figure 4.15 shows that the relationship between the normalized energy and the measured displacement ductility can be given by Eq. 4.6 which was the best fit of a linear equation to the data presented.
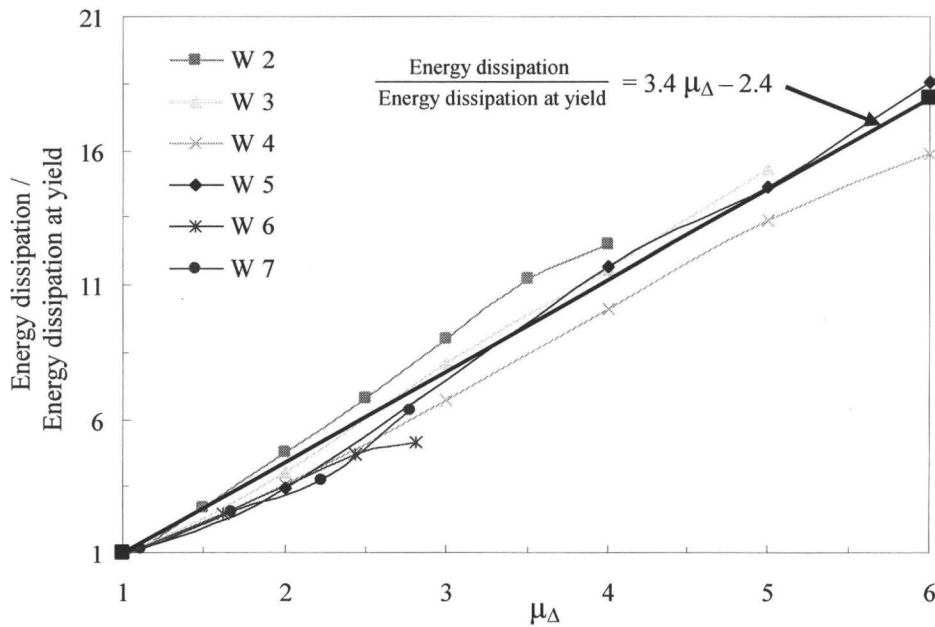
Fig. 4. 15: Normalized energy dissipation for the test walls

$$E_i / E_y = 3.4 \, \mu_\Delta - 2.4 \qquad \text{Eq.4. 6}$$

where: E_i = Energy dissipation at displacement level (i)
E_y = Energy dissipation at yield displacement
μ_Δ = Displacement ductility corresponding to displacement at level (i)

Equivalent viscous hysteretic damping can be described by the equivalent viscous damping ratio, ξ_{eq}, which is based on an equal area approach that represents the same amount of energy loss per cycle (Chopra (1995), and Seible and Hose

(2000)). The method used for calculating the equivalent viscous damping was shown previously in Fig. 4.12, where the area within the inelastic force-displacement response curve, E_d, is a measure of the hysteretic damping or the energy dissipation capacity of the structure. Alternatively, the hatched region, E_s, represents the elastic strain energy stored in an equivalent linear elastic system. The ratio between the dissipated energy and the stored strain energy affects the equivalent viscous damping ratio, ξ_{eq}, which is calculated using Eq. 4.7 (Chopra (1995), and Seible and Hose (2000)).

$$\xi_{eq} = \frac{1}{4\pi} \times \left(\frac{E_d}{E_s} \right) \qquad\qquad \text{Eq.4. 7}$$

The equivalent viscous damping ratio, ξ_{eq}, is plotted against the displacement ductility, μ_Δ, in Fig. 4.16 (a) and against the lateral displacement (and % drift) in Fig. 4.16 (b) for all test walls. Both figures indicate an increase in the equivalent viscous damping ratio, ξ_{eq}. As shown in Fig. 4.16 (a), the equivalent viscous damping ratio at initial yield (μ_Δ=1) varies between 8% and 10%, whereas, this ratio at two times the yield displacement varies between 15% and 17%. This indicates that reinforced concrete masonry shear walls have high damping after initial yielding which may result in decreased seismic demand.

It is commonly assumed that reinforced masonry walls have damping ranging between 7% and 10% (Paulay and Priestley (1992)). However; increasing the damping ratio for reinforced masonry shear walls can result in decreasing the design forces. At 1% drift, as shown in Fig. 4.16 (b), the equivalent viscous damping

ratio varies between 15% and 20% for all test walls. The increase in the drift level from 0.3% to 1% results in increasing the equivalent viscous damping ratio from about 10% to about 18%, which again indicates that reinforced masonry shear walls can exhibit high damping.
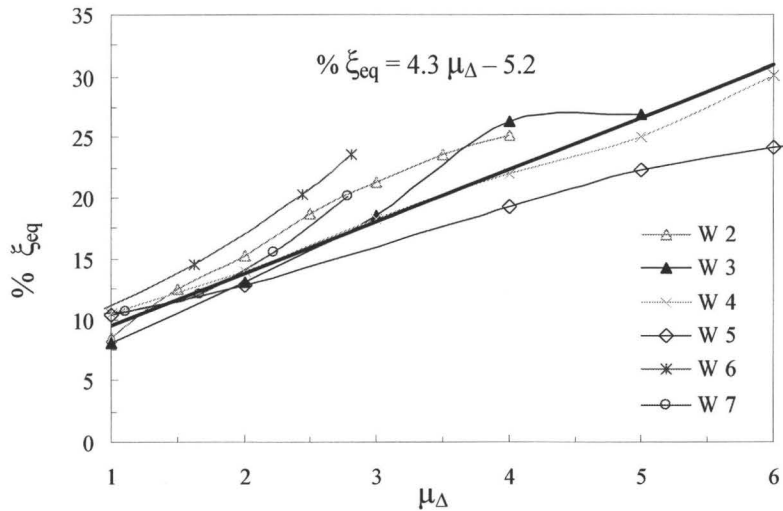
(a) Equivalent viscous damping ratio with respect to displacement ductility
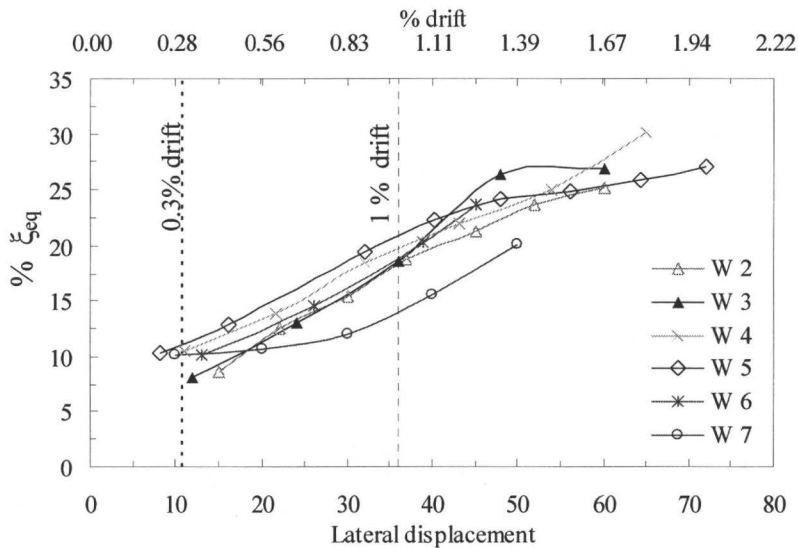
(b) Equivalent viscous damping ratio with respect to lateral displacement

Fig. 4. 16: Equivalent viscous damping ratio

Figure 4.16 (a) shows that the relationship between the equivalent viscous damping ratio and the measured displacement ductility can be given by Eq. 4.8.

$$\% \; \xi_{eq} = 4.3 \; \mu_{\Delta} + 5.2 \qquad\qquad\qquad \text{Eq.4. 8}$$

where: ξ_{eq} = Equivalent viscous damping ratio (%)
μ_{Δ} = Displacement ductility

This fitted equation shows that the hysteresis damping increases with increase of the displacement ductility of the walls, which means that a different value for the damping ratio should be assigned to structures expected to exhibit higher deflection. This would apply to cases when a performance based approach was used for the design. Although the equivalent viscous damping should be defined for the structure, this equation may give some indication of the general response of masonry structures that are usually constructed with symmetrical walls connected by rigid diaphragms.

4.8   Plastic hinge length and extent of plasticity

Plastic hinge length is an important factor in determining the inelastic response of shear walls subjected to earthquake loading since it influences the displacements at ultimate load and, consequently, affects the displacement ductility.

The extent of plasticity was estimated from the average curvature profiles along the wall heights, presented in Chapter 3 for the six test walls. Plasticity zones are the heights above the base beam where average curvatures higher than the yield curvatures were recorded. These lengths, observed from the average curvature profiles, were then compared to lengths above the base beam where deflection measurements revealed relatively large curvatures. The observed lateral

deflection profiles over the wall heights indicated relatively small curvatures in the upper parts of the walls. Strain gauges readings on the outermost bars were also used to verify the estimated plasticity length and indicated that, for all walls, yielding of the outermost bars was recorded up to 900 mm above the base beam. The extent of plasticity estimated from the experimental results is presented in Table 4.11.

Table 4. 11: Height of plasticity zone

Wall (reinforcement) [axial stress]	Extent of plasticity (mm)					
	W 2 (9#25) [0 MPa]	W 3 (5#25) [0 MPa]	W 4 (9#20) [0 MPa]	W 5 (5#15) [0 MPa]	W 6 (9#25) [0.75 MPa]	W 7 (9#25) [1.5 MPa]
Measured 1[*]	900	900	1000	1500	800	800
L_p / l_w	0.50	0.50	0.56	0.83	0.47	0.44
Measured 2[**]	700	800	800	1100	700	700

[*] Extent of plasticity estimated from the curvature profile for each wall, see Chapter 3.
[**] Extent of plasticity estimated from the deflection profile for each wall, see Chapter 3.

The test results indicate that the extent of plasticity, L_p, for all walls varies between 44% and 83% of the wall length, l_w, as indicated in Table 4.11. It can be seen from Table 4.11 that extent of plasticity may tend to increase slightly with smaller bar sizes as seen for Walls 3 and 4 having similar amounts but different distribution of vertical reinforcement. However, the difference is small considering the use of average curvature over relatively large increments of wall height. The measured heights tended to decrease with increase in the amount of vertical reinforcement as shown in Fig. 4.17 (a). The applied axial stress on the walls did not have a very significant effect on the extent of plasticity as shown in

Fig. 4.17 (b). The test results indicate that Wall 3, having almost the same amount of reinforcement as Wall 4, had a shorter plasticity height than Wall 4 which can explain the observation of having less displacement ductility and energy dissipation compared to Wall 4 as indicated in Sections 4.6 and 4.7, respectively. It can be seen from the test results that the extent of plasticity is not the same for all walls having the same aspect ratio and dimensions.

(a) Effect of steel ratio   (b) Effect of axial compression stress
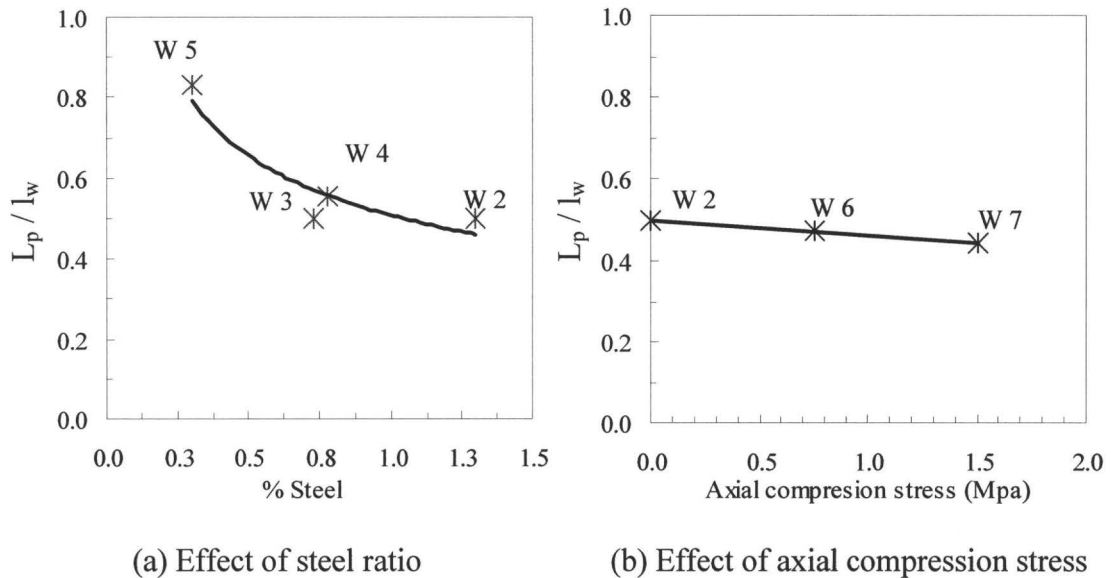
Fig. 4. 17: Effect of steel ratio and axial stress on the extent of plasticity

Equivalent plastic hinge lengths based on experimental data from this study were calculated by rearranging Eq. 1.1 to solve for the equivalent plastic hinge length, l_p. The ultimate displacement is defined as the total displacement at 1% drift, $\Delta_{1\% \text{ drift}}$, (which is close to maximum load, Q_{max}), in order to establish a common basis for the comparison. Yield curvature, φ'_y, based on Paulay and Priestley (1992), is defined as the curvature at which the yield displacement, Δ'_y ("ideal yield"), takes place on the elasto-plastic approximation diagram of load-

displacement, as shown in Fig. 4.18. This adjustment is made as the idealized yield curvature does not necessarily coincide with first yield of tensile reinforcement, where first yield will likely occur at smaller curvature than the idealized yield curvature (Paulay and Priestley (1992)). The displacement ductility is defined as the ratio of deformation at a given response level to the deformation at the idealized yield point (Priestley et al. (1996)).

$$(\mu'_\Delta \quad = 1 + 3 \ (\mu'_\varphi - 1) \ (l_p / h_w) \ (1 - 0.5 \ l_p / h_w) \qquad Eq. \ 1.1)$$
$$where: \ \mu'_\Delta \quad = \Delta_{1\% \, drift} / \Delta'_y$$
$$\mu'_\varphi \quad = \varphi_{1\% \, drift} / \varphi'_y$$
$$\Delta'_y \quad = \Delta_y \ P_y' / P_y \ and \ \varphi'_y = \varphi_y \ P_y' / P_y$$
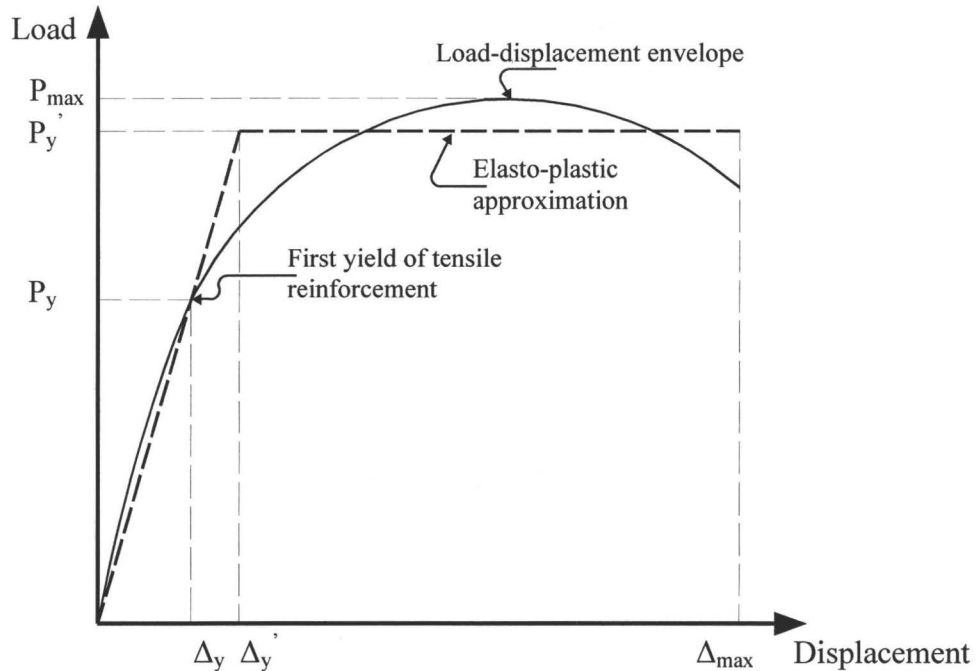
Fig. 4. 18: Elasto-plastic approximation of the load-displacement envelope

The yield displacement of the elasto-plastic approximation is defined as the intersection of the secant stiffness through the first yield displacement with the yield force, P_y', of the elasto-plastic approximation (see Fig. 4.18). The yield

force of the elasto-plastic approximation was found by matching the area under the actual load-displacement envelope to that of the elasto-plastic approximation using the Trapezoidal Rule ((Eikanas (2003)).

The measured average curvatures after yielding were considerably larger than the calculated (predicted) curvatures which is consistent with the observations of Sasani and Kiureghian (2001). They indicated that the calculated compressive strain is considerably less than the measured strain which is also indicated by most of the strain profile diagrams along the length of the test walls as presented in Chapter 3. The measured curvature ductility for all walls at 1% drift, which is the ratio between the average curvature at 1% drift and the average curvature at initial yield over the bottom 100 mm of the wall, ranged between 6.9 and 10.0, whereas, the theoretically calculated (predicted) curvature ductility at ultimate load (close to 1% drift) ranged between 1.2 to 6.8 (see Appendix F). The significant differences between measured and predicted values can be explained as the theoretically predicted values result from flexural deformations, whereas, the measured values account for flexural deformations plus elongation and debonding of the vertical bars in the base which can cause rotation at the base of the wall resulting in increases in average curvature over the bottom 100 mm.

The high actual curvature ductility (presented in Table 4.12), compared to estimated values (presented in Appendix F), result in a significantly reduced the calculated equivalent plastic hinge length for the same displacement ductility level. Given that the displacement ductility is related to the product of the

curvature ductility and the equivalent plastic hinge length, increasing the curvature will in turn reduce the equivalent plastic hinge length over which this curvature must occur in order to achieve a specific displacement ductility. Obviously, the use of theoretically predicted curvatures would require larger equivalent plastic hinge lengths to match the measured displacements. The exception is Wall 7 which had reinforcement with very high yield strength.

Table 4. 12: Calculated equivalent plastic hinge length

Wall (reinforcement) [axial stress]	W 2 (9#25) [0 MPa]	W 3 (5#25) [0 MPa]	W 4 (9#20) [0 MPa]	W 5 (5#15) [0 MPa]	W 6 (9#25) [0.75 MPa]	W 7 (9#25) [1.5 MPa]
Δ_y	15.00	11.00	11.00	7.00	16.00	17.00
$\Delta'_y{}^*$	19.95	14.59	15.25	10.09	22.05	24.02
$\Delta_{1\%drift}$	36.00	36.00	36.00	36.00	36.00	36.00
$\mu'_\Delta = \Delta_{1\%drift} / \Delta'_y$	1.80	2.47	2.36	3.57	1.63	1.50
$\varphi_{y\,(x\,10^{-6})}$	1.20	1.36	1.40	1.70	1.32	1.43
$\varphi'_{y\,(x\,10^{-6})}$	1.60	1.80	1.94	2.45	1.81	2.02
$\varphi_{1\%drift\,(x\,10^{-6})}$	11.98	12.57	13.6	10.7	--**	16.2
$\mu_\varphi{}^+ = \varphi_{1\%drift} / \varphi_y$	10.0	9.3	7.4	9.7	--**	6.9
$\mu'_\varphi{}^x = \varphi_{1\%drift} / \varphi'_y$	7.57	7.02	5.36	6.75	--**	4.92
$\Delta'_y / \Delta_y = \varphi'_y / \varphi_y$	1.33	1.33	1.39	1.44	1.37	1.41
$l_p{}^{***}$ (mm)	149	306	396	584	--**	156
l_p / l_w	0.08	0.17	0.22	0.22	--**	0.08
l_p (mm) (Eq. 1.2)	567.4	502.5	567.4	398	567.4	567.4
l_p (mm) (Eq. 1.3)	518.4	518.4	518.4	518.4	518.4	518.4

* Yield deflections from the elasto-plastic approximation (Paulay and Priestley (1992).
** Measurement loss for Wall 6 due to spalling of face shells, see Section 3.7.
*** Equivalent plastic hinge lengths were calculated by rearranging Eq.1.1 and using $\mu'_\varphi{}^x$.
+ Curvature ductility is the ratio of the measured curvatures at 1% drift and at first yield.
x Curvature ductility is the ratio of the measured curvatures at 1% drift and at ideal yield.

The values for displacement ductility and curvature ductility for all walls calculated from the elasto-plastic approximation and presented in Table 4.12, were used to calculate the equivalent plastic hinge lengths. Values calculated using Eqs. 1.2 and 1.3, reported in the literature review for estimating the equivalent plastic hinge length, are also included in Table 4.12. It can be seen that the yield curvatures from the elasto-plastic approximation are about 38% higher than the actual measured curvature at first yield. The difference is consistent with the findings of Paulay and Priestley (1992) who suggested an increase of 33% between the curvature at first yield of vertical bars and the curvature at yield from the elasto-plastic approximation.

From Table 4.12, it can be seen that Eq. 1.2 estimates the equivalent plastic hinge length depending on the bar size and neglects the effects of amount of vertical reinforcement and axial stress. However, test results showed that the equivalent plastic hinge length is different for Walls 2, 3, 6 and 7 with No. 25 bar used for vertical reinforcement. Equation 1.3 bases the equivalent plastic hinge length on aspect ratio and neglects the effect of size and amount of vertical reinforcement as well as the effect of axial stress. However, test results showed that the equivalent plastic hinge lengths are not similar for the same aspect ratio.

4.9   Summary

The effects of the amount of vertical reinforcement and the magnitude of the applied axial compression stress on some basic characteristics of shear walls

such as stiffness, strength, and ductility were documented in the chapter. Comparison between displacements predictions and experimental results were also presented. Energy dissipation through hysteretic behaviour was evaluated and the trend of its increase after yielding was highlighted. Plastic hinge length was estimated for all test walls and again the effects of the test parameters on its variation were discussed.

The following observations were the outcome from analysis of the test results:

1. The stiffnesses for all walls degrade rapidly to about 30 - 40% of the initial stiffness at very low displacement (drift) levels, whereas, less rapid decreases were observed at higher displacement levels. An empirical equation relating the variation of stiffness of the test walls with respect to wall drift was suggested.

2. Wall capacities are highly depended on the amount of vertical reinforcement as well as on the level of applied axial stress.

3. Displacement corresponding to initial yield of reinforcement is highly dependent on the amount of vertical reinforcement, whereas, it is less dependent on the magnitude of the applied axial stress.

4. Compared to initial yielding, the displacement corresponding to the maximum load tends to be less dependent on the amount of vertical steel and the applied axial stress.

5. Shear deformation should not be neglected for reinforced masonry walls having an aspect ratio of two. Further investigation should be conducted at other aspect ratios to quantify the contribution of shear deformation.

6. Displacement ductility is highly sensitive to increases in the amount of vertical reinforcement while it is less dependent on the applied axial stress.

7. Energy dissipation through hysteresis damping increase significantly after initial yielding occurs. Results indicated that reinforced masonry shear walls exhibit high damping.

8. The extent of plasticity in the test walls ranged between 44% and 83% of the wall length. It tends to decrease with increase of the amount of vertical reinforcement while it is almost the same for different levels of applied axial stress.

9. Higher curvatures than theoretically predicted at the base are to be expected for reinforced masonry walls subjected to cyclic loading. These high values are due to debonding of the vertical reinforcement at the base level and additional rotation between the wall and the base beam.

CHAPTER 5

CONCLUSIONS

5.1   Summary

The principal objectives of this study were to experimentally evaluate the behaviour and ductility of reinforced concrete masonry shear walls under cyclic loading. The inelastic response and the post-peak behaviour of masonry shear walls were investigated to examine the possibilities of achieving high levels of ductility and energy dissipation by flexural yielding. The study focused on investigating the effect of amount and distribution of vertical reinforcement and the effect of the applied axial load on the ductility of the walls and on the length of the plastic hinge.

The main experimental program included testing six reinforced concrete masonry shear walls, with aspect ratio of two, under cyclic loading up to failure. The walls had variable amounts of vertical reinforcement as well as different distributions and were subjected to different levels of axial load.

Test results included recording of visual behaviour, loads, displacements, and reinforcement strains. Visual observations were made throughout the tests. Load-Displacement hysteresis plots were developed, on which locations of various limit states were identified. Displacement ductilities were calculated, and plots of average curvatures and deflection profiles along the wall height were developed.

Analyses of the test results were performed to evaluate the effects of amount of reinforcement and the applied axial load on the behaviour of reinforced masonry shear walls. Dissipated energy as well as displacement ductilites were quantified. Plots of curvature calculations were used to identify the plastic hinge length. The calculated equivalent plastic hinge lengths were compared to various predictions found in the literature.

5.2   Conclusions

5.2.1 Grouting

The use of additives and plasticizers, in order to achieve high workability of the grout, by may be, in part, a reason for poor filling of some walls especially when the grouting operation was conducted in stages as for Walls 1 and 3. Although the additives and the plasticizers created a fluid grout, quick hardening occurred after some water was absorbed by the concrete blocks. The use of grout aids and self-consolidating grouts may be a worthwhile area for more research.

The use of splitter units at the ends of the walls (having smaller cells than the stretcher units) is common practice to create half blocks for running bond and to create a flat end on the wall. The significantly reduced size of the cell made it more difficult to achieve complete filling. Also, the presence of hairpin shaped hooks at the ends of the horizontal reinforcement extended over the ends of the walls, and the use of large sizes of vertical reinforcements (No. 25 bars used in Walls 1 and 3) contributed to the incomplete filling of these walls. Dismantling of

the walls showed that hardened mortar dropping over the hairpin shaped ends of the horizontal reinforcement contributed to the poor filling at the ends of the walls.

Filling the walls in one stage is recommended as it resulted in good filling of the cells for the 3.6m high walls. Otherwise, partially hardened grout adhering to the sides of the cells and to the vertical and horizontal reinforcement caused a reduction in the size of the opening for the subsequent grout lifts. Good cleaning of mortar dropping during construction especially at the ends of the walls is essential to achieving fully grouted cells. The repair technique used in filling the empty and partially filled cells was efficient as the repaired walls behaved almost symmetrically for loading in both directions. It is essential that injection of the grout starts from the lowest point of the unfilled zones and that filling is conducted in an upward direction with enough check points to verify the filling of the cells.

5.2.2 Masonry compressive strength

The results from the prism tests indicated some differences in the compressive strength of masonry. Although the overall dimensions of the prisms were similar, using different configurations led to different values for the compressive strength as shown from the results of the three different types of prisms tested (see Table 2.8). Also the use of splitter blocks at the ends of the walls and stretcher blocks elsewhere may result in different compressive strengths along the wall length. The results also showed that the presence of the knock-out

webs in the prisms affect the measured compressive strength. It is important to model the zone which is of interest in the wall (usually the toe under compression) by the appropriate configuration of prisms to have better estimates of the design compressive strength.

It is worth noting that the modulus of elasticity of the masonry, E_m, calculated from the prism tests, gradually changes even at relatively low stresses considered to be within or near the elastic range as shown in Appendix G. The use of a single value for E_m (= 850 f'_m) at any stage of loading (pre-cracked or cracked) will lead to inconsistent results especially when the modulus of elasticity is used for deflection or stiffness calculation.

5.2.3 Flexural strength and masonry strain

Measured flexural capacities for all walls were similar to the predicted capacities applying simple beam theory when neglecting compression reinforcement in strength calculation and assuming the masonry compressive strain equal to 0.003 at maximum load. Although toe crushing did not occur until well beyond the critical masonry compressive strain of 0.003, as indicated in Chapter 3 in the discussion of the strain profile along the wall length, the use of 0.003 as the maximum compressive strain for masonry resulted in good predictions of flexural strength. The higher than predicted masonry compressive strain at maximum load (which is consistent with the conclusion of Eikanas (2003)) resulted in increases in wall curvature and, therefore, increases in lateral deflection at maximum load.

It is worth noting that the predicted flexural strength for the test walls using maximum compression masonry strain of 0.003 results in a maximum increase of 5.2% (except for Wall 7) compared to calculations using a maximum masonry strain of 0.0025. This comparison is valid in the cases of including or not including compression reinforcement. Predicted capacities using maximum compression strain of 0.0025 and including compression reinforcement were higher but within 4.6% of the experimental results. Alternatively, using maximum compression strain of 0.003 and not including compression reinforcement gave predicted results that were lower but within 3.1% of the experimental results.

5.2.4 Extent of yielding of reinforcement

Strain gauges located on the outermost reinforcing bars indicated that yielding of the outermost vertical reinforcement extended for most walls to about 900 mm above the base beam regardless the amount or size of the vertical bars. The extent of yielding of vertical reinforcement inside the base beam was less than 300 mm, as presented in Chapter 3, with higher propagation of strain into the base for large sizes of reinforcement compared to smaller sizes. In comparing the extent of yielding, it should be remembered that the concrete and masonry compressive strengths were about 40 MPa and 15 MPa, respectively, as presented in Chapter 2. Even though the extent of yielding inside the base beam was not large, the overall effect of elongation of the reinforcement inside the base on increasing the deflection at maximum load was significant.

5.2.5 Average curvatures and curvature ductility

At yield displacement, the measured average curvatures, over the bottom 100 mm above the base beam, varied between 0.0012 rad/m to 0.0017 rad/m (about $0.0021/L_w$ and $0.0031/L_w$, respectively). At maximum load, these curvatures varied between 0.011 rad/m to 0.016 rad/m for all walls (about $0.020/L_w$ and $0.029/L_w$, respectively), as presented in Chapter 3 in the discussion on the average curvature profile. The resulting curvature ductility calculated from these measured values varied between 7 and 10; the predicted curvature ductility varied between 1.2 and 6.8 as presented in Table F.1 in Appendix F. The high measured curvature ductilities resulted in higher deflections at maximum load for the test walls and higher displacement ductilities than predicted. These high values are due to debonding of the vertical reinforcement at the base level and additional rotation between the wall and the base beam in addition to the flexural deformations.

5.2.6 Equivalent plastic hinge length

Equivalent plastic hinge length was calculated using the elasto-plastic approximation of the load-displacement envelope. Test results showed that the equivalent plastic hinge lengths, for a target displacement close to 1% drift, varied between 0.08 to 0.32 times the wall length. The observed equivalent plastic hinge lengths were lower than the values calculated from the equations suggested by Paulay and Priestley (1992). The idealized values of measured curvatures used in determining the equivalent plastic hinge length were not only due to flexural

deformation but also due to the effect of debonding of vertical reinforcement within the wall and the base beam. The resulting rotation of the bottom of the wall at the base level is related to the penetration of the yielding inside the base beam as presented in Chapter 3.

5.2.7 General wall response

The test results indicated that reinforced masonry shear walls (with aspect ratio of 2) characteristically had high ductility capacities and low strength degradation as shown from the load-displacement plots presented in Chapter 4. The hysteretic behaviour of all walls showed a stable wall response having relatively fat loops which provides high energy dissipation. The observed high displacement ductility and high energy dissipation indicate that reinforced masonry shear walls can be used in high seismic areas. Although this conclusion is based only on a limited number of experimental tests for walls with aspect ratio of 2, there is no reason not to expect similar performance for reinforced masonry shear walls designed to fail in flexure. More tests are required to confirm this expectation.

5.2.8 Displacements

Shear deformations should not be neglected in deflection predictions for reinforced masonry shear walls with aspect ratio of 2. Based on the test results, shear deformations contributed an average of 30% (as indicated in Section 4.5) of the total wall deflection.

5.3 Comments on application of this research

5.3.1 Ductility factor R_d

Using the same value for R_d for structures regardless of the height of the structure or its period of vibration may result in inaccurate estimation of the actual force modification factor of the structure. As presented earlier in Section 1.5.6, for different ranges of periods, different approaches should be used in estimating the force modification factor. For walls having "h / (t + 10) < 18", which is the case for the test walls, CSA S304.1 (2004) specifies a ductility modification factor R_d equal to 1.5, where "t" is the thickness of the wall. The calculated values for R_d with respect to a ductility level measured at 1% drift using the equal energy and equal displacement principles are presented in Table 5.1 along with the corresponding values given by CSA S304.1 (2004).

It can be seen from the results in Table 5.1 that the force modification factors, R_d, calculated at 1% drift for all the test walls are not similar. These results indicate that all walls having the same overall dimensions will not have the same value for R_d. Also, the R_d value will change with respect to the level of structural damage expected / accepted. Thus, for design of a structure for collapse prevention, a large amount of damage may be expected and be acceptable which may result in a higher value for R_d. Alternatively, designing a structure for a fully operational level of performance will imply a much lower value for R_d as much smaller deformations will be allowed.

Table 5. 1: Force modification factors

Wall	Measured μ_Δ at 1% drift	R_d		
		CSA S304.1 (2004)	Equal Energy[*]	Equal displacement[**]
W2	2.4	1.5	1.9	2.4
W3	3.3	1.5	2.4	3.3
W4	3.3	1.5	2.4	3.3
W5	5.1	1.5	3.0	5.1
W6	2.3	1.5	1.9	2.3
W7	2.1	1.5	1.8	2.1

[*]$R_d = \sqrt{2\mu_\Delta - 1}$

[**]$R_d = \mu_\Delta$

Conceptually, allowance for different damage levels can be achieved by establishing a period dependent R_d value for the different levels of performance expected from various structures. Different magnitudes of earthquake could be linked to probability of different levels of accepted damage and appropriate R_d values could beneficially be linked to the different periods associated with the various ranges of response.

5.3.2 Overstrength factor R_o

An additional strength reduction can be considered in the design of a structure to take into account the fact that the structures usually have a lateral load strength higher than the design strength. The over-strength modification factor can be due to rounding of sizes and dimensions, R_{size}, difference between nominal and factored resistance, R_φ, ratio of actual yield to minimum specified yield, R_y,

strength enhancement of the steel at large deformations due to strain hardening, R_{sh}, and development of sequential plastic hinges in redundant structures, R_{mech} (Harries (2004)).

The overstrength factor, R_o, is therefore calculated as the product of a number of overstrength factors, which should be evaluated independently for each particular structural system. For a better understanding of the effect and magnitude of each component of the overstrength factor R_o, discussion for each component will be presented along with the corresponding values drawn from the test results.

The ratio between the measured strengths of the test walls and the design strengths, presented in Table 5.2, can illustrate capacity reduction factors used in design, that is $\varphi_s = 0.85$ and $\varphi_m = 0.60$. These may be thought to combine to represent the product $R_\varphi R_{sh}$ as the ratio of measured to design capacities. Other effects such as actual versus specified strengths would further increase this ratio.

Table 5. 2: Modification factor R_φ and R_{sh}

	Design capacity (kN)	Measured capacity (kN)	$R_\varphi R_{sh}$
W2	246	360	1.46
W3	185	235	1.27
W4	188	246	1.30
W5	95	122	1.28
W6	243	377	1.55
W7	232	541	2.33

It is commonly found that actual material strengths are greater than nominal strengths specified by codes. It is not unusual to have the actual yield strength 10- 20% greater than the nominal strength provided by the supplier in order to achieve a 95% confidence level. Actually, in this study, the specified yield strength from the supplier was 400 MPa whereas the actual yield strength of the vertical reinforcement was about 500 MPa, giving a value for R_y equal to 1.25.

During the design phase, due to rounding up of the required area of reinforcement, availability of bar sizes, and space limits on number of bars, the resisting capacity of any members is always greater than the required capacity. For an efficient and economical design, it is suggested here that the overstrength should not be greater than 10% resulting in a value for R_{size} equal to 1.10.

The development of plastic hinges in redundant structures is sequential as not all walls are identical but assuming plastic hinges at the base of the walls would form at the same time, R_{mech} would be equal to 1.0. Alternatively, if some shear wall coupling exists, the resulting redundancies create opportunity for plastic behaviour to significantly increase lateral load resistance beyond capacities predicted by elastic analysis and/or statically determinate analysis.

The overstrength factor, R_o, is therefore calculated as the product of the discussed parameters ($R_o = R_y R_\varphi R_{sh} R_{size} R_{mech}$). Assuming the lower bound for each of the above parameters will result in a value for R_o equivalent to 1.54 (= 1.1x 1.27x 1.1x 1.0) which is very similar to the assigned value for $R_o = 1.50$ specified by the NBCC (2005).

Finally, it should be noted that the above discussion was based on a limited number of experimental tests for walls having the same aspect ratio. To establish more general conclusions on the behaviour of reinforced masonry shear walls, additional tests to include different aspect ratios, variable masonry compressive strength and different sizes of walls should be undertaken.

5.4   Future research

The following are suggestions for future research on topics related to the present research:

1. Tests should be conducted on reinforced masonry shear walls with different aspect ratio to investigate the contribution of shear deformations to the total deflection of the walls and to the level of energy dissipation.

2. The propagation of yielding inside the base beam should be investigated and its effect on the plastic hinge length and total deformation needs further research. Analytical models should be developed to estimate the plastic hinge length for better prediction of deflections.

3. Development of a numerical method to model the walls is recommended. In the long term, expanding it to model 3D structure to better calculate the force modification factor is essential. All such models should be evaluated by comparisons with experimental results such as those presented herein.

References

ATC, 1995. Structural response modification factors, ATC-19 report, Applied Technology Council, Redwood City, California.

Benjamin, J., and Williams, H. *"The behaviour of one storey brick shear walls"* J. Struct. Eng. Div., Vol. 84, No. ST4, 1958.

Brunner, J., and Shing, P. *"Shear strength of reinforced masonry walls."* Masonry Society Journal, Vol. 14, No.1, August 1996.

Canadian Standards Association. *"Design of concrete structures"*. CSA A23.3 (1994), Rexdale, Ontario.

Canadian Standards Association. *"Design of masonry structures"*. CSA S304.1 (2004), Mississauga, Ontario.

Chopra, A. *"Dynamics of structures."* Prentice Hall, 1995.

Collins, M., and Mitchell, D. *"Prestressed concrete structures."* Response publication, 1997.

Drysdale, R., Hamid, A., and Baker, L. *"Masonry structures- behaviour and design."* second edition, The Masonry Society, Boulder Colorado 1999.

Eikanas, I. *"Behaviour of concrete masonry shear walls with varying aspect ratio and flexural reinforcement."* M.A.Sc. Thesis, Department of Civil and Environmental Engineering, Washington State University, USA, 2003.

Elghadamsi, F., and Mohraz, B."*Inelastic earthquake spectra."* Earthquake Engineering and Structural Dynamics, Vol. 15, pp. 91-104, 1987.

Halucha, J. *"In-plane behaviour of reinforced concrete masonry panels."* M.A.Sc. Thesis, Department of Civil Engineering, McMaster University, Ontario, Canada, 2002.

Harries, K *"Discussion of seismic force modification factors for the proposed 2005 edition of the National Building Code of Canada."* Canadian Journal of Civil Engineering, Vol. 31, 2004.

Ibrahim, K., and Suter, G. *"Ductility of concrete masonry shear walls subjected to cyclic loading."* 8th North American Masonry Conference, June 6-9, 1999, USA.

International Code Council, Inc. (ICC). (2000). 2000 International Building Code (IBC), Ch.16, Falls Church, Virginia.

Jamison, J. "*Monotonic and cyclic performance of structurally insulated panel shear walls.*" Master Thesis, Department of Civil Engineering, Virginia Polytechnic Institute and State University, 1997.

Khattab, M., and Drysdale, R. "*The effect of reinforcement on the shear response of grouted concrete masonry.*" Masonry Society Journal, Vol. 12, No.1, August 1993, pp. 38-44.

Kikuchi, K. Yoshimura, K., and Tanaka, A. "*Effect of the presence of masonry units on the seismic behaviour of reinforced fully grouted concrete masonry walls.*" 8th North American Masonry Conference, June 6-9, 1999, USA.

Massone, L., and Wallace, J. "*Load-deformation responses of slender reinforced concrete walls.*" ACI Structural Journal, Vol. 101, No.1, January 2004, pp. 103-113.

Meli, R., "*behaviour of masonry walls under lateral loads.*" '*Proceedings of 5th World Conference on Earthquake Engineering, Rome, 1972.*

Miller, S. "*Experimental evaluation of the shear capacity of reinforced masonry shear walls.*" Draft of M.A.Sc. Thesis, Department of Civil Engineering, McMaster University, Ontario, Canada, 2006.

Miller, S., El Dakhakhni, W., and Drysdale, R. "*Experimental evaluation of the shear capacity of reinforced masonry shear walls.*" 10th Canadian Masonry Symposium, Banff, Alberta, June 8 – 12, 2005.

Miranda, E. "*Site dependent strength reduction factors.*" J. Structural. Engineering, ASCE, Vol. 119, No. 12, 1993.

MSJC (2005). Masonry Standards Joint Committee, "Building code requirements for Masonry Structures," ACI 530-05/ASCE 5 -05/TMS 402-05, American Concrete Institute, American Society of Civil Engineers, and The Masonry Society, Detroit, New York, and Boulder.

Nassar, A., and Krawinkler, H. "*Seismic demands for SDOF and MDOF systems.*" Report No. 95, The John A. Blume Earthquake Engineering center, Stanford University, Stanford, California, 1991.

NBCC, National Building Code of Canada (2005), Institute for Research in Construction, National Research Council of Canada, Ottawa, ON, 2005.

NEHRP, Recommendation provisions for seismic regulations for new buildings and other structures, FEMA 302 (1997), Federal emergency management agency, Washington, D.C.

Newmark, N., and Hall, W. *"Seismic evaluation and upgrading of existing buildings."* Report No. 46, Building practices for disaster mitigation, National bureau of standards, U.S. Department of Commerce, pp. 209-236, 1973.

Paulay, T. *"Earthquake-resisting shear walls- New Zealand Design Trends."* ACI Structural Journal, Vol. 77, No. 3, May-June 1980, pp. 144-152.

Paulay, T. and Priestley, M. *"Seismic design of reinforced concrete and masonry buildings."* John Wiley and Sons, New York, N.Y, 1992.

Paulay, T., and Priestley, M. *"Stability of ductile structural walls."* ACI Structural Journal, Vol. 90, No. 4, July-August 1993, pp. 385-392.

Paulay, T., Priestley, M., and Synge, A. *"Ductility in earthquake resisting squat shear walls."* ACI Structural Journal, Vol. 79, No. 4, July-August 1982, pp. 257-269.

Pilakputas, K., and Elnashai, A. *"Cyclic behaviour of reinforced concrete cantilever walls, Part 1: Experimental results."* ACI Structural Journal, Vol. 90, No.3, May-June 1995, pp. 271-281.

Priestley, M. *"Seismic design of concrete masonry shear walls."* ACI Structural Journal, Vol. 83, No. 1, January-February 1986, pp. 58-68.

Priestley, M., Seible, F., and Calvi, G. *"Seismic design and retrofit of bridges."* First, John Wiley and Sons, New York, N.Y, 1996.

Riddell, R., and Newmark, N. *"Statistical analysis of the response of nonlinear systems subjected to earthquakes."* Structural research series No. 468, Department of Civil Engineering, University of Illinois, Urbana, 1979.

Riddell, R., Hidalgo, P., and Cruz, E. *"Response modification factors for earthquake resistant design of short period structures."* Earthquake Spectra, Vol. 15, No. 3, pp. 571-590, 1989.

Sasani, M., and Kiureghian, A. *"Seismic fragility of RC structural walls: Displacement approach."* Journal of Structural Engineering, February 2001, pp. 219-228.

Schneider, R. *"Tests on reinforced grouted brick masonry shear walls"*. Report issued by California State Division of Architecture, Los Angles, 1959.

Scrivener, J. *"Concrete masonry wall panel tests – stati cracking tests with predominant flexural effects."* New Zealand concrete construction, July 1966.

Scuoglu, H. and McNiven, H. *"Seismic shear capacity of reinforced masonry piers."* J. Structural. Div., ASCE, Vol. 117, No.7, July 1991, pp. 2166-2186.

Seible, F., and Hose, Y. *"Performance evaluation database for concrete bridge components, sub-assemblages and systems under simulated seismic loads."* PEER program, University of California, San Diego, Department of Structural Engineering, January 2000.

Seible, F., Hegemier, G., Priestley, M., Kingsley, G., Igarashi, A., and Kurkchubasche A. *"Preliminary results from the TCCMAR 5- storey full scale reinforced masonry research building test."* Masonry Society Journal, Vol. 12, No.1, August 1993.

Shedid, M., Hamid, A., and Drysdale, R. *"Ductility of reinforced masonry shear walls and impact of incomplete grouting"*. 10th Canadian Masonry Symposium, Banff, Alberta, June 8 – 12, 2005.

Shing, P., Noland, J., Klamerus, E., and Spaeh., H. *"Inelastic behaviour of concrete masonry shear walls."* J. Structural. Div., ASCE, Vol. 115, No.9, September, 1989.

Shing, P., Noland, J., Spaeh, H., and Klamerus, E. *"Inelastic behaviour of masonry wall panels under in-plane cyclic loads."* 4th North American Masonry Conference, Los Angles, California, 1989.

Shing, P., Schuller, M., and Hoskere, V. *"In-plane resistance of reinforced masonry shear walls."* J. Structural. Div., ASCE, Vol. 116, No.3, March, 1990.

Shing, P., Schuller, M., Hoskere, V., and Carter, E. *"Flexural and shear response of reinforced masonry walls."* ACI Structural Journal, Vol. 87, No.6, December, 1990.

Thomsen, J., and Wallace, J. *"Displacement-based design of slender reinforced concrete structural walls- Experimental verification."* J. Structural. Div., ASCE, Vol. 130, No.7, April 2004, pp. 618-630.

Tikalsky, P., Atkinson, R., and Hammons, M. *"Compression strength of reinforced masonry under lateral tension."* J. Structural. Div., ASCE, Vol. 121, No.2, February, 1995, pp. 283-289.

Tremblay, R., leger, P., and Lu, J. *"Inelastic seismic response of concrete shear walls considering P-delta effects."* Canadian Journal of Civil Engineering, Vol. 28, 2001.

Uniform Building Code, Chapter 21- Masonry, international conference of building officials, Whittier, California, 1997.

Vecchio, F. and Collins, M. *"The modified compression field theory for reinforced concrete elements subjected to shear."* ACI Structural Journal, Vol. 83, No. 3, March-April 1983, pp. 219-231.

Vidic, T., Fajfar, P., and Fischinger, M. *"A procedure for determining consistent inelastic design spectra."* Proc. Workshop on nonlinear seismic analysis of RC structures, Bled, Slovenia, July 1992.

Voon, K., and Ingham, J. *"Shear strength of concrete masonry walls."* 7th Australasian Masonry Conference, 2004, pp. 102-112.

Williams, D. *"Seismic behaviour of reinforced masonry shear walls"* PhD. Thesis, University of Canterbury, New Zealand, 1971.

Zhang, Y., and Wang, Z. *"Seismic behaviour of reinforced concrete shear walls subjected to high axial loading."* ACI Structural Journal, Vol. 97, No. 5, September-October 2000, pp. 739-749.

APPENDIX A

Flexural design

The following equations were used to predict the ultimate flexural strength of the test walls. Units used for all of the following equations are N and mm.

$$P = C_m + C_s - T_s$$

$$C_m = 0.85 \, f'_m \, t \, (0.8 \, c)$$

$$C_s = \sum A_s f'_s \quad , \text{where } 0 \le f'_s \le f_y \quad , f'_s = \frac{c - d_i}{c} \, 0.003 \, E_s < f_y$$

$$T_s = \sum A_s f_s \quad , \text{where } 0 \le f_s \le f_y, \quad , f_s = \frac{d_i - c}{c} \, 0.003 \, E_s < f_y$$

$$M_u = C_m \left(\frac{l_w}{2} - 0.4 \, c \right) + \sum A_s f_s \left(d_i - \frac{l_w}{2} \right),$$

where:

d_i = Distance from the compression fibre to the location of reinforcement;

c = Distance from compression fibre to the neutral axis;

t = Thickness of wall;

l_w = Wall length;

P = Applied axial load;

C_m = Compression force in cross section of a masonry wall

T_s = Tensile force in reinforcement in cross section of a masonry wall

C_s = Compression force in reinforcement

f_y = Yield strength of vertical reinforcement;

f_s = Tensile stress in vertical reinforcement;

f'_s = Compressive stress in vertical reinforcement

f'_m = Average compressive strengths of masonry;

E_s = Modulus of elasticity for steel reinforcement;

M_u = Moment resistance at maximum strain in masonry; and

A_s = Area of vertical reinforcement in the wall.

The following equations were used to predict the yield flexural strength of the test walls. Units used for all of the following equations are N and mm.

$$P \quad = \quad C_m + C_s - T_s$$

$$C_m \quad = \quad 0.5\ \varepsilon_m\ E_m\ t\ c$$

$$C_s \quad = \quad \sum A_s\ f'_s \qquad , \text{where } 0 \le f'_s \le f_y$$

$$T_s \quad = \quad \sum A_s\ f_s \qquad , \text{where } 0 \le f_s \le f_y$$

$$T_i \quad = \quad A_s\ \frac{d_i\text{-}c}{d_1\text{-}c}\ f_y$$

$$\varepsilon_m \quad = \varepsilon_y\ c\ /\ (d\text{-}c)$$

$$M_u \quad = \quad C_m\left(\frac{l_w}{2} - 0.33\ c\right) + \sum A_s\ f_s\left(d_i - \frac{l_w}{2}\right) + \sum A_s\ f'_s\left(\frac{l_w}{2} - d_i\right)$$

where:

ε_m = Compressive strain in the extreme masonry fibre

E_m = Modulus of elasticity of masonry ($850 \times f'_m$)

ε_y = Yield strain of the outermost reinforcing bar in tension

APPENDIX B

Shear design

The following equations were used in predicting the shear strength for the tested walls. Units used for all of the following equations should be N and mm.

Equations in CSA S304.1 (2004):

$$V_u^s \quad = \quad V_{steel} + V_{masonry}$$

$$V_{steel} \quad = \quad 0.6\, f_y\, A_h\, \frac{0.8 \times l_w}{S_h}$$

$$V_{masonry} \quad = \quad (0.16 \times \sqrt{f_m} + 0.25\, \frac{P}{A_g})\, t\, (0.8\, l_w)$$

But V_u^s should not be greater than:

$$V_{max} \quad = \quad 0.4\, \sqrt{f_m}\ t\, (0.8\, l_w)$$

Clause 10.17.5.3.1

In the plastic hinge region, the contribution of masonry strength and axial compression is reduced by half.

Equations presented by Paulay and Priestley (1992):

a) In all regions except potential plastic hinges.

$$V_u^s \quad = \quad V_{steel} + V_{masonry}$$

$$V_{steel} \quad = \quad f_y\, A_h\, \frac{0.8 \times l_w}{S_h}$$

$$V_{masonry} \quad = \quad (0.17\, \sqrt{f_m} + 0.3\, \frac{P}{A_g})\, t\, (0.8\, l_w)$$

Given that $V_{masonry}$ should not be greater than:

$$V_1 = \quad (0.75 + 0.3\, \frac{P}{A_g})\, t\, (0.8\, l_w)$$

$$\text{nor} \quad V_2 = \quad 1.3\ t\ (0.8\ l_w)$$

But V_u^s should not be greater than:

$$V_{max1} \quad = \quad 0.2\ f_m\ t\ (0.8\ l_w)$$

$$\text{nor} \quad V_{max2} \quad = \quad 2.4\ t\ (0.8\ l_w)$$

b) In regions of plastic hinges.

$$V_u^s \quad = \quad V_{steel} + V_{masonry}$$

$$V_{steel} \quad = \quad f_y \; A_h \; \frac{0.8 \times l_w}{S_h}$$

$$V_{masonry} \quad = \quad (0.05 \; \sqrt{f_m} + 0.2 \; \frac{P}{A_g}) \; t \; (0.8 \; l_w)$$

But $V_{masonry}$ should not be greater than:

$$V_1 \quad = \quad (0.25 + 0.3 \; \frac{P}{A_g}) \; t \; (0.8 \; l_w)$$

nor $\quad V_2 \quad = \quad 0.65 \; t \; (0.8 \; l_w)$

and V_u^s should not be greater than:

$$V_{max1} \quad = \quad 0.15 \; f_m \; t \; (0.8 \; l_w)$$

nor $\quad V_{max2} \quad = \quad 1.8 \; t \; (0.8 \; l_w).$

where:

V_u^s = Shear strength of masonry wall;

V_{steel} = Shear strength of masonry wall provided by horizontal steel;

$V_{masonry}$ = Shear strength of masonry wall provided by the masonry;

V_{max} = Maximum shear strength of the wall

P = Applied axial load on the wall;

f_m = Average compressive strengths of masonry four course prisms;

A_g = Horizontal cross section area of wall (ie: length x thickness);

S_h = Vertical spacing between horizontal reinforcement;

A_h = Area of horizontal reinforcement in a typical cross section;

f_y = Yield strength of horizontal reinforcement;

t = Thickness of wall; and

l_w = Wall length.

APPENDIX C

Relationship between displacement ductility and force modification factor

The relationship between displacement ductility, μ_Δ, and the force modification factor, R, can be setup using the concept of equal energy (Paulay and Priestley (1992), and Drysdale et al. (1999)) as most masonry structures are considered to have low period (0.4s to 0.8s).
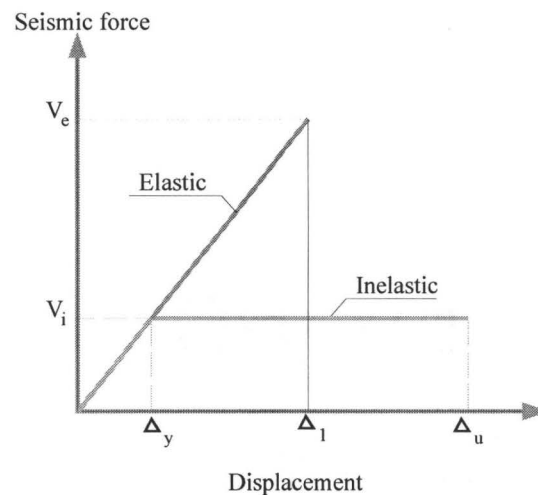
Fig. C.1: Elastic and inelastic behaviour

The background of the relationship between the displacement ductility and force modification factor is presented by the following basic mechanics:

$$\text{Area for elastic response} \quad = \quad V_e \, \frac{\Delta_l}{2}$$

$$\text{Area for inelastic response} \quad = \quad V_i \, \frac{2\,\Delta_u - \Delta_y}{2}$$

Equating both equations knowing that: $\quad R \;=\; \dfrac{V_e}{V_i}$

$$R \;=\; \frac{2\,\Delta_u - \Delta_y}{\Delta_l} \quad , \qquad \text{which gives} \quad \Delta_l = \frac{2\,\Delta_u - \Delta_y}{R}$$

Equating the two areas but subtracting the triangular area between V_i and Δ_y from both areas.

$$\frac{V_e + V_i}{2} \ (\Delta_1 - \Delta_y) \ = \ V_i \ (\Delta_u - \Delta_y)$$

$$\frac{V_e + V_i}{V_i} = 2 \ \frac{\Delta_u - \Delta_y}{\Delta_1 - \Delta_y}$$

dividing left term by "Δ_y" and having: $\mu_\Delta = \dfrac{\Delta_u}{\Delta_y}$

$$R + 1 \ = \ 2 \ \frac{\mu_\Delta - 1}{\Delta_1 / \Delta_y - 1}$$

having: $\Delta_1 = \dfrac{2 \, \Delta_u - \Delta_y}{R}$

$$\Delta_1 / \Delta_y = \frac{2 \, \Delta_u - \Delta_y}{R \ x \ \Delta_y} = \frac{2 \, \mu_\Delta - 1}{R}$$

$$\Delta_1 / \Delta_y - 1 = 2 \ \frac{\mu_\Delta - 1}{1 + R}$$

$$\frac{2 \, \mu_\Delta - 1}{R} - 1 = 2 \ \frac{\mu_\Delta - 1}{1 + R}$$

$$\frac{2 \, \mu_\Delta - 1}{R} - 1 - R + 2 \, \mu_\Delta - 1 = 2 \, \mu_\Delta - 2$$

$$2 \, \mu_\Delta - 1 = R^2$$

$$R = \sqrt{2 \, \mu_\Delta - 1}$$

where: Δ_y = Lateral wall displacement at first yield of reinforcement;

Δ_u = Lateral wall displacement at maximum compressive strain;

Δ_1 = Lateral wall displacement corresponding to elastic response;

V_e = Force corresponding to elastic wall behaviour;

V_i = Force corresponding to inelastic wall behaviour;

μ_Δ = Displacement ductility; and

R = Force modification factor.

APPENDIX D

Displacement prediction
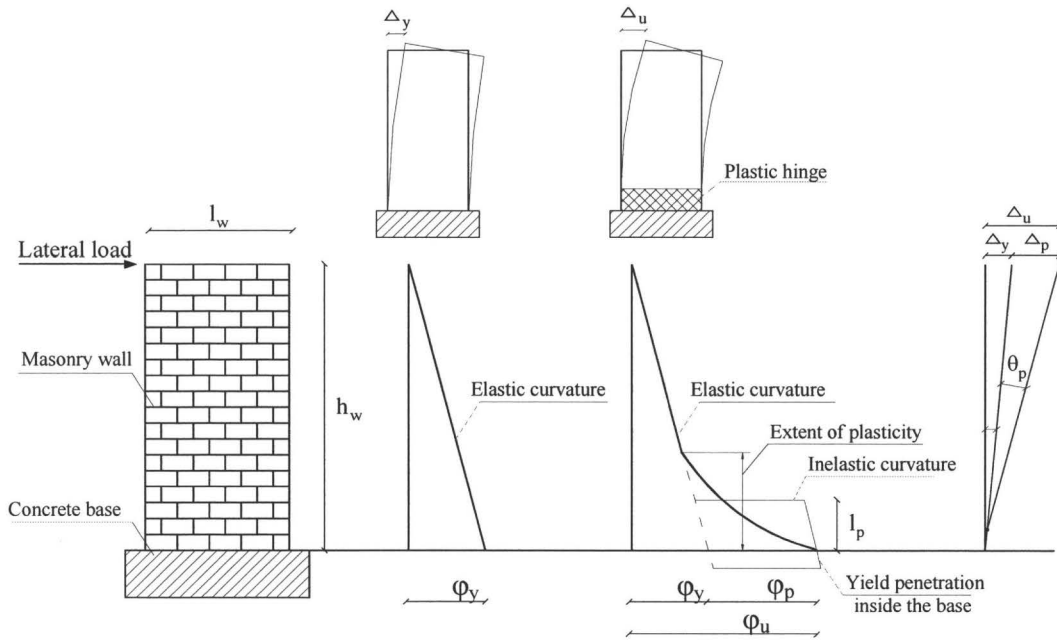
Fig. D.1: Elastic and inelastic deformation

The approach relies on predicting the displacements based on calculating curvatures at the base of the wall at first yield of extreme reinforcing bars and at maximum compressive strain in masonry. The equations used for predictions are presented below:

$$V_y = \frac{M_y}{h_w}$$

$$\varphi_y = \frac{d_1 - c_y}{\varepsilon_y}$$

$$\theta_y = \varphi_y \, \frac{h_w}{2}$$

$$\Delta_y = \varphi_y \, \frac{h_w^2}{3} = \theta_y \, \frac{2}{3} \, h_w \quad , \text{then} \quad \% \, \text{Drift}_y = \frac{\Delta_y}{h_w} \times 100$$

$$V_u = \frac{M_u}{h_w}$$

$$\varphi_u = \frac{c_u}{\varepsilon_m}$$

$$\theta_p = \varphi_p \, l_p, \quad \text{where: } \varphi_p = \varphi_u - \varphi_y$$

$$\Delta_p = \theta_p \, (h_w - 0.5 \, l_p) \quad , \text{then} \quad \% \, \text{Drift}_u = \frac{\Delta_u}{h_w} \times 100$$

233

where, $\Delta_u = \Delta_y + \Delta_p$

$\mu_\varphi = \dfrac{\varphi_u}{\varphi_y}$

$\mu_\Delta = \dfrac{\Delta_u}{\Delta_y} = 1 + \dfrac{\Delta_p}{\Delta_y} = 1 + 3\,(\mu_\varphi - 1)\ \dfrac{l_p}{h_w}\ (1 - 0.5\ \dfrac{l_p}{h_w})$

where:

d_1	=	The distance from extreme compression fibre to the first tension bar;
ε_y	=	yield strain of steel reinforcement;
ε_m	=	Maximum compressive strain in masonry;
c_y	=	Length of compression zone at first yield of reinforcement;
c_u	=	Length of compression zone corresponding to maximum load;
M_y	=	Moment resistance at first yield of reinforcement;
V_y	=	Lateral load resistance at first yield of reinforcement;
M_u	=	Moment resistance at maximum strain in masonry;
V_u	=	Lateral load resistance at maximum strain in masonry;
φ_y	=	Curvature at the base of the wall at first yield of reinforcement;
φ_u	=	Curvature at the base of the wall at maximum strain in masonry
θ_y	=	Rotation of the wall at first yield of reinforcement;
θ_p	=	Plastic rotation of the wall;
Δ_y	=	Lateral displacement of wall at first yield of reinforcement;
Δ_p	=	Plastic displacement of wall;
Δ_u	=	Maximum Lateral displacement of wall;
μ_φ	=	Curvature ductility;
μ_Δ	=	Displacement ductility;
R	=	Force modification factor;
l_w	=	Wall length; and
l_p	=	Equivalent plastic hinge length.

APPENDIX E

Decoupling of flexural and shear displacements
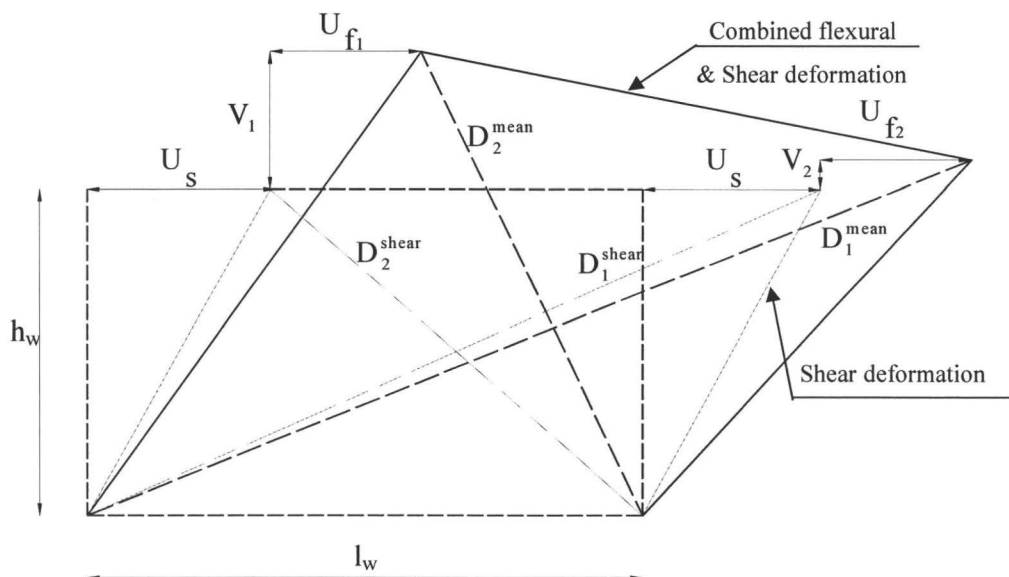
Figure E.1: Decoupling of total displacement (Massone and Wallace (2004))

Flexural displacements (U_f) are calculated by assuming a triangular curvature distribution over the wall height having its centroid at two third of the height from the top of the wall as suggested in by Massone and Wallace (2004). Corrected shear displacements (U_o) are calculated after isolating the effect of vertical displacement from the diagonal readings.

$$U_f = \alpha_h \, \theta_h \, h_w$$

Where $\qquad \theta_h = \dfrac{v_1 - v_2}{l_w}$, $\alpha_h = 0.67$

$$U_c = \frac{\sqrt{D_1^{means^2} - (h_w + v_2)^2} - \sqrt{D_2^{means^2} - (h_w + v_1)^2}}{2} - U_f$$

$$U_o = \frac{\sqrt{D_1^{means^2} - h_w^2} - \sqrt{D_2^{means^2} - h_w^2}}{2}$$

APPENDIX F

Description of test walls

The following table presents the design values for strength and displacements for all walls.

Flexure strength calculations are based on equations presented in Appendix A. Displacement calculations are based on equations presented in Appendix D. Force modification factor, R, is calculated based on equations presented in Appendix C.

Masonry strain equal to 0.0025 is used for all calculation, yield strength of vertical bars equal to 500 MPa except for Wall 7, and plastic hinge length equal to half the wall length = 900 mm. Yield strength for vertical reinforcement used for Wall 7 was 625 MPa.

Table F. 1: Design values for test walls

	W5	W4	W3	W2	W6	W7
Steel bars	5 # 15	9 # 20	5 # 25	9 # 25	9 # 25	9 # 25
ρ_v	0.29	0.78	0.73	1.31	1.31	1.31
P_t (kN)	26	26	26	26	282	539
P/A (% f'm)	0	0	0	0	5	10
M_y (kN.m)	302.42	671.06	679.12	1047.90	1188.97	1483.67
V_y (kN)	84.00	186.41	188.64	291.08	330.27	412.13
c_y (mm)	326.23	456.48	445.41	532.23	583.56	657.72
$\varphi_y \times 10^{-6}$	1.78	1.95	1.94	2.07	2.16	3.00
Δ_y (mm)	7.69	8.43	8.36	8.95	9.32	12.95
drift$_y$ (%)	0.21	0.23	0.23	0.25	0.26	0.36
M_{ult} (kN.m)	427.42	937.42	921.88	1378.08	1450.01	1653.91
V_{ult} (kN)	118.73	260.39	256.08	382.80	402.78	459.42
c_{ult} (mm)	205.38	414.15	372.21	527.15	586.65	674.55
$\varphi_u \times 10^{-6}$	12.17	6.04	6.72	4.74	4.26	3.71
θ	0.00935	0.00368	0.00430	0.00240	0.00189	0.00064
Δ_p (mm)	29.46	11.58	13.55	7.57	5.96	2.01
Δ_{max} (mm)	37.15	20.01	21.92	16.52	15.29	14.96
$\mu \varphi$	6.84	3.09	3.47	2.29	1.97	1.24
$\mu \Delta$	4.83	2.37	2.62	1.85	1.64	1.15
R	2.94	1.94	2.06	1.64	1.51	1.14
ϵ_{steel}	0.0182	0.0078	0.0089	0.0056	0.0047	0.0038
Strain x ε_y	7.28	3.10	3.57	2.22	1.90	1.22

APPENDIX G

Prism test results

The elastic modulus calculated for all masonry prisms tested are included in the following table. The secant modulus at 33% of f'$_m$, and at 50% of f'$_m$ are presented for each prism in Table G.1. Three prisms (a, b, and c) were to be tested for each group (G1 to G9). For further information refer to Section 2.4.6 and to Fig. 2.11 in Chapter 2. Stress-strain relationships for all prisms are presented in Fig. G1.

Table G.1: Prism test results (extension to Table 2.8)

Group	Secant E_m (N/mm^2)	Masonry prisms			Average E_m	Factor x f'$_m$
		a	b	c		
G1	[f'$_m$] MPa at 33%	[15.4] 12723	[14.3] 19699	[13.3] 14140	[14.4] 15521	1078
	at 50%	12335	12744	13375	12818	890
G2	[f'$_m$] at 33%	[15.2] 16587	[14.0] 13701	----	[14.6] 15144	1034
	at 50%	14116	12474	----	13296	911
G3	[f'$_m$] at 33%	[16.1] 17488	[16.7] 14695	[15.1] 14701	[16.0] 15628	974
	at 50%	13557	13903	13231	13564	848
G4	[f'$_m$] at 33%	[13.9] 13603	[13.1] 18227	----	[13.6] 15915	1172
	at 50%	10495	13072	----	11784	866
G5	[f'$_m$] at 33%	[13.7] 12621	[14.4] 11560	[14.3] 13921	[14.2] 12701	897
	at 50%	12444	11223	11669	11779	829
G6	[f'$_m$] at 33%	[15.8] 16799	----	----	[15.8] 16799	1063
	at 50%	15326	----	----	15326	970
G7	[f'$_m$] at 33%	[16.3] 17181	[15.8] 11775	[16.2] 13187	[16.1] 14048	873
	at 50%	14133	11727	12263	12708	789
G8	[f'$_m$] at 33%	[17.2] 12179	[16.4] 10542	----	[16.8] 11361	676
	at 50%	11533	9585	----	10559	629
G9	[f'$_m$] at 33%	[12.9] 18998	[13.4] 14303	----	[13.2] 16651	1261
	at 50%	15818	11087	----	13452	1019

From review of the potentiometer displacement data, inconsistencies in the data are readily apparent, especially at low stresses. Therefore, for the secant modulus over the low range (up to 0.33 f'_m), some discretion was used in choosing the lower limit nominally set at 0.05 f'_m. In fact, it typically was about 0.07 f'_m but was an extreme of 0.15 f'_m for specimens G1 (a) and G3 (a). To provide a more consistent evaluation of E_m, the second secant modulus reported used a constant 0.10f'_m (except for specimen G1 (a) and G3 (a)) and the upper limit of 0.50 f'_m. As can be seen, these latter values were much more consistent between groups. They are also much closer to the CSA S304.1 value of 850 f'_m and generally fall within the normally observed range.
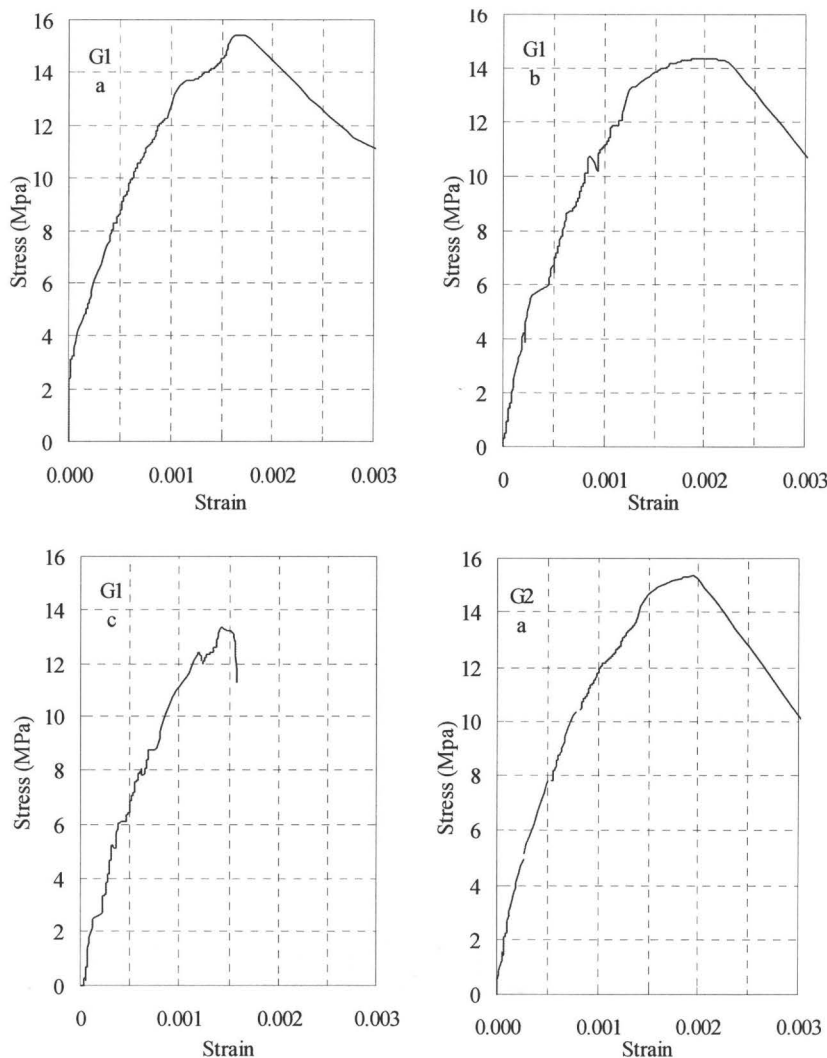

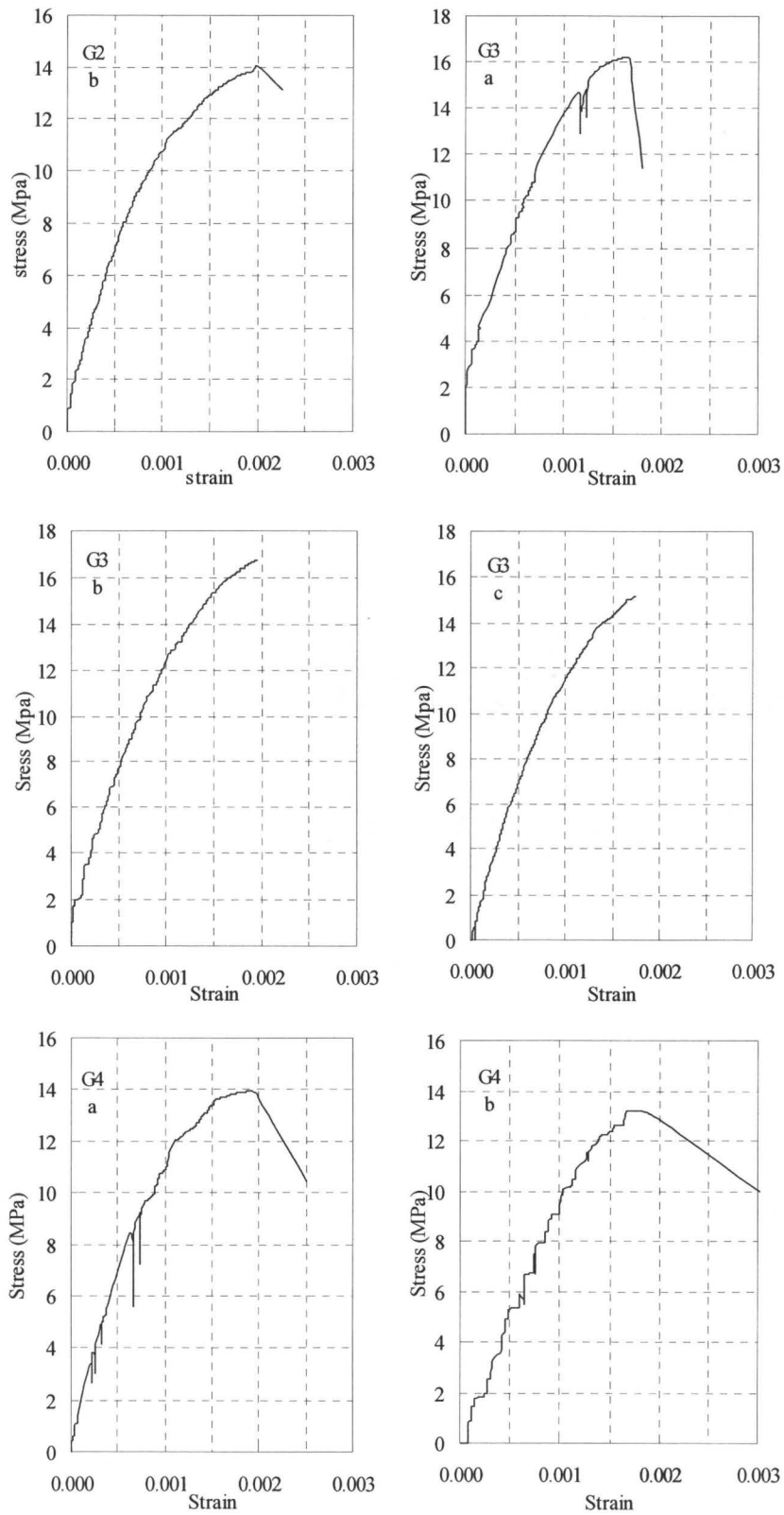Fig. G1: Stress-Strain relationships for test prism

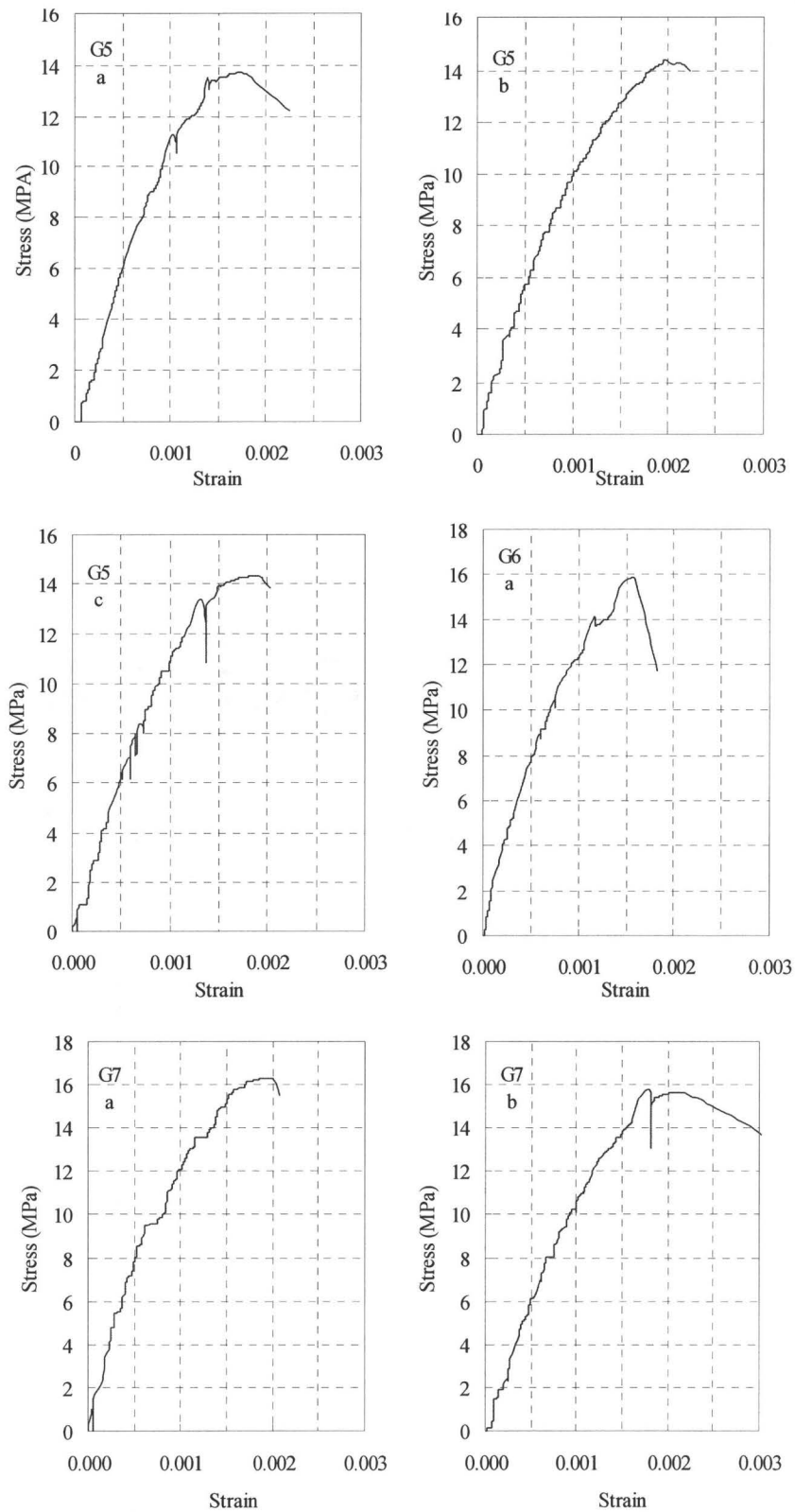Fig. G1: Stress-Strain relationships for test prism (cont.)

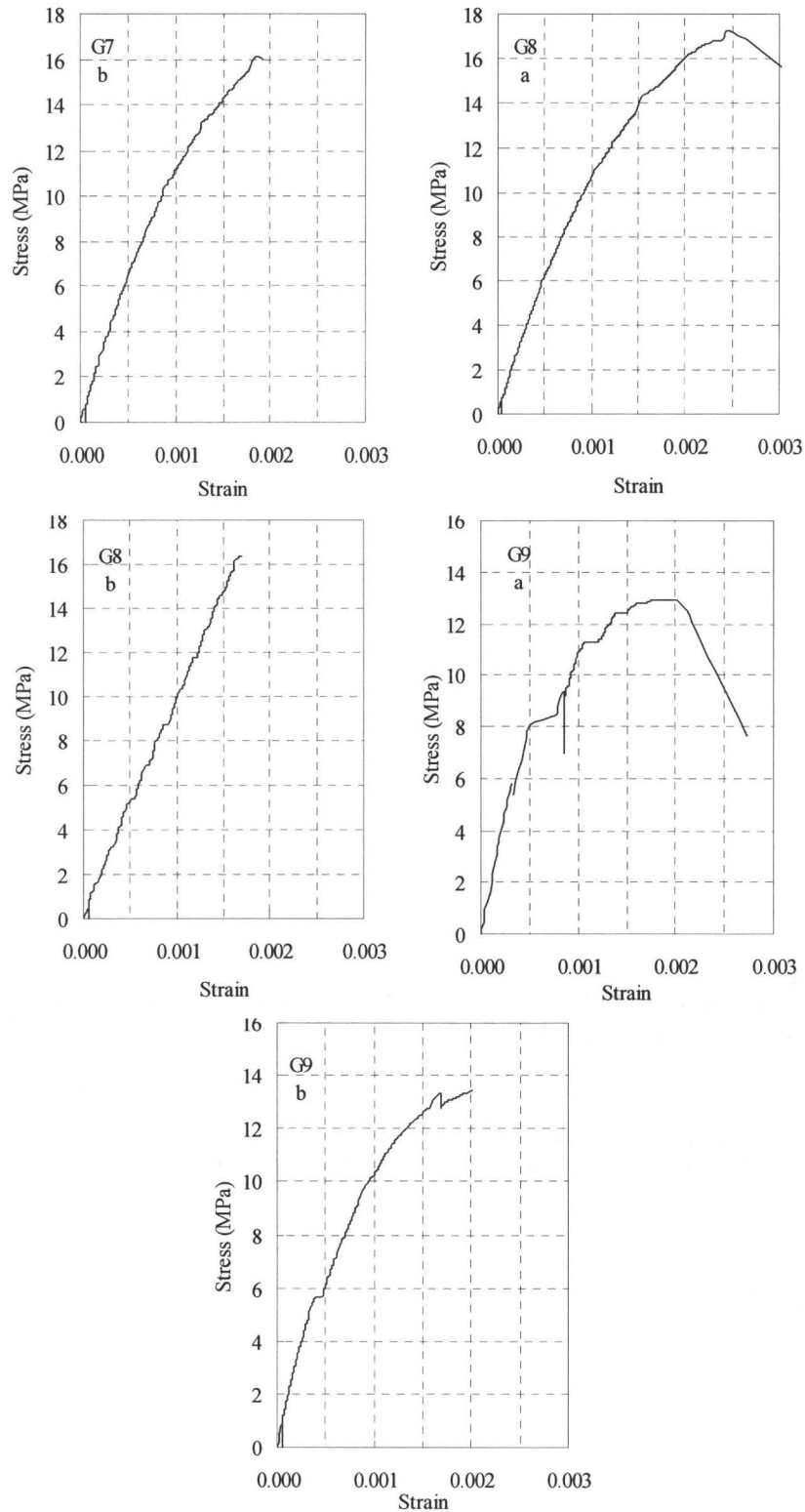Fig. G1: Stress-Strain relationships for test prism (cont.)

Fig. G1: Stress-Strain relationships for test prism (cont.)

APPENDIX H

Stiffness calculations

The estimated stiffnesses of the walls reported in Table 4.1 were calculated based on the values of gross moment of inertia, I_g, cracked moment of inertia, I_{cr}, gross masonry area, A_g, cracked masonry area, A_{cr}, and modulus of elasticity for masonry taken equal to 850 f'$_m$. The contribution of vertical reinforcement to moment of inertia of the section was included in the calculations of I_g and I_{cr}.

Table H.1: Section properties of the test walls

	I_g (x10^{11} mm^4)	$E_m I_g$ (x10^{15} Nmm^2)	k_g * (kN/mm)	kd** (mm)	A_{cr}/A_g (%)	I_{cr} (x10^{10} mm^4)	$E_m I_{cr}$ (x 10^{14} Nmm^2)	k_{cr} *** (kN/mm)
W3 (0.73%) [0 MPa]	1.04	1.33	70.41	408.74	22.7	2.63	3.36	17.48
W5 (0.3%) [0 MPa]	0.97	1.24	66.44	295.57	16.4	1.23	1.58	8.81
W4 (0.78%) [0 MPa]	1.03	1.31	69.75	419.45	23.3	2.57	3.28	17.24
W2 (0.3%) [0 MPa]	1.10	1.40	73.64	493.82	27.4	3.81	4.86	24.36
W6 (1.3%) [0.75MPa]	1.10	1.40	73.64	541.70	30.1	3.79	4.84	24.77
W7 (1.3%) [1.50MPa]	1.10	1.40	73.64	566.71	31.5	3.81	4.87	25.12

*k_g is the uncracked stiffness of the masonry section from Eq. 4.1

*kd is the length of the uncracked masonry area

*k_{cr} is the cracked stiffness of the masonry section from Eq. 4.1

APPENDIX I

Discussion of changes in period of variation

Changes in period result from changes in stiffness of the walls. These changes in the period of the elements in the structure will affect the global period of the structure which in turn will influence the force attracted during earthquake loading.

Given that, in this case, there is no value for the mass to use in calculating the periods, but based on this mass being constant, a normalized period given by the following equations is presented to indicate the trend of changes in period that can be expected for a structure having the given levels of stiffness degradation. The normalized period, T_{norm}, at any drift level is calculated based on the square root of the inverse of the normalized stiffness (see Fig. H.1).

$$T_{norm} = \sqrt{\frac{K_{initial}}{K_i}}, \ T_{norm} = \frac{T_i}{T_{initial}}, \text{ and } T_i = 2 \ \Pi\sqrt{\frac{m}{K_i}}$$

where: $K_{initial}$ = the initial stiffness
$\quad\quad\quad K_i$ = the secant stiffness at drift level (i)
$\quad\quad\quad T_{initial}$ = calculated period at initial stage
$\quad\quad\quad T_i$ = calculated period at drift level (i)
$\quad\quad\quad m$ = the mass of the structure

The increase in the normalized period with respect to the decrease in stiffness is plotted in Fig. H.1 (a) to show the effect of the significant decrease in stiffness on the corresponding period. It can be seen from the figure that, at drift levels of 1%, the period will vary between three and five times the period corresponding to the initial stage. As suggested in Section 4.3, this may result in a much lower force to be resisted by the walls under earthquake loading. Also, the use of a different approach for calculating the force modification factors may be appropriate. The normalized period plotted in Fig. H.1 (b) with respect to the displacement ductility indicates that, at first yield, the period at least doubles with respect to the period corresponding to initial stage and triples at a displacement ductility of 3.

It can be seen that the use of a single value for the period in estimating the equivalent elastic force may lead to very inaccurate estimations of the

design forces for structures. In designing different structures using different performance based levels such as fully operational, life safety or collapse prevention, assigning different values for the period to be used in design will provide a better estimate of the equivalent elastic design force for earthquake loading.
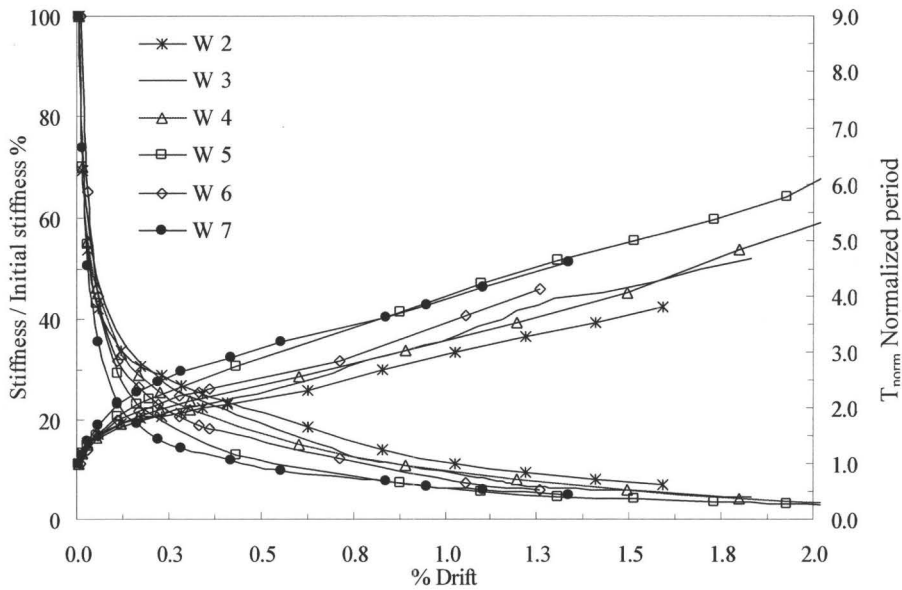
(a): Stiffness and period ratio versus percent drift
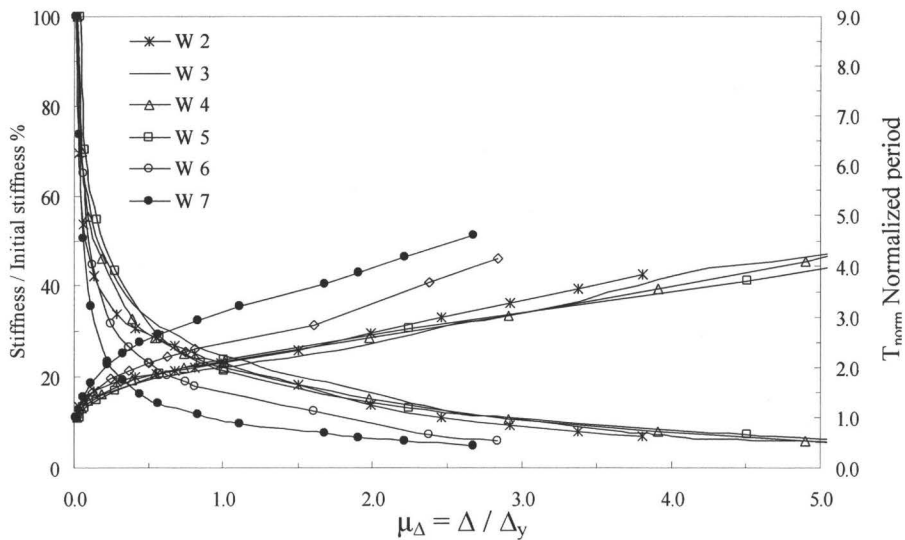
(b): Stiffness and period ratio versus displacement ductility

Fig. H.1: Variation in period related to changes in stiffness

Ductile structures have an inherent "safety valve" where damage from high loads changes the frequency and reduces the loads that they must be able to resist.